# EXPLORING OPTICAL SENSORS FOR HYDROGEN PEROXIDE ON SILK AND PAPER PLATFORMS USING CHEMICAL DYE, PEROXIDASE AND GOLD NANOCLUSTERS AS SIGNAL GENERATING SYSTEMS

by

**Phurpa Dema Thungon**

Roll No.: 146106001

*A Thesis*

Submitted in Fulfillment of the
Requirements for the Award of the Degree of

**DOCTOR OF PHILOSOPHY**

at the

**Indian Institute of Technology Guwahati**

Department of Biosciences and Bioengineering
Indian Institute of Technology Guwahati
Guwahati, Assam, India

*March 2022*

**INDIAN INSTITUTE OF TECHNOLOGY GUWAHATI**

**Department of Biosciences and Bioengineering**

**Guwahati – 781039**

---

## STATEMENT

I do hereby declare that the matter embodied in this thesis entitled "**Exploring optical sensors for hydrogen peroxide on silk and paper platforms using chemical dye, peroxidase and gold nanoclusters as signal generating systems**" is the result of investigations carried out by me in the Department of Biosciences and Bioengineering, Institute of Technology Guwahati, Assam, India, under the guidance of **Prof. Pranab Goswami.**

In keeping with the general practice of reporting scientific observations, due acknowledgements have been made wherever the work described is based on the findings of other investigators.

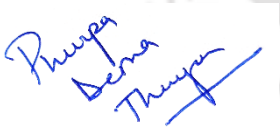

**March 2022**

**Phurpa Dema Thungon**

**INDIAN INSTITUTE OF TECHNOLOGY GUWAHATI**

**Department of Biosciences and Bioengineering**

**Guwahati – 781039**

---

## CERTIFICATE

It is certified that the work described in this thesis, entitled "**Exploring optical sensors for hydrogen peroxide on silk and paper platforms using chemical dye, peroxidase and gold nanoclusters as signal generating systems**", done by Ms. **Phurpa Dema Thungon** (Roll No. 146106001) for the award of degree of Doctor of Philosophy is an authentic record of the results obtained from the research work carried out under my supervision in the Department of Biosciences and Bioengineering, Indian Institute of Technology Guwahati, India.

The results embodied in this thesis have not been submitted to any other University or Institute for the award of any degree.

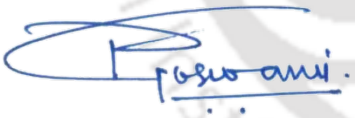

**Prof. Pranab Goswami**

**(Thesis Supervisor)**


*Dedicated to,*

*Achi (Papa)*

*Late. Shri. Ledo Thungon*

# Acknowledgement

*I take this opportunity with much pleasure to express my sincere gratitude to all those who have supported me through the course of my journey towards producing this thesis. First, I am thankful to Indian Institute of Technology Guwahati for giving me the opportunity to carry out Ph.D. in this esteemed Institute. I would like to extend my deepest gratitude towards my thesis supervisor* ***Prof. Pranab Goswami*** *for mentoring me to throughout this PhD journey and teaching me perseverance and patience in research work. His constant encouragement, time, ideas, and the freedom to do research work has helped me to propel my work in a fruitful direction. I would also like to thank him for the well-equipped laboratory, vast resources and dedicated work culture that has made working in his laboratory a pleasant experience. His optimism and down to earth and helpful nature make him one of the best teachers in my life.*

*I am thankful to my doctoral committee members, members* ***Prof. R. Tamuli****,* ***Prof. A. Ramesh****, and* ***Prof. V. V. Goud*** *for critically evaluating my research work and for their valuable suggestions which helped me produce better research work.*

*I would also like to thank my Oversee-Supervisor in University of Alberta, Canada,* ***Prof. A. Meldrum*** *for giving me the wonderful opportunity to work in his laboratory under the SERB Oversees Doctoral Fellowship (2019). I learnt so much in under his guidance about science & research, Mathematica, Photoluminescence, Biking, Politics and Russian literature. I am thankful to our collaborator* ***Sergei Vagin*** *from Technical University of Munich, Germany for providing me with his knowledge and help and for synthesizing the fluorophore used in my thesis. I extend my sincere gratitude to the* ***Science and Engineering Research Board (SERB),*** *Government of India for providing me with their prestigious SERB Oversees Doctoral Fellowship (2019) for executing a part of my research in the University of Alberta, Canada.*

*I would like to thank CIF especially* ***Milan Mahadani*** *from FETEM lab, BSBE, COE for providing the access to various instruments without which this study would not be feasible.*

*Special thanks to my past and present lab members,* ***Babina, Priyamvada, Ankana di, Lightson, Priyanki, Sharbani, Naveen, Santhosh bhaiya, Abdul, Vinay, Smita, Pooja, Malay, Nabajyoti, Kangkana,***

***Rupinder,*** *and* ***Mrinal bhaiya*** *who have shared their struggles and supported me in all my endeavours. A special thanks to my M. Tech juniors* ***Torsha*** *and* ***Nishu*** *who helped me in my research work.*

*I would also like to thank and appreciate my friends,* ***Nama, Beth, Kaushiki, Ruchika, Shruti, Mariana, Lijuan, Tanisha, Hui*** *and* ***Inês*** *who always brightened my days and cheered me up when things got tough, and for the wonderful memories we shared together during the PhD time.*

*I also express my profound debt to my family members, especially my late father* ***Achi****, and* ***Ama*** *as well as my sisters* ***Leki****,* ***Sonam*** *and* ***Priyanjali*** *for their unconditional love, encouragement, sacrifices, and faith in my capabilities to fulfil this journey.*

*Most importantly, I would like to praise and thank* ***Father God Almighty****, who has granted me countless blessing, knowledge, and opportunity, so I could be able to accomplish this thesis.*

***Phurpa Dema Thungon***

# Table of Contents

## CHAPTER II



## CHAPTER III

# Abstract

The current investigation focuses on the development of optical sensors for the detection of hydrogen peroxide ($H_2O_2$) using silk and paper as platforms and peroxidase, protein stabilized gold nanoclusters and organic dye as signal generating systems. Based on the investigation we put forward three independent proofs of concepts for optical detection of $H_2O_2$ namely, (A) Development of a paper-based sensor for optical detection of $H_2O_2$ using an organic fluorophore, and its application for developing a paper-microfluidic fluorescent-based alcohol biosensor. The fluorophore on interaction with $H_2O_2$ showed fluorescent emission shift from blue to red/orange and was embedded on a paper disc to prepare a simple optical $H_2O_2$ sensor. Further, a microfluidic paper-based analytical device (µPAD) was designed using the fluorophore-infused paper for sensing ethanol. (B) Development of peroxidase-based colorimetric detection for $H_2O_2$ and the application of this sensor to develop a silk-paper hybrid platform-based colorimetric alcohol biosensor for on-site application. Here, peroxidase was co-entrapped with alcohol oxidase (AOx) within the same silk fibroin (SF) film to develop a bi-enzyme film, which showed good stability and activity. Lastly, (C) Fluorometric and colorimetric detection of $H_2O_2$ using protein stabilized gold nanoclusters (AuNCs). This study used catalase (Cat) to synthesize two types of Cat-Au NCs. The interactions of the NCs with $H_2O_2$ were then investigated and the concept was translated for detecting $H_2O_2$. The performances of all the developed sensors were examined by using different parameters such as limit of detection (LoD), dynamic range and operational stability. We critically evaluated our works and forwarded our views on the future scopes for translating these proofs of concept to commercially viable products.

*(A) Development of a paper-based sensor for optical detection of $H_2O_2$ using an organic fluorophore, and its application for developing a paper-microfluidic fluorescent-based alcohol biosensor*

Paper-based devices for the detection of $H_2O_2$ and ethanol were developed in this work. The method was based on a fluorophore consisting of a short-chain conjugated molecular unit susceptible to the protonation of its terminal pyridine groups (c-P4VB), with a carboxyl-functionalized sidechain that acts as a binder and renders it water-soluble. c-P4VB in presence of $H_2O_2$ showed fluorescent emission shift from blue to red/orange. This fluorophore was embedded on paper and the resulting fluorescent paper device also yielded large fluorescent emission changes when exposed to $H_2O_2$ in

aqueous solutions. The limit of detection (LoD) of this simple paper- $H_2O_2$ sensor was 16.7 mM with a dynamic range up to 2.9 M $H_2O_2$. Next, using AOx-catalyzed rection that produces $H_2O_2$ from ethanol, we developed a two-zone cut-out µPAD, containing a reactor zone in which the analyte was dropped and an adjacent sensor zone (c-P4VB paper) where a fluorescence color shift proportional to the ethanol concentration occurred. The LoD of the microfluidic ethanol biosensor was 8.5 mM or 0.05 v/v%. This biosensor was employed to detect the ethanol concentration in commercially available vodkas using pixel intensity as the response signal captured through a smartphone camera.

*(B) Development of peroxidase-based colorimetric detection for $H_2O_2$ and its application in the development of a silk-paper-based hybrid µPAD biosensor for colorimetric detection of alcohol*

The commercial success of a paper-based microfluidic optical biosensing device with enzymes as recognition elements may be achieved at a greater speed by improving the stability of the enzyme, averting the coffee-ring effect on the detection film, and making it a stand-alone system without embarking on any additional steps for dispensing the reagents. In this study, these critical issues were addressed by introducing silk-fibroin (SF) film as immobilizing matrices for the enzymes and chromogenic reagent (ABTS) and wave-design microfluidic channels in the chromatographic paper for developing a hybrid microfluidic paper-based analytical device (µPAD) for methanol detection following peroxidase (HRP) based reaction. Firstly, HRP was entrapped in non-dissolvable SF film. This HRP SF film was tested as an $H_2O_2$ biosensor which gave good sensitivity, LoD of 0.58±0.001 mM $H_2O_2$ and a dynamic range of up to 300 mM, as well as showing good stability. Next, the activity of the AOx as a biorecognition element for methanol could be wholly retained in a non-dissolvable SF film (pore size < 3.5 microns) until 40 days of storage at room temperature (RT), and the reason is attributed to the reduced oxygen permeability to the film, that protected the AOx from the inhibitory effect of oxygen. Similarly, ABTS in the dissolvable SF film was protected from air oxidation with sustained chemical integrity even up to two months of storage at RT. The detection approach exploited purple color as a high contrast response signal generated from ABTS di-cation formed from the reaction of SF protein with the ABTS radicals generated from the substrate-dependent peroxidase reaction. The wave-designed microfluidic channels could significantly reduce the coffee ring effect in the detection film by imparting turbulence behavior to the fluid and reducing the evaporation flux of the reagents. Both AOx and HRP were co-entrapped to prepare the bi-enzyme SF films which offered high sensitivity to the µPAD device with an LoD of 1±0.05 mM and a large dynamic range of 1 mM-2 M for methanol discerned from a polynomial fitting. The stand-alone hybrid µPAD biosensor for methanol developed through this investigation has great potential for commercial applications.

*(C) Fluorometric and colorimetric detection of $H_2O_2$ using catalase protein-stabilized gold nanoclusters (Au NCs) as optical probes.*

The research on protein-stabilized gold nanoclusters is gaining pace due to their high prospect of replacing many protein-based enzymes for developing stable and low-cost catalysts for diverse applications. Herein, catalase was successfully transmuted into an $H_2O_2$ sensing probe by removing the heme prosthetic group and inducting gold nanoclusters (AuNCs) in the protein matrix. Two types of catalase protein-stabilized AuNCs (Cat-AuNCs), red fluorescent (RF) and blue-fluorescent (BF) Cat-AuNCs of different sizes, were prepared by using 1 mM and 5 mM $Au^{3+}$ solutions, respectively. We postulated that the variations of the AuNCs sizes are due to the changes in the secondary structure of the protein caused by the initial pH, where the $\beta$-sheet structures may play role in the synthesis of smaller (1.5 nm) BF Cat-AuNCs. The BF Cat-AuNCs quantum dots were transformed into plasmonic nanoparticles with an average size of 10 nm through an internal aggregation process of the clusters upon their interactions with $H_2O_2$. The intensity of the plasmonic signal ($\lambda_{520nm}$) was increased with the increasing concentration of $H_2O_2$, offering a linear detection range of 20-200 mM ($R^2$=0.99) and an LoD of 1 mM for the peroxide. The visual identification of the plasmonic color change could also be exploited to develop a qualitative method for $H_2O_2$ detection. Additionally, a dynamic quenching-based interaction of RF Cat-AuNCs with $H_2O_2$ was extrapolated to develop a fluorescence-based analytical method for $H_2O_2$ that offered an LoD of 0.6 mM and a linear range of 1-50 mM ($R^2$ = 0.986). These Cat-AuNCs probes are highly promising for quantitative detections of $H_2O_2$ in a broad concentration range for diverse applications.

Finally, we critically evaluated our works and forwarded our views on the future scopes of translating these proofs of concepts to commercially viable products.

# List of abbreviations

| | |
|---|---|
| ABTS | 2,2'-azino-bis(3-ethylbenzothiazoline-6-sulphonic acid) |
| $ABTS^{\bullet+}$ | ABTS cation radical |
| $ABTS^{2+}$ | ABTS dication |
| Ag | Silver |
| AgNPs | Silver nanoparticles |
| AKD | Alkyl ketene dimer |
| AOx | Alcohol oxidase |
| Au | Gold |
| AuNCs | Gold nanoclusters |
| $Au_8NCs$ | Clusters with 8 Au atoms |
| $Au_{25}NCs$ | Clusters with 25 Au atoms |
| AuNPs | Gold nanoparticles |
| BF | Blue fluorescent |
| BPE | Bipolar electrode |
| BSA | Bovine serum albumin |
| Cat | Catalase |
| c-P4VB | Sodium 6-(4-methoxy-2,5-bis((E)-2-(pyridin-4-yl)vinyl)phenoxy)hexanoate |
| CD | Circular Dichroism |
| $CDCl_3$ | Deuterated chloroform |
| CNTs | Carbon nanotubes |
| Cpd I | Compound I |
| Cpd II | Compound II |
| Cu | Copper |
| CuNPs | Copper nanoparticles |
| CuNCs | Copper nanoclusters |

| | |
|---|---|
| DE | Driving electrode |
| DFT | Density functional theory |
| DLS | Dynamic light scattering |
| DMSO | Dimethyl sulfoxide |
| DNA | Deoxyribonucleic acid |
| DOEs | Diffractive optical elements |
| DSB | Distyrylbenzenes |
| EDC | 1-Ethyl-3-(3-dimethylaminopropyl) carbodiimide |
| ELISA | Enzyme-linked immunosorbent assay |
| EtOH | Ethanol |
| FAD | Flavine adenine dinucleotide |
| FESEM | Field Emission Scanning Electron Microscope |
| $FeSO_4$ | Ferrous sulphate |
| FRET | Fluorescence resonance energy transfer |
| GO | Graphene oxide |
| GOx | Glucose oxidase |
| g-$C_3N_4$ | Graphite-like carbon nitrides |
| GQDs | Graphene quantum dots |
| $HAuCl_4$ | Aurichlorohydric acid |
| HCl | Hydrocholric acid |
| HBr | Hydrobromic acid |
| $H_2O_2$ | Hydrogen peroxide |
| $^1H$ NMR | Proton nuclear magnetic resonance |
| Hb | Hemoglobin |
| HRP | Horseradish Peroxidase |
| IFE | Inner field effect |
| IoT | Internet of Things |
| $K_4Fe(CN)_6$ | Potassium ferrocyanide |
| KOtBu | Potassium tertiary butoxide |

| | |
|---|---|
| KOH | Potassium Hydroxide |
| LiBr | Lithium Bromide |
| LabCD | Lab-on-a-disc |
| LoC | Lab-on-chip |
| LoD | Limit of detection or detection limit |
| LSPR | Localized surface plasmon resonance |
| µPAD | Microfluidic paper based analytical devices |
| MeOH | Methanol |
| $MnO_2$ | Manganese dioxide |
| MOF | Metal organic framework |
| MQ | MilliQ |
| 11-MUA | 11-mercaptoundecanoic acid |
| MWCNTs | Multi walled Carbon Nanotubes |
| $NaH_2PO_4$ | Sodium dihydrogen phosphate |
| $Na_2HPO_4$ | Disodium hydrogen phosphate |
| NaOH | Sodium hydroxide |
| NADP | Nicotinamide adenine dinucleotide phosphate |
| NADPH | Reduced nicotinamide adenine dinucleotide phosphate |
| NCs | Nanoclusters |
| NHS | N- Hydroxysuccinimide |
| NPs | Nanoparticle |
| np-P4VB | bis(4-pyridyl) dineopentoxyl-p-phenylenedivinylene |
| NIR | Near infrared |
| NMR | Proton nuclear magnetic resonance |
| $O_2$ | Dioxygen |
| P2VB | (1,4-bis(β-pyridyl-2-vinyl)benzene) |
| P4VB | (1,4-bis(4-pyridyl-2-vinyl)benzene) |
| PB | Prussian Blue |
| PC | Poly- carbonate |

| | |
|---|---|
| PDMS | Poly- (dimethylsiloxane) |
| PEI | Polyethyleneimine |
| PET | Photoinduced electron transfer |
| PEG | Polyethylene glycol |
| PhLoC | Photonic LoCs |
| PMMA | Poly (methyl methacrylate) |
| PoC | Point of care |
| PPD | p-phenylenediamine |
| PL | Photoluminescence |
| PVA | Polyvinyl alcohol |
| RDTs | Rapid detection tests |
| ROS | Reactive oxygen species |
| RF | Red fluorescent |
| SF | Silk fibroin |
| DOEs | Diffractive optical elements |
| SWCNTs | Single walled Carbon Nanotubes |
| SPR | Surface plasmon resonance |
| t-BuOH | tertiary Butyl alcohol |
| THF | Tetrahydrofuran |
| TEM | Transmission electron microscope |
| trp | Tryptophan |
| tyr | Tyrosine |
| TMB | 3,3',5,5'-Tetramethylbenzidine |
| UV | Ultraviolet |
| WHO | World Health Organization |

# List of Symbols

| | |
|---|---|
| % | Percentage |
| ≥ | Greater than equal to |
| λ | Wavelength |
| Φ | Quantum yield |
| ν | Frequency |
| σ | Standard deviation |
| τ | Excited lifetimes |
| $\eta_R$ | Refractive index of the solvent in which rhodamine is dissolved |
| $\eta_x$ | Refractive index of the solvent in which the test sample is dissolved |
| °C | Degree Celsius |
| μm | Micrometer |
| μL | Microlitre |
| 2D | Two dimensional |
| 3D | Three dimensional |
| c | Speed of light |
| cm | Centimetre |
| Da | Dalton |
| $E_g$ | Band gap energy |
| $E_f$ | Fermi energy |
| *h* | Planck's constant |
| $I_R$ | Fluorescence intensity integral of rhodamine |
| $I_x$ | Fluorescence intensity integral of the test sample |
| g | Gram |
| kDa | Kilodalton |
| kV | Kilovolt |
| kW | Kilowatt |

| | |
|---|---|
| Km | Michaelis-Menten constant |
| nm | Nanometer |
| nM | Nanomolar |
| min | Minute |
| mM | Millimolar |
| mm | Millimeter |
| mmol | Millimole |
| mg | Milligram |
| mL | Millilitre |
| M | Molarity |
| meV | Millielectronvolt |
| mV | Millivolt |
| MHz | Megahertz |
| MΩ | Megaohm |
| MPa | Megapascal |
| ppi | Pixels per inch |
| $OD_R$ | Maximum absorbance of rhodamine |
| $OD_x$ | Maximum absorbance of the test sample, |
| pmol | Picomole |
| $R^2$ | Regression coefficient |
| rpm | Revolutions per minute |
| $t_{1/2}$ | Half life |
| US$ | US dollar |
| U $mL^{-1}$ | Unit per millilitre |
| v/v | Volume/volume |
| w/v | Weight/volume |
| $Q_R$ | Quantum yield of rhodamine |

# List of Figures

Attribution License; (c) Scheme of the formation of resorufin by the reaction of MBFh1 with enzymatically generated $H_2O_2$ to prepare a fluorescent sensor (Hitomi et al., 2011) Copyright 2011, reprinted with permission from ACS Publications.

**Figure 1.6:** Chemical structures of a) DSB (PPV), b) P2VB, and c) np-P4VB. The key change between DSB and P2VB is the pyridine ring on each end. The difference between the P2VB and P4VB structures is the position of the nitrogen in the pyridine rings. The np-P4VB synthesized here is similar to P4VB but with the addition of branched neopentyloxy groups on the central benzene ring (Lane et al., 2018) Copyright 2018, this is an open access article distributed under the Creative Commons Attribution License.

**Figure 1.7**: (a) Template for diffusion and chaotic mixers. The pillars are guides for silicone tubing integration and the external frame contains the PDMS during curing. (b) Detail of the chaotic mixer design. (c) Detail of the chaotic bitmap edited refinements. (d) Printed template. (e) 100 μm deep diffusion mixer showing the mixture of 1 mM fluorescein with 1 mM rhodamine B at 60 μL $min^{-1}$. (f) 100 μm deep chaotic mixer imaged in the same conditions as in (e). (g) Idem to (f) operated at 30 μL $min^{-1}$. (h) Idem to (g) but for a 500 μm deep channel. (i) Detail of the 500 μm deep chaotic mixer 3D structure (Comina et al., 2014) Copyright 2014, reprinted with permission from Royal Society of Chemistry.

**Figure 1.8**: (a) Blank and (b) sample BPE sensor indicating PB formation around BPE. (c) Schematic representation of the fundamental mechanism of using $K_4Fe(CN)_6/FeSO_4$ in reporting cell of P-BPE sensor (Rafatmah and Hemmateenejad, 2019) Copyright 2019, reprinted with permission from Springer Nature.

**Figure 1.9**. Obvious capillary outflow at low evaporation temperature (T = 30 °C) (a) Image with streamlines of capillary flow, (b) scheme of the transport of the suspended particles to drop edge leading to the formation of ring stains during the evaporation of the fluid (Li et al., 2016) Copyright 2016, this is an open access article distributed under the terms of the Creative Commons CC BY license.

**Figure 2.1:** $^1H$ NMR (300 MHz, $CDCl_3$) spectrum of 6-(4-methoxyphenoxy)-1-hexanoic acid

**Figure 2.2**: $^1H$ NMR (300 MHz, $CDCl_3$) spectrum of 6-(2,5-bis-(bromomethyl)-4-methoxyphenoxy)-1-hexanoic acid

**Figure 2.3**: $^{1}H$ NMR (300 MHz, $CDCl_3$) spectrum of ethyl 6-(2,5-bis((diethoxyphosphoryl)-methyl)-4-methoxyphenoxy)hexanoate (3)

**Figure 2.4**: $^{1}H$ NMR (300 MHz, methanol-d4) spectrum of sodium 6-(4-methoxy-2,5-bis((E)-2-(pyridin-4-yl)vinyl)phenoxy)hexanoate (**c-P4VB**, 4)

**Figure 2.5**: Signals of protons of **c-P4VB** in the aromatic region at 500 MHz (top, more concentrated) and 300 MHz (bottom, less concentrated), referenced to the signal of deuterated methanol.

**Figure 2.6**. Molecular structure of (a) **np-P4VB** and (b) **c-P4VB**. Corresponding images under a fluorescence microscope (365 nm excitation) are shown in (c) and (d) of crystals formed after evaporation from ethanol at room temperature.

**Figure 2.7**. (a) Absorption spectra of 0.02 mM **c-P4VB** in ethanol, with the double Gaussian fit. This sample contains 0.057 mM toluenesulfonic acid. The relative strength of each of the absorptions (relative absorption) was found by taking the area under the peaks, and the results are shown as a function of acid concentration for **np-P4VB** in (b) and **c-P4VB** in (c). The onset of protonation is significantly delayed (i.e., it occurs at higher acid concentrations) for the **c-P4VB** due to the presence of the carboxylic group.

**Figure 2.8**. Simulated structures of **c-P4VB** with a sodium counter-ion. (a) "twisted" cis with the ion shared between the carboxyl tail and the pyridine site, (b) trans with the ion interacting with pyridine site only, (c) trans with the ion interacting with carboxyl tail. (c) is the most stable form; (a) and (b) are higher in free energy by 15 and 87 meV, respectively, in ethanol. These differences change significantly in other solvents or with different counter-ions (e.g., H+) but the transform shown in (c) is always the most stable. Blue represents nitrogen, red is oxygen, gray is carbon, white is hydrogen, and sodium is violet.

**Figure 2.9**. (a) Normalized absorption (dashed lines) and fluorescence intensity (solid lines) spectra for 0.02 mM **c-P4VB** in DMSO, ethanol (EtOH), methanol (MeOH) and water.

**Figure 2.10**. Fluorescence spectra for (a) **np-P4VB** and (b) **c-P4VB** at different concentration of HCl (all intensities are normalized; 0.2 mM fluorophore in ethanol)

**Figure 2.11.** (a) Absorbance spectra for different concentrations (v/v %) of $H_2O_2$ in aqueous solutions of 0.02 mM **c-P4VB** (b) Fluorescence spectra of aqueous $H_2O_2$ solutions in 0.02 mM **c-P4VB** in ethanol. In all cases, the reaction solution had a 1:1 volume ratio of ethanol and water. The control

refers to pure ethanol solution with **c-P4VB** and 0% means that only pure water was used. The aqueous $H_2O_2$ solutions were prepared by dilution of commercial 30% aqueous $H_2O_2$ with MQ water. All spectra are normalized for visual clarity.

**Figure 2.12**: (a) Photos of paper discs under UV lamp : (i) infused with **c-P4VB** solution, not washed; (ii) infused with **c-P4VB** solution, washed with water; (iii) infused with **np-P4VB** (ethanol solution of high dye concentration) and washed with methanol; (iv) infused with **np-P4VB** (ethanol solution of low dye concentration) and washed with methanol; (v) infused with **c-P4VB** solution and washed according to our protocol with water and then methanol followed by sonication; (vi) in the middle – a blank paper sample. (b) Normalized fluorescence intensity of **c-P4VB** paper at different storage times and its reversibility characteristics with MeOH treatment

**Figure 2.13**. Photographs taken under a UV lamp (top) and corresponding fluorescence spectra of **c-P4VB** treated with different analytes (bottom). The photographs were taken with a smartphone camera with no filtering applied. (a) blank filter paper; (b) **c-P4VB** paper only and treated with: (c) water; (d) Zinc nitrate (0.5 M); (e) acetic acid (1 M), (f) HCl (5 mM) and (g) $H_2O_2$ (10 v/v%).

**Figure 2.14**. (a) Photographs of **c-P4VB** paper treated with different concentrations of $H_2O_2$ were taken under a UV lamp using a smartphone camera without any filtering. (b) Normalized fluorescence spectra corresponding to **c-P4VB** treated with various concentrations (v/v %) of $H_2O_2$. (c) Calibration curve of the paper sensor for different $H_2O_2$ concentrations in aqueous solution. The inset magnifies the low-concentration region from which LoD was calculated. The error bars represent the calculated standard error from measurements on three separate disks.

**Figure 2.15**. (a) Image of the paper-based alcohol sensor with the dimensions of each zone; (b) Photographs taken using a smart phone after the reaction with different concentrations of ethanol (v/v %); (c) Calibration plot for the pixel intensity ratio (B / R) with a model fit, as described in the text. The errors represent the standard deviations from three separate disks.

**Figure 3.1:** (a) Transmittance analysis of the different enzyme SF films. Inset images to show transparency of (i) SF film, (ii) HRP SF film, (iii) AOx SF film and (iv) Bi-enzyme SF film. FESEM images showing the thickness of (b) SF film, (c) HRP SF film, (d) AOx SF film and (e) bi-enzyme SF film.

**Figure 3.2**: (a) Absorbance spectra of $H_2O_2$ (25 mM) and with (III) and without (II) SF. Inset: photo of ABTS reaction solution without SF (green) and with SF (purple); (b) Schematic representation of the reaction of different oxidation states of ABTS when it interacts with HRP, $H_2O_2$ and then SF.

**Figure 3.3:** (a) The response plot of non-dissolvable HRP SF films towards $H_2O_2$. Inset top panel figures are the corresponding color images captured after the reaction with different concentrations of the peroxide. Inset graph is the calibration plot for $H_2O_2$. (b) The enzyme activity in HRP SF films under different temperatures on a time scale of 40 days. The error bars indicate standard error (n=3).

**Figure 3.4**: Activity in terms of rate for the AOx enzyme in free form and in SF (7 % w/v) film over five days, stored under room temperature (25 ℃) reacted with 25 mM of methanol.

**Figure 3.5**: Optimization studies of concentration of (a) SF, (b) AOx and (c) HRP in silk film.

**Figure 3.6:** Residual activity versus incubation time for (a) dissolvable AOx SF films measured at $\lambda_{405nm}$ after 1 min and (b) non-dissolvable AOx SF films measured by mean pixel intensity of the purple color at 4 ºC (black), 25 ºC (red) and 37 ºC (green) after 30 min. FESEM images of (c) dissolvable SF film; and (d) non-dissolvable SF film with their corresponding cumulative pore volume versus pore diameter: (e) dissolvable SF film; and (f) non-dissolvable SF film.

**Figure 3.7:** Images of non-dissolvable AOx-SF films (a) without methanol in substrate solution and (b) with 25 mM methanol in solution. The solution remains green while the film turns purple.

**Figure 3.8:** (a) The response curve for non-dissolvable bi-enzyme SF films towards methanol; Inset top panel showing the images of the corresponding color developed over the film. Inset graph is the calibration plot for the methanol sensing. (b) the stability of the bi-enzyme SF films under different conditions. The error bars indicate standard error (n=3).

**Figure 3.9**: Images of ABTS of concentrations 10 mM and 20 mM: (a) entrapped in SF films and (b) immobilized on paper. ABTS on paper show color changes much greater than the control.

**Figure 3.10**: Scheme of pattern designs for Spacer with (a) circular hydrophilic zone and (b) hydrophilic channels within circular zone. The detection films of μPAD after reaction using 1 M methanol with pattern designs for Spacer with (c) circular hydrophilic zone and (d) hydrophilic micro-channels within circular detection zone; and (e) the schematic diagram of the movement of fluid within the channels that is along the channel surface.

**Figure 4.9**: TEM images of RF Cat-AuNCs (a) without and (b) with 100 mM $H_2O_2$; and BF Cat-AuNCs (c) without and (d) with 100 mM $H_2O_2$.

**Figure 4.10**: (a) Response curve for $H_2O_2$ using RF Cat-AuNCs as a fluorescence probe (Image: RF Cat-AuNCs treated with increasing $H_2O_2$ concentration under UV light). (b) Calibration plot for $H_2O_2$ sensing using RF Cat-AuNCs as fluorescence probe. (c) Response curve for $H_2O_2$ using BF Cat-AuNCs as a colorimetric probe (Image: BF Cat-AuNCs treated with increasing $H_2O_2$ concentration under visible light). (d) Calibration plot for $H_2O_2$ sensing using BF Cat-AuNCs as colorimetric probe.

# List of Schemes

# List of Tables

# CHAPTER I

## INTRODUCTION AND REVIEW OF LITERATURE

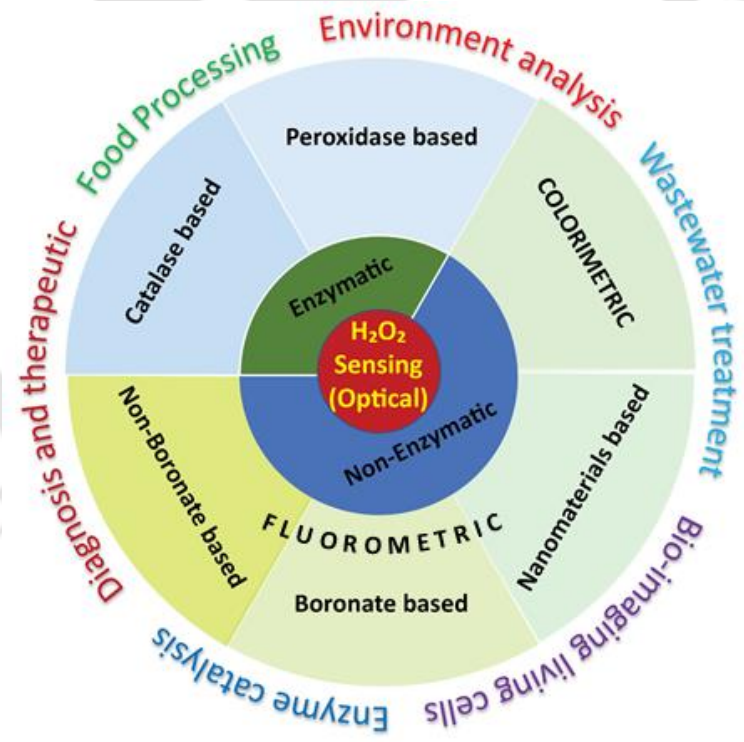

# Chapter I
# Introduction and Review of Literature

## 1.1. Introduction

Hydrogen peroxide ($H_2O_2$) is a widely used oxidizing agent in the pharmaceutical, textile, food manufacturing, paper, and environmental industries (Chen et al., 2012). It is also involved as reactive oxygen species (ROS) in many biological processes such as immune cell activation, apoptosis, and root growth (Laloi et al., 2004; Liu et al., 2015a). Furthermore, the accumulation of a high concentration of $H_2O_2$ is detrimental to human health, causing cellular damage in tissues, cell ageing, diabetes, cardiovascular disorder and even cancer (Dröge and Schipper, 2007; Giorgio et al., 2007S; Rhee, 2006). $H_2O_2$ is also a by-product of several biochemical reactions catalyzed by redox enzymes (Equation 1.1) and hence, is an indirect analyte for the detection of various primary analytes such as glucose (You and Pak, 2014), alcohols (Chinnadayyala et al., 2015; Thungon et al., 2017), cholesterol (Saxena and Goswami, 2012), and bilirubin (Santhosh et al., 2016) in clinical sectors.

$$Substrate \xrightarrow{redox\ enzyme} Product + H_2O_2 \qquad (1.1)$$

Therefore, quantitative detection of $H_2O_2$ has enormous importance in various industrial, environmental, and clinical sectors. Many laboratory-based analytical methods following titrimetric, chromatographic, spectroscopic, and electrochemical approaches are available to detect and quantify $H_2O_2$. These methods are highly sensitive and provide precise results, however, they are not ideal for point of care (PoC) and onsite applications due to the requirement of large and sophisticated equipment, trained operators, and high cost (Meier et al., 2019). In this regard, biosensors and allied rapid detection tests (RDTs) have emerged to facilitate the PoC and onsite detection of various analytes. Biosensors are self-contained integrated devices that provide specific quantitative or semi-quantitative analytical information using a biological recognition element that is in direct spatial contact with a transducer. The biorecognition elements commonly employed for developing biosensors are enzymes, antibodies, aptamers, DNA, and cells (Goswami, 2020). The electrochemical and optical transduction principles are widely used to develop biosensors. Biosensor research holds promise for developing portable devices for rapid, sensitive, selective, reproducible, and economical detection of many analytes of clinical importance. In regards to the development of $H_2O_2$ biosensors, electrochemical and optical sensors are commonly used (Bai et al., 2016; Deng et

al., 2014; Ding et al., 2018; Rezende et al., 2018). The electrochemical sensors function through various electrical transducers (Yunus et al., 2011), among which potentiometric and amperometric sensors have been intensively investigated due to their high sensitivity and scope for label-free detection capabilities (Meier et al., 2019). In these electrochemical sensors, peroxide-degrading enzymes such as peroxidase (e.g., horse radish peroxidase or HRP), laccase, and catalase (Cat) are usually used as biorecognition elements for the detection of $H_2O_2$ (Tortorich et al., 2018). Many nanomaterial-based electrochemical peroxide sensors are also reported (Kumar et al., 2009; Singh et al., 2015). Different electron transfer strategies such as direct electron transfer and mediated (indirect) electron transfer approaches, nanomaterials, and metal complexes are used to generate response signals for $H_2O_2$ in these electrochemical sensors, as depicted in Scheme 1.1. (Wu et al., 2006; Li et al., 2004; Chen et al., 2012; Presnova et al., 2008). Various nanomaterial forms of graphene (Mutyala and Mathiyarasu, 2016; Ping et al., 2011; Shamkhalichenar and Choi, 2020; Zhou et al., 2009), metal nanoparticles (He et al., 2004; Dey and Raj, 2010) and metal complexes (Li et al., 2004) have been applied to catalyze the oxidation or reduction of $H_2O_2$ to construct non-enzymatic sensors (Chen et al., 2013). There have been a couple of reports on the application of Ferric hexacyanoferrate or Prussian blue (PB), denoted as an ‘‘artificial peroxidase’’ for developing $H_2O_2$ amperometric sensors (Li et al., 2004; Karyakin et al., 2000; Li et al., 2007; Zhai et al., 2009). Some sporadic reports are also available on the application of different gold (Au) nanocrystals, including Au nanocages (Zhang et al., 2011), Au nanospheres and nanorods (Won et al., 2011), and nanoporous Au films (Zheng et al., 2012) for sensitive and selective detection of $H_2O_2$. Although electrochemical sensors offer good performance in terms of selectivity and sensitivity, the complexity of the immobilization process of the enzymes, assembling of mediators and nanomaterials as well as the interference in the electrodes or leaching of enzymes from the electrode render some disadvantages of these sensors (Chen et al., 2014).

Over the last years, the interest in optical transducer-based sensors has been steeply growing due to their certain advantages that may fulfil some critical requirements, mainly low cost and simplicity, for commercial success. The emergence of low-cost biocompatible materials such as papers, silk, and poly- (dimethylsiloxane) (PDMS) as optical sensor platforms has dramatically boosted the progress in this direction (Xu et al., 2011a; Koh et al., 2015; Comina et al., 2014). The optical sensors on such platforms could also be developed for rudimentary applications with a yes/no format following visual observation of the color as a response signal. Additionally, the response color signal could be read using a smartphone as an analytical instrument for qualitative and quantitative detection of the target analytes (Geng et al., 2017). The introduction of smartphone systems in these interfaces

has further facilitated the application potential of optical sensors for remote sensing through data transfer by various means, including the Internet of Things (IoT).

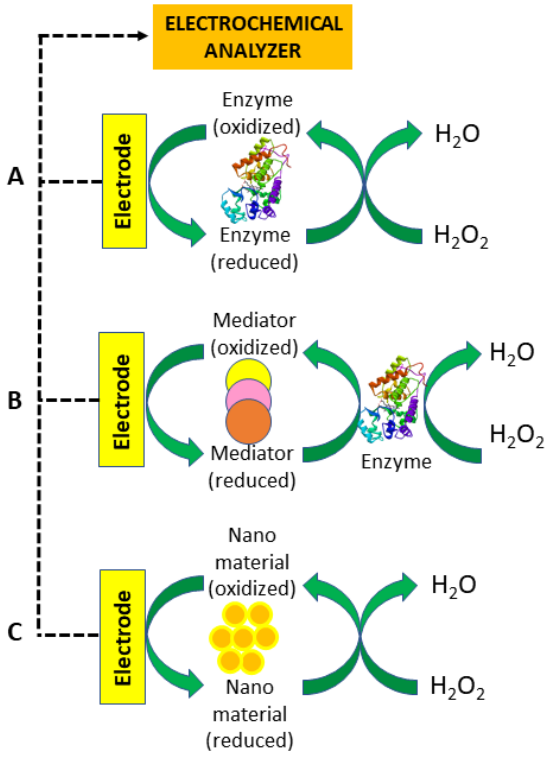


**Scheme 1.1**: The schematic diagram of different setups for electrochemical $H_2O_2$ sensor: (A) direct enzyme oxidation, (B) Mediator based oxidation using enzyme and, (C) Direct oxidation by nanomaterials.

Optical-based sensors function through the detection of light emitted from a reacted sample and can be primarily based on the change of color (colorimetric) or fluorescence (fluorometric). In the case of a fluorescence sensor, an external energy source is required for the excitation of the probe. These fluorescence sensors frequently exhibit changes in emission intensity, but they can also function through shifts in their emission profiles (Chang et al., 2018; Wu et al., 2005; Zhao et al., 2014). Other than this, chemiluminescence sensors for $H_2O_2$ have also been reported, in which a chemical compound itself is excited in the presence of $H_2O_2$ (Lebiga et al., 2014; Navas Díaz et al., 1998). Horseradish Peroxidase (HRP) has been used as the model enzyme for several optical detection systems of $H_2O_2$ due to its ability to oxidize chromogen while degrading $H_2O_2$. Over the last decade, different nanomaterials have been reported that exhibited “peroxidase” like activity and were used for $H_2O_2$ detection. Additionally, many organic dyes were explored as chemical fluorophores and

chromophores for sensing $H_2O_2$ in biological samples. The optical sensors for $H_2O_2$ are usually designed by using enzyme-, nanomaterial, and organic dye- (chemical) as signal-transducing elements, as depicted in Scheme 1.2. Each category will be explained in more detail in the following section.

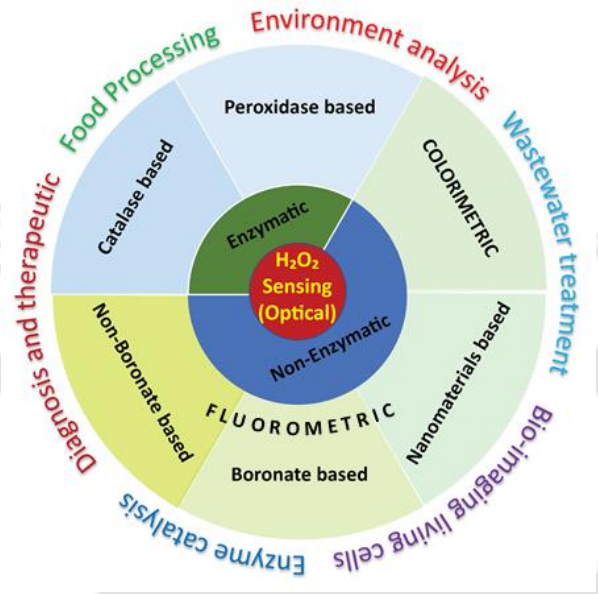


**Scheme 1.2:** Illustration of different types of optical-based sensing systems for $H_2O_2$. The second innermost pie chart shows the broad categories of optical sensors that are based on enzymatic or non-enzymatic detection; the area of the pie chart also tentatively represents the amount of recent work done in each category, which is mostly non-enzymatic based. The next pie describes the different methods of detection, chemical and nanomaterials in case of non-enzymatic, and catalase and peroxidase enzyme in case of enzymatic detection approaches. Finally, the outermost circle projected the applications of $H_2O_2$ sensors in various sectors.

## 1.2 Enzyme-based optical $H_2O_2$ sensors

The enzymes commonly used for the detection of $H_2O_2$ are Catalase and HRP. Of these two enzymes, the latter has been more extensively used for the optical detection of $H_2O_2$ because of its suitable catalytic reaction that offers a stark color-change as a response signal in the assay.

### *1.2.1. Catalase for detection of $H_2O_2$*

Catalase is a heme-based enzyme used in industrial fields due to its efficient catalytic function for the degradation of $H_2O_2$ (Amorim et al., 2002). It is one of the very stable enzymes available in the

living systems and catalyzes the decomposition of $H_2O_2$ into water and oxygen as per the following reaction:

$$H_2O_2 \rightarrow H_2O + O_2 \quad (1.2)$$

Catalase is a homo-tetrameric protein having a molecular weight ~250KDa and pI ~5.4 (Fig. 1.1a). Each of the four enzyme subunits contains an Iron ion bound to the protoheme IX group (Porphyrin), which acts as the prosthetic group. There are some reports on its strong binding with NADP (Rapoport et al., 1994). At the molecular level, the reaction occurs as follows (Fig 1.1c) (Goodsell, 2004):

$$H_2O_2 + \text{Fe (III)-Enzyme} \rightarrow H_2O + \text{O=Fe (IV)-Enzyme (+)} \quad (1.3)$$

$$H_2O_2 + \text{O=Fe (IV)-Enzyme (+)} \rightarrow H_2O + \text{Fe (III)-Enzyme} + O_2 \quad (1.4)$$

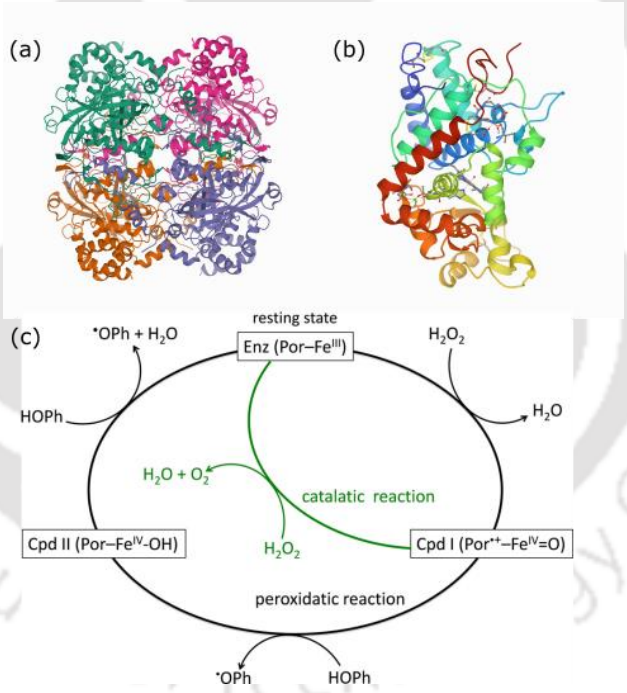


**Figure 1.1**: Crystal structure of (a) Catalase from bovine liver without NADPH and (b) Horseradish Peroxidase (From www.rcsb.org). (c) Reaction mechanisms involved in the degradation of $H_2O_2$ catalyzed by peroxidases and catalases (Campomanes et al., 2015) Copyright 2015, reprinted with permission from ACS Publications.

The catalase activity could be analyzed spectroscopically by monitoring the sample at $\lambda_{240nm}$ (A240), the wavelength at which $H_2O_2$ exhibits absorption (He et al., 2013). This enzyme activity could be

visually distinguished from the analogue peroxidase enzymes by monitoring the formation of $O_2$ bubbles in the reaction systems, as no such gas is released in the peroxidase catalysis. The reaction of each enzyme has been described in more detail in the next section.

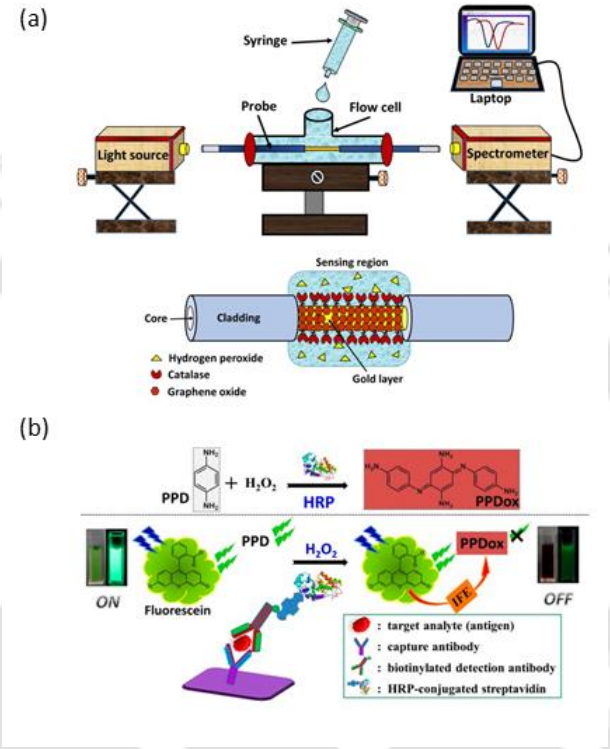


Figure 1.2: (a) Schematic diagram on probe design for catalase-based sensing setup for $H_2O_2$ (Semwal and Gupta, 2021) Copyright 2021, reprinted with permission from Elsevier; (b) top: Schematic representation of the reaction employed for fluorescent assay for $H_2O_2$. Bottom: Schematic representation of the IFE-enabled fluorescent immunoassay based on $H_2O_2$ on the conventional sandwich ELISA platform (Sun et al., 2018) Copyright 2018, reprinted with permission from ACS Publications.

The active heme group in the enzyme has rendered catalase use in electrochemical methods for $H_2O_2$ detection (Periasamy et al., 2011; Varma and Mattiasson, 2005; Vatsyayan et al., 2010), while there have been some reports on the use of catalase for the optical detection of $H_2O_2$ as well (Laser, 1955; Wu et al., 2003). In an interesting work, catalase was used with superoxide dismutase and methanol to develop a unique fluorescence-based assay for $H_2O_2$ (Rapoport et al., 1994). Recently, a surface plasmon resonance (SPR) based fiber optic was fabricated for $H_2O_2$ sensing using catalase. The

optical fiber was cladded with gold and graphene oxide (GO), and catalase was immobilized via EDC-NHS coupling to this construct (Semwal and Gupta, 2021). The high refractive index of GO was used for optical sensing, where the interaction of GO nanosheets with water molecules released from catalase catalyzed decomposition of $H_2O_2$ led to the change in effective refractive index (Fig 1.2a).

### *1.2.2. Peroxidase for detection of $H_2O_2$*

Like catalase, peroxidases (Fig 1.1b) also degrade hydrogen peroxide, however, through a different reaction mechanism as depicted in Fig 1.1c. The catalytic cycle begins with converting the resting state to Compound I (Cpd I) for both the oxidoreductase enzymes. In Cat, Cpd I is reduced back to the resting state by a second molecule of $H_2O_2$ (catalytic reaction) (equation 1.3). In contrast, peroxidase (e.g., HRP) preferentially recovers the resting state via the peroxidase reaction, in which Cpd I sequentially reacts with two molecules of a one-electron donating substrate (e.g., phenol, PhOH), passing through another intermediate named Compound II (Cpd II) (Fig 1.1c). The activity of Cat can be monitored by measuring the formation of oxygen, and the peroxidase-like activity can be determined via colorimetric assay specific for HRP using chromogens such as TMB (3,3',5,5'-Tetramethylbenzidine), ABTS (2,2'-azino-bis(3-ethylbenzothiazoline-6-sulphonic acid), ortho dianisidine and other suitable chromogens (Claiborne and Fridovich, 1979; Campomanes et al., 2015). These chromogenic compounds are transformed via a free radical mechanism into oxidized or polymerized products as shown in the reaction:

$$\text{Electron Donor/ Dye} + H_2O_2 \rightarrow \text{Oxidized Electron Donor/ Dye} + H_2O \qquad (1.5)$$

This unique peroxidase activity has been exploited in developing optical $H_2O_2$ biosensors using chromogenic dyes as a colorimetric probe. Among the chromogens, ABTS is widely used to detect hydrogen peroxide. During the peroxidase reaction, the colorless ABTS molecule is oxidized to the green ABTS cation radical ($ABTS^{\bullet+}$). Further oxidation of this radical will lead to the purple/ red colored ABTS dication ($ABTS^{2+}$) (Scheme 1.3) (Gramss, 2017). The last color change is due to the formation of the chromogenic –N=N– azo group and its interaction with the adjacent molecular structures (Solís-Oba et al., 2005). This additional oxidation of ABTS leading to the purple color was reported to occur very slowly (75 hours) in the laccase-based reaction (Gramss, 2017). The generated green $ABTS^{\bullet+}$ shows spectrophotometric absorbance peaks at $\lambda$ = 417, 645, 728, and 810 nm in the visible light spectrum while the dication, $ABTS^{2+}$ exhibits a single peak around $\lambda$ = 520–570 nm (Kadnikova and Kostić, 2002). The ability of peroxidases to yield chromogenic products at low

concentrations makes them well-suited enzymes for the preparation of enzyme-linked immunosorbent assay (ELISA) kits, which are used to diagnose various diseases. They have also been used to construct several types of biosensors to determine $H_2O_2$ (Li et al., 2001; Bocanegra-Rodríguez et al., 2020).

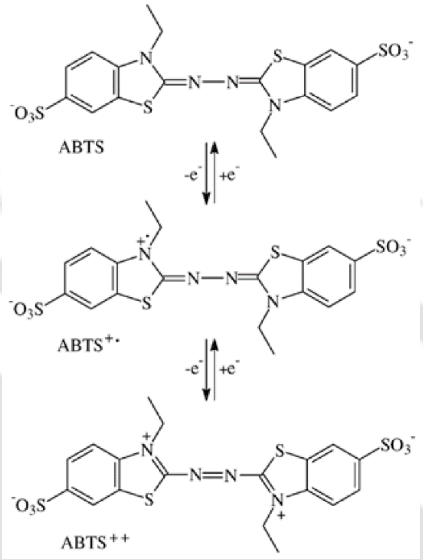


Scheme 1.3. Oxidation of the heterocyclic ABTS molecule (shown as a dianion) to $ABTS^{2+}$ by two consecutive electron abstractions (Gramss, 2017) Copyright 2017, this is an open access article distributed under the Creative Commons Attribution License.

There have been several reports on the development of HRP-based optical $H_2O_2$ sensors using other dyes. Amplex Red (10-acetyl-3,7-dihydroxyphenoxazine) is a popular colorless nonfluorescent compound, which can be oxidized to resorufin in an $H_2O_2$/HRP-catalyzed reaction (Zhou et al., 1997). In conjunction with HRP, this dye has also been used for $H_2O_2$ quantification in living cells (Chakraborty et al., 2016; Wang et al., 2017). Resurofin is a fluorescent pink compound, which can be easily detected by photometry and fluorometry. Using this dye with HRP, highly sensitive detection of $H_2O_2$ with LoD as low as 5 pmol $L^{-1}$ in a simple set-up has been reported (Rezende et al., 2018).

The peroxidases with iron (heme group) in their redox center are also electrochemically active enzymes and are widely used to develop electrochemical biosensors. Several chemiluminescence sensors using the luminol-HRP reaction have been reported. Luminol in the presence of HRP and $H_2O_2$ induces chemiluminescence, which is proportional to the concentration of $H_2O_2$ (Alpeeva and Sakharov, 2005; Navas Díaz et al., 1998; Bocanegra-Rodríguez et al., 2020). An unconventional

colorimetric and fluorometric sensor was developed using HRP- catalyzed specific conversion of p-phenylenediamine (PPD) into chromogenic oxidized PPD with $H_2O_2$ as the oxidizing agent (Sun et al., 2018). This reaction was accompanied by the fluorescence quenching effect on fluorescein. The quenching of fluorescein was reported to be due to the inner filter effect, and this sensitive off-fluorescent sensing system was used to monitor HRP activity in biological samples in real-time (Fig 1.2 b). Peroxidase, along with other oxidoreductase enzymes, has also been used in designing several colorimetric biosensors for other analytes such as alcohol, glucose, and cholesterol (Vijayakumar et al., 1996; Mangos and Haas, 1996; Jung et al., 2015; Thepchuay et al., 2020; Williams and Reese, 1950; Blum, 1993; Reddy et al., 1998; Taga et al., 1993; Krug et al., 1992). The absorbance spectrum of HRP changes upon its interaction with $H_2O_2$ due to the generation of several peroxidase intermediate species in the reaction, as shown in Fig 1.3. These chemical events are the basis of developing a few auto-indicating optical $H_2O_2$ sensors (Sanz et al., 2007; De Marcos et al., 2014).

### 1.3. Nanomaterials for optical $H_2O_2$ sensing

A plethora of reports available on the enzyme-like function of many nanomaterials including magnetic nanoparticles, metal nanoparticles, carbon dots and metal nanoclusters, under physiological conditions that are popularly known as "nanozymes" (Gao and Yan, 2016; Manea et al., 2004). These nanozymes are comparable in size to natural enzymes and possess a high surface area to volume ratio with many catalytically active sites on their surface and better stability than protein-based enzymes (Kuah et al., 2016). Furthermore, these nanozymes could be synthesized through straightforward routes at a low cost (Das and Goswami, 2020). These advantages have incited significant research interest in nanozymes for their deployment in place of natural enzymes. Table 1.1 represents a few prominent examples of various kinds of nanomaterials that exhibit peroxidase-like activity.

**Table 1.1.** Optical sensors for $H_2O_2$ using different nanomaterial and their performance and sensing mechanism

| **$H_2O_2$ sensing probe** | **Mechanism** | **Type of signal** | **LoD** | **Linear Range** | **Ref** |
|---|---|---|---|---|---|
| 11-mercaptoundecanoic acid-bound AuNCs | Oxidation of Au-S bond by $H_2O_2$ leading to fluorescence quenching | Fluorometric | 1 µM | 30 µM-1 mM | (Shiang et al., 2009) |

| | | | | | |
|---|---|---|---|---|---|
| Bio@AgNPs nanohybrid | $H_2O_2$ led etching of AgNPs | Colorimetric<br>Fluorometric | 73.5 µM<br>93.5 µM | Up to 1 mM | (Xu et al., 2019) |
| DNA-AuNPs | Aggregation of AuNPs in presence of $Fe^{2+}$ and $H_2O_2$ | Colorimetric | 1 µM | 0-3 µM | (Lin et al., 2018) |
| Carbon dots/AgNPs | $H_2O_2$ induces etching of AgNPs to NCs and quenching of CD | Fluorometric | 0.86 µM | 0-20 µM | (Liu et al., 2019b) |
| Carbon nanodots | C-Dots as peroxidase mimic | Colorimetric | 0.2 µM | 0.001-0.1 mM | (Shi et al., 2011) |
| Chitosan-AuNPs | peroxidase-like activity of AuNPs | Colorimetric | 0.6 µM | 1 nM-20 mM | (Jiang et al., 2017) |
| $Cr_2O_3$–$TiO_2$-Modified Filter Paper | $Cr_2O_3$–$TiO_2$ nanocomposite as peroxidase mimic | Colorimetric | 3 nM | 0.005-100 µM | (Jamil et al., 2021) |
| BSA-AuNCs | Peroxidase-mimic property of AuNCs | Colorimetric | 0.2 nM | 0.5-20 µM | (Wang et al., 2011) |
| | Fluorescence quenching due to degradation of Au-S bond by $H_2O_2$ | Fluorometric | 0.3 µM | 1-100 µM | (Jin et al., 2011) |
| Per-AuNCs | Fluorescence quenching due to enzyme activity | Fluorometric | 30 nM | 100 nM-100 µM | (Wen et al., 2011) |

| | | | | | |
|---|---|---|---|---|---|
| Cat-AuNCs | Fluorescence quenching due to enzyme activity | Fluorometric | 25 nM | 10-80 µM | (Meng et al., 2018) |

### *1.3.1. Peroxidase-like nanomaterials*

As described in section 1.2.2., "peroxidase" activity is related to the transformation of chromogenic dyes into their oxidized or polymerized form (Shi et al., 2011). Several nanomaterials have been reported to exhibit peroxidase-like activity and are termed "peroxidase mimics" (Chang et al., 2016; Cui et al., 2011; Deng et al., 2016; Gao et al., 2007; Ghosh et al., 2008; Hayat et al., 2015; Hu et al., 2013; Jiang et al., 2017, 2014; Liu et al., 2016; Liu et al., 2019c; Mu et al., 2012; Ragavan et al., 2018; Wei and Wang, 2008; Zeng et al., 2016; Zhao et al., 2014). However, a fraction of this literature used the terminology even when the nanomaterial probes do not involve in the oxidation of a chromogen and the activity is registered merely due to the change in fluorescence intensity.

Ferromagnetic nanoparticles have been reported to show peroxidase activity and have been employed for developing several colorimetric $H_2O_2$ sensors (Gao et al., 2007). ABTS was usually used as chromogen, and these $H_2O_2$ sensors were further developed for sensing glucose via the oxidase-peroxidase reaction (Yu et al., 2009; Wei and Wang, 2008). Carbon-based nanomaterials, such as carbon nanotubes (CNTs) (Cui et al., 2011; Song et al., 2010), graphene (Guo et al., 2011b, 2011a), graphite-like carbon nitrides (g-$C_3N_4$) (Lin et al., 2014; Tian et al., 2013), and graphene quantum dots (GQDs) (Lin et al., 2015; Zheng et al., 2013), carbon nanodots or carbon quantum dots (Long et al., 2016; Shi et al., 2011; Wang et al., 2018a; Wu et al., 2013; Das et al., 2021a, 2021c) are reported to possess the intrinsic peroxidase-like activity and have been applied to various applications. The peroxidase mimic activity of carbon nanomaterials such as single-walled carbon nanotubes (SWCNTs) was first reported by Song et al. (Song et al., 2010). Another study revealed that the peroxidase activity of helical CNTs was affected by Fe content, and with the concentration of Fe, the catalytic activity increased (Cui et al., 2011).

Metal-based nanomaterials including gold nanoparticles (AuNPs) (Long et al., 2011; Ni et al., 2014; Shah et al., 2015; Wang et al., 2012b; Zeng et al., 2012; Jiang et al., 2017) and gold nanoclusters (AuNCs) (Jiang et al., 2014; Wang et al., 2015a), silver nanoparticles (AgNPs) (Jiang et al., 2012; Karim et al., 2018), platinum nanomaterial (Cai et al., 2013; Gao et al., 2013; Jin et al., 2017), copper

nanoparticles (CuNPs) (Wang et al., 2015b) and copper nanoclusters (CuNCs) (Hu et al., 2013) have shown great intrinsic peroxidase-like activity and applied to various applications. The first report of AuNPs having peroxidase-like activity was reported by Jv et al. in 2010 (Jv et al., 2010). They found that the positively charged AuNPs could catalyze the oxidation of substrate TMB in the presence of $H_2O_2$ to generate a blue color. A further systematic study of the origin of the peroxidase-like activity of AuNPs was reported by Wang and co-workers (Wang et al., 2012b). The authors examined the effects of surface modification, and the results revealed that the activities could be adjusted by transforming the affinities between the nanoparticles and substrates. CuNCs were found to mimic peroxidase and could catalyze the oxidation of substrate TMB in $H_2O_2$ to generate a blue color, and the CuNCs had a comparable affinity to TMB compared to HRP (Hu et al., 2013). Furthermore, nickel nanosheets with peroxidase activity were synthesized. The clusters developed a sensitive $H_2O_2$ colorimetric sensor with LoD of 8 nM using TMB as the chromogen (Fig 1.3a) (Chen et al., 2018). Bovine serum albumin (BSA) stabilized AuNCs were also reported to show peroxidase activity and it was employed to develop an optical sensor for xanthine by using TMB as the chromogen (Wang et al., 2011). A study of BSA-AuNCs with photoinduced electron transfer (PET) quenchers found that these quenchers quench the fluorescence of the clusters and regulate their intrinsic peroxidase-like activity (Chen et al., 2020).

### *1.3.2. Nanomaterials for colorimetric detection of $H_2O_2$*

Many metal nanoparticles exhibit distinct plasmonic absorption characteristics following their interaction with different analytes. This phenomenon has also been exploited for sensing $H_2O_2$. Acacia gum–stabilized silver nanoparticles (AgNPs) were used as a highly sensitive and cost-effective localized surface plasmon resonance (LSPR) colorimetric sensor to determine reactive oxygen species, such as $H_2O_2$. In the presence of $H_2O_2$ the yellow color of acacia gum–stabilized AgNPs changed to transparent, and a remarkable change in the LSPR absorbance change also occurred (Alzahrani, 2017). The change in the solution color was due to the aggregation of AgNPs induced by the $H_2O_2$ solution. Peng et al. developed a unique reaction mechanism to detect $H_2O_2$, where hydrogen peroxide oxidizes gold acid to produce gold nanoparticles. The formation of gold nanoparticles results in the development of red color in the reaction solution (Fig 1.3b) (Peng et al., 2014).

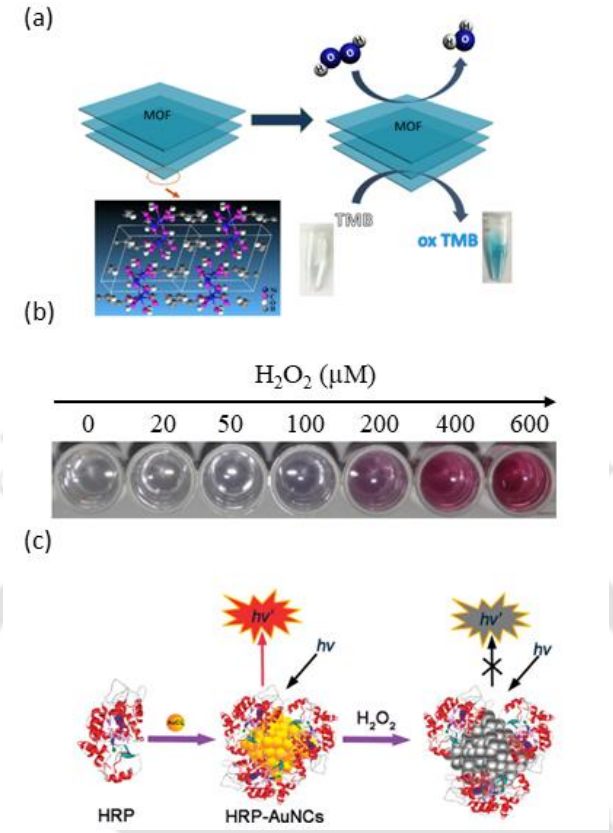


**Figure 1.3:** (a) Schematic illustration of the colorimetric detection of $H_2O_2$ based on the peroxidase-like activity of 2D metal-organic framework (MOF) Nanosheets (Chen et al., 2018) Copyright 2018, reprinted with permission from Elsevier; (b) Photograph showing the generation of AuNPs solutions with different colors depending on the concentration of $H_2O_2$ and intensities after 10 min (Peng et al., 2014) Copyright 2014, this is an open access article distributed under the Creative Commons Attribution License; (c) Schematic of the formation and the $H_2O_2$ Directed Quenching of HRP-AuNCs (Wen et al., 2011) Copyright 2011, reprinted with permission from ACS Publications.

### *1.3.3. Metal nanoclusters as hydrogen peroxide sensing probe*

When the sizes of the metal nanoparticles and bulk metals are reduced to the sizes of the Fermi wavelength, the continuous-band structures of the metals transformed into discrete energy levels occurring in the phenomenon of quantum confinement. The smaller sizes of the metals with quantum confinement phenomena are categorized as metal nanoclusters (NCs) (Zheng et al., 2007). Under this situation, the properties of nanoparticles like conductivity and surface plasmonic effect disappeared. However, these clusters still interact with light through electronic transitions between the energy levels and show bright luminescence, similar to organic dye molecules (Zhang and Wang, 2014).

These few-atom nanoclusters with molecule-like properties offer the ‘‘missing link’’ between metal atoms and nanoparticles (Zheng et al., 2004).

The stability and confinement of the metal NCs can be explained by the Jellium model and the “magic number” rule. Jellium model originated from the nuclear-shell model and was modified as a spherical jellium model and used for emission energy or the energy level spacing between adjacent levels of nanoclusters. According to the Jellium model, if there are ‘N’ number of atoms in a cluster, the size of nanoclusters is related to the emission energy via the simple relation, $E_f/ N^{1/3}$, where $E_f$ is the Fermi energy of the bulk metal. This energy scaling law was used as a model to describe the size-dependent electronic structure and relative electronic transitions of small clusters. Thus, as the number of atoms increases, the emission energy decreases (Review: Thungon et al., 2020). In Figure 1.4, it is shown that with the increase in the size of AuNCs, the energy changes which leads to different fluorescence emissions. The smallest clusters (< 2 nm) show blue fluorescence whereas the larger ones are green and further increase in size (~3 nm) emit red fluorescence.

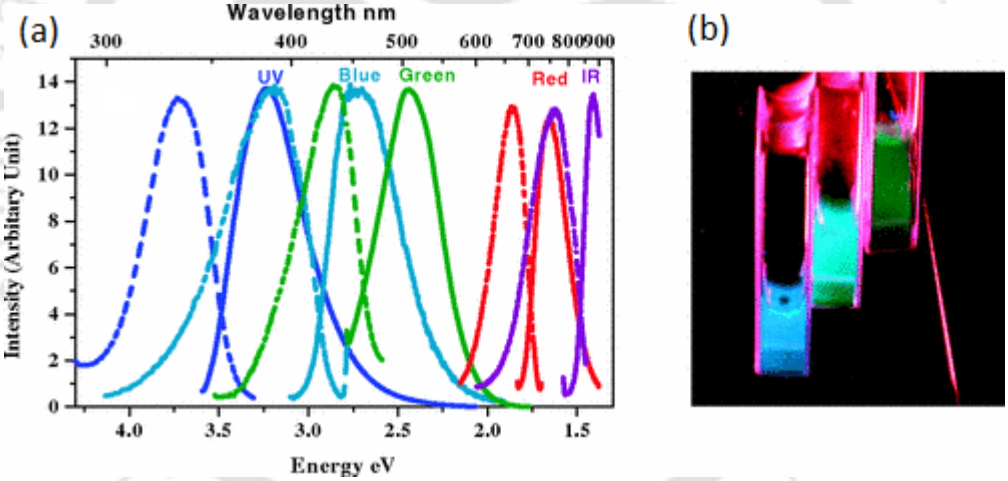


**Figure 1.4**: (a) Excitation (dashed) and emission (solid) spectra of different AuNCs. Excitation and emission maxima shift to longer wavelength with increasing initial Au concentration, suggesting that increasing nanocluster size leads to lower energy emission. (b) Emission from the three shortest wavelength emitting AuNCs solutions (from left to right) under long-wavelength UV lamp irradiation (366 nm) (Zheng et al., 2004) Copyright 2004, reprinted with permission from American Physical Society.

While preparing Sodium clusters, a periodic pattern of intense peaks was observed for clusters containing the number of atoms N = 2, 8, 18, 20…which had greater stability than other clusters. The number of atoms is called “magic” number (Zheng et al., 2007). Similarly, during the preparation of

metal NCs, according to mass spectrometry, it was found that certain masses of clusters were produced in relatively large quantities. These ‘‘magic’’ sizes corresponded to the closing of atomic shells or the electronic (Wilcoxon and Abrams, 2006). These clusters have a complete and regular outer geometry such as hexagonal or spherical and are described as full-shell or “magic number” clusters. Successive packing of the metal atoms into layers or shells around a single atom provides good stability as the structures are densely packed and provide maximum number of metal-metal bonds (III and Finke, 1999). The relationship between the total numbers of metal atoms in case of a hexagonal full-shell, y, per nth shell is given by:

$$y = 10\ n^2 + 2 \qquad (1.6)$$

(where n>0). Therefore, the full-shell metal clusters may contain 13 atoms (1+12) if there is one shell, 55 (13+42) if there are two shells, and 147 (55+92) if three shells and so on (Schmid, 1990).

Their high-yield photoluminescence, good photostability with high emission rates and large strokes shift as well as low-toxicity have rendered their application in biosensing and bioimaging as well as therapy and diagnosis. There are many metal NCs which have been synthesized composed of gold (Au), silver (Ag), copper (Cu) and even mixed metals using either top-down or bottom-up approaches (Sun and Sakka, 2014). Ligands are required to stabilize these nanoclusters that help avoid their aggregation into nanoparticles. Several ligands such as thiol groups, proteins, and oligonucleotides, have been explored and interestingly, the fluorescence properties of the metal nanoclusters are also dependent on these ligands. Metal NCs are considered a new class of fluorescent labels showing size-dependent fluorescence, which can be explored for developing fluorescent-based sensing systems.

Metal NCs have been reported to offer good sensitivity toward $H_2O_2$ in developing fluorescence-based sensors (Hu et al., 2013; Li et al., 2014; Wen et al., 2011). In 2009, a quantitative $H_2O_2$ sensor was developed using 11-mercaptoundecanoic acid bound (MUA)-AuNCs. In the presence of $H_2O_2$, 11-MUA units bound to the cluster surface through Au—S bonds get easily oxidized to form an organic disulfide product, resulting in reduced luminescence (Shiang et al., 2009). Further combination of the luminescent MUA-AuNCs with glucose oxidase enabled the sensitive determination of glucose. A label-free detection system for $H_2O_2$ and glucose was developed using polyethyleneimine (PEI)-capped copper nanoclusters as a fluorescence probe in an aqueous solution (Ling et al., 2014). Blue-emitting AuNCs stabilized by hemoglobin (Hb-AuNCs) were used as fluorescence-enhancing–quenching (on-off) sensors for the direct detection of low levels of glucose

in serum samples via the $H_2O_2$ sensing. In the presence of glucose (substrate) and GOx (catalyst), $H_2O_2$ is produced which enhances the fluorescence intensity of Hb-AuNPs (Molaabasi et al., 2015).

*1.3.3.1. Protein stabilized metal nanoclusters*

In nature, organisms undergo a biomineralization process in which proteins sequester inorganic ions or minerals to decrease their harmful effects. Inspired by these natural events, researchers exploited proteins and peptides as hosts to synthesize metal NCs. BSA is the first protein to be used as a template to prepare 25 gold atoms AuNCs (Xie et al., 2009). Proteins as a ligand for synthesizing NCs function as both stabilizing and reducing agents. This "green" synthesis of these NCs paved the path for many studies on using other proteins as a ligand for synthesizing fluorescent metal NCs (Shang et al., 2011). Several proteins such as BSA (Xie et al., 2009), HRP (Wen et al., 2011), catalase (Meng et al., 2018), and lysozyme (Wei et al., 2010) have been used as ligands to synthesize AuNCs.

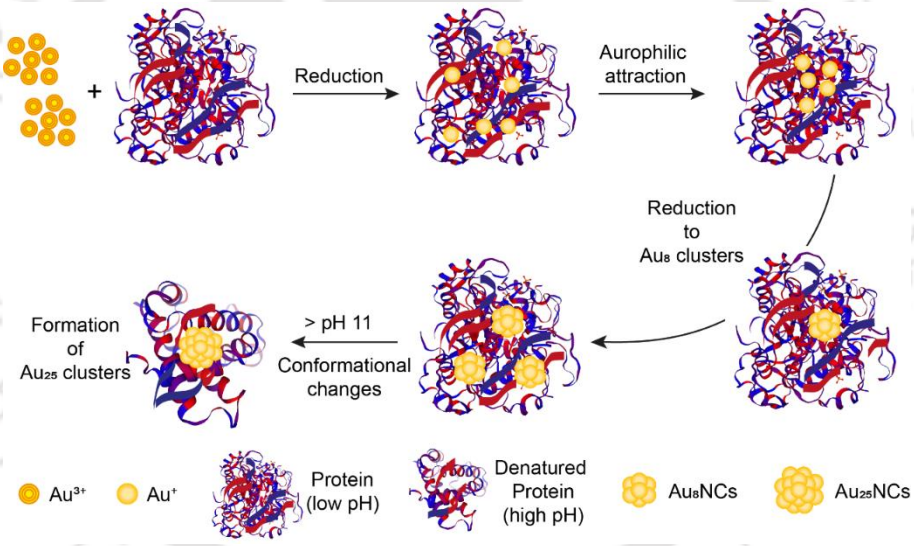


**Scheme 1.4:** Growth mechanism for the synthesis of protein stabilized AuNCs.

Protein-stabilized AuNCs offer many advantages over other AuNC systems, including green synthesis, biocompatibility, high water solubility, and the ease of chemical conjugation with other molecules or substrates (Xu et al., 2014). The growth of AuNCs within the protein matrix has been reported in many studies, and the basic steps have been illustrated in Scheme 1.4. Firstly, the protein binds with $Au^{3+}$ through the coordination of $Au^{3+}$ and tyrosine/ histidine residues. Next, the $Au^{3+}$ ions are reduced with the carboxyl group of acidic amino acids into $Au^{+}$ to form protein-$Au^{+}$ complexes. This reduction continues at lower pH (usually ≤pH 8). At that event, the $Au^{+}$ ions aggregate through aurophilic attraction to form smaller clusters (with 8 Au atoms, $Au_8$NCs). Upon elevating the pH, the

protein becomes denatured, resulting in larger space within the structures that leads to the stabilization of larger NC (with 25 atoms, $Au_{25}$NCs) (Chen and Tseng, 2012). The formation of intermediate $Au_8$ clusters in the conversion of protein-$Au^+$ complexes to $Au_{25}$ clusters has been reported in some studies (Chen and Tseng, 2012; Chaudhari et al., 2011; Le Guével et al., 2011).

These NCs were also sensitive to $H_2O_2$ and were used to develop optical detection methods for $H_2O_2$ (Shang et al., 2011). A new strategy has been reported to construct enzyme functionalized fluorescent AuNCs to detect $H_2O_2$. Bifunctional fluorescent AuNCs were synthesised *in situ* using HRP as a scaffold (Fig 1.3c) (Wen et al., 2011). The enzyme remains active in the clusters and enables the catalytic reaction of HRP- Au NCs and $H_2O_2$, resulting in the fluorescence quenching that can be applied to $H_2O_2$ detection with high sensitivity (LoD: 30 nM). Another ratio-metric $H_2O_2$ detection system was prepared using BSA-AuNCs encapsulated with insensitive FluoSpheres (FSs) within polymeric capsules (Biswas et al., 2017). However, the sensing mechanism, which is mostly due to the quenching of the fluorescence with the concentration of $H_2O_2$, has not been adequately investigated in these reports.

### 1.4. Organic dyes as hydrogen peroxide sensing probes

Organic dyes are chemical compounds which have been widely studied for detection of $H_2O_2$ because they do not succumb to stability issues and the chemistry of their mechanism is well understood. Most of these organic dyes are fluorophores whose fluorescence is either quenched or enhanced in the presence of $H_2O_2$. These dyes can be broadly divided into boronate-based and non-boronate based.

#### *1.4.1. Boronate-based probes*

The chemical reaction of $H_2O_2$ with boronate-groups was reported in 1930 (Ainley and Challenger, 1930) and the first probes inspired by this reaction were reported in 2003 (Lo and Chu, 2003). Since then there have been over 20 boronate-linked probes reported, which have been used for measuring and imaging $H_2O_2$ in living systems (Lin et al., 2013; Lippert et al., 2011; Miller et al., 2005; Rezende et al., 2018; Żamojć et al., 2016). Boronate-linked probes are organic compounds consisting of an electrophilic boron center linked to different functional groups which are aliphatic, phenolic/aromatic or fluorogenic. Under mild alkaline conditions, $H_2O_2$ reacts with boronate groups, converting the probes to their corresponding hydroxyl derivatives or phenolic products (in aromatic-containing probes)(Kuivila, 1955). This often releases the functional groups that are easy to monitor by absorbance, fluorescence, or fluorescence resonance energy transfer (FRET) (Rezende et al., 2018;

Chen et al., 2011). Furthermore, the chemical modifications can render these probes to be water-soluble and better signal transducers. A phenyl boronic acid-functionalized quinone-cyanine probe was designed for dual (colorimetric and fluorometric) detection of $H_2O_2$ in living cells (Narayanaswamy et al., 2016). In presence of $H_2O_2$, the fluorescence was turned on as well as the color of the solution changed from yellow to red.

Additionally, two $H_2O_2$-selective fluorescent probes, termed MI-H2O2 and ER-H2O2, were reported based on a boronic acid/ester deprotection. In both the probes, upon reaction with $H_2O_2$, the boronic acid group is removed, and the fluorescent moiety is exposed turning the probe on (Fig 1.5a,b)(Xiao et al., 2016). The development of boronate-based probes has mainly been focused on synthetic chemistry and not on redox biology or sensor development. Hence, the biological properties and the suitability of boronates for $H_2O_2$ detection *in vivo* have not been adequately evaluated (Rezende et al., 2018).

### *1.4.2. Non-boronate-based probes*

There have been reports of other chemical probes for the detection of $H_2O_2$ which do not have boronate-groups. Most of the reactions involve the oxidation of the probes by $H_2O_2$ which leads to either enhanced emission or quenching. These probes mostly include organic dye based on fluorescein derivatives (Rezende et al., 2018; Maeda et al., 2004; Schäferling et al., 2011; Żamojć et al., 2016). The "switch on" detection mechanism involves the elimination of a functional group, such as benzil or sulfonyl by $H_2O_2$, to regenerate the green fluorescence of fluorescein (Rezende et al., 2018; Maeda et al., 2004).

Different metal complexes such as europium(III) (Wolfbeis et al., 2002; Wu et al., 2005; Żamojć et al., 2016; Kozhevnikov et al., 2005), Iron complex-based probes (Hitomi et al., 2014, 2013, 2011; Zhang et al., 2008) as well as selenium based (Schäferling et al., 2011) probes have also shown high sensitivity towards $H_2O_2$. A fluorescent probe for $H_2O_2$ called MBFh1, was prepared with an iron complex as a reaction site for $H_2O_2$ and a 3,7-dihydroxyphenoxazine derivative as the fluorescent reporter unit. The iron complex reacts quickly with $H_2O_2$ to form oxidants, and then these oxidants in turn convert the closely appended non-fluorescent 3,7-dihydroxyphenoxazine moiety to resorufin (fluorescent) in an intramolecular fashion (Fig 1.5c). This fast response to $H_2O_2$ was employed to detect the enzymatic evolution of $H_2O_2$. An organic fluorescent probe, which the authors called HP green, based on the yellow fluorophore, 4-amino-1,8-napththalimide coupled to p-anisidine (as a redox-active group) was developed for the determination of $H_2O_2$. The mechanism of HP green

action relies on photoinduced electron transfer (PET) in which the fluorescence is quenched by PET process that occurs between the p-anisidine redox moiety and the naphthalimide luminophore. The p-anisidine group is oxidized by $H_2O_2$, suppressing the PET and increasing the fluorescence intensity and a microtiter plate-based setup was used for fluorescent detection of $H_2O_2$ using this probe (Burmistrova et al., 2014). Furthermore, the addition of HRP enhanced the oxidation of HP green which improves the detection limit of $H_2O_2$ (Schäferling et al., 2011). Though there have been many organic dyes (including organometallic compounds) for $H_2O_2$ detection, the sensing mechanism for most fluorophores is based on fluorescence quenching (switch off) or enhancing (switch on) which may suffer from photobleaching problems. Thus, there is still room for synthesizing novel chemicals that show fluorescence shift rather than just quenching for more sensitive detection of $H_2O_2$.

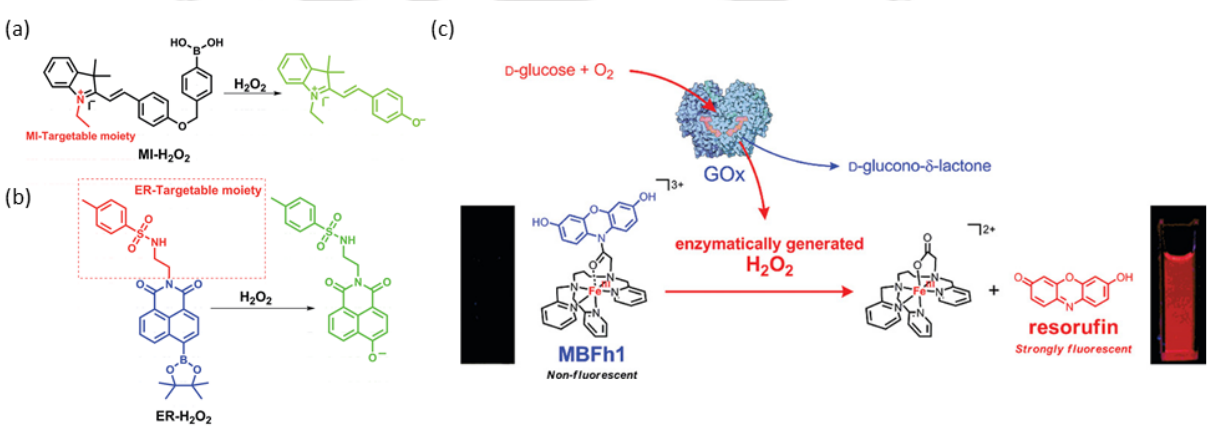


**Figure 1.5:** The chemical structures of (a) MI-H2O2 and (b) ER-H2O2 and corresponding response mechanism for $H_2O_2$ sensing in mitochondria and endoplasmic reticulum during apoptosis (Xiao et al., 2016) Copyright 2014, this is an open access article distributed under the Creative Commons Attribution License; (c) Scheme of the formation of resorufin by the reaction of MBFh1 with enzymatically generated $H_2O_2$ to prepare a fluorescent sensor (Hitomi et al., 2011) Copyright 2011, reprinted with permission from ACS Publications.

Distyrylbenzenes (**DSB**) are a class of fluorescent-conjugated organic molecules that can be functionalized by different substituents or functional groups in the desired position (Fig 1.6a). **P2VB** (1,4-bis(β-pyridyl-2-vinyl)benzene) is a **DSB** derivative with pyridine groups that tend to interact with the surrounding electronic structure (Fig 1.6b). **P4VB** (1,4-bis(4-pyridyl-2-vinyl)benzene) has nitrogen atoms on the more accessible fourth ring position, but it appears to associate more readily. However, this compound had limited solubility in an organic solvent. A relatively bulky and unreactive neopentyl side group are added onto the **P4VB** base structure to synthesize a new

fluorophore bis(4-pyridyl) dineopentoxyl-p-phenylenedivinylene (**np-P4VB**) which showed increasing solubility (Fig 1.6c). The fluorophore which exhibited high solubility in organic solvents, displayed fluorescence color-shift properties (Lane et al., 2018). When the highly accessible nitrogen atoms on the pyridine rings are protonated, a fluorescence emission shift from blue to orange occurred from the extensive electron delocalization in the lowest unoccupied molecular orbital (Wang et al., 2019). This fluorophore was immobilized onto paper for the detection of $CO_2$. The exposure of $CO_2$ to water led to the formation of carbonic acid, which generates the signal through protonation of the fluorophore (Wang et al., 2020a). Another quinoline-based fluorophore was prepared which showed color shifting optical properties in presence of a wide pH range (2-12) (Wang et al., 2020b). Such color-shifting fluorophores can be explored for $H_2O_2$ sensing.

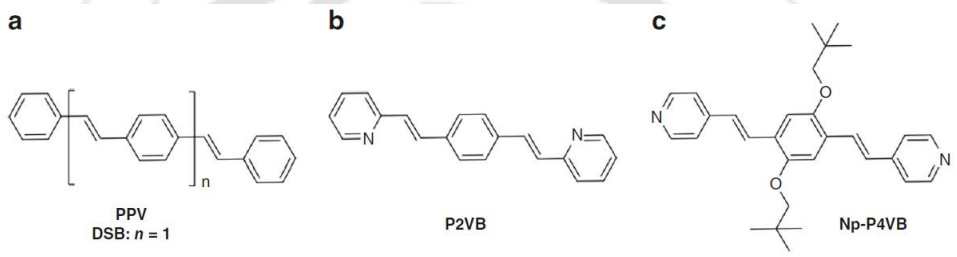


**Figure 1.6**: Chemical structures of a) **DSB** (PPV), b) **P2VB**, and c) **np-P4VB**. The key change between DSB and P2VB is the pyridine ring on each end. The difference between the P2VB and P4VB structures is the position of the nitrogen in the pyridine rings. The **np-P4VB** synthesized here is similar to P4VB but with the addition of branched neopentyloxy groups on the central benzene ring (Lane et al., 2018) Copyright 2018, this is an open access article distributed under the Creative Commons Attribution License.

### 1.5. Emerging trends in miniaturization and platform design

Various miniaturization techniques and advanced materials for platform designing are growingly used in the field of diagnostics and detection stepping towards technological fronts on translating the proof of concept to a marketable product. In this area microfluidics and micro-sensors have emerged as potential strategies for effective manipulation, treatment, and separation of sample contaminants for rapid and specific detection of analytes (Review: Thungon et al., 2017).

Microfluidics is the study of fluids in channels with a size that varies from a few units to hundreds of micrometres. The fabrication of Lab-on-chip (LoC) or Lab-on-a-disc (LabCD) systems, by miniaturizing different functionalities that are typically required in a whole biochemical laboratory into a chip or a compact disc, is possible using microfluidics. There are several advantages of these systems including high sensitivity, a requirement of low volumes of samples and reagents, faster

analysis as well as provision for standardisation and automation of the processes (Ibarlucea et al., 2011). These miniaturization-based concepts can help overcome many limitations of the conventional sensors such as long reaction and analysis time, and low portability of the systems. There are various materials which have been used for developing and designing these microfluidic platforms. The selection of material to develop the sensor platform is critical and should possess suitable chemical and mechanical properties to withstand different biological and chemical entities of the samples. Additionally, the material should also be biocompatible to accommodate various labile biological recognition elements, particularly, enzymes or microbes (Review: Kaushik et al., 2020). Another important parameter for choosing the right materials, especially for the development of disposable sensors is its biodegradability. With the increase in the amount of non-biodegradable wastage generated by using synthetic polymers, the scientific community must shift towards "green" and environmentally friendly technologies. The different substrate materials for the development of sensor platforms are discussed in the following section.

### *1.5.1. PDMS-based microfluidics*

The development of polymeric materials has had a tremendous impact on the realization LoC concept. Poly- carbonate (PC), poly (methyl methacrylate) (PMMA) and poly- (dimethylsiloxane) (PDMS) are among the most widely applied materials for the fabrication of LoC, which provide high versatility and reduction of both time and cost of the fabrication process (Ibarlucea et al., 2011). Among them, PDMS is the most widely used material due to its several advantages. It is a cheap material, polymerising at low temperatures. PDMS is also optically transparent in a very wide wavelength range (from UV to NIR) which is beneficial for development of optical detection methods (Makamba et al., 2003). It is also compatible with biological materials because of its non-toxicity, non-permeability to water and permeability to gases. Moreover, it has great physical properties such as flexibility and elasticity, with Young's modulus of 2.5 MPa when it is fabricated with a 10:1 ratio of base: curing agent (Makamba et al., 2003).

Photonic LoCs or, PhLoC use light as an interrogation mechanism and they are immune to electromagnetic interferences and/or enable multiplexed detection in a single system (Crespi et al., 2010). A hollow prism configuration made of PDMS, where the inner wall surface was modified with hydroxyl groups was reported. The hydroxyl groups were further silanised using a silane containing an aldehyde end-group and HRP was covalently attached via the interaction with the silane functionalized PDMS inner surface to prepare a PhLoC system for colorimetric sensor for $H_2O_2$ (Ibarlucea et al., 2011).

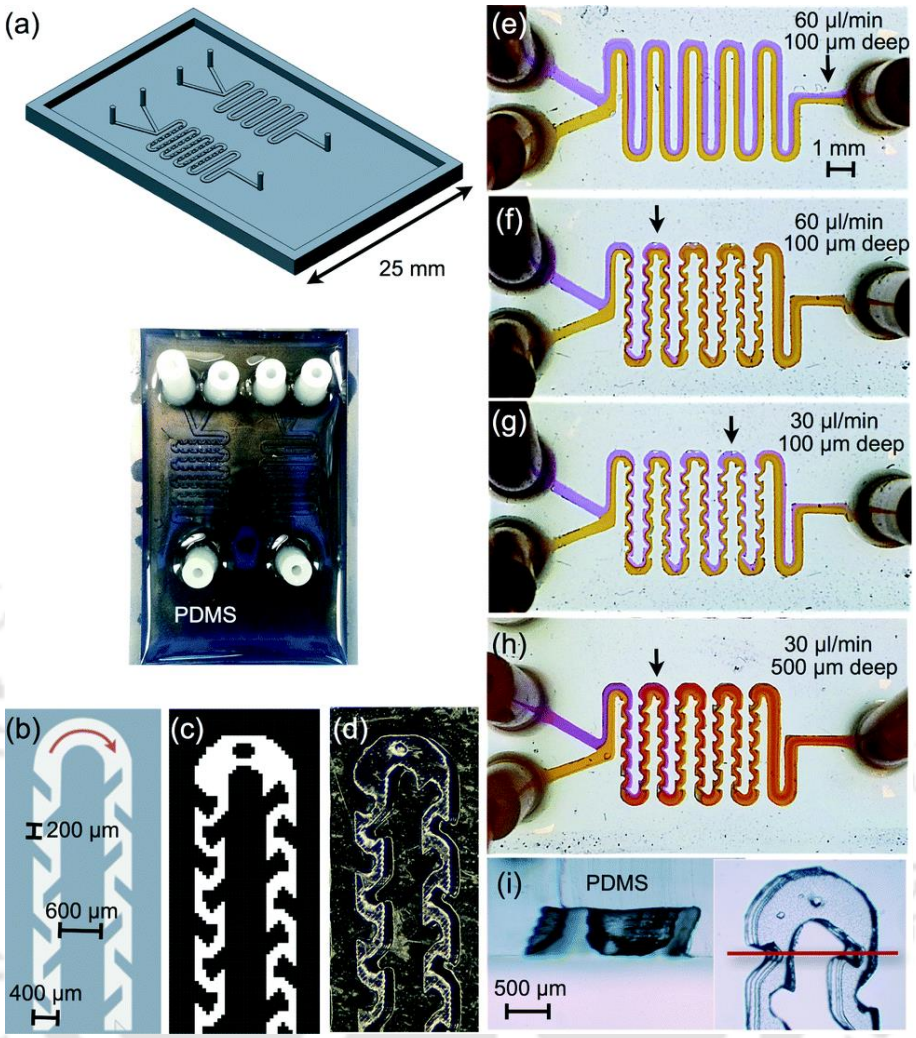


**Figure 1.7**: (a) Template for diffusion and chaotic mixers. The pillars are guides for silicone tubing integration and the external frame contains the PDMS during curing. (b) Detail of the chaotic mixer design. (c) Detail of the chaotic bitmap edited refinements. (d) Printed template. (e) 100 µm deep diffusion mixer showing the mixture of 1 mM fluorescein with 1 mM rhodamine B at 60 µL $min^{-1}$. (f) 100 µm deep chaotic mixer imaged in the same conditions as in (e). (g) Idem to (f) operated at 30 µL $min^{-1}$. (h) Idem to (g) but for a 500 µm deep channel. (i) Detail of the 500 µm deep chaotic mixer 3D structure. (Comina et al., 2014) ) Copyright 2014, reprinted with permission from Royal Society of Chemistry.

Another PhLoC was developed by using PDMS on glass surface. A 3D printed templated was prepared by using Miicraft®14, an MS 3D printer (2299 US$) with 450 ppi (~56 µm) lateral, and 50 µm vertical resolution (Comina et al., 2014), thereby, replacing the clean room resources. Different printed templates were prepared using an optimized process and conditions. To create a mixer within the channels, different depths of channels and flow speeds were explored. It was the pillars with a

rough texture that was added within the channels that led to more chaotic movement of the fluid within the channels leading to better mixing (Fig 1.7). This optimized template was used to prepare a colorimetric LoC glucose biosensor by co-immobilizing it with HRP. Furthermore, PDMS has been coated onto paper to develop an electrochemical $H_2O_2$ sensor (Tortorich et al., 2018; Lee et al., 2018).

### *1.5.2. Paper-based microfluidics*

The cellulose-based materials such as chromatography paper and filter paper have emerged as an attractive substrate for developing various optical sensing platforms (Martinez et al., 2010). Microfluidic channels could be easily created on these substrates to produce chip-based designs of the sensors for handing extremely low sample volume and multiplex analysis (Nishat et al., 2021). Microfluidic paper-based analytical devices (μPAD) have garnered extreme popularity in recent years as they qualify ASSURED (accurate, sensitive, specific, user-friendly, rapid, robust, equipment free, and deliverable to end users) criteria prescribed by WHO (Peeling et al., 2006). In general, paper as a sensor substrate has many advantages. Paper is also biocompatible and can be modified with various functional groups to covalently bind to proteins (Song et al., 2019), DNA (Seed, 1982) and other biomolecules (Mahadeva et al., 2015). The scope for rapid analysis has transformed paper-based platforms into easy and attractive analytical tools with possibilities for miniaturization and mass production (López-Marzo and Merkoçi, 2016). Furthermore, the simple fabrication approaches, sometimes using just paper cutting, to create channels also make paper microfluidics a very attractive technology. The basic principle in creating channels on paper is by creating hydrophobic zones on the hydrophilic paper. This has been achieved using wax printing, photolithography as well as laser printing (Nishat et al., 2021). Table 1.2 enlists the different fabrication techniques for μPAD design.

**Table 1.2**: Comparison of different fabrication techniques for paper-based microfluidic devices.

| **Technique** | **Equipment required** | **Advantages** | **Disadvantages** | **Ref** |
|---|---|---|---|---|
| ***Paper Cutting*** | Scissors, punchers, or laser cutter | Simple, no chemicals required | Size and design limitations, require a platform such as a polymer or tape. | (Jamil et al., 2021)(Liu et al., 2019a)(Nie et al., 2013)(Lebiga et al., 2015) |

| | | | | |
|---|---|---|---|---|
| ***Wax printing*** | Solid ink (wax) printer and hot plate | Simple and rapid, high resolution, mass production possible and no organic solvent required | Edges not sharp as wax spread. Unavailability of wax printer. | (Ragavan et al., 2018)(Strong et al., 2019)(Sechi et al., 2013) |
| ***Photo-lithography*** | Photomask, UV light source | High resolution | Complex and expensive fabrication process. | (Kakoti et al., 2015)(Martinez et al., 2008) |
| ***Laser Printing*** | Laser printer and hot plate | Low cost, minimal equipment required | Difficult to modify ink | (Rafatmah and Hemmateenejad, 2019)(Ghosh et al., 2019) |
| ***Inkjet Printing*** | Inkjet printer, hot plates, and modified cartridges ink | Simple, rapid, and low-cost process, possible to mass produce | Require solvent treatment of paper | (Chakma et al., 2016)(Yamada et al., 2015) |
| ***Screen Printing*** | Screen | Low cost | New screens required | (Dungchai et al., 2011) |

Several paper-based electrochemical $H_2O_2$ sensors have been reported using silver nanoparticles (Sharma et al., 2020) and multi-walled carbon nanotubes (MWCNTs) (Shamkhalichenar and Choi, 2017; Sánchez-Calvo et al., 2020). Recently, $MnO_2$ nanostructures were coated on tea bag filter paper to develop a bendable and self-standing electrochemical $H_2O_2$ sensor (Priyanga et al., 2021). Furthermore, colorimetric (Xu et al., 2011a) and fluorometric (Chang et al., 2018) based paper sensors for $H_2O_2$ have also been reported.

A µPAD-based colorimetric assay for detection of $H_2O_2$ was reported using a starch-iodide-gelatin composite system. Here, the detection principle used the fact that $H_2O_2$ oxidizes the potassium iodide to iodine which reacts with starch, changing the white paper strip to blue. The addition of gelatin not only made the color darker and amplified the intensity but also acted as an immobilization matrix for

enzyme, GOx to prepare a colorimetric glucose biosensor (Liu et al., 2019a). Chitosan was reported to possess peroxidase activity and a colorimetric µPAD was prepared using chitosan for $H_2O_2$ sensing with TMB as the chromogen (Ragavan et al., 2018). Wax printing was used to fabricate the µPAD.

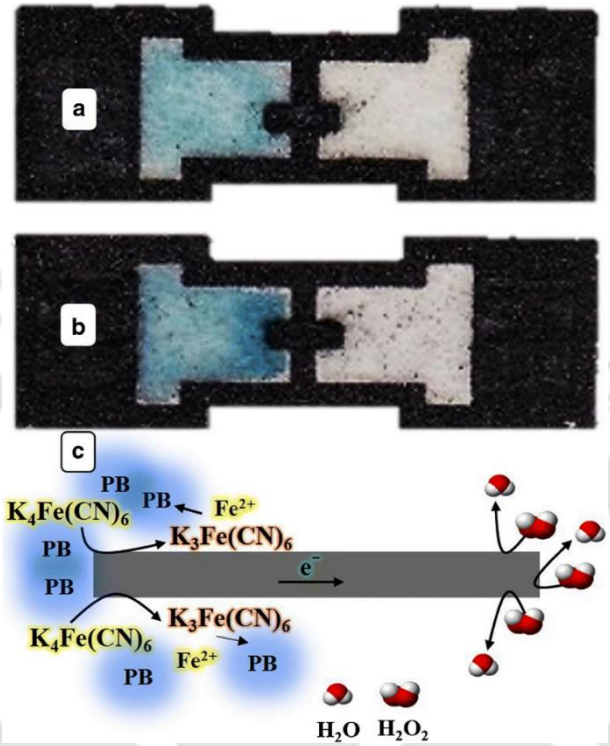


**Figure 1.8:** (a) Blank and (b) sample BPE sensor indicating PB formation around BPE. (c) Schematic representation of the fundamental mechanism of using $K_4Fe(CN)_6/FeSO_4$ in reporting cell of P-BPE sensor (Rafatmah and Hemmateenejad, 2019) Copyright 2019, reprinted with permission from Springer Nature.

A unique disposable paper-based colorimetric-electrochemical biosensor for $H_2O_2$ was reported. It consists of a bipolar electrode (BPE) and a driving electrode (DE) which were constructed on paper strips using laser printing for the microfluidic design, and pencil graphite for the electrodes (Fig 1.8a) (Rafatmah and Hemmateenejad, 2019). The detection principle of this BPE is based on the reduction of $H_2O_2$ on the electrode (left side) when an external potential is applied, which in turn causes the oxidation of $K_4Fe(CN)_6$ in the presence of Fe(II) ions and subsequently form Prussian Blue (PB) particles in the reporting cell (right side) (Fig 1.8 b,c). The PB has a deep blue color which is distinguishable from the initial light blue color, and this allowed the colorimetric detection of $H_2O_2$. This setup was then used to fabricate a glucose biosensor and the color change was captured using a

smartphone. Moreover, paper used base/ foundation platforms with PDMS (Tortorich et al., 2018; Lee et al., 2018), and plastic (Lebiga et al., 2015) to fabricate optical $H_2O_2$ sensors.

Though paper-based devices offer many advantages, a few disadvantages have also been encountered. The major disadvantage is the coffee ring effect which may interfere with the optical signal of the constructed sensors. The coffee ring effect has been attributed to two factors: 1) pinning of the contact line on the deposition of a drop of fluid on a solid surface and 2) the drying of the fluids via evaporation. Briefly, once a drop is deposited on a solid surface, the edge of the drop is pinned at the contact line. As the drying due to evaporation takes place, liquid first evaporates from the edges. To replenish the loss, fluid from the interior flows outward due to capillary force (Fig 1.9) (Li et al., 2016). The resulting outward flow carries the dispersed material in the fluid to the edge creating the coffee ring effect (Deegan et al., 1997). Capillary wicking is an intrinsic property of paper which is considered a critical factor for the distribution of any solute over an area (Cao et al., 2020). Several chemical treatments with surfactants (Sempels et al., 2013; Trofimchuk et al., 2020) as well as the configuration of the solutes (Yunker et al., 2011) have been implemented to reduce this effect (Cao et al., 2020).

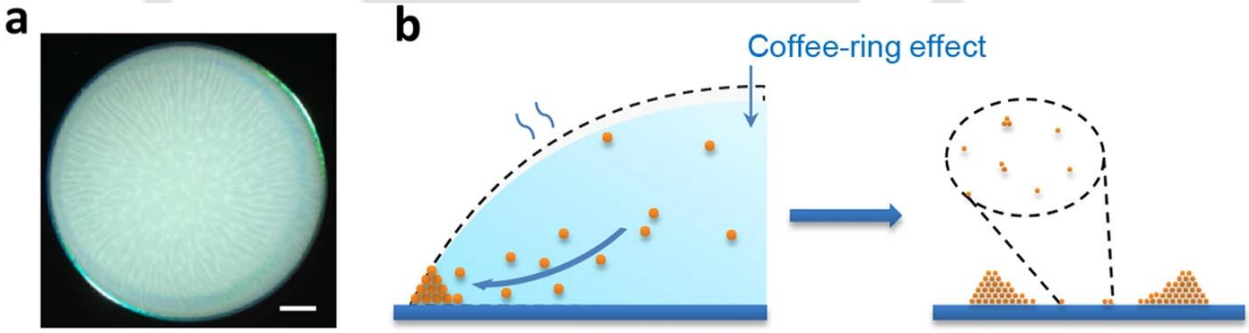


**Figure 1.9**. Obvious capillary outflow at low evaporation temperature (T = 30 °C) (a) Image with streamlines of capillary flow, (b) scheme of the transport of the suspended particles to drop edge leading to the formation of ring stains during the evaporation of the fluid (Li et al., 2016) Copyright 2016, this is an open access article distributed under the terms of the Creative Commons CC BY license.

### *1.5.3. Silk fibroin-based platforms*

The stability of the biomolecules such as enzymes and microbes on the sensor surface is extremely important for real-world application of biosensors as the functionality of the whole sensor is largely dependent on the activity of the immobilized biomolecule. The silk fibroin (SF), a fibrous protein found in the cocoons of *Bombyx mori* (*B. mori*) silkworm, is a versatile biomaterial due to its high

intrinsic stability to temperature and moisture changes. Its biocompatibility renders its application in biosensing and other areas (Kaushik et al., 2020; Drachuk et al., 2013). Moreover, it could be transformed into different types of scaffolds, such as fiber, film, or hydrogels (Saxena and Goswami, 2010). By tuning the secondary structure of SF, these formats can also be tuned further (Vepari and Kaplan, 2007; Kaushik et al., 2020). Among the different formats, SF films are considered versatile because enzymes and other bio recognition elements could be easily immobilized in them by using direct entrapment methods. Enzymes are mixed in SF solution, and the mixture is cast on surfaces and air-dried. The solubility and the hydrophobicity ($\beta$-sheet structure) of these films can be tuned by annealing with water or methanol. The thickness of the film could be monitored by adjusting the concentration of the SF solution, casting volume, and drying rate (Rockwood et al., 2011). Miyairi et al. first reported the SF film as a support for enzyme immobilization. $\beta$-Glucosidase was entrapped in the SF film, and its activity was monitored. The immobilized enzyme showed 80 % retained activity after heat treatment up to 60 ℃ and protease treatment (Miyairi et al., 1978). Since then, several other enzymes, such as HRP (Lu et al., 2009a; Lu et al., 2010), GOx (Lu et al., 2009b; You and Pak, 2014) have been entrapped in SF films with testified reports of their stability and activity.

As mentioned earlier, HRP is an important enzyme for the preparation of $H_2O_2$ biosensors. HRP has low stability in solution which is thus, a disadvantage for its use in developing HRP-based biosensors. There have been several reports of the enzyme being immobilized and stabilized in SF films via bulk-entrapment (Review: Kaushik et al., 2020). A study conducted by Lu et al., 2010, demonstrated that after HRP was immobilized in SF films, its activity and storage stability increased. This unique behaviour was also presented for GOx entrapped in SF films (Lu et al., 2009b). The authors postulated that the denatured enzymes renatured to their native state over time within the SF film structure. During the film preparation, spontaneous denaturation takes place, which may become reversible under some suitable conditions. The micro-environment within SF films contains about 10 wt % water, as well as the presence of hydrophobic and hydrophilic pockets, allowing the mobility of the enzyme molecules for refolding/renaturation as shown in Scheme 1.5. HRP in SF films was reported to have the residual activity 24%, 22%, and 17% after 5 months, when stored at 4 °C, room temperature (25 ℃), and 37 °C, respectively (Lu et al., 2009a). HRP, along with lysozyme, was entrapped in SF films with increased $\beta$-sheet structure and crystallinity and their release pattern was studied. The results suggested that the SF films with a controllable level of crystallinity would be a reliable support for drug release (Hofmann et al., 2006). Another study reported that the interaction between heme in HRP and electrode depended on the morphology of the SF films being used as immobilizing matrix (Wu et al., 2006). HRP was integrated into a silk solution and cast on diffractive

molds to prepare patterned SF films, which could be used for the development of optical peroxide sensors (Lawrence et al., 2008a). Glycerol-modified SF films further increased this stability. HRP in 30% glycerol SF film retained more than 90% of the initial activity at even 37 °C over 2 months (Lu et al., 2010). Enzymes HRP and catalase were entrapped into the diffractive optical elements (DOEs) functionalized with SF membranes (SF DOEs). The enzymes entrapped in SF DOEs showed better stability and activity than those entrapped in glass DOEs, and thus appeared as a promising platform for developing optical biosensors (Zhou et al., 2017).

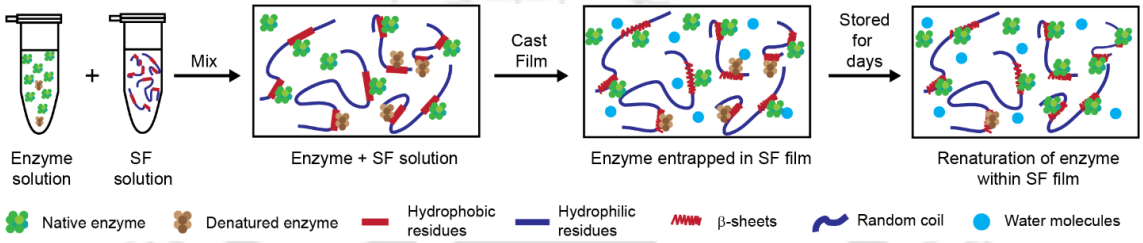


**Scheme 1.5**: Schematic illustration of postulated mechanism of enzyme activity change in SF films. The interaction between enzyme and hydrophobic region (*β*-sheet structure) and constrained mobility stabilized the enzyme in SF films. Enzyme activity increased overtime due to the enzyme's reversible denaturation during the film preparation and the renaturation takes place upon interaction with the silk material.

Diffusion of substrate through an immobilizing membrane or platform is crucial for the function of the sensors. This can be improved in SF films by increasing their porosity. PEG was used as a dissolvable matrix to prepare PEG-SF film. Once the membrane was made non-dissolvable, PEG was removed from the film by simply dissolution with water to get the porous SF membrane. GOx was then entrapped in this film, where the substrate diffusion was improved (Demura and Asakura, 1991).

### 1.6. Significant Gaps in the Research

A plethora of reports is available on developing various methods for detecting $H_2O_2$ through optical transduction principles, as observed from the above literature survey. However, only meagre number of these reports have focussed on developing the sensor platforms for real-world applications. A systematic study on the application of emerging microfabrication techniques and biocompatible materials for developing such $H_2O_2$ sensors is yet to be pursued even though these techniques and materials' intervention in the constructions are known to improve the cost-economy and various performance factors of a sensor. Microfluidics has already been validated as a potential microfabrication technique for developing lab-on-chip sensors. In unison, introducing paper-based

materials in lab-on-chip sensor platforms has great potential to create disposable and low-cost sensing devices. We have also noticed a significant gap in integrating the $H_2O_2$ detection with the detection of various analytes of clinical importance, such as alcohols on the portable sensor platforms, even though many enzymatic oxidations of these substrates also release the peroxide. While developing enzymatic sensors, it is also imperative to ensure the stability of the enzymes on these sensor platforms. So, appropriate material and immobilization techniques need to be explored while preparing enzymatic lab-on-chip-based biosensor devices. Most importantly, we find that there is enough scope to explore suitable $H_2O_2$ detection strategies through optical transduction principles particularly, by exploiting chemical chromogen and fluorophore, protein stabilized AuNCs, and conventional peroxidase reactions on sensor platforms. We made an effort to bridge these gaps by formulating the objectives outlined below.

### 1.7. Objectives of the study

Considering the importance of the detection of hydrogen peroxide and the gaps in developing portable sensors, the overall objective defined for this thesis is the development of optical signal-based hydrogen peroxide sensor. Efforts have been made to reach this objective by exploring the characteristic properties of an organic dye, peroxidase enzyme, and protein-stabilized gold nanoclusters for the development of stable and sensitive $H_2O_2$ sensing platforms with an endeavour to develop lab-on-chip sensor devices.

The following sub-objectives are thus considered for this study:

1. **Organic dye-based $H_2O_2$ detection:** Study the optical properties of a novel water-soluble organic dye in presence of $H_2O_2$, immobilize the organic dye onto paper substrate and explore the prepared reagent-less system for the peroxide and alcohol sensing applications.
2. **Peroxidase-based $H_2O_2$ detection:** Immobilization of peroxidase (HRP) into silk fibroin films, its interaction study with ABTS and SF, and explore the findings for reagent-less sensor for alcohol by coupling this reaction with alcohol oxidase enzyme in the sensor platform.
3. **Protein stabilized gold nanoclusters based $H_2O_2$ detection:** Synthesis and characterization of AuNCs stabilized in catalase, developing sensitive fluorometric as well as colorimetric based methods for $H_2O_2$ sensing.

### 1.8. Structure of the thesis

This thesis has been subdivided into five chapters as briefly described below.

**Chapter I: Introduction and Review of Literature**

This chapter will cover the recent detection methods and sensors for hydrogen peroxide ($H_2O_2$) and their applications. Overview of different optical methods exploiting enzymatic, nanomaterials and organic dye-based systems employed to detect $H_2O_2$ has been presented. Various emerging materials such as paper, proteins (silk fibroin) and polymers which have been used for designing miniaturized sensors are also discussed.

**Chapter II: Fluorescent organic dye-based sensing of hydrogen peroxide and its application for alcohol detection**

In this chapter, a new organic dye, carboxy-functionalized P4VB (**c-P4VB**) with a short-chain conjugated molecular unit susceptible to the protonation of its terminal pyridine groups, causing a large shift in the emission colour from blue to orange or red was synthesized. This dye was soluble in water and sensitive to $H_2O_2$ due to its weak acidic nature. It was successfully immobilized onto paper discs to develop a disposable paper-based $H_2O_2$ sensor. Next, the application of this paper sensor was used to develop a fluorescent, two-zone, cut-out paper microfluidic device for alcohol detection.

**Chapter III: Peroxidase-based sensing of hydrogen peroxide and its application in developing a reagent-free alcohol biosensor**

This chapter first describes a simple colorimetric sensor for $H_2O_2$ by entrapping peroxidase in non-dissolvable SF film and using ABTS as the chromogen. Next, a multimeric enzyme, alcohol oxidase (AOx) was co-entrapped with peroxidase in SF films to prepare a simple colorimetric sensor for alcohol. Finally, we developed a reagent-free colorimetric alcohol sensor by entrapping ABTS as well in SF film. A two-layer hybrid µPAD with ABTS SF film and the bi-enzyme SF film within paper microfluidic platform was designed. A detail characterization of performance parameters and their stability were studied.

**Chapter IV: Protein stabilized gold nanoclusters as hydrogen peroxide sensing probe**

In this chapter, the synthesis and characterization and application for $H_2O_2$ sensing of the two AuNCs stabilized within catalase protein (Cat), red fluorescent (RF) and blue fluorescent (BF) have been described. Through spectrometry and circular dichroism studies, we postulated that the initial pH during the synthesis may play an important role in increasing the $\beta$-sheet secondary and the synthesis of blue-fluorescent clusters. Next both the Cat-AuNCs were monitored under different concentrations of $H_2O_2$. The fluorescence intensity of RF Cat-Au NCs decreased with the $H_2O_2$ concentration, and this method was used to develop fluorescent ratiometric sensing of $H_2O_2$. In case of BF Cat-Au NCs, with the interaction of $H_2O_2$, the AuNCs were transformed into AuNPs, and this novel phenomenon was used to develop a colorimetric sensing method for $H_2O_2$ without using any chromogen or dye. Furthermore, the sensing mechanism was explored using TEM and time resolve spectroscopy.

**Chapter V: Conclusions and future directions of research**

Finally, this chapter describes the overall conclusion of the thesis, comparing the performances of the different optical sensing methods developed. A critical evaluation of the work with the scope for future work has also been included.

# CHAPTER II

## FLUORESCENT ORGANIC DYE-BASED SENSING OF HYDROGEN PEROXIDE AND ITS APPLICATION FOR ALCOHOL DETECTION

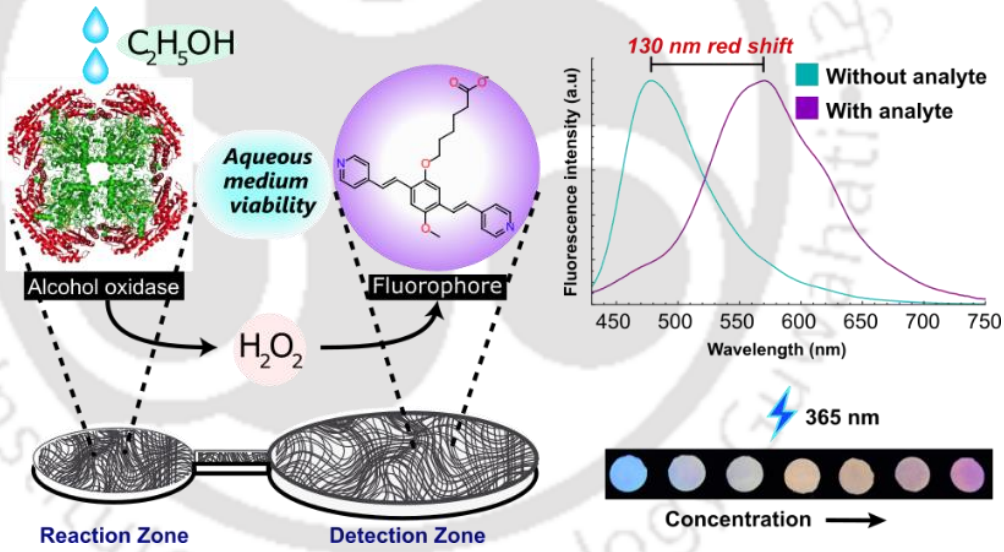

# CHAPTER II

# Fluorescent organic dye-based sensing of hydrogen peroxide and its application for alcohol detection

## 2.1. Introduction

A novel organic fluorophore called bis(4-pyridyl) dineopentoxyl-p-phenylenedivinylene or **np-P4VB** was recently reported which has the unique ability to fluoresce or even lase at almost any wavelength in the visible spectrum (Lane et al., 2018; Wang et al., 2019). It possesses an excellent fluorescence sensing capacity because of the nitrogen atoms on the accessible fourth ring position of its terminal pyridine groups (Fig 2.6a). The sensing mechanism is based on the protonation of these pyridines, leading to a blue-to-orange color shift (red shift) as a function of pH. The major challenge of using this fluorophore on solid platform is its low aqueous solubility that dissolute this dye during the sample treatment process at the time of detection. In this chapter, the np-P4VB was modified and functionalized with carboxylic group (-COOH) (denoted by **c-P4VB**) (Fig 2.6b) by our collaborators at the Technical University of Munich. The carboxyl functionalization in principle allows a reaction site for organic molecules for chemical binding or physisorption processes as well as making the fluorophore soluble in aqueous solutions rendering better applications on solid substrates such as paper (Wang et al., 2018b). We explored the weak acid property of $H_2O_2$ to fabricate a simple, cost-effective fluorescence paper sensor for detection of $H_2O_2$. We investigated the basic optical properties of **c-P4VB** and then incorporated it into a cellulose paper to prepare a simple paper-based fluorescence probe for detection of $H_2O_2$, and we finally demonstrate an alcohol sensor based on enzyme-catalyzed production of $H_2O_2$.

The detection of ethanol is important for forensic sectors, and for the clinical, chemical, pharmaceutical and fermentation industries. Simple, inexpensive ethanol sensors are also needed to verify the alcohol content of commercial liquors and to help ensure their authenticity. With ethanol possibly becoming a legislated biofuel in many countries, a simple and rapid system for detection of ethanol in solution may become increasingly important (Thungon et al., 2017). Alcohol oxidase (AOx) is an oxido-reductase enzyme that catalyses the oxidation of alcohols using molecular oxygen

($O_2$) into their corresponding aldehydes (equation 2.1), along with the production of hydrogen peroxide ($H_2O_2$).

$$RCH_2OH + O_2 \xrightarrow{AOx} RCHO + H_2O_2 \quad (2.1)$$

Most paper-based alcohol sensors work on the electrochemical method (Bihar et al., 2016; Cinti et al., 2017); only few use colorimetric techniques (Thepchuay et al., 2020), and fluorescent techniques (Gotor et al., 2019; Duan et al., 2021). This is the first report of a fluorescent µPAD alcohol sensor based on AOx enzyme.

## 2.2. Experimental section

### *2.2.1. Chemicals and reagents*

Alcohol oxidase (AOx) (EC 1.1.3.13 from *Pichia pastoris*) [1000 U $mL^{-1}$] and Whatman Grade 1 Filter paper were purchased from Sigma Aldrich (USA). Hydrogen peroxide (~50 w/v%) and ethanol (99.9%) was purchased from Himedia Laboratories Pvt. Ltd. (Mumbai, India). All ethanol working standard solutions were prepared daily in MilliQ water (18.2 MΩ.cm). All solvents and reagents used in the synthesis were purchased from commercial sources and were applied without additional purification unless stated otherwise.

### *2.2.2. Optical characterization*

The solution-based fluorescence spectroscopy was excited with the combined $\lambda_{351nm}$ and $\lambda_{364nm}$ lines of an $Ar^+$ ion laser (~1.25 $kW/m^2$), while the paper-based setup generally used a $\lambda_{405nm}$ pulsed diode laser at lower power densities, which minimized the weak fluorescence inherent to paper under UV excitation. The fluorescence was collected directly with an optical fiber (numerical aperture = 0.5), passed through a $\lambda_{400nm}$ or $\lambda_{450nm}$ long pass filter, and measured with an intensity-calibrated miniature spectrometer from Ocean Optics (Model:USB2000+). Fluorescence microscopy was performed with a Nikon TE2000e inverted epifluorescence microscope. UV-vis spectroscopy was performed using a model Cary-50 single beam spectrophotometer from Varian.

### *2.2.3. Preparation of functionalized fluorophore c-P4VB*

The **c-P4VB** fluorophore was synthesized at Technical University of Munich, Germany, according to the following protocol. Briefly, 6-(4-methoxyphenoxy)hexanoic acid was prepared via the Williamson ether synthesis approach under optimized reaction conditions starting from 4-methoxyphenol and 6-bromohexanoic acid. This was subsequently bromomethylated with paraformaldehyde and HBr in acetic acid using a standard protocol. Thus obtained 6-(2,5-bis-

(bromomethyl)-4-methoxyphenoxy)hexanoic acid was reacted with excess triethyl phosphite at 150°C to yield ethyl 6-(2,5-bis-((diethoxyphosphoryl)-methyl)-4-methoxyphenoxy)hexanoate, which was further converted to sodium 6-(4-methoxy-2,5-bis((E)-2-(pyridin-4-yl)vinyl)phenoxy)hexanoate (**c-P4VB**) by reaction with 4-pyridincarboxaldehyde (Horner-Wadsworth-Emmons reaction conditions), producing a fine yellow to orange powder after purification. The details of the synthesis process have been described in our published work (Thungon et al., 2022). The **c-P4VB** was then dissolved in DMSO, EtOH or MeOH (0.2 mM) for optical investigations. For comparative study purposes, **np-P4VB** was also synthesized using previously-described methods (Wang et al., 2019). $^{1}$H NMR spectra were measured on Bruker AV-III 300 MHz and Bruker AV-III HD 500 MHz spectrometers.

### *2.2.4. Optical response of c-P4VB with acid and $H_2O_2$*

Different concentrations of $H_2O_2$ (0.1 mL) and HCl (0.1 mL) were added to 0.9 mL of **c-P4VB** (0.2 mM) solution prepared in EtOH and the fluorescence response was measured.

### *2.2.5. Preparation of c-P4VB-infused paper*

Paper disks (0.5 inch diameter) made from Whatman No. 1 filter paper were prepared by using a puncher or simple cutting. A reaction solution was prepared, consisting of 0.1 mL of 0.5 mM **c-P4VB** (in EtOH) added to 0.9 mL of pH 8 potassium phosphate buffer (50 mM). A slightly basic pH was chosen to prevent protonation and to improve the fluorophore solubility compared to buffers with lower pH. The solubility of the fluorophore in the buffer solution depends on buffer concentration, with a lower solubility at higher buffer concentration (*e.g.*, above 500 mM it becomes nearly insoluble). 10 paper disks were incubated in this reaction solution for 1 hour. Next, they were rinsed separately in water twice and then methanol. Finally, the treated disks were sonicated for 30 minutes in methanol to remove the excess fluorophore. After the sonication, the disks were placed in a fume hood to dry for 15 minutes. A schematic diagram of the entire process is shown in Scheme 2.1.

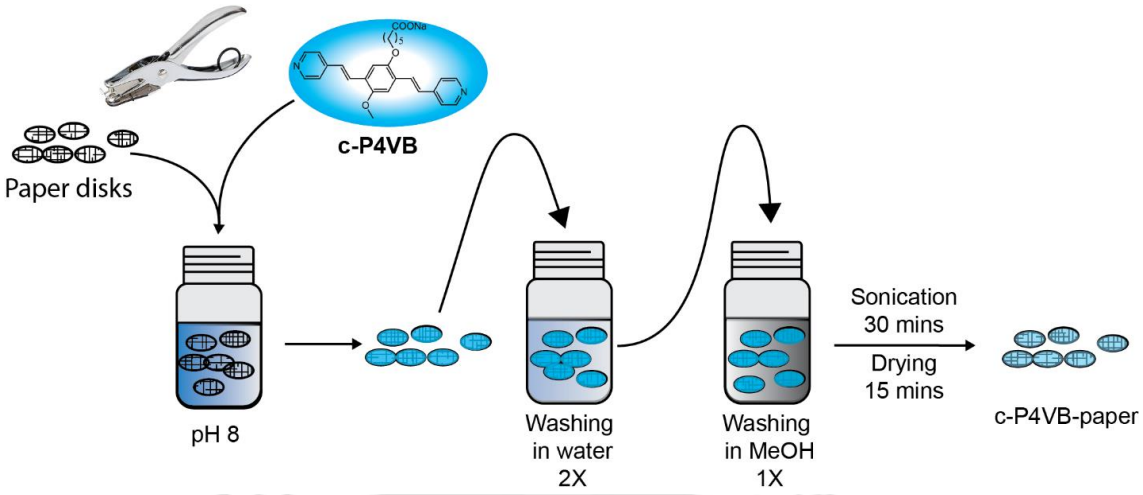


**Scheme 2.1:** Steps involved in preparing **c-P4VB** infused paper.

### *2.2.6. Hydrogen peroxide sensing with c-P4VB-paper*

To test the response of **c-P4VB**-paper, the paper disks were dipped into 2 ml of different concentrations of $H_2O_2$ solution, and the fluorescence emission changes were measured immediately. To test whether the stabilizers (which are sometimes acidic) in commercial $H_2O_2$ solutions interfered with the response, $H_2O_2$ was distilled using a rotary vacuum evaporator and the optical experiments were confirmed with this "clean" hydrogen peroxide. The final concentration of the distilled solution was measured using enzyme assay.

### *2.2.7. Ethanol µPAD fluorescence biosensor*

A µPAD ethanol sensor was prepared using two paper zones connected by a microfluidic channel. The first paper disk was the micro-reaction zone (**R**) (0.25 inch in diameter) with immobilized alcohol oxidase (AOx) that catalyzes the oxidation of primary alcohol to the corresponding aldehyde and $H_2O_2$. 10 µL of AOx (20 U $mL^{-1}$ in water) was dropped onto **R** zone and allowed to dry under a laminar flow hood for 1 hour. The second disk was the sensor zone (**S**) (0.5 inch in diameter) infused with **c-P4VB**. The entire set-up was prepared on scotch tape to attach the two zones with the linking channel (Fig 2.8). Next, 10 µL of ethanol prepared in MilliQ was dropped on the **R** zone and allowed to incubate for 5 minutes to complete the reaction of AOx to produce $H_2O_2$, following which 20 µL of MilliQ was dropped on the same zone to carry the reaction products into the **S** zone. After 5 minutes photographs of the treated **S** zone were taken using a smart phone. The signal was captured by choosing a group of 5000 pixels near the input channel where the signal was strongest, splitting

the image into the three-color channels (RGB), and dividing the average intensity in the blue channel by that in the red. Error bars represent the standard deviation of three separate measurements.

### *2.2.8. Real sample analysis*

Two commercially available Vodka brands, Smirnoff (SM) and Magic Moments (MM), were procured from a local liquor store in India. Samples were taken from each bottle and were diluted by adding 10 µL of each liquor samples to 990 µL of MQ water. 10 µL of the diluted samples were dropped onto the **R** zone and incubated for 5 minutes to allow the enzymatic reaction sufficient time. Next, 20 µL of MilliQ was dropped on the **R** zone to carry the products to the **S** zone. After another 5 minutes, images of the **S** zone were taken under UV light using a smartphone. The pixel intensity of the **S** zones was then analyzed as described in ethanol biosensor experimental section. The pH of the samples was measured using Mettler Toledo Benchtop pH meter. A further confirmation of the alcohol content was done using an enzyme oxidase assay (Mangos and Haas, 1996). ABTS was used as chromogen for the peroxidase reaction using peroxidase enzyme (62.5 U $mL^{-1}$). The reaction solution consisted of 930 µL ABTS solution (2 mM in 100 mM phosphate buffer, pH 7.5), 3 µL peroxidase (62.5 U $mL^{-1}$) and 30 µL AOx (0.2 U $mL^{-1}$). 30 µL of varying concentration of ethanol and consumer vodkas (either SM and MM) were added to the reaction solution and the final solution was incubated for 10 minutes in room temperature. The alcohol concentration was measured from the absorbance at $\lambda_{405nm}$, which was performed with a Cary 300 Bio UV–vis spectrophotometer. The blank for this assay was prepared by using MilliQ instead of ethanol solution.

### *2.2.9. Statistical analysis of data*

The statistical analysis of the data was performed in OriginPro 9.0. A minimum of triplicate analyses was performed for all the samples. The mean with the standard deviation is represented as error bars in the data. The limit of detection (LoD) was calculated using the formula $3\sigma/m$, where $\sigma$ is the standard deviation of the mean grey pixel intensity of the blank sample and $m$ represents the slope of the calibration curve.

## 2.3. Results and Discussion

### 2.3.1. NMR analyses of products

#### 2.3.1.1. NMR analysis of 6-(4-methoxyphenoxy)-1-hexanoic acid

The NMR spectrum of the yielded 1.6 g (83%) of 6-(4-methoxyphenoxy)-1-hexanoic acid is shown in Fig 2.1. along with its chemical structure.

$^{1}$H NMR (300 MHz, $CDCl_3$), δ (ppm): 6.83 (s, 4H), 3.91 (t, $^{3}J$ = 6.4 Hz, 2H), 3.77 (s, 3H), 2.40 (t, $^{3}J$ = 7.4 Hz, 2H), 1.84-1.64 (m, 4H), 1.58-1.46 (m, 2H).

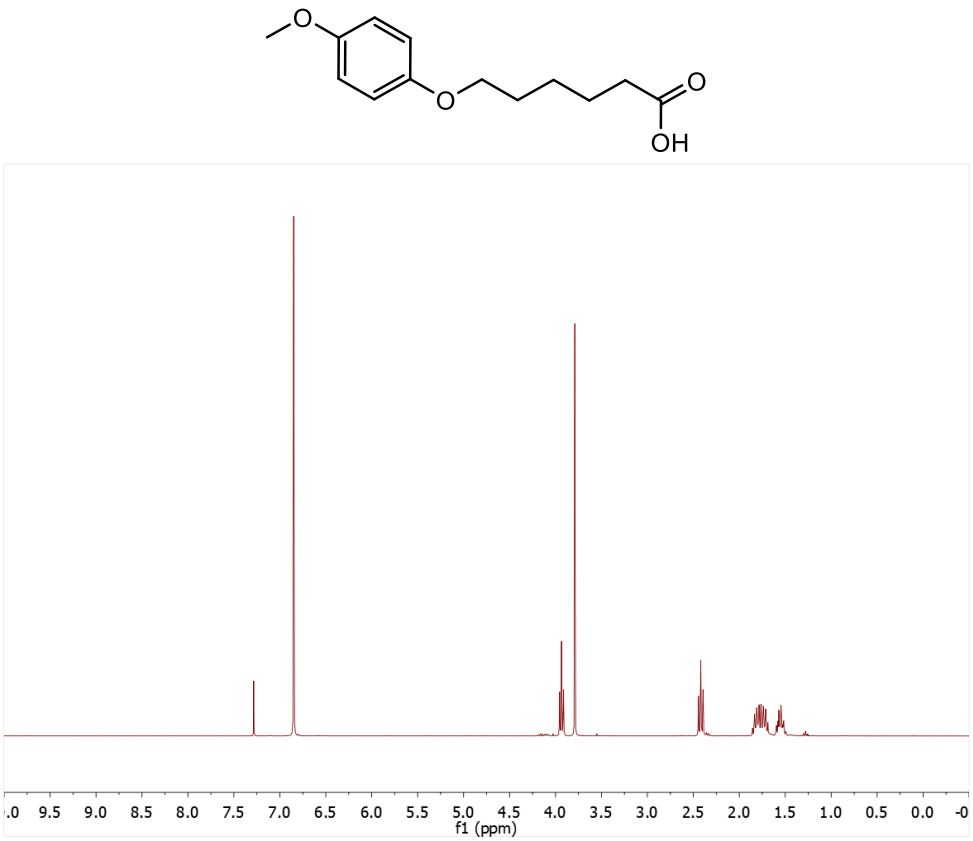


**Figure 2.1:** $^{1}$H NMR (300 MHz, $CDCl_3$) spectrum of 6-(4-methoxyphenoxy)-1-hexanoic acid

### 2.3.1.2. NMR analysis of 6-(2,5-bis-(bromomethyl)-4-methoxyphenoxy)-1-hexanoic acid

The NMR spectrum of the yielded 2.8 g (66%) of 6-(2,5-bis-(bromomethyl)-4-methoxyphenoxy)-1-hexanoic acid is shown in Fig 2.2. along with its chemical structure.

$^{1}$H NMR (300 MHz, $CDCl_3$), δ (ppm): 6.79, 6.77 (2s, 2H), 4.44, 4.43 (2s, 4H), 3.91 (t, $^{3}J$ = 6.3 Hz, 2H), 3.77 (s, 3H), 2.25 (t, $^{3}J$ = 7.3 Hz, 2H), 1.81-1.69 (m, 2H), 1.68-1.55 (m, 2H), 1.54-1.41 (m, 2H). (Addition of a droplet of methanol maybe necessary to achieve a complete dissolution of the sample).

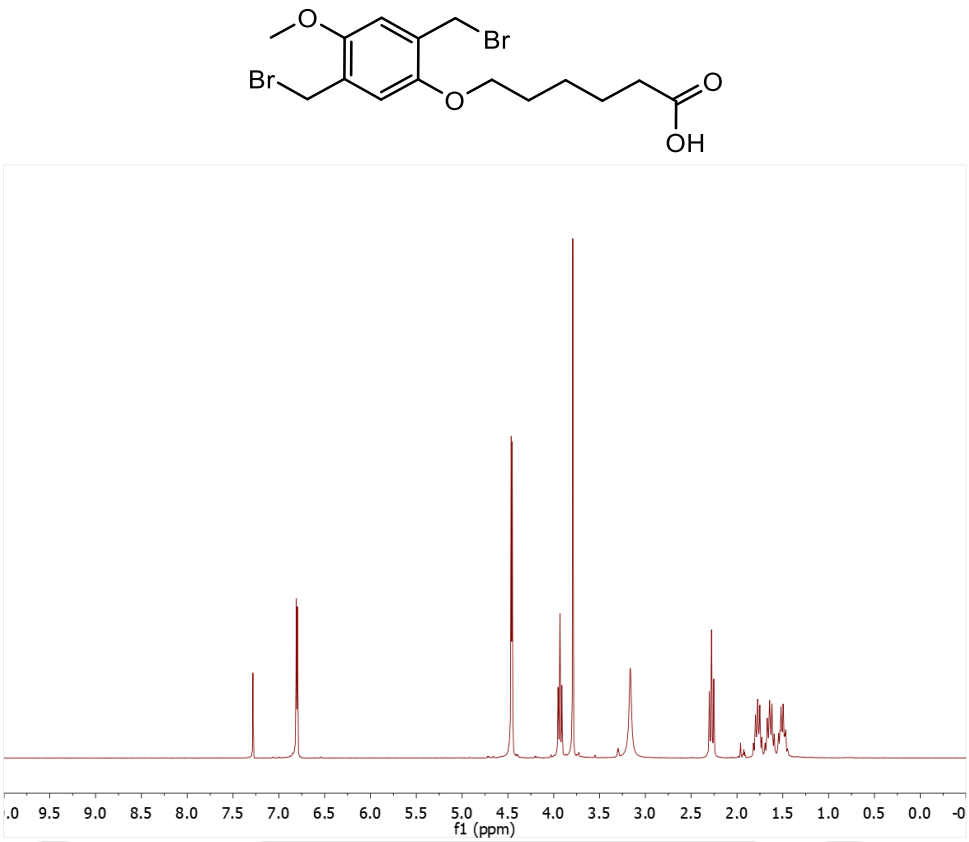


**Figure 2.2:** $^{1}$H NMR (300 MHz, $CDCl_3$) spectrum of 6-(2,5-bis-(bromomethyl)-4-methoxyphenoxy)-1-hexanoic acid

### 2.3.1.3. NMR analysis of Ethyl 6-(2,5-bis((diethoxyphosphoryl)-methyl)-4-methoxyphenoxy) hexanoate

The NMR spectrum of the yielded 1.16 g (87%) of liquid ethyl 6-(2,5-bis((diethoxyphosphoryl)methyl)-4-methoxyphenoxy) hexanoate is show in Fig 2.3. along with its chemical structure.

$^{1}$H NMR (300 MHz, $CDCl_3$), δ (ppm): 6.92-6.87 (m, 2H), 4.12 (q, $^{3}J$ = 7.1 Hz, 2H), 4.06-3.95 (m, 8H), 3.91 (t, $^{3}J$ = 6.4 Hz, 2H), 3.78 (s, 3H), 3.27-3.13 (m, 4H), 2.32 (t, $^{3}J$ = 7.5 Hz, 2H), 1.84-1.62 (m, 4H), 1.54-1.41 (m, 2H), 1.28-1.18 (m, 15H).

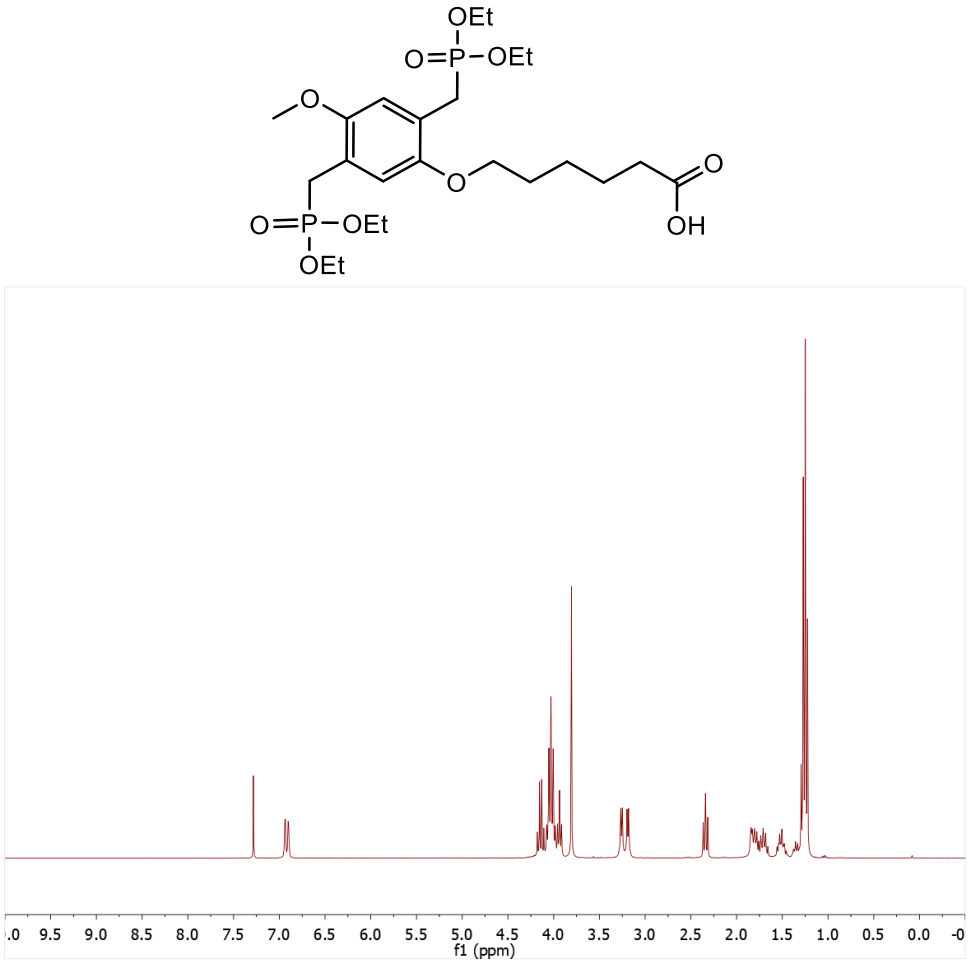


**Figure 2.3:** $^{1}$H NMR (300 MHz, $CDCl_3$) spectrum of ethyl 6-(2,5-bis((diethoxyphosphoryl)-methyl)-4-methoxyphenoxy)hexanoate

### 2.3.1.4 NMR analysis of Sodium 6-(4-methoxy-2,5-bis((E)-2-(pyridin-4-yl)vinyl)phenoxy) hexanoate (c-P4VB)

The yielded 155 mg (40%) of **c-P4VB** typically with ca. 98% purity according to $^{1}$H NMR (Fig. 2.4). The nuclear magnetic resonance spectroscopy (Fig. 2.4) was consistent with the molecular structure shown in Fig. 2.6(b).

$^{1}$H NMR (500 MHz, methanol-d4, 20 mg/ml), δ (ppm): 8.49-8.43 (m, 4H), 7.77-7.69 (m, 2H), 7.56-7.51 (m, 4H), 7.30-7.18 (m, 4H), 4.10 (q, $^{3}J$ = 6.5 Hz, 2H), 3.94 (s, 3H), 2.24 (t, $^{3}J$ = 7.4 Hz, 2H), 1.91 (p, $^{3}J$ = 6.7 Hz, 2H), 1.81-1.68 (m, 2H), 1.67-1.54 (m, 2H).

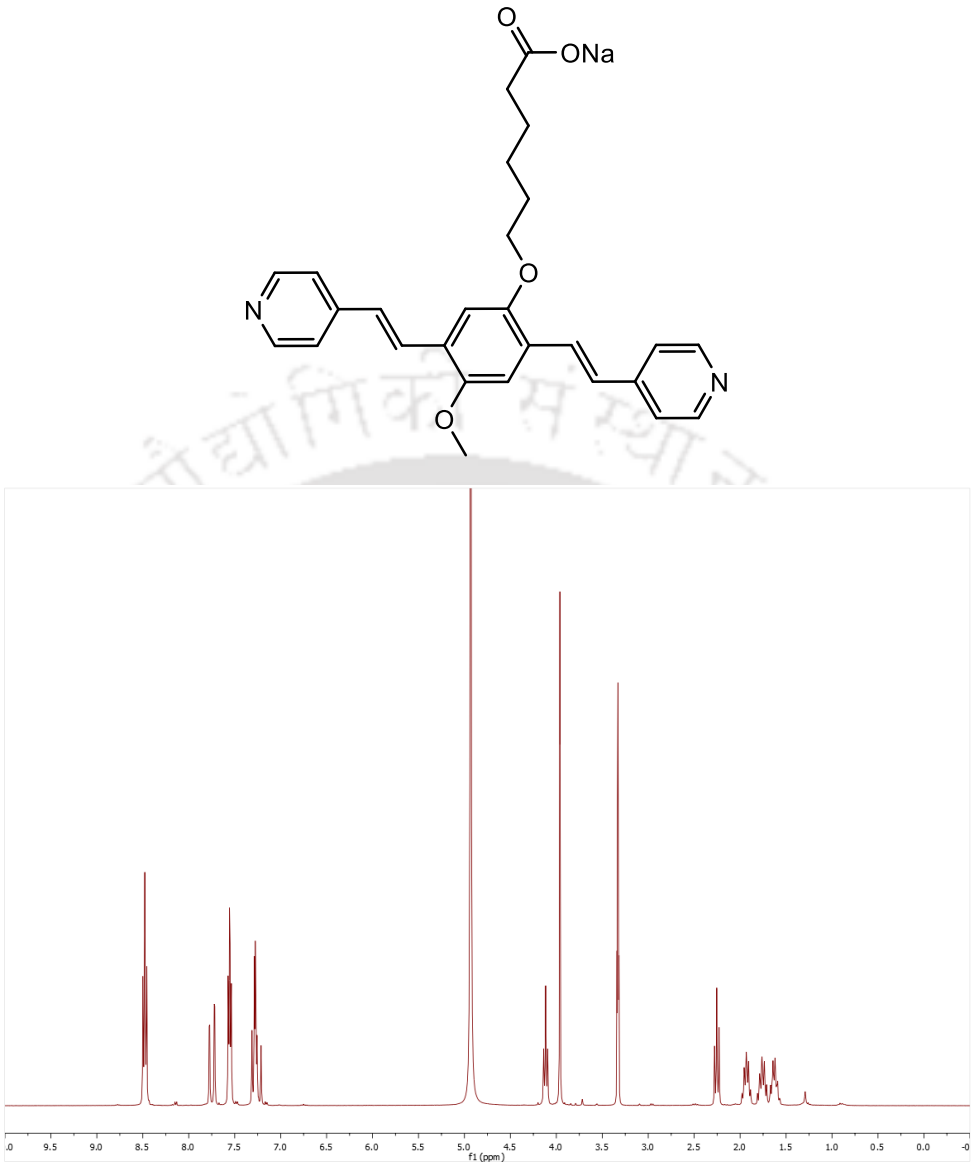


**Figure 2.4:** $^{1}$H NMR (300 MHz, methanol-d4) spectrum of sodium 6-(4-methoxy-2,5-bis((E)-2-(pyridin-4-yl)vinyl)phenoxy)hexanoate (**c-P4VB**)

Furthermore, the chemical shifts of the protons in the aromatic region are sensitive to the concentration and to the water content in deuterated methanol. Due to the unsymmetrical substitution pattern at the central benzene ring of **c-P4VB**, the signals of positionally-equivalent protons in two pyridine groups as well as in two vinylene groups are spectrally not equivalent, giving rise to a somewhat more complicated pattern as compared for example with **np-P4VB** (Lane et al., 2018). This becomes clear when spectra measured on spectrometers with different field strength are compared (Fig. 2.5).

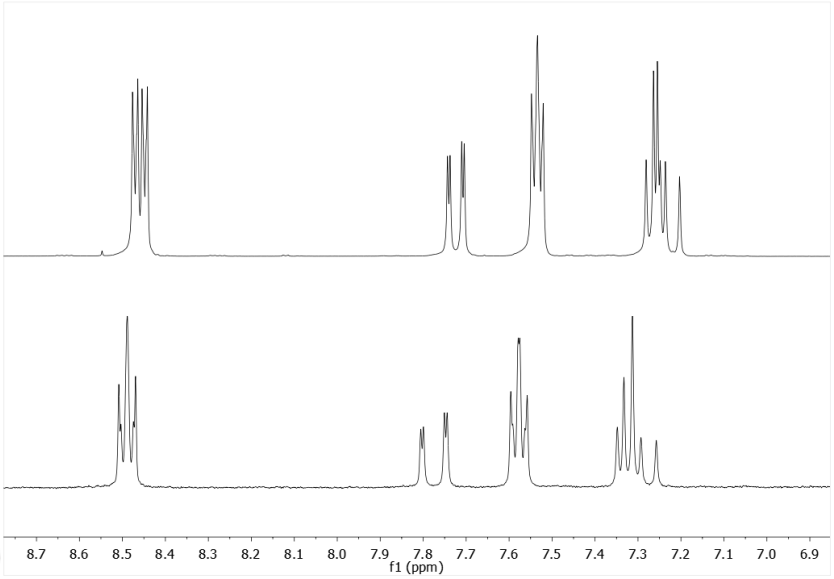


**Figure 2.5:** Signals of protons of **c-P4VB** in the aromatic region at 500 MHz (top, more concentrated) and 300 MHz (bottom, less concentrated), referenced to the signal of deuterated methanol.

### *2.3.2. Structure and basic optical properties of np-P4VB and c-P4VB*

The modified fluorophore **c-P4VB** was derived from the non-functional **np-P4VB** form; therefore it is necessary to understand the differences as well as similarities between the two fluorophores' optical properties. The basic structure of P4VB is illustrated in Fig. 2.6, showing the 3-ring conjugated backbone with the sterically accessible nitrogen atoms on the pyridine end-groups. When the pyridine groups are protonated, the fluorescence undergoes a large redshift from teal-blue to orange (Wang et al., 2020a). In contrast to the **np-P4VB** with its bulky neopentyloxy side-groups (Fig. 2.6 a), the carboxy-functionalized form (**c-P4VB**) has a methoxy side-group and an oxy-hexanoate group at the central benzene ring that presents an additional reactive site (Fig. 2.6 b). While the **np-P4VB** formed prismatic solid crystals with a greenish-yellow fluorescence, the **c-P4VB** showed a similar greenish-yellow emission but instead formed much smaller aggregates of fibrous or needle-like crystals in the solid form (Fig. 2.6 c,d).

A comparison of the protonation equilibria in **np-P4VB** and **c-P4VB** was performed first. The fluorophores were protonated with a strong acid (toluenesulfonic acid) in ethanol, producing the overall blue-to-orange color shift in the fluorescence and corresponding changes in the absorption maxima. The absorption spectra in ethanol for both P4VB molecular types show a double-peaked structure consistent with the $S_1$ and $S_2$ excited states (Table 2.1). The absorbance curves were modeled as a combination of double-Gaussians and the un-protonated and doubly protonated peaks

were found by fitting the un-protonated starting spectra and the fully saturated (*i.e.*, fully protonated) spectra, respectively. The means and standard deviations for these cases were then fixed for every subsequent measurement. The mono-protonated absorption peaks were found by modeling the spectrum that was shifted halfway between the un-protonated and doubly-protonated states by including one additional pair of Gaussian peaks to best fit the spectrum, which were then also fixed for every subsequent measurement. Only the relative intensities were allowed to vary. The peak positions for all three contributions and their ratios at different acid concentrations are summarized in Table 2.1 and Fig. 2.7, respectively. The results suggest that the first protonation constant is approximately an order of magnitude higher than the second protonation constant of the P4VB fluorophores. Thus, first one of the pyridines is protonated and then, at higher acid concentration, the second one becomes protonated. There is also a clear delay in the protonation of **c-P4VB** as compared to that in **np-P4VB** (Fig 2.7 c).

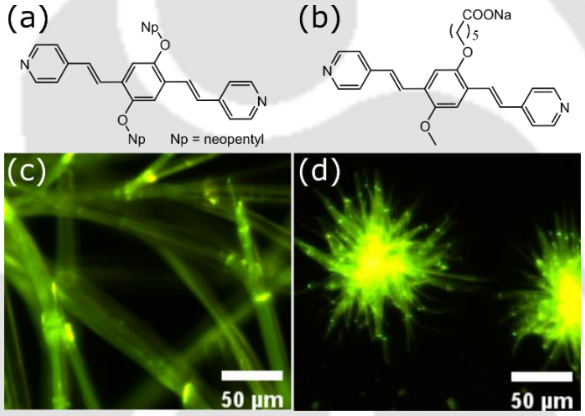


**Figure 2.6.** Molecular structure of (a) **np-P4VB** and (b) **c-P4VB**. Corresponding images under fluorescence microscope ($\lambda_{365nm}$ excitation) are shown in (c) and (d) of crystals formed after evaporation from ethanol at room temperature.

**Table 2.1:** Measured $S_1$ and $S_2$ absorption peak wavelengths for **np-P4VB** and the functionalized counterpart **c-P4VB**. Wavelength units are in nm. In brackets are given the positions of the absorption peaks, as computed from DFT.

| | **np-P4VB** | | **c-P4VB** | |
|---|---|---|---|---|
| state | $S_1$ | $S_2$ | $S_1$ | $S_2$ |
| unprotonated | 327.0 | 401.9 | 326.5 [306] | 400.7 [392] |
| singly protonated | 335.0 | 437.9 | 332.0 [332] | 431.9 [439] |
| doubly protonated | 362.7 | 461.4 | 359.2 | 459.1 |

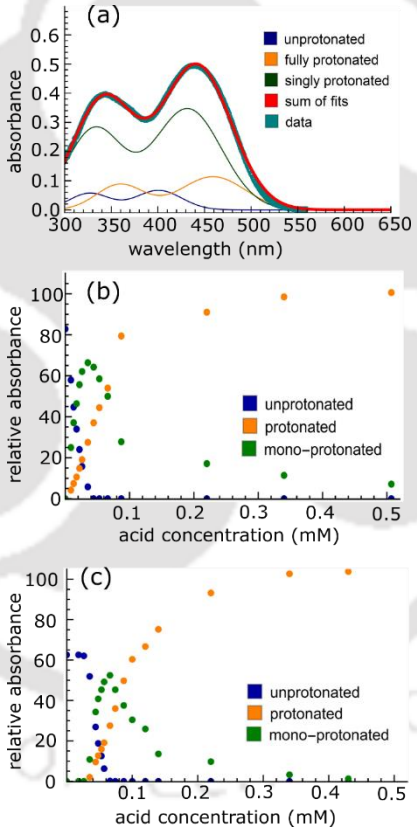


**Figure 2.7.** (a) Absorption spectra of 0.02 mM **c-P4VB** in ethanol, with the double Gaussian fit. This sample contains 0.057 mM toluenesulfonic acid. The relative strength of each of the absorptions (relative absorption) was found by taking the area under the peaks, and the results are shown as a function of acid concentration for **np-P4VB** in (b) and **c-P4VB** in (c). The onset of protonation is significantly delayed (i.e., it occurs at higher acid concentrations) for the **c-P4VB** due to the presence of the carboxylic group.

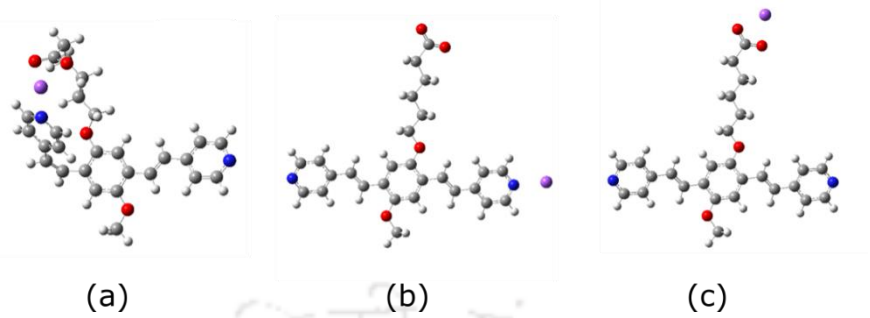


**Figure 2.8.** Simulated structures of **c-P4VB** with a sodium counter-ion. (a) "twisted" *cis* with the ion shared between the carboxyl tail and the pyridine site, (b) *trans* with the ion interacting with pyridine site only, (c) *trans* with the ion interacting with carboxyl tail. (c) is the most stable form; (a) and (b) are higher in free energy by 15 and 87 meV, respectively, in ethanol. These differences change significantly in other solvents or with different counter-ions (e.g., $H^+$) but the *trans* form shown in (c) is always the most stable. Blue represents nitrogen, red is oxygen, gray is carbon, white is hydrogen, and the sodium is violet.

A quantum chemical analysis was performed on the **c-P4VB** to understand its electronic structure and solvent interactions relevant to its sensing performance. The calculations were based on density functional theory (DFT), performed using the Gaussian software package with the CAM-B3LYP exchange-correlation functional and a 6-31++G(d,p) Gaussian basis set, accounting for solvent effects with the implicit polarizable continuum solvation model. These DFT calculations were performed at University of Mons, Belgium. The absorption spectra were simulated in ethanol using time-dependent DFT for the optimized ground and first excited state structures. Similar to the **np-P4VB**, the vinylene groups in the conjugated backbone of **c-P4VB** can form *cis* and *trans* isomers (Fig 2.8 a, b) (Wang et al., 2020a), but a third stable structure was identified where the counter-ion interacts with the carboxylate group (Fig 2.8 c). The *cis* isomer allows a sharing of the counter-ion between the carboxyl tail and the pyridine site, which may stabilize it and affect the prevalence of the *trans* isomer (Fig 2.8 a). For **c-P4VB** with a sodium counter-ion, the *trans* form is more stable by about 15 meV in ethanol, in agreement with the NMR results (see Fig 2.5) which indicated only a *trans* component at room temperature. Additionally, there was little experimental evidence for the *cis*-related absorption peaks at $\lambda_{292nm}$ and $\lambda_{363nm}$ as calculated by DFT. The un-protonated absorption maxima in implicit ethanol were calculated to occur at $\lambda_{306nm}$ and $\lambda_{392nm}$ for the most stable situation in which the $Na^+$ counter-ion is bound to the carboxylate group, which are reasonably close to the values of $\lambda_{326nm}$ and $\lambda_{400nm}$ observed experimentally (Fig. 2.9, **c-P4VB** in ethanol).

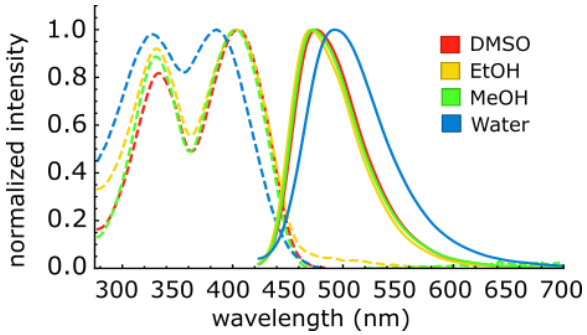


**Figure 2.9.** (a) Normalized absorption (dashed lines) and fluorescence intensity (solid lines) spectra for 0.02 mM **c-P4VB** in DMSO, ethanol (EtOH), methanol (MeOH) and water.

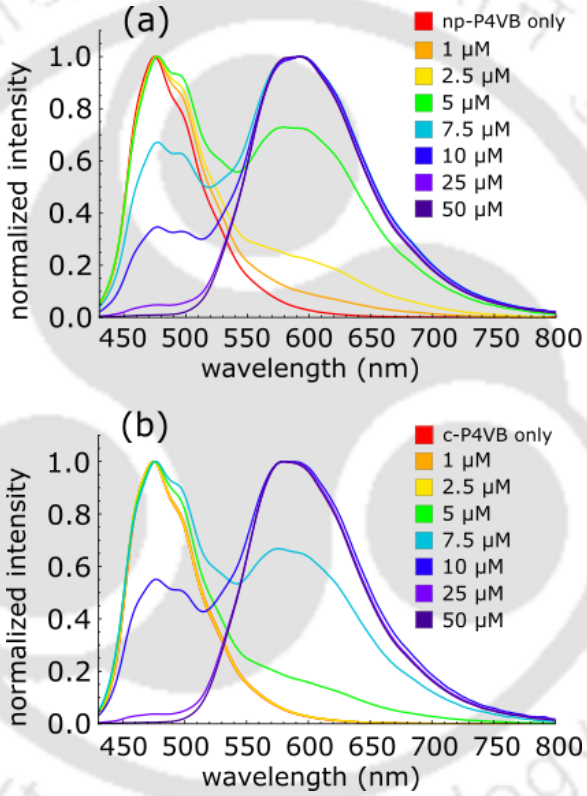


**Figure 2.10.** Fluorescence spectra for (a) **np-P4VB** and (b) **c-P4VB** at different concentration of HCl (all intensities are normalized; 0.2 mM fluorophore in ethanol)

Relevant to the sensing behavior of the **c-P4VB**, the molecular properties for the three configurations were investigated with a proton replacing the sodium counter-ion. In this case, as well, a single proton prefers to neutralize the $COO^-$ site directly (Fig 2.8 c), with the second most favorable option represented by a twisting of the alkyl chain toward a *cis*-oriented pyridine, such that the two sites (pyridine and the hexanoate arm) effectively share the proton (Fig 2.8 a). Thus, the DFT results conclude that a single counter-ion ($Na^+$ or $H^+$) interacting with **c-P4VB** prefers first to neutralize the

$COO^-$ site, and when that site is saturated, then excess counter-ions can bind to the pyridine. Thus, the protonation of the pyridines will be "delayed" in **c-P4VB** until the carboxylic group has been neutralized which is observed in the absorbance (Fig 2.7 c) as well as fluorescence spectra (Fig 2.10 b), in which the singly protonated state of **c-P4VB** reaches maximum intensity at higher acid concentration than it does for **np-P4VB** (Fig 2.10 a).

### *2.3.3. Optical properties of c-P4VB in aqueous solutions of $H_2O_2$*

The as-synthesized **c-P4VB** is soluble in water up to 2 mg $mL^{-1}$, which is advantageous for developing sensors for aqueous analytes. Next, the absorption and fluorescence response of **c-P4VB** solutions to aqueous $H_2O_2$ was examined. Various concentrations of $H_2O_2$ prepared in fresh MilliQ was added to 0.02 mM **c-P4VB** dissolved in ethanol for absorbance and fluorescence study, to form a (1:1) solution by volume. The addition of small concentration of $H_2O_2$ (0.2 v/v%) caused the $\lambda_{500nm}$ protonation-related absorption peak to appear, while the fluorescence red-shifted (Fig 2.11), consistent with the protonation of the pyridine groups also appeared. $H_2O_2$ is widely known to behave as a weak acid yet yields suitable protonation of **c-P4VB** at reasonably low concentrations, presenting an opportunity to seize on the acidic nature of $H_2O_2$ as an alternative to the usual oxidation methods.

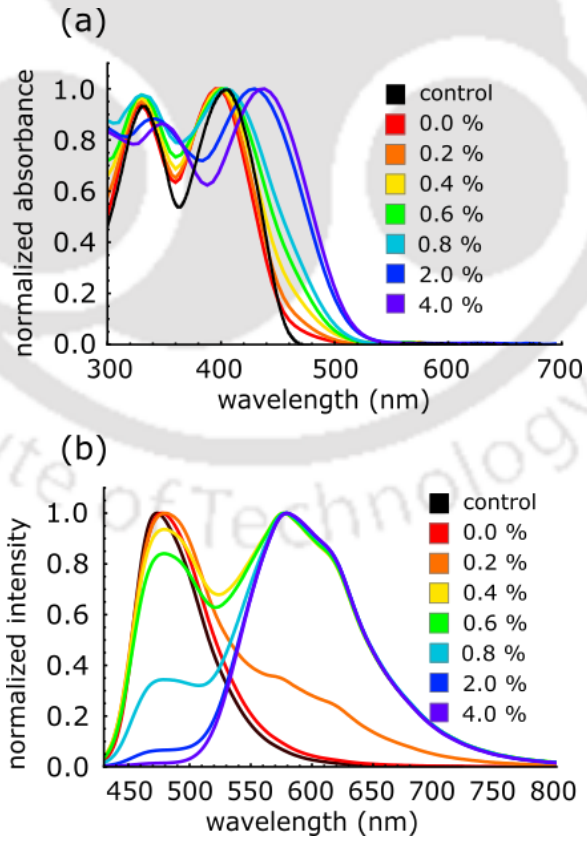

**Figure 2.11**. (a) Absorbance spectra for different concentrations (v/v%) of $H_2O_2$ in aqueous solutions of 0.02 mM **c-P4VB** (b) Fluorescence spectra of aqueous $H_2O_2$ solutions in 0.02 mM **c-P4VB** in ethanol. In all cases the reaction solution had a 1:1 volume ratio of ethanol and water. The control refers to pure ethanol solution with **c-P4VB** and 0% means that only pure water was used. The aqueous $H_2O_2$ solutions were prepared by dilution of commercial 30% aqueous $H_2O_2$ with MQ water. All spectra are normalized for visual clarity.

### *2.3.4. Properties of c-P4VB-infused paper*

To create a disposable microsensor, **c-P4VB** was immobilized into Whatman no. 1 filter paper (Scheme 2.1). The dye could not be removed even after 30 minutes of sonication. In contrast to **c-P4VB**, **np-P4VB** was effectively removed by a single methanol wash (Fig 2.12 a), indicating its much poorer affinity towards cellulose. Indeed, cellulose is known to show excellent adsorption or hydrogen bonding to materials that contain carboxylic groups (Khazraji and Robert, 2013), ensuring minimal leaching of adsorbed **c-P4VB** upon exposure to aqueous solutions. The as prepared **c-P4VB** papers sensors can be used immediately after preparation but must be stored in dark and low humidity conditions; we found that Petri plates, enclosed with parafilm and foil were sufficient. The fluorescence of **c-P4VB** paper was monitored for 20 days and found to show red peak rise ($\lambda_{550nm}$-$\lambda_{650nm}$), which could be due to humidity (Fig 2.12 b). However, this change was completely reversible after treatment with methanol (Fig 2.12 b), which is like the washing process.

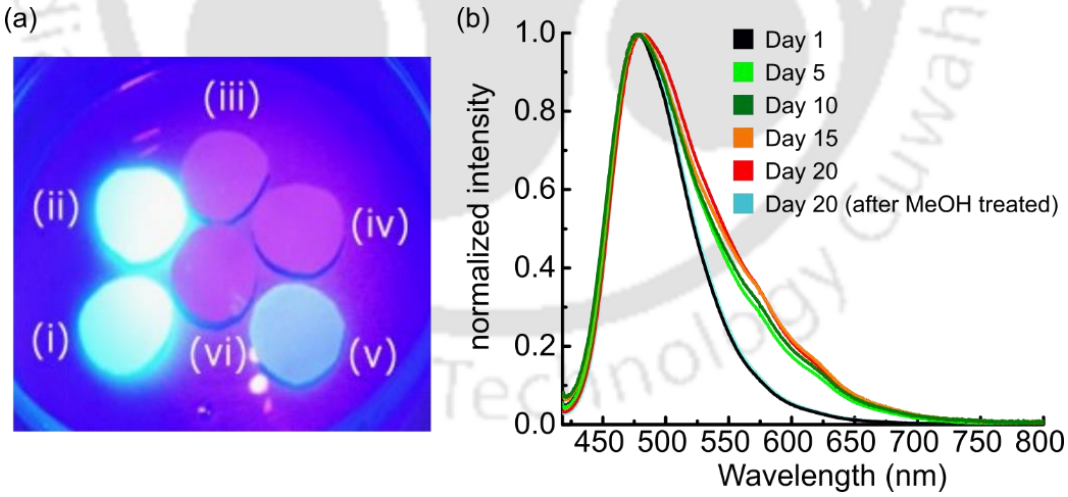


**Figure 2.12:** (a) Photos of paper discs under UV lamp : (i) infused with **c-P4VB** solution, not washed; (ii) infused with **c-P4VB** solution, washed with water; (iii) infused with **np-P4VB** (ethanol solution of high dye concentration) and washed with methanol; (iv) infused with np-P4VB (ethanol solution of low dye concentration) and washed with methanol; (v) infused with **c-P4VB** solution and washed according to our protocol with water and then methanol followed by sonication; (vi) in the middle – a blank paper

sample. (b) Normalized fluorescence intensity of **c-P4VB** paper at different storage times and its reversibility characteristics with MeOH treatment.

The **c-P4VB**-infused paper disks emitted teal blue fluorescence under UV light and responded to different analytes by turning green when treated with zinc nitrate, pinkish with acetic acid, yellow-orange with HCl, and reddish when treated with $H_2O_2$ (Fig 2.13). This indicates at least some level of distinction in the fluorescence response of $H_2O_2$ as compared to other possible interferents. The reddish fluorescence for $H_2O_2$ could be due to the aggregation of the protonated dye molecules originating from the formation of contact ion pairs between the weak acids and the fluorophore (*e.g.* through hydrogen bonding), which does not occur in case of strong acids. This aggregation can slowly lead to precipitation of **c-P4VB** from aqueous solutions. Aggregation seems to be an important factor explaining the sensitivity of **c-P4VB** to hydrogen peroxide since intermolecular interactions are known to cause an extended red emission in aggregates of conjugated polymers or dyes. Even through the fluorescence spectra, there is a redder shift in case of **c-P4VB** paper treated wit $H_2O_2$ as compared to other acids (Fig 2.13).

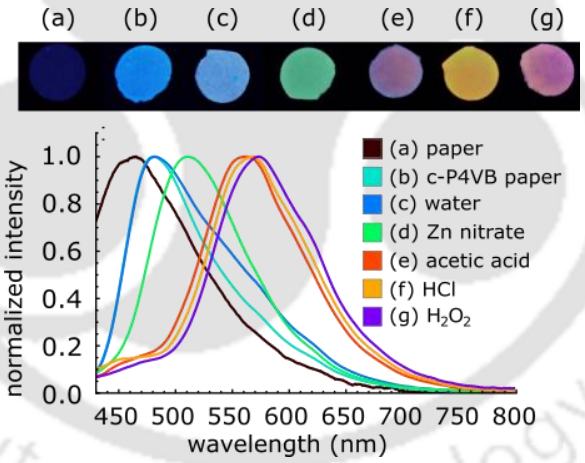


**Figure 2.13.** Photographs taken under a UV lamp (top) and the corresponding fluorescence spectra of **c-P4VB** treated with different analytes (bottom). The photographs were taken with a smartphone camera with no filtering applied. (a) blank filter paper; (b) **c-P4VB** paper only and treated with: (c) water; (d) Zinc nitrate (0.5 M); (e) acetic acid (1 M), (f) HCl (5 mM) and (g) $H_2O_2$ (10 v/v%).

### *2.3.5. Hydrogen peroxide paper sensor performance*

To verify the response of the paper sensor, different **c-P4VB** paper disks were dropped into 2 mL of different concentrations of aqueous $H_2O_2$ solutions, and the fluorescence change was observed on each separate disk. The change in the fluorescence can be clearly seen on the paper sensors under the UV lamp (Fig 2.14 a). A ratiometric signal given by $S = I_{605}/I_{470}$, where $I_{605}$ and $I_{470}$ are the measured fluorescence intensities at $\lambda_{605nm}$ and $\lambda_{470nm}$, respectively, was used to extract the sensitivity of the sensor. The detection shows an initially low sensitivity (as indicated by the slope) but which rapidly increases with the concentration of $H_2O_2$ (Fig 2.14 b). This response delay may be associated with competition in the carboxyl side group, as discussed previously. At higher $H_2O_2$ concentrations (above ~0.4 v/v%) the fluorescence ratiometric signal yielded a higher sensitivity as the pyridine groups become increasingly protonated increasing the red peak to emerge (Fig 2.14 c).

A ratiometric equation in which the two wavelengths shift at low concentration (Fig 2.14 c inset) was chosen to model the data, given by

$$y = \frac{a}{b-x} + d \qquad (2.2)$$

where $a$, $b$, and $d$ are fitting parameters and $x$ is the concentration. The lower $H_2O_2$ concentration data and the resulting fits according to the equation are shown in Fig 2.14c inset. The limit of detection LoD for $H_2O_2$ in the paper sensor was estimated as three times the standard deviation from 3 measurements of the blank divided by the slope of the working fitted curve at low concentration. The LoD for $H_2O_2$ in these paper-sensors was 0.057 v/v% or 16.7 mM with a dynamic range up to 10 v/v% or 2.9 M $H_2O_2$. At higher concentrations where the slope of the signal increases, the ability to detect changes in the $H_2O_2$ concentration was roughly an order of magnitude better due to the increased sensitivity in this range.

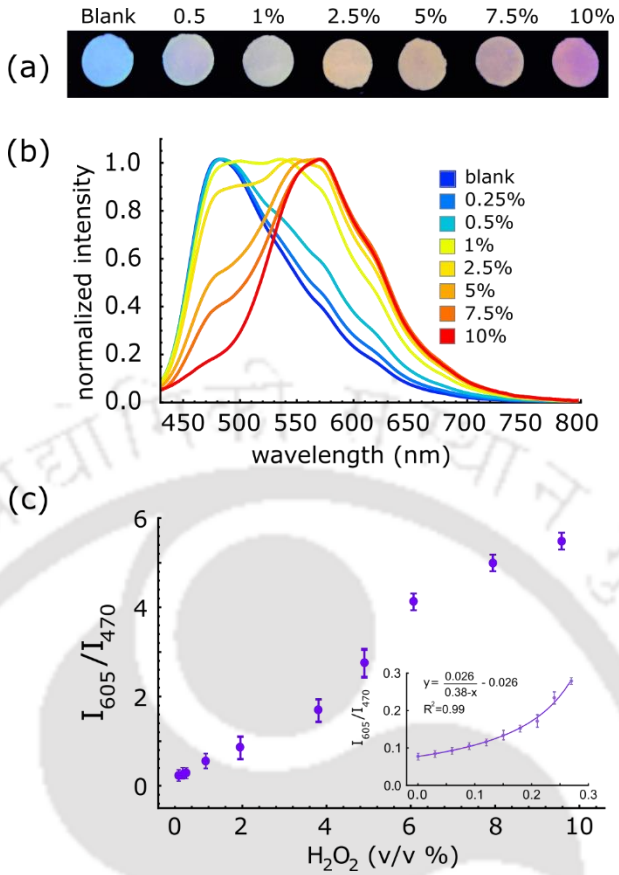


**Figure 2.14.** (a) Photographs of **c-P4VB** paper treated with different concentrations of $H_2O_2$, taken under a UV lamp using a smartphone camera without any filtering. (b) Normalized fluorescence spectra corresponding to **c-P4VB** treated with various concentrations (v/v%) of $H_2O_2$. (c) Calibration curve of the paper sensor for different $H_2O_2$ concentrations in aqueous solution. The inset magnifies the low-concentration region from which LoD was calculated. The error bars represent the calculated standard error from measurements on three separate disks.

### *2.3.6. µPAD sensor for ethanol*

After characterizing the behavior of **c-P4VB** upon exposure to aqueous $H_2O_2$ and demonstrating that the paper sensors can detect relevant concentrations of $H_2O_2$, we proceeded to develop a microfluidic paper-based ethanol biosensor. A µPAD system was prepared by linking two paper disks, a reaction (**R**) disk with AOx immobilized into it through adsorption, and a sensor (**S**) disk infused with **c-P4VB** by a paper channel as described in the experimental section (Fig 2.15 a). 10 µL of aqueous samples with various concentrations of ethanol were dropped onto the **R** zone and allowed to incubate for 5 minutes; then 20 µL of MilliQ was then dropped onto the same disk to move the reaction produced $H_2O_2$ to the **S** zone. After 5 minutes incubation, the **S** zone was photographed under a UV lamp ($\lambda_{365nm}$), using a smartphone (Fig 2.15 b). In order to generate the best signal, area in the sensor

zone near the input channel was selected for sensing. For the calibration parameter, red (R), green (G) and blue (B) intensity of the selected area was obtained using ImageJ software. The RGB intensities were converted to hue values for numerical analysis using the Preucil equation (Preucil, 1953; Khoo and Ong, 2014) (equation 2.3).

$$h_{rgb} = \text{atan}\frac{\sqrt{3}*(G-B)}{2*(R-G-B)} \quad (2.3)$$

The hue value($h_{rgb}$) which is the degree (°) of the color in the hue space, represents the main property of a colour, which is here directly related to the dominant wavelength of **c-P4VB** paper fluorescence emission. Converting the measured RGB signals into hue values appeared to be more precise and less prone to error while intrinsically correcting unexpected light intensity variations like fluctuation of the LED, unequal coating of a strip, or daylight pollution (Gotor et al., 2019). This method does not require a spectrometer, which would add considerable cost; a hand-held UV lamp and a smartphone are the only physical accessories.

The first step was to calibrate the response to prepared ethanol solutions. The signal changed monotonically with the concentration of ethanol up to 2 v/v%, consistent with the AOx-catalyzed conversion of ethanol to $H_2O_2$. The data fit closely to a linear plot (Fig 2.15 c inset) with $R^2$=0.99. Blanks using this sensing device without enzyme loading did not show any response to ethanol. As before, the LoD (for ethanol) was estimated as three times the standard deviation from separate paper sensors divided by the slope of the working curve at low concentration. The data thus yielded an LoD of 0.05 v/v% or 8.5 mM from the standard deviation of three different paper sensors. When using ethanol concentrations above 2% the response of the sensor became erratic, likely because the abundant $H_2O_2$ produced in the reaction zone denatured the enzyme, which can lead to a decreased enzyme activity (Cicek et al., 2014). AOx was found to be functional for two weeks under 4 ℃, after which sensor performance began to degrade.

### *2.3.7. Real sample analysis*

We finally demonstrate a “real world” sensing application in two alcoholic beverages using our simple paper-based alcohol biosensor. Two vodka brands commercially available in India, Smirnoff (SM) and Magic Moments (MM) were chosen for this study. Both liquors have a stated 42.8% ethanol content written on the bottle. The samples were diluted by a factor of 100 and were analyzed by placing 10 µL onto the reaction zone and following the same procedure described in ethanol sensing. In addition, we performed a separate check of the ethanol concentration in these beverages using the enzyme assay method (Mangos and Haas, 1996) (Table 2.2). We also measured the pH of

MM and SM using a Mettler Toledo benchtop pH meter and obtained values of 7.18 and 7.26, respectively, indicating that acid-related interferences are absent from the measurements. While there is some minor scatter in the data, we find that the simple paper-based ethanol sensor developed here performed well given its simplicity, yielding ethanol contents of 43.27% and 42.49% for SM and MM respectively.

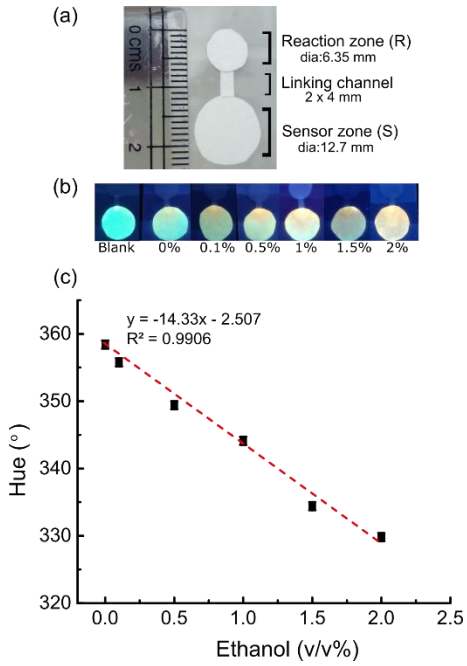


**Figure 2.15**. (a) Image of the paper-based alcohol sensor with the dimensions of each zone; (b) Photographs taken using a smart phone after the reaction with different concentrations of ethanol (v/v %); (c) Calibration plot for the hue measured of S zone with different concentration of ethanol-treated on the R zone as described in the text. The errors represent the standard deviations from three separate disks.

**Table 2.2:** Measurement of ethanol concentration in two commercial liquors. The errors represent one standard deviation from three repeats of each measurement.

| Sample | Measured (v/v %) | Reported (v/v%) | Enzymatic analysis (v/v%) |
|---|---|---|---|
| SM | 43.27 ± 0.9 | 42.8 | 41.9 ±0.5 |
| MM | 42.49 ± 0.4 | 42.8 | 41.7 ±0.3 |

This may be the first inexpensive fluorescence µPAD sensor that works in real-world alcohol sensing applications. Interestingly, it is founded on the acidic rather than on the oxidizing nature of the

hydrogen peroxide reaction product. However, there is a major limitation that needs to be acknowledged. The signal of the sensor is prone to interference from acids that may be present in some consumer liquors or other samples of interest. For acidic samples, the same paper-based ethanol sensor technique would require extra steps; for example, calibrating the sensor at a similar pH to that of the analyte or first neutralizing the acidic species in the liquor. Another potential option would be to remove any excess $H^+$ in the sample using an anion exchange resin, which has been reported to remove organic acids in biological and alcohol solutions (Cren et al., 2009; Cui et al., 2016). Nevertheless, this work is a step toward the development of low-cost $H_2O_2$ and alcohol sensors.

### 2.4. Conclusion

In this chapter, we reported the synthesis of a functionalized fluorescence-change fluorophore, **c-P4VB**, designed to be soluble in aqueous solutions as well as sticky to cellulose. Protonation of the pyridine groups causes the fluorescence to shift from blue to orange or red, enabling stable ratio-based analysis approaches. Firstly, the basic photophysics of the new fluorophore was investigated by fluorescence and absorption spectroscopy and by DFT simulations, which indicated that **c-P4VB** should, in practice, be a good fluorescence-based sensor for $H_2O_2$, while also showing excellent aqueous solubility and good binding to paper. Next, we infused **c-P4VB** into a cellulose paper disc to prepare a simple paper-based fluorescence probe for direct detection of $H_2O_2$. The sensor responded well to $H_2O_2$: by simply dipping the **c-P4VB** infused paper into $H_2O_2$ solution, and a fluorescence color change is quickly observed. This is useful because it enables many potential types of reactions that produce $H_2O_2$ to be used for analyzing the quantity of the reactant analyte in a paper-based sensing strategy. To demonstrate this concept, we built an ethanol biosensor by connecting a reaction paper infused with AOx through a thin paper channel to a fluorescent sensor zone (**c-P4VB** infused paper). AOx serves to convert ethanol to acetaldehyde and $H_2O_2$ in the reaction zone, which was then detected via fluorescence changes in the sensor zone that can be easily captured with a standard smartphone camera. Trial devices showed that good results can readily be obtained for commercial liquors, presenting a simple paper-based check against the stated ethanol content. To the best of our knowledge, this is the first report of a paper-based fluorescent ethanol detection technique. The major draw-back of this $H_2O_2$ sensor is, however, the low selectivity. Since the detection mechanism is based on protonation of the pyridine groups in the fluorophore, an acid or acidic environment could give unwanted signals. The selectivity for any analyte is seen in enzyme catalyses, here, particularly peroxidase for $H_2O_2$ sensing. Thus, in the next chapter, we will explore the enzyme peroxidase for $H_2O_2$ sensing as well as its application in preparing a functional alcohol biosensor.

# CHAPTER III

## PEROXIDASE-BASED SENSING OF HYDROGEN PEROXIDE AND ITS APPLICATION IN THE DEVELOPING A REAGENT-FREE ALCOHOL BIOSENSOR

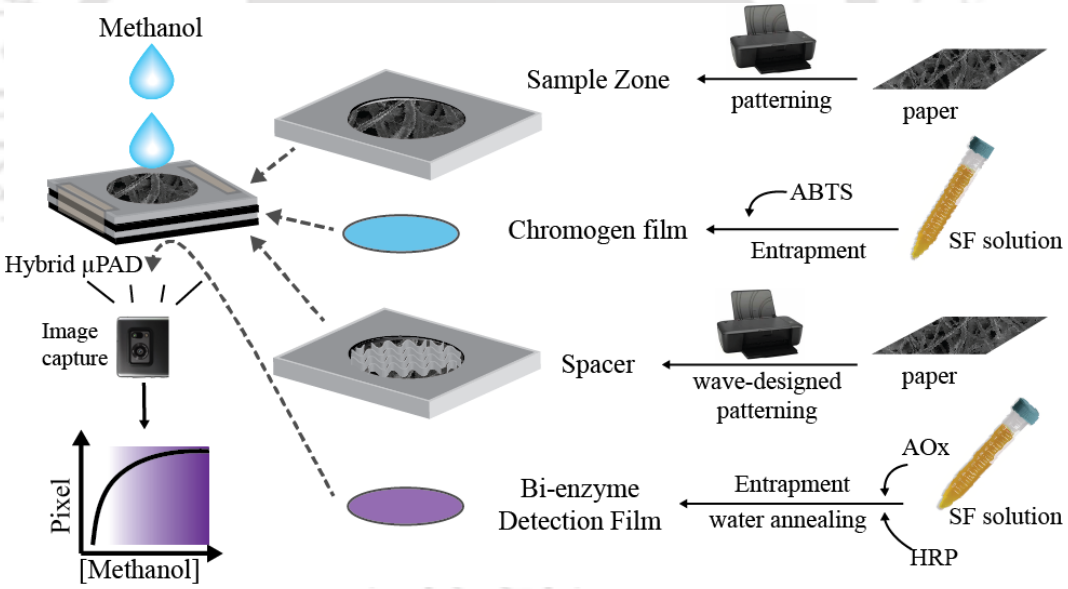

# Chapter III

# Peroxidase-based sensing of hydrogen peroxide and its application in developing a reagent-free alcohol biosensor

## 3.1. Introduction

Enzymes are considered excellent biorecognition elements for developing biosensors due to their extreme substrate selectivity, non-toxic nature, and high catalytic activity at room temperature and physiological pH (Nelson and Cox, 2009). However, the major drawback that impedes their applications for developing biosensors of commercial interest is the low stability of the proteinaceous enzymes (Mateo et al., 2007; Zdarta et al., 2018). The functional activity of enzymes is known to maintain by their native protein structure, which is highly sensitive to temperature, pH, and solvents (Lu et al., 2009a). To alleviate the drawback, enzymes are usually immobilized on a suitable support material that helps maintain their stability and reduces the overall cost and complexity of the developed enzyme-based devices (Datta et al., 2013).

As mentioned earlier, horse radish peroxidase (HRP) is widely used for developing $H_2O_2$ biosensor. However, low stability of this peroxidase is a major hurdle for its real-world biosensor applications. Nevertheless, the emergence of silk fibroin (SF) films as bulk-entrapment matrix for the enzyme has brought hope in this direction (Kaushik et al., 2020). HRP in SF films was reported to have a residual activity of 24%, 22%, and 17% of the initial activity after 5 months of storing at 4 °C, 25 °C, and 37 °C, respectively (Lu et al., 2009a). There has also been an earlier report of HRP being co-immobilized with other enzymes such as lysozyme (Hofmann et al., 2006) and catalase in SF membranes for drug release and sensing applications (Zhou et al., 2017). However, the stability of the highly labile multimeric enzymes such as alcohol oxidase (AOx) has not yet been studied in SF films.

AOx (Alcohol: $O_2$ Oxidoreductase; EC 1.1.3.13; Mw ~600 kDa.) is an octameric enzyme receiving significant research interest over the last few years due to its bright prospect as a catalyst for alcohol oxidation for various technological ventures, particularly in the emerging fields of biosensors, biofuel, and biofuel cell (Goswami et al., 2013; Thungon et al., 2017). Alcohol sensors have great importance in various industrial and legislative sectors such as fermentation, cosmetics, drugs and pharmaceuticals, forensic analysis, traffic regulations, and agricultural and environmental analysis (Azevedo et al., 2005). Furthermore, alcohol as an alternative fuel source may also boost the demand

for portable and sensitive alcohol sensors in the near future. The alcohol sensors currently available in the market are based on chemical, electrochemical, and infrared (IR) principles that are mostly less selective, expensive, and technically complex devices (Thungon et al., 2017). However, the low stability and labile nature of AOx pose a great challenge of using this enzyme for developing commercial alcohol biosensors.

In this chapter, we first explored HRP as a biorecognition element for developing optical $H_2O_2$ biosensor. Following this, the concept was translated to develop a methanol biosensor by combining this peroxidase with AOx enzyme on the sensor surface. An effort was made to transform the sensing strategy into colorimetric lab-on-chip type biosensors with stand-alone operational mode. The main challenges encountered in achieving this goal are: 1) immobilization of enzymes, 2) immobilization of the reagent (ABTS), and finally, 3) assembling all the immobilized materials into a single system to make an independent device. To address the first two challenges, both bi-enzyme systems (AOx and HRP) and ABTS were entrapped in SF films separately. To address the final challenge, we explored paper microfluidics to prepare a hybrid µPAD for fabricating the methanol biosensor.

## 3.2. Experimental section

### *3.2.1. Chemicals and reagents*

Silkworm cocoons of *Bomyx mori* were obtained from a local sericulture farm, Guwahati, Assam, India. Peroxidase from horseradish (HRP) [250 U $mL^{-1}$], alcohol oxidase (AOx) (EC 1.1.3.13 from Pichia pastoris) [1000 U $mL^{-1}$], 2, 2'-azino-bis [3-ethylbenzothiazoline-6-sulfonic acid] (ABTS), and Whatman Grade 1 Filter paper were purchased from Sigma Aldrich (USA). Hydrogen peroxide (~50 w/v%), methanol (99.9%) and Fast Green FCF was purchased from Himedia Laboratories Pvt. Ltd. (Mumbai, India). Alkyl ketene dimer 1840 (AKD) was purchased from Flourish Paper and Chemicals Limited (Mumbai, India). The enzyme solutions were prepared in 100 mM of phosphate buffer pH 7.5. All $H_2O_2$ and methanol working standard solutions were prepared daily in MQ (18.2 MΩ.cm). All other chemicals were of analytical grade and used without further purification.

### *3.2.2. Extraction of silk fibroin*

Silk fibroin (SF) was extracted from cocoons of *Bombyx mori* following a reported method (Rockwood et al., 2011). Briefly, the cocoons were cut and boiled for 30 min, in 0.02 M of sodium carbonate solution. The degummed fibres were washed with ultrapure water to remove sericin and then dried in laminar hood overnight. The dried SF fibers were dissolved in 9.3 M of LiBr solution for 4 hours at 60 °C. The solution was then dialyzed against deionized water for 3 days to remove

the LiBr using a dialysis tube (MWCO 1000 Da, GE). The dialyzed solution was centrifuged (9000 rpm, 20 min, 4 °C) to remove insoluble particulates. The final concentration of silk fibroin aqueous solution obtained was ~10% (w/v). This concentration was determined by weighing the residual solid of a known volume of solution after drying at 60 °C. The SF solution was stored at 4 °C and could be used for one month before it turned into gel.

### *3.2.3. Preparation of different SF films*

Four different types of SF films were prepared; three were enzyme entrapped SF films, while the fourth one was used to entrap ABTS.

(1) HRP entrapped SF films (HRP-SF films) where the film was prepared by mixing 5 µL of HRP (0.5 mg $mL^{-1}$) with 35 µL of SF (7% w/v) solution.
(2) AOx entrapped SF films (AOx-SF films) where 10 µL of AOx (1 mg $mL^{-1}$) was mixed in 35 µL of SF (7 % w/v) solution.
(3) AOx-HRP (bi-enzyme) SF films, where 10 µL of AOx (1 mg $mL^{-1}$) and 5 µL of HRP (0.5 mg $mL^{-1}$) were mixed with 35 µL SF (7% w/v) solution.
To prepare a single film, a total volume of 50 µL of enzyme-SF solution (volume adjusted with 100 mM phosphate buffer pH 7.5 where required) was pipetted onto a petri plate and allowed to dry overnight in the laminar hood to form SF films of dissolvable nature.

Next, all three dissolvable enzymes immobilized SF films were made non-dissolvable, by water annealed as described in (Rockwood et al., 2011). Briefly, the bottom of a vacuum desiccator was filled with water and the dried dissolvable films were placed in it. A vacuum was applied through the vacuum port and the films were left in this condition for 24 hours. After which the films were taken out and dried for 2 hours in the laminar hood to remove the water droplets and then stored under 4 °C till further use.

(4) Dissolvable ABTS SF film (chromogen film) was the fourth type of film, prepared using 15 µL of ABTS (10 mM) mixed with 35 µL of SF (7% w/v) solution. Then 50 µL of ABTS SF solution was drop cast on a petri plate and kept overnight in a laminar hood for drying. These films were then stored at 4 °C and before further use.

### *3.2.4. Film characterization*

Field Emission Scanning Electron Microscope (FESEM) (Sigma 300, ZEISS) was used to investigate the morphology and thickness of the different SF films at an operating voltage of 3 kV. Each film

was cut and placed vertically on the carbon tape to get the cross-sectional views of the film. All the film samples were gold coated for 120 s at 5 mA before analysis in FESEM.

The transparency of the SF films was analyzed by UV–vis spectrophotometer (Cary 300 Bio, Varian) using 1 cm path length quartz cuvette at 25 °C. The prepared films were evenly placed inside the cuvette with an adhesive tape and the transmittance was recorded over $\lambda_{300nm}$ to $\lambda_{800nm}$. The transmittance with just the adhesive tape was considered as the blank and all the readings were calculated by considering the blank value as 100% transmittance. The transmittance denoted how much light passes through a substance, 100% being completely transparent and 0% for opaque substance (Zheng et al., 2015).

### *3.2.5. Activity study of the enzyme(s) immobilized in SF films*

The activity of the dissolvable HRP-SF films was analyzed using ABTS based reaction. The ABTS solution was prepared by using 2 mM of ABTS in 100 mM phosphate buffer (pH 7.5). The substrate solution was prepared by mixing 740 µL ABTS solution with 50 µL of $H_2O_2$ of varying concentrations. The activity of the dissolvable AOx-SF films was analyzed by the peroxidase-coupled assay. Here, the substrate solution was prepared by mixing 740 µL ABTS solution with 50 µL of methanol of varying concentrations and 10 µL of HRP (0.5 mg $mL^{-1}$). The activity of both types of dissolvable films was analyzed by dropping the film in the substrate solution and then measuring the absorbance at $\lambda_{405nm}$ using UV-vis spectrometer. For dissolvable bi-enzyme (AOx-HRP) SF films, similar method was followed, except the substrate solution did not separately contain HRP solution.

For activity study of the non-dissolvable HRP-SF films, the substrate $H_2O_2$ was used without adding HRP separately in the reaction mixture. In case of non-dissolvable AOx-SF films and bi-enzyme SF films, the activities were studied by adding the substrate methanol in the reaction medium with and without HRP, respectively. The films were incubated in substrate solution containing different concentrations of methanol. Following the reaction, the films were removed from the solution using forceps and the color developed on these films was captured by using a smartphone. The activity was analyzed based on the change in the color intensity of the films by measuring total grey pixel intensity using ImageJ software. The intensity of the blank film, $I_o$, was subtracted from the intensity of the reacted film, $I_i$, to get the $\Delta$ mean pixel intensity for that film. This method was followed for activity analysis of the final µPAD biosensor.

### *3.2.6. Optimization of enzyme(s) in silk fibroin films*

A range of concentration of SF solution (1-8 % w/v) prepared in MQ was mixed with 0.1 mg $mL^{-1}$ of AOx to prepare dissolvable AOx-SF films. The activity of AOx in each SF films was examined. Next, the optimized SF solution was mixed with a range of concentrations of AOx (0.01-1.5 mg $mL^{-1}$) prepared in 100 mM phosphate buffer (pH 7.5), and their activity was analyzed. Finally, a range of concentrations of HRP (0.01-1 mg $mL^{-1}$) was mixed with the optimized AOx and SF concentration to prepare the bi-enzyme SF film. The activities of the as prepared films were then analyzed.

### *3.2.7. Stability study of the enzyme(s) in SF films*

The HRP SF, AOx-SF and bi-enzyme SF films were kept at different temperatures and their activities were analyzed over several days. The activities of the dissolvable films were calculated spectroscopically using UV-vis spectrometer in the substrate solutions, whereas for the non-dissolvable films, it was calculated by measuring the mean gray pixel intensity of the color developed on the film using ImageJ software as described in section 3.2.7.

### *3.2.8. Fabrication of microfluidic pattern on paper surface*

Microfluidic designs were created by using Adobe illustrator (version 2020) based on which, AKD wax printing on chromatographic paper No.1 was performed to create hydrophilic and hydrophobic zone (Chakma et al., 2016). Briefly, the cartridge of the HP deskjet-100 printer was modified by replacing the hydrophobic foam with hydrophilic chromatography paper. The ink cartridge was filled with 1% (w/v) AKD solution in *n*-heptane. The printed-paper was heated on a hot plate at 100 °C for 5 minutes and then allowed to cure for 30 minutes at 60 °C prior use. The coffee ring effect on the microfluidic paper for each design was analyzed by using the dye Fast Green FCF (0.5 mg $mL^{-1}$). Briefly, 5 µL of the ink was dropped on the designed zones and allowed to dry the ink in the paper for 5 minutes under room temperature. The color image on the paper was then captured by using a smart phone. The mean green pixel intensity of the color was measured by using ImageJ software.

### *3.2.9. Design of µPAD methanol sensor*

Hybrid µPAD was designed by using two zones of paper strips (1.4 cm x 1.2 cm) using AKD wax printing as described above. Scheme 3.1 displays the different sections of the hybrid µPAD construct.

The top paper strip acted as sample application zone (**S**) that helps to remove particles from the samples. The lower paper strip with wave design was used as spacer between the SF films (Fig 3.1). The two paper strips were superimposed to each other with the dissolvable ABTS-SF film in between,

while the non-dissolvable bi-enzyme SF detection (**D**) film was placed to the Spacer strip from the rear side. The whole assembly was fixed as a single unit using adhesive tape keeping the S zone exposed for dropping the sample. The steps involved in the fabrication of the µPAD, and its use are described in Scheme 3.2. Different concentrations of methanol sample were dropped on the S zone and the color developed on D film was captured and analyzed.

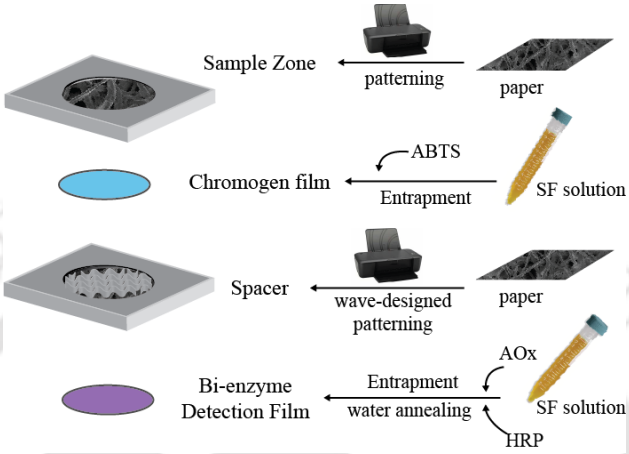


**Scheme 3.1**: Schematic diagram of different sections of the hybrid µPAD construct.

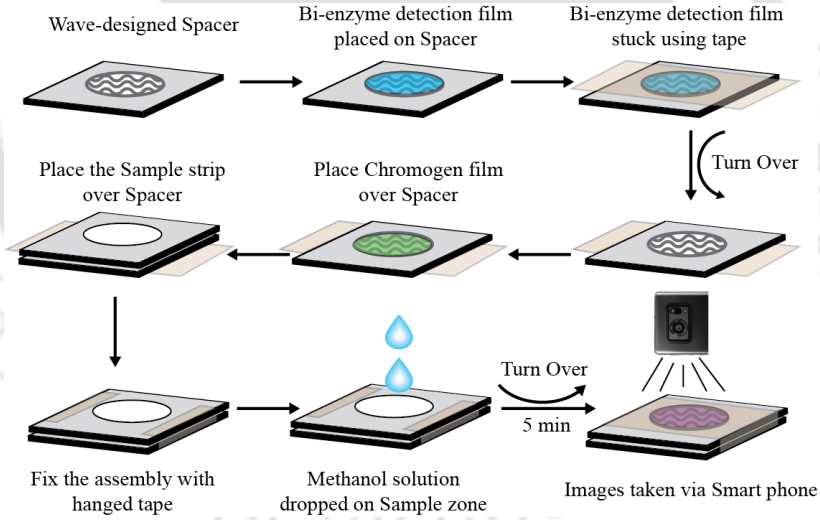


**Scheme 3.2**: Schematic diagram of the steps involved in the fabrication of the hybrid µPAD and its use as reagent-free methanol biosensor.

### *3.2.10. Statistical analysis of data*

Minimum triplicate analyses were carried out for all the samples. OriginPro 9.0 was used to perform the statistical analysis of the data. The error bars represent the standard deviations of the data. The limit of detection (LoD) was calculated using the formula $3\sigma/m$, where $\sigma$ is the standard deviation of the mean grey pixel intensity of the blank sample and $m$ represents the slope of the calibration curve.

### 3.3. Results and Discussion

#### *3.3.1 Optical properties of the enzyme immobilized SF films*

The transparency of SF films was significantly reduced upon immobilization of enzymes in it. The transmittance (%) for the enzyme-free film, HRP immobilized film, AOx immobilized film, and the bi-enzyme film was 80 %, 4 %, 4 % and 1 %, respectively (Fig 3.1a). With increasing the immobilized enzyme concentrations, the films developed whitish texture. The feature appeared suitable for developing colorimetric sensors due to high color contrast from the background surface. The average film thickness marginally increased with the immobilization of enzymes as discerned from the FESEM image. The thickness (micron) of the SF film, HRP SF film, AOx SF film and bi-enzyme SF film were 32.6 µm, 34.4 µm, 35.5 µm, and 37.9 µm, respectively (Fig 3.1b,c,d,e). The generated SF films were smooth with a diameter of 0.8 cm.

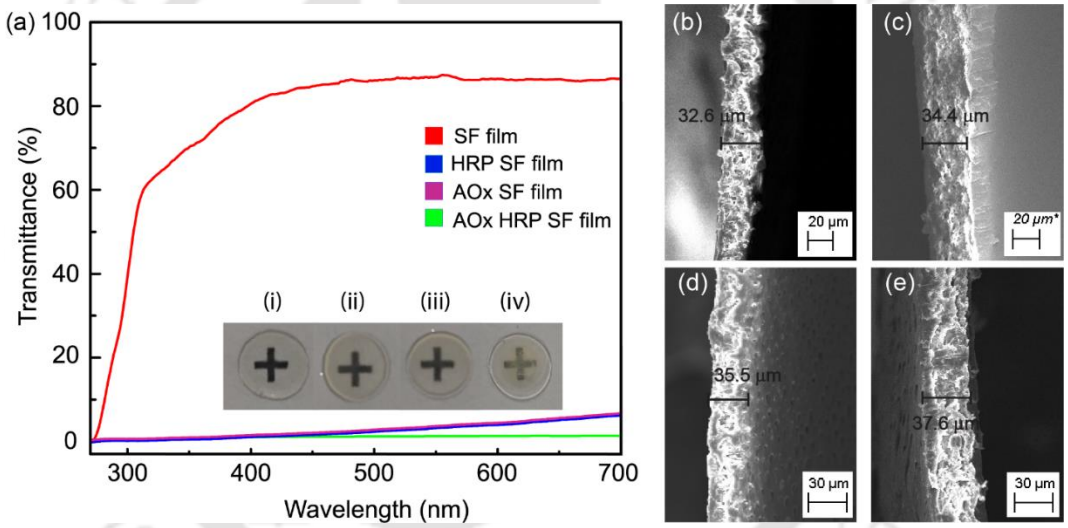


**Figure 3.1:** (a) Transmittance analysis of the different enzyme SF films. Inset images to show transparency of (i) SF film, (ii) HRP SF film, (iii) AOx SF film and (iv) Bi-enzyme SF film. FESEM images showing the thickness of (b) SF film, (c) HRP SF film, (d) AOx SF film and (e) bi-enzyme SF film.

#### *3.3.2 Effect of SF on the colorimetric peroxidase reaction*

The activity of the HRP entrapped in dissolvable SF films was analyzed by using ABTS solution with $H_2O_2$ as the substrate. Initially, the absorbance at $\lambda_{405\ nm}$ increased in presence of the substrate, $H_2O_2$. Interestingly, with increasing reaction time, the solution gradually turned into purple instead of the usual dark green color, which is formed by the ABTS radicals. Spectral analysis showed that addition of SF solution to the reaction system ($ABTS^+ + H_2O_2$ + HRP) lowers the typical peak

intensity of ABTS radical at $\lambda_{405\ nm}$ with a concomitant generation of a new peak at ~ $\lambda_{560\ nm}$ (Fig 3.2a) turning the final solution into purple one (Fig 3.2a inset). The results demonstrated the key role of SF in transmuting the spectral and linked color characteristics in the reaction system. The radical scavenging property of the silk fibroin protein may be attributed to the observed fact (Åkerstro¨m et al., 2007; Bungthong et al., 2021). The absorbance peak for ABTS at ~ $\lambda_{560\ nm}$ is due to the ABTS dication or azodication ($ABTS^{2+}$) formed from the $ABTS^{\bullet+}$ radical (Solís-Oba et al., 2005) generating the purple color due to the formation of the chromogenic –N=N– azo group and its interaction with the adjacent molecular structures (Solís-Oba et al., 2005; Liu et al., 2015b). The fact that ABTS (I) in presence of the catalytic reaction of HRP and $H_2O_2$ transforms into ABTS radical (II), which is responsible for $\lambda_{405nm}$ peak, is well known. We postulate that this radical is further oxidised to ABTS dication (III) by SF rising at the $\lambda_{560nm}$ peak (Fig 3.2b). This rapid peak change along with the formation of dark purple color has significant advantage for developing SF-based colorimetric peroxide sensors because of the clear color change and the formation of two reciprocally generated peaks ($\lambda_{405\ nm}$ vs. $\lambda_{560\ nm}$).

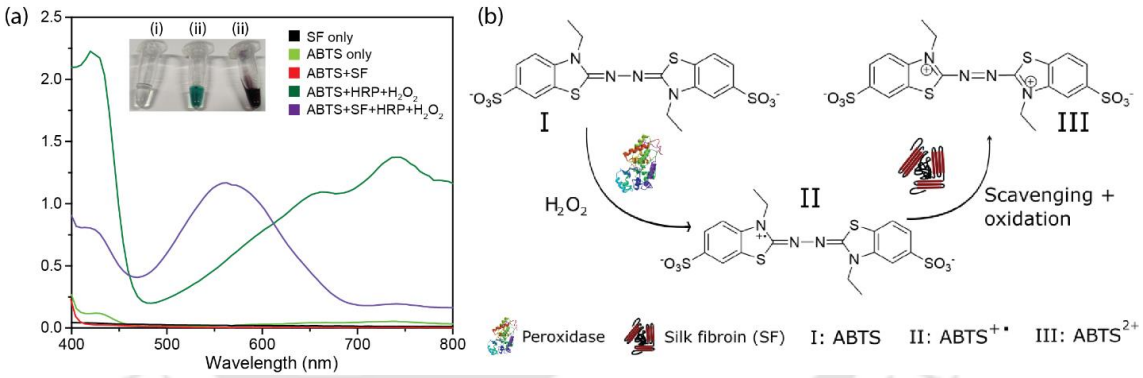


**Figure 3.2**: (a) Absorbance spectra of $H_2O_2$ (25 mM) and with (III) and without (II) SF. Inset: photo of ABTS reaction solution without SF (green) and with SF (purple); (b) Schematic representation of the reaction of different oxidation states of ABTS when it interacts with HRP, $H_2O_2$ and then SF.

### *3.3.3. Colorimetric detection of hydrogen peroxide using HRP SF film*

The non-dissolvable HRP SF film when treated with ABTS solution (2 mM) with varying $H_2O_2$, gave purple color whose intensity increased with increasing $H_2O_2$ concentration. This simple system was used to develop an $H_2O_2$ biosensor. The advantages of the biosensors comprised easy detection of the target as the response color change could be visually detected and the response time was less than 1 minute (Fig 3.3a upper inset). For quantitative detection of the target, the picture of the treated HRP SF film was captured using a smartphone and the mean pixel intensities of the color developed were

used to generate a calibration plot (Fig 3.3a). The plot generated from the lower $H_2O_2$ concentration range gave a polynomial fitting with the equation, $y=ax^2+bx+c$, with an $R^2$ value of 0.995 (Fig 3.3a inset graph). The derivation of this plot when x = 0, gives the slope for calculation of the detection limit through the formula, LoD=3*sigma/slope. Here sigma=1.95, which is the standard deviation of the mean pixel intensity of the blanks (n=3), which includes the error of the sensor without $H_2O_2$ reaction. The biosensor offered an LoD of 0.58±0.001 mM and a dynamic range of up to 300 mM of $H_2O_2$. Due to the high turnover number of HRP (32.7±0.4 $s^{-1}$) with ABTS as the chromogen (Zhang et al., 2016), the reaction was not only fast (< 1 minute), the saturation of the color was also achieved at a low $H_2O_2$ concentration.

Next, we checked the activity of the enzyme in non-dissolvable HRP SF film at different temperatures to understand the stability of the constructed colorimetric sensor (Fig 3.5 b). The enzyme activity in the film on day 0 was the activity obtained immediately after the preparation (water annealing process). For better comparison, the residual activity at day 0 has been normalized to 1. For HRP SF films stored at 4 ℃, the residual activity of the enzyme was increased by 18 % by the end of $10^{th}$ day and further increased by 40 % by the end of 20 days. In case of 25 ℃ storage too, the activity increased by 32 % by the end of 20 days. This unusual phenomenon of increased enzyme activity for HRP has been reported earlier (Lu et al., 2009b). The results suggested that the enzymes are partially denatured during the film preparation process but over time they renature in the micro-environments within the films with limited water content (Lu et al., 2010). In case of 4 ℃ and 25 ℃, the residual activity after 40 days of incubation was 90 % and 82 % of the initial activity, respectively. At 37 ℃ storage condition, the enzyme retained 20 % activity after 40 days. Therefore, we can say that the HRP is quite stable when entrapped in SF films.

The success of HRP SF films as colorimetric $H_2O_2$ biosensor sparked the idea of using them in combination with AOx to develop an alcohol biosensor. AOx is a well-known enzyme for its specific catalysis of alcohol to its aldehyde releasing $H_2O_2$ as a by-product. However, the major drawback of this enzyme lies in its labile nature and low stability under even ambient conditions (Thungon et al., 2017). Thus, in the next section, we will explore SF film for the stabilization of AOx and then implement the concept to develop a reagent-free alcohol biosensor.

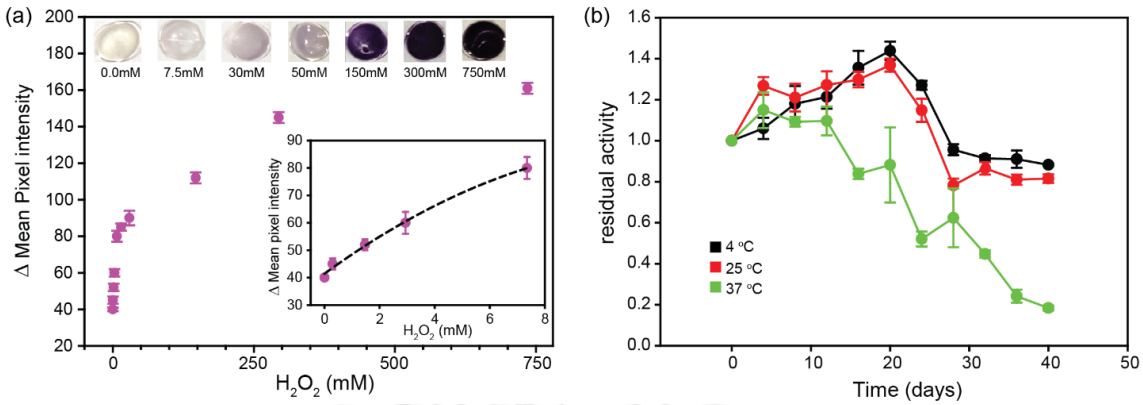


**Figure 3.3:** (a) The response plot of non-dissolvable HRP SF films towards $H_2O_2$. Inset top panel figures are the corresponding color images captured after the reaction with different concentrations of the peroxide. Inset graph is the calibration plot for $H_2O_2$. (b) The enzyme activity in HRP SF films under different temperatures for 40 days. The error bars indicate standard error (n=3).

### *3.3.4. Activity of AOx in SF film*

Herein, we examined the activity of AOx in SF film. Unlike the free AOx, the entrapped AOx retained the entire activity at least up to 5$^{th}$ day of its preparation at RT (Fig 3.4). Under similar conditions, the free enzyme loses ~ 65 % of its activity following the incubation period. Interestingly, there was a significant increase in activity of the immobilized enzyme with the increasing concentration of SF up to its level of 5% (w/v) in the film (Fig 3.5a). The result implies that the SF not only stabilizes the enzyme but also facilitates the enzyme-substrate interaction by creating a congenial microenvironment in the soluble state for diffusion of the substrate. We however used 7% (w/v) SF for preparing the films to facilitate the handling of the delicate film. The optimum concentrations of AOx and HRP in the dissolvable films for maximum activity were identified as 0.5 mg $mL^{-1}$ for each; the optimization experiments were performed following one variable at a time approach (Fig 3.5b,c).

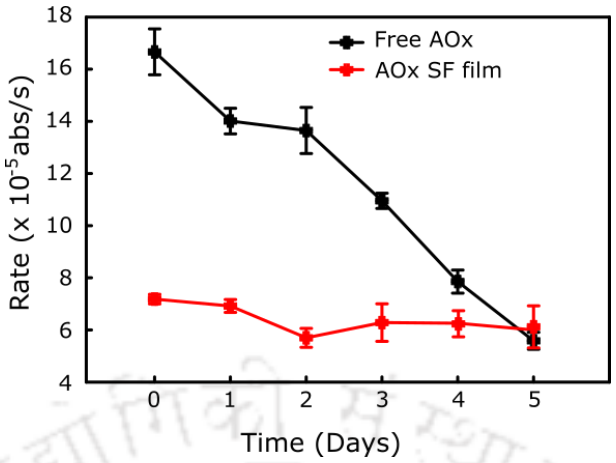


**Figure 3.4**: Activity in terms of rate for the AOx enzyme in free form and in SF (7 % w/v) film over five days time, stored under room temperature (25 ℃) reacted with 25 mM of methanol.

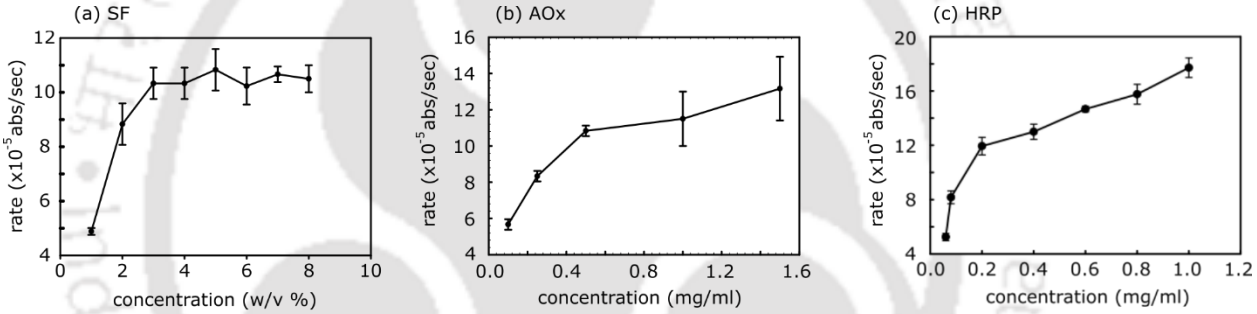


**Figure 3.5**: Optimization studies of concentration of (a) SF, (b) AOx and (c) HRP in silk film.

These optimized concentrations of the enzymes were then used for development of HRP-SF, AOx-SF, and bi-enzyme SF films to be discussed in the next section. The kinetics of the entrapped AOx in mono-enzyme, as well as bi-enzyme SF films were examined immediately (after setting for 24 h, considered 0 day) after preparation and compared the results with the free AOx. The $K_m$ (mM) of the enzyme in free AOx solution, AOx SF film and bi-enzyme SF films were 1.48 ± 0.2 (20 x $10^{-3}$), 8.41 ± 0.8 (15.2 x $10^{-3}$), and 2.47 ± 0.1 (18.8 x $10^{-3}$), respectively with the corresponding rate of reaction (abs $min^{-1}$) shown in the parentheses. The higher $K_m$ values and lower reaction rate of the enzyme entrapped in SF films as compared to native AOx may be related to the immobilization effect on the substrate diffusion and interaction with the enzyme binding sites (Chung et al., 2009). The $K_m$ value of AOx in bi-enzyme SF was lower and the rate of reaction was better than that of AOx SF films. The reason may be ascribed to the development of an altered microenvironment with the inclusion of HRP in the film that is congenial for substrate diffusion and AOx catalysis.

Interestingly, though the activity of the immobilized enzyme in AOx-SF dissolvable film was less in the starting period of its preparation as discussed above, over time it was significantly increased until day 10 of incubation at both 4 and 25 ℃. Whereas, at 37 ℃ the activity rapidly declined after day 10 following a brief lag period of activity (Fig 3.6a). The increase in activity following 10 days of incubation at 4 ℃ and 25 ℃ were 45% and 15%, respectively. The increased activity at 4 ℃ was sustained and stabilized to 25% following 40 days of incubation. However, at 25 ℃ the activity was marginally reduced and attained original activity (98%) after 40 days (Fig 3.6a). This unusual phenomenon of increased enzyme activity was also seen with HRP entrapped in SF film in section 3.3.3 as well. In a previous study, the activity of GOx entrapped in SF film was reported to follow a similar pattern (Lu et al., 2009b). The results suggested that the enzymes are partially denatured during the film preparation process but over time they renature in the micro-environments within the films with limited water content (Lu et al., 2010).

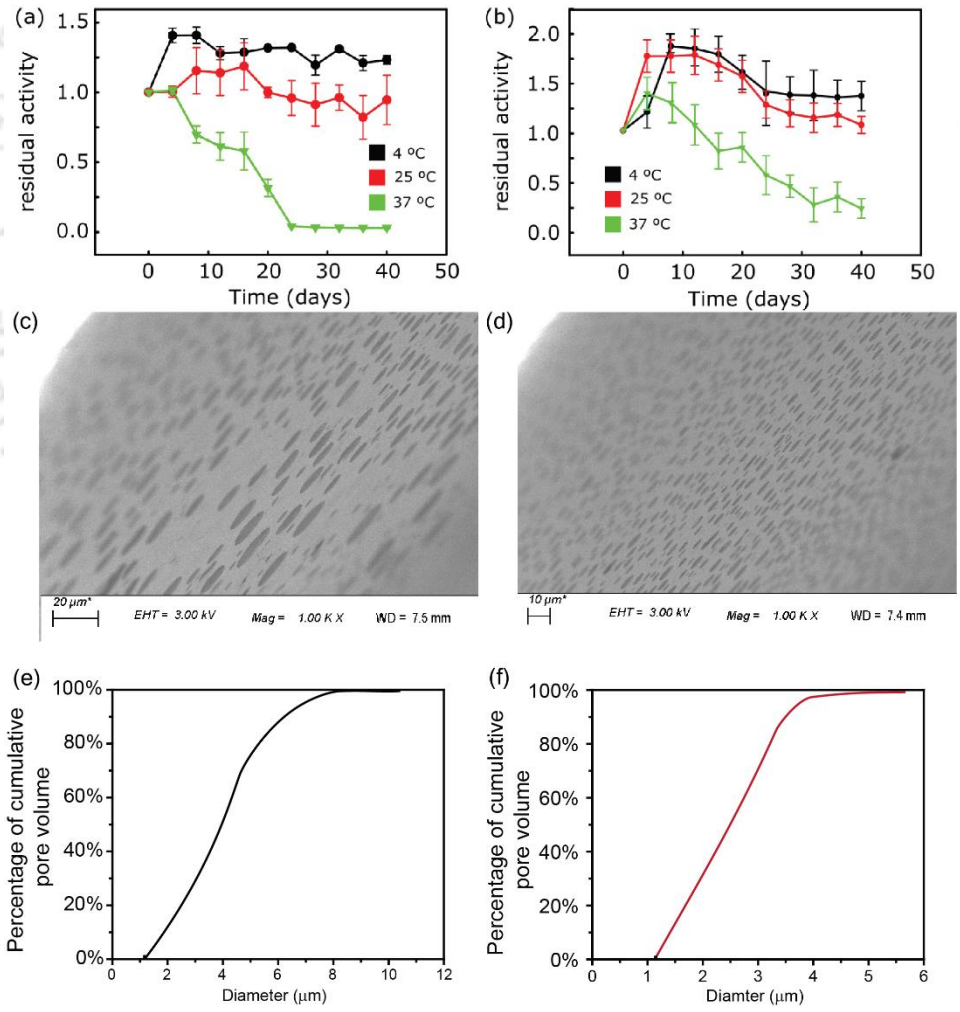


**Figure 3.6**: Residual activity versus incubation time for (a) dissolvable AOx SF films measured at $\lambda_{405\ nm}$ after 1 min and (b) non-dissolvable AOx SF films measured by mean pixel intensity of the purple

color at 4 ºC (black), 25 ºC (red) and 37 ºC (green) after 30 min. FESEM images of (c) dissolvable SF film; and (d) non-dissolvable SF film with their corresponding cumulative pore volume versus pore diameter: (e) dissolvable SF film; and (f) non-dissolvable SF film.

Next, the stability of the enzyme was studied in non-dissolvable AOx-SF films (Fig 3.6b). Interestingly, the color of the reaction solution turned in to green, while the film turned purple (Fig 3.7), which confirmed our results discussed above that the SF protein plays a critical role in transforming the ABTS radical to its dication form (Fig 3.2). Thus, in the rest of the studies the purple color developed in the film was measured in terms of pixel intensity to analyze the immobilized enzyme activity. The reaction time for these non-dissolvable films was fixed for 30 minutes due to the slow reaction (color development), which is caused by the slow interaction between the product ($H_2O_2$) in the film and HRP and ABTS in solution (Lawrence et al., 2008b). The increase in AOx activity in the non-dissolvable SF films over storage time was ~12 % more than the dissolvable film and the increase was observed for all the incubating temperatures after 5-10 days of incubation (Fig 3.6a,b). The corresponding increase in activity was 85%, 76%, and 28% for the films stored at 4 ℃, 25 ℃ and 37 ℃ after 10 days. Following 40 days of storage, the activity retained in the films was 142%, 110%, and 25% for 4 ℃ and 25 ℃ and 37 ℃, respectively.

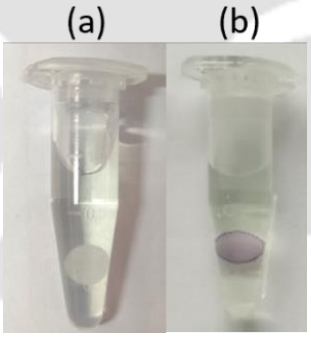


**Figure 3.7**: Images of non-dissolvable AOx-SF films (a) without methanol in substrate solution and (b) with 25 mM methanol in solution. The solution remains green while the film turns purple.

The multimeric (octamer) FAD-based AOx is known to undergo rapid denaturation even under room temperature and neutral pH conditions (Lopez-Gallego et al., 2007; Kumar and Goswami, 2008). However, recently, our lab could achieve unprecedented high stability (half-life of 372 days) of the enzyme by keeping it in anoxic storage condition and confirmed that the prolonged interaction of dioxygen, which is the natural co-substrate for the enzyme, inhibits its activity without affecting the structural integrality of the enzyme protein (Das et al., 2022). Another study revealed that oxygen permeability is low in water-annealed films (Lawrence et al., 2010). The lowering of oxygen content

also reduces metabolic activity and delayed the decay of perishable foods (Marelli et al., 2016). Porosity of the membrane also plays an important role in its oxygen permeability (Kaneko et al., 2020). We analyzed the porosity of the prepared SF films by FESEM (Fig 3.6c,d). The pore volume distribution study through imaging (Li et al., 2015), is an useful approach to describe the porosity. As expected, the dissolvable films exhibited large pores (Fig 3.6c), while the non-dissolvable films exhibited smaller pores (Fig 3.6d). In the dissolvable films, 90% of the total pore volume includes pores with diameter up to 7 µm (Fig 3.6e); whereas, in non-dissolvable SF film, 90% of total pore volume includes pores with diameter up to 3.5 µm with 50% reduction in the pore size (Fig 3.6f). The high enzyme stability we achieved in the non-dissolvable SF film could be explained based on the above facts that the low dimension of pores limited oxygen permeability to the films thereby prolonged the stability of the enzyme the film matrices.

There have been few reports on the stabilization of AOx in different systems under refrigerated conditions (4 ℃). AOx was co-immobilized with catalase in a photoreticulated poly(vinyl alcohol) membrane to prepare conductometry biosensor that offered 95 % retention of its activity even after 4 months (Hnaien et al., 2010). In another study, AOx was covalently immobilized on a modified electrode containing functionalized conducting polymer and multiwall carbon nanotubes (MWCNTs) and showed excellent stability with only 2 % activity loss after 30 days of storage time (Soylemez et al., 2014). The author's lab reported AOx based electrochemical biosensor which showed high retention of activity after 30 days of storage time when the enzyme was immobilized within a nano matrix containing nafion, polyethylenimine, MWCNTs (Das and Goswami, 2013) and also in a sol–gel chitosan film (Chinnadayyala et al., 2014). The most recent study by the author's lab showed exceptionally high stability of AOx with a half-life of 372 days, when the enzyme was stored in an anoxic environment. However, this is the first report where highest stability of the AOx could be achieved under non-refrigerated storage conditions (25 ℃).

### *3.3.5. Detection of methanol using bi-enzyme SF films*

The bi-enzyme SF film was first examined for detection of methanol and was rendered to non-dissolvable form by water annealing process. We found that the color formation in the bi-enzyme entrapped film was faster (max. 15 min) than the one containing only AOx (30 min). The congenial catabolic cooperation between these two redox enzymes due to their closed conjunction under entrapped conditions accelerated the reactions and linked color formation in the bi-enzyme system. The purple color of the films increased with the increasing methanol concentration following the reaction time of 15 minutes (Fig 3.8a and inset). The Δ mean grey pixel intensity of the images of

the films was calculated over a range of methanol concentration and discerned the LoD of 2±0.2 mM with a dynamic range of 2-600 mM for the fabricated bi-enzyme SF-membrane.

The stability of the bi-enzyme system in SF film was studied at the three temperatures (4 ℃, 25 ℃ and 37 ℃). Unlike the previous trends for HRP and AOx SF films (Fig 3.3b and Fig 3.6a, b), the initial increase pattern of the activity was not observed for the films (Fig 3.8b). The reason may be attributed to the less denaturation of the AOx in the bi-enzyme film than in the one with mono-enzyme film at the initial preparation time. The activity of the enzyme in non-dissolvable films in terms of Δ mean gray pixel intensity was 70 and 90 (with 250 mM methanol) for mono and bi-enzyme film, respectively. The activity of AOx in bi-enzyme was thus better than the mono-enzyme film. The activity retention of bi-enzyme SF films was 90±2 % of its initial activity following 40 days of incubation at 4 ℃.

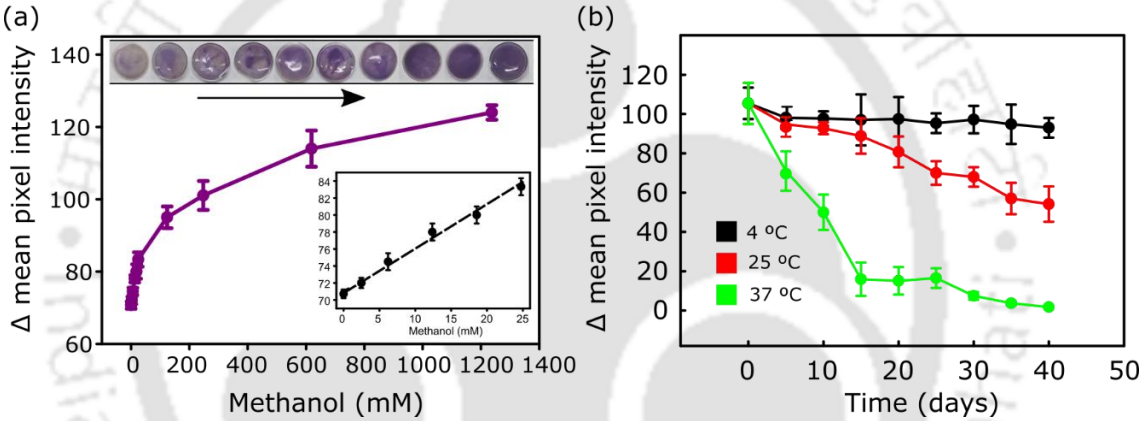


**Figure 3.8**: (a) The response curve for non-dissolvable bi-enzyme SF films towards methanol; Inset top panel showing the images of the corresponding color developed over the film. Inset graph is the calibration plot for the methanol sensing. (b) the stability of the bi-enzyme SF films under different conditions. The error bars indicate standard error (n=3).

### *3.3.6. Development of µPAD methanol sensor*

For fabrication of the µPAD device, we immobilized ABTS in SF-film instead of in chromatographic paper because ABTS gives significant background color noise in paper due to its aerobic oxidation as revealed from our study (Fig 3.9). We chose dissolvable SF films to entrap ABTS to facilitate quick diffusion of the chromogen from the film to the sample flow through the Spacer strip to the bi-enzyme detection film where the reaction will take place (Scheme 3.1). The maximum concentration of the entrapped ABTS that did not succumb to aerobic oxidation led color change for prolong storage (at least 2 months) was 10 mM. The µPAD device was fabricated by using two-microfluidic paper strip with hydrophilic circular zones-one for sample application (**S**) and the other for Spacer, and two

SF film circular zones – one with entrapped ABTS while the other with immobilized enzymes (AOx+HRP). Detailed dimensions and assembly are shown in Fig 3.10a. To test this sensor, 1 M of methanol was dropped on the **S** zone and the color change was observed in the **D** film. Interestingly, the reaction time required for developing color in the µPAD device was 5 minutes, which is significantly lesser than the one obtained by using just the bi-enzyme SF film in solution as mentioned in the previous section. This decrease in the reaction time could be due to low diffusional reaction barrier among the sample, reagent (ABTS), and enzyme-entrapped films, which are physically in close contact for fast chemical communications. The D film however showed strong coffee ring effect, which made the signal unsuitable for quantitative data analysis (Fig 3.10c). To reduce the coffee ring effect on SF film, we introduced the wave designed paper spacer through which the reagents (methanol sample and dissolved ABTS-SF) flow to the bi-enzyme detection film uniformly across the whole detection film.

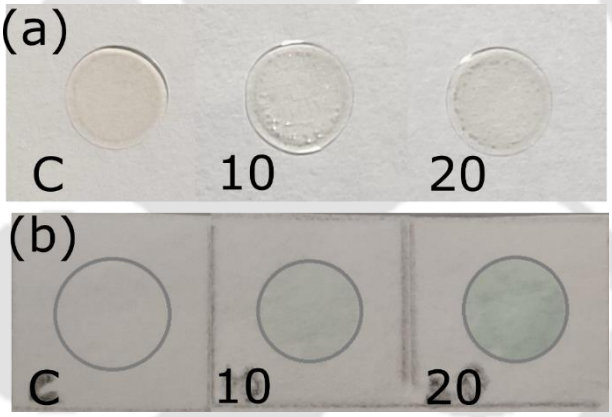


**Figure 3.9**: Images of ABTS of concentration 10 mM and 20 mM: (a) entrapped in SF films and (b) immobilized on paper. ABTS on paper show color change much greater than the control.

The coffee ring effect has been attributed to two factors: 1) pinning of the contact line on the deposition of a drop of fluid on a solid surface and 2) the drying of the fluids via evaporation. Briefly, once a drop is deposited on a solid surface, the edge of the drop is pinned at the contact line. As the drying due to evaporation takes place, liquid first evaporates from the edges. To replenish the loss, fluid from the interior flows outward due to capillary force. The resulting outward flow through capillary wicking carries the dispersed material in the fluid to the edge creating the coffee ring effect in paper (Deegan et al., 1997; Cao et al., 2020). The movement of liquid through a porous medium like paper could be described by using Darcy's equation (Whitaker, 1986):

$$Q = \frac{\kappa A\, \Delta P}{\mu D} \quad (3.1)$$

where $Q$ is the volumetric flow rate ($m^3/s$), of the fluid through a porous medium (here paper) through the cross-sectional area $A$ ($m^2$), κ ($m^2$) is the permeability of the fluid and μ (Pa.s) its dynamic viscosity, and $\Delta P$ (Pa) is the change in pressure over a given distance $D$ (m). The equation (3.1) could be written as:

$$Q = \alpha\, A \quad (3.2)$$

where $\alpha = \frac{\kappa \Delta P}{\mu D}$, which remains constant for a particular chromatographic paper of a defined size.

If the surface area is reduced, then the value of 'Q' would be reduced accordingly, hence the evaporation flux, J (m/s) will also reduce proportionally, which in turn levied less capillary driving force to the fluid flow and at the same time, the particle movement will be restricted into the subdivided finite boundaries. The analysis could also be viewed through 2-dimensional shape taking into account the thickness (x) of the paper, in which case

$$A = xL \quad (3.3)$$

Where L is the width of the paper zone (Fig 3.10e). Smaller the L, lower will be the evaporation flux of the fluid over the paper as could be discerned from the equation (3.2). Thus, segmenting the circular paper zone is likely to reduce the coffee ring effect.

Guided by the above principle, we created wave-like designs, using AKD wax-printing technique, within the Spacer zone in the μPAD device which was in close contact with the bi-enzyme detection film (Fig 3.10b). The wave design was selected to create more barriers on the edges that will create turbulence flow of the fluid further slowing the flow as well as mixing the components in the fluids. Hydrophobic wave channels each 0.15 mm thickness, keeping apart by hydrophilic space (L mm) between the channels, were created in the zone. With varying L, the coffee ring effect was checked and as the L was reduced, the dye uniformly dispersed over the zone and the pixel intensity increased (Table 3.1). Hence, the L of 1 mm was selected to design the spacer zone for the hybrid μPAD which showed a much better signal on the D film as compared to design without the wave pattern when reacted with 1 M of methanol (Fig 3.10d).

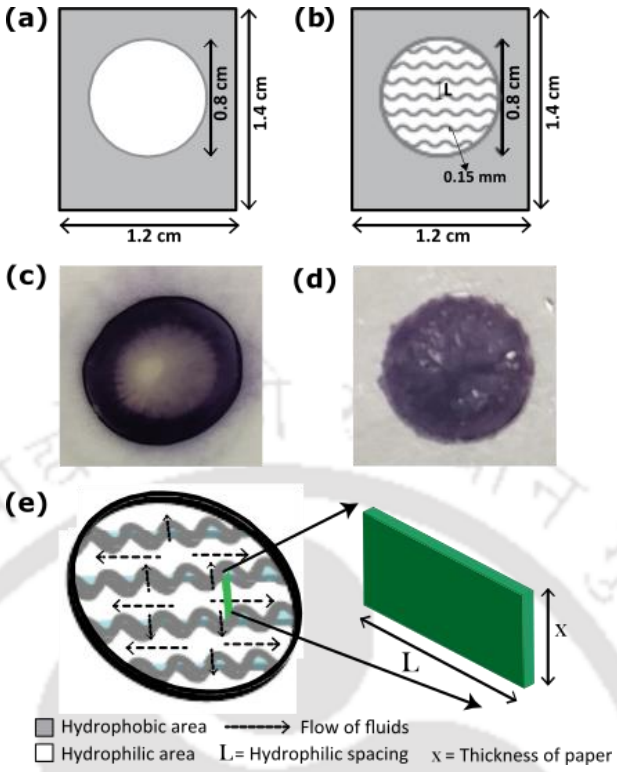


**Figure 3.10**: Scheme of pattern designs for Spacer with (a) circular hydrophilic zone and (b) hydrophilic channels within circular zone. The detection films of µPAD after reaction using 1 M methanol with pattern designs for Spacer with (c) circular hydrophilic zone and (d) hydrophilic micro-channels within circular detection zone; and (e) the schematic diagram of the movement of fluid within the channels that is along the channel surface.

**Table 3.1**: Different microfluidic circular designs in Spacer with varying width, L, and their respective mean green pixel intensity.

| Design | Hydrophilic spacing between waves, L (mm) | No. of waves | Mean green pixel intensity | |
|---|---|---|---|---|
| 1 | 8 (Diameter) | 0 | 40±1 |  |
| 2 | 3 | 3 | 68±2 |  |
| 3 | 1 | 7 | 91±1 | 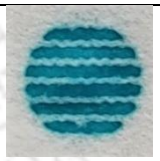 |

### *3.3.7. Performance of the µPAD methanol sensor with wave-designed paper platform*

The purple color developed on the D zone could be identified by even naked eyes in a 5 min reaction time (Fig 3.11a inset). The mean pixel intensities of the color were captured, and a calibration plot was generated. The plot of lower methanol concentration gave a polynomial fitting with the equation, $y=ax^2+bx+c$, where a=-0.06, b= 3.7, c=5.8. The derivation of this plot when x = 0, gives the slope for calculation of the detection limit through the formula, LoD=3*sigma/slope. Here sigma is the standard deviation of the mean pixel intensity of the blanks (n=10), which includes the error of the sensor without methanol reaction. The calculated LoD was 1±0.05 mM, with a dynamic range of 1 mM-2 M for the µPAD methanol biosensor.

The stability of the hybrid µPAD biosensor was analyzed by measuring the mean pixel intensity in the D zone. The activity retention at the end of 40 days of storage at 4 ºC was 83±5% (Fig 3.11b). The half life activity calculated for 4 ℃ and 25 ℃ storage conditions were 113 days and 44 days, respectively. Additionally, we find that the ABTS entrapped in the SF films did not succumb to oxidation at least for 2 months of storage contrary to the common phenomena of its increased air oxidation developed the green color over time (Matilainen et al., 2012)·(Scott et al., 1993). The SF film with low oxygen permeability limited the interaction between the entrapped ABTS and ambient

oxygen, hence halting the oxidation. The overall performance of all the non-dissolvable SF films with entrapped enzyme(s) has been presented in Table 3.2.

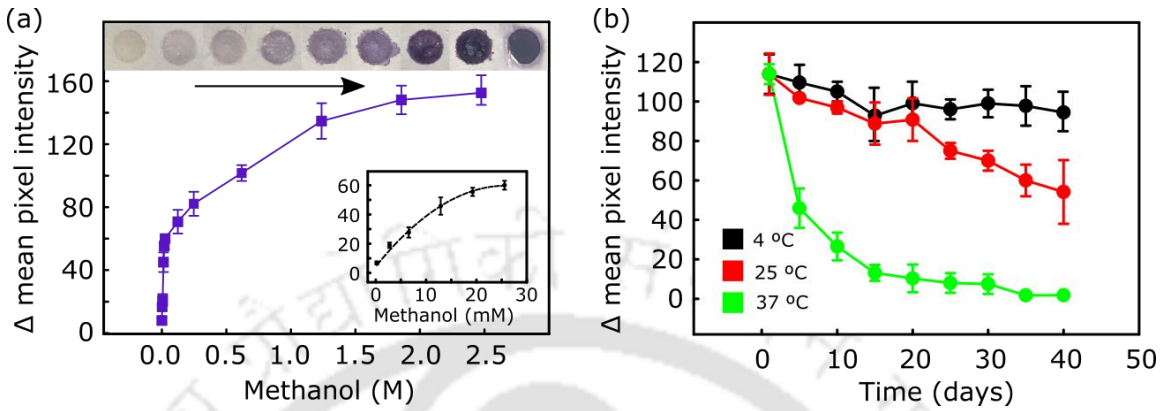


**Figure 3.11**: (a) Performance of the µPAD methanol biosensor; inset are the photos of reacted µPAD with increasing concentration of methanol. (b) Stability study of the µPAD. The error bars indicate standard error (n=3).

**Table 3.2**: Different non-dissolvable enzyme(s) SF films and their sensing performance.

| **Type of SF film** | **Reaction time (minutes)** | **LoD (mM)** | **Dynamic range (mM) and analyte** | **Stability (% activity retention after 40 days)** | |
|---|---|---|---|---|---|
| | | | | 25 °C | 4 °C |
| ***HRP-SF film*** | >1 | 0.58±0.001 $H_2O_2$ | 0.58-300 $H_2O_2$ | 82 | 90 |
| ***AOx-SF film*** | 30 | 5±0.8 MeOH | 5-250 MeOH | 110±3 | 142±2 |
| ***Bi-enzyme SF film*** | 15 | 2±0.2 MeOH | 2-600 MeOH | 57±5 | 90±2 |
| ***Hybrid µPAD*** | 5 | 1±0.05 MeOH | 1-200 MeOH | 55±7 | 83±5 |

### 3.4. Conclusion

In this chapter, we explored the enzyme based $H_2O_2$ detection for the development of a novel optical µPAD biosensor device for detection of methanol using AOx as a biorecognition element coupled with HRP-ABTS based peroxidase reaction. The unique feature of the devise comprises improved shelf-life of the enzymes, sharp color change as response signal for methanol and reduced coffee-

ring effect on the detection film. The shelf life of the highly labile AOx could be markedly improved by immobilizing it along with HRP in a non-dissolvable biocompatible SF-film with pore sizes less than 3.5 µm that prevent free diffusion of atmospheric oxygen through the film and thus protected the redox enzyme from the inhibitory effect of its co-substrate. This invention has also opened up a new avenue to explore the non-dissolvable SF-film for stabilizing other redox enzymes for various applications. This unprecedented, improved shelf-life under room temperature of this AOx enzyme of enormous clinical and industrial importance will greatly boost its prospect for real-world applications. Contrary to the typical green color developed during the ABTS-based peroxidase reaction, purple was formed in the presence of SF. The formation of intense purple color appeared as an additional advantage to the optical device. We also addressed the challenge of using ABTS on the solid platform for developing a sensor device. The challenge is posed by the low stability of the dye in an aerobic environment and its leaching susceptibility from the immobilized support system. Using even dissolvable SF-film, the dye could be entrapped in the film matrix during its preparative step, which prolonged its activity over a long time (2 months) by averting its aerobic oxidation. The next important feature of the developed µPAD device is the void of the coffee ring effect in the detection zone performed by introducing a wave-designed microfluidic channels in the spacer paper. The smaller waved micro-channels facilitated uniform distribution of the dye particles and samples across the paper spacer zone that in turn enabled uniform contact of these reactants with the enzyme particles for homogeneous color distribution over the detection film. The coffee ring free detection film abetted error-free capture of pixel signal for quantitative detection of methanol. The stand-alone µPAD biosensor device for detecting methanol developed through this investigation is a step forward for its practical application. The application of the biosensor may be extended to ethanol detection as well, as the enzyme AOx is reactive to this alcohol with a bit high *Km* value (1 mM). The µPAD biosensor was sensitive to ethanol as well with LoD of 0.87 mM. Coupling this biosensor with a smartphone device to visualize the results in digital form and introducing the scope to transmit the data remotely through IoT technology may significantly accelerate its commercial application.

Though extremely sensitive and selective, biological enzymes are still prone to denaturation and thus activity loss. There have been in recent times reports of several nanomaterials showing enzyme like activity called “nanozymes”. Therefore, in the next chapter we aim to develop $H_2O_2$ optical sensors by exploring protein stabilized nanoclusters as signal generating system.

# CHAPTER IV

## PROTEIN STABILIZED GOLD NANOCLUSTERS AS HYDROGEN PEROXIDE SENSING PROBE

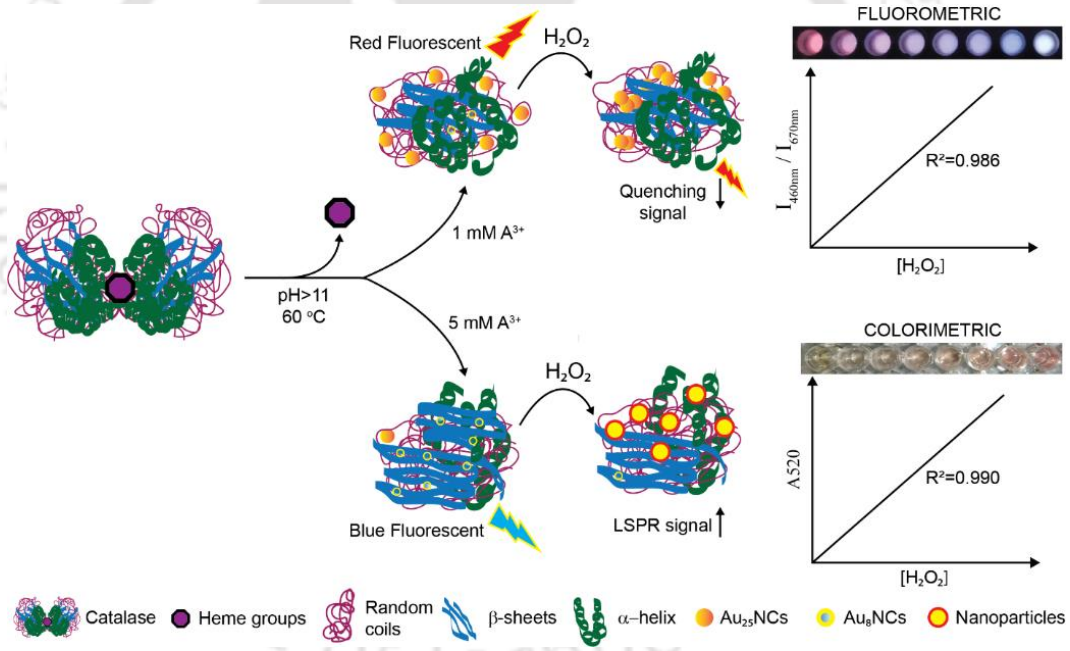

# Chapter IV

# Protein stabilized gold nanoclusters as hydrogen peroxide Sensing Probe

## 4.1. Introduction

The peroxidase-mimic is an emerging topic in the field of catalysis owing to its great prospects in analytical sciences and tailored technological fronts including sensors and chemical processes (Review: Das and Goswami, 2020). The major driving forces that propel this research are the high demand for stable and low-cost catalysts for degrading $H_2O_2$. Conventionally, various chemical and biological catalytic reactions are exploited and among which peroxidase-based enzymatic reactions are widely used (Ali et al., 2011; Mazzei et al., 2007; Okawa et al., 2015; Qian et al., 1997; Rocchitta et al., 2016; Solanki et al., 2011; Thepchuay et al., 2020; Xu et al., 2011b; Zhao and Jiang, 2010). As discussed in the previous chapter, enzyme-based catalysis though, possess advantage of very high selectivity over the other catalysts, the labile nature of the enzymes and their high production cost prompted to explore novel peroxidase mimics (Shamkhalichenar and Choi, 2017). Over the last few years, many nanozymes have emerged as attractive peroxidase mimic due to their low production cost and uncomplicated synthesis routes (Wei and Wang, 2013; Das et al., 2021b; André et al., 2013). However, the practical applications of these nanozymes are yet to be adequately achieved due to several hurdles, among which, the lack of suitable stabilizing matrix for their convenient immobilization on solid platforms for repeated use and void of clear knowledge on their mechanism of action for designing the catalytic process rationally are prominent (Das et al., 2021b). In this direction, protein stabilized metal nanoclusters bring hope to resolve these issues to develop more stable $H_2O_2$ sensing platforms for various analytical applications including designing peroxide sensors (Shamkhalichenar and Choi, 2020).

Metal nanoclusters (NCs) are small nanoparticles (size<3 nm), possess intrinsic photoluminescence behaviours, and explored for various applications (Thungon et al., 2020; Chakraborty and Pradeep, 2017; Tao et al., 2015). Among them, gold nanoclusters (AuNCs) have been widely investigated because of their biocompatibility, easy preparation procedure and high photostability (Zhang et al., 2019; Zheng et al., 2017). Various ligands are used to stabilize the AuNCs. Protein is one of the most preferred ligands due to their unique structures, intrinsic fluorescence behaviour, multiple functional

groups on the surface, high aqueous solubility and their distinctive biological functions (Chevrier et al., 2012;Guo et al., 2020). The reactivity of such protein stabilized metal-NCs does not directly depend on the function of the amino acids of the protein but rather the intrinsic optical nature of the NCs itself (Wen et al., 2011). This approach enables to maintain the catalytic activity of the nanoclusters even when the protein is denatured. Additionally, the NCs could be conveniently coupled to various solid platforms through different functional groups present on the surface of the stabilizing protein molecules for developing immobilized NC systems for diverse applications. Furthermore, by varying the molar ratio of protein/$Au^{3+}$ (gold precursor), and pH of the reaction during synthesis, different AuNCs sizes and fluorescence emission characteristics could be prepared (Thungon et al., 2020; Kawasaki et al., 2011).

In this chapter, we focus our attention on catalase protein as stabilizing matrix for AuNCs to generate $H_2O_2$ sensing activity because catalase protein structure is tolerant to high concentration of $H_2O_2$. Catalase is evolved through an evolutionary process to degrade the oxidant, with extremely high turnover rate (~4 x $10^7$ $s^{-1}$ $M^{-1}$). Notably, the detrimental effect of $H_2O_2$ on the protein structures is already known (Veal et al., 2007). In this work, the catalytic function of catalase was rescinded by removing the heme prosthetic group from the protein matrix during the synthesis of AuNCs. The characteristics of the AuNCs formed in the protein matrix were then investigated following different spectroscopic and microscopic techniques and identified two types NCs with distinct sizes and photophysical properties, emitting red and blue fluorescence, respectively. This investigation shed new lights on the cause of formation of the AuNCs pertaining to the protein secondary structure and reaction conditions and their interactions with the substrate hydrogen peroxide. Interestingly, the blue-fluorescent AuNCs could be transformed into plasmonic nanoparticles following their interactions with the $H_2O_2$ and the phenomenon could be effortlessly translated to develop colorimetric method for detecting the peroxide. The critical findings achieved were then extrapolated to develop two analytical platforms for detection of $H_2O_2$, one fluorometric while the other one is SPR based colorimetric methods.

## 4.2. Experimental section

### *4.2.1. Chemicals and reagents*

Catalase (EC No. 1.11.1.6) from bovine serum was purchased from Sigma-Aldrich. Hydrogen peroxide (~50 w/v%), aurichlorohydric acid ($HAuCl_4.3H_2O$) and Sodium hydroxide (NaOH) were purchased from HIMEDIA (India). Ethanol, sodium dihydrogen phosphate ($NaH_2PO_4$) and disodium hydrogen phosphate ($Na_2HPO_4$) were purchased from Merck (India). Carbon coated copper TEM

grids for morphology study were purchased from TED Pella, Inc, USA. All the chemicals were of reagent grades and used without any further purification. All solutions were prepared using nanopure water, MQ (18.2 MΩ.cm), Millipore Co., (USA).

### *4.2.2. Synthesis and purification of catalase stabilized fluorescent gold nanoclusters (Cat-AuNCs)*

For the synthesis, all the glassware was washed with aquaregia and the solvent for all samples was MQ. Cat-AuNCs were synthesized using a reported protocol (Lu et al., 2014) with some partial modification. One mL of $HAuCl_4$ solution was properly mixed with 1 mL catalase solution (16 mg $mL^{-1}$ or 67 µM) using water as reaction medium and incubated for 2 minutes. Following which, 100 µL NaOH (1M) was added to the solution to maintain the pH above 11. The solutions were then incubated at 60°C for 4 h. The color of the reaction solutions was changed from greenish yellow to brownish yellow indicating the formation of AuNCs. The AuNCs solutions were then purified by dialysis against MQ water using a dialysis tube with molecular weight cut-off of 1 kDa. The dialysis was performed for 24 h with water changed every 8 hours. The final solutions were stored at 4°C for further use. The as prepared Cat-AuNCs were characterised by UV-visible absorption spectroscopy, fluorescence spectroscopy and Transmission Electron Microscopy (TEM). Further, the secondary structures of catalase in the Cat-AuNCs were analyzed by Circular dichroism (CD) spectrometry.

### *4.2.3. Spectroscopic characterization of Cat-AuNCs*

Absorbance analyses were done on a spectrophotometer (Cary 400 Scan UV-Visible Spectrophotometer) using 1 cm path length quartz cuvette at a scan rate of 100 nm $min^{-1}$. The protein concentration of both Catalase and Cat-AuNCs were kept at 7.62 mg $mL^{-1}$. Fluorescence measurements were performed using fluorescence spectrometer (HORIBA scientific Fluorimax-4 instrument) at 25 °C and scan rate of 50 nm $min^{-1}$. Both emission and excitation slit width were kept at 5 nm during the measurement.

### *4.2.4. Circular dichroism (CD) studies*

CD spectra of Catalase and Cat-AuNCs were performed using a spectropolarimeter (J-815, Jasco, Japan.) calibrated with 0.06 % (w/v) aqueous solution of (±)–10–camphor sulfonic acid with the protein concentration kept at 0.5 mg $mL^{-1}$ for each sample. The spectra were recorded in the range of $\lambda_{240nm}$–$\lambda_{190nm}$, in 0.1 cm path length suprasil quartz cuvette, at a scan rate of 100 nm $min^{-1}$, 1 nm bandwidth, with a time constant of 2 s, and an average of 3 scans. The temperature of the cell was maintained at 25 °C by using a peltier temperature control unit. The spectrum was corrected for baseline and smoothed by Savitsky–Golay filter using Jasco spectral analysis software. The

secondary structure analysis was performed using online server DICROWEB structure estimation program, which utilizes CONTIN program to evaluate the structure.

#### *4.2.5. Electron microscopy studies*

Morphology and size of the Cat-AuNCs were analyzed by using Field Emission Transmission Electron Microscope (FETEM) (JOEL, Model: 2100F) operated at an accelerating voltage of 200 kV. Samples for TEM analysis were prepared by evaporating a drop of 200 times diluted solution of the AuNCs on a TEM grid.

#### *4.2.6. Zeta Potential studies*

Zeta surface potentials of the Catalase, RF Cat-AuNCs and BF Cat-Au NCs were determined using a zetasizer instrument (Malvern ZEN 3600 Zetasizer). Catalase, RF Au NCs and BF Au NCs each with protein concentration of 1 mg $mL^{-1}$ was prepared in MilliQ filtered through 0.22-micron syringe filter. The sample solutions were charged into specially designed folded capillary cell with gold plated copper electrode (Model: DTS1070, Malvern Instruments Limited, UK). Data were acquired at 25 °C, repeated 20 times and averaged.

#### *4.2.7. Catalase activity study*

Catalases degrade $H_2O_2$ to release $O_2$ and $H_2O$. The reaction can be monitored by measuring absorbance at $\lambda_{240nm}$ for $H_2O_2$. The absorbance decreases with time due to the catalytic degradation of $H_2O_2$ in the reaction solution. 100 µL of pure catalase (100U $mL^{-1}$) in water was mixed with 1 µM $H_2O_2$, and the absorbance at $\lambda_{240nm}$ was monitored over 3 minutes using spectrophotometer (Cary 400 Scan UV-Visible Spectrophotometer). Similar procedure was followed for analyzing the catalase activities in Cat-AuNCs (equivalent of 100U $mL^{-1}$ catalase) and alkali treated catalase after adjusting the pH (optimum pH value of 7) by dialysing against water.

#### *4.2.8. Analysis of Band gap and Quantum yield*

The band gaps of the two Cat-AuNCs were obtained using Tauc method which assumes that the energy-dependent absorption coefficient α can be expressed by the following equation (Makuła et al., 2018):

$$(\alpha * h\nu)^{\frac{1}{\gamma}} = B(h\nu - E_g) \quad (4.1)$$

where $h$ is the Planck constant, ν is the photon's frequency, B is a constant and $E_g$ is the band gap energy. The γ factor depends on the nature of the electron transition and is equal to 1/2 or 2 for the

direct and indirect transition band gaps, respectively. In the present case, we assume that the transition is direct with γ=1/2 and plot the graph of $h\nu$ vs $(\alpha * h\nu)^2$, where α is the absorbance value divided by the path length of the cuvette (1 cm here), and $\nu$ is C/λ, C= Speed of light and λ= wavelength.

The region of the plot showing a linear and steep increase of light absorption with increasing energy has been a known characteristic of semiconductor materials. The x-axis intersection point of the linear fit of this Tauc plot gives an estimate of the band gap energy.

To calculate the quantum yield ($\Phi$) of AuNCs, Rhodamine was used as the reference and the following formula used was:

$$\Phi = Q_R * (\frac{I_x}{I_R}) * (\frac{OD_R}{OD_x}) * (\eta_x^2 * \eta_R^2) \quad (4.2)$$

Where, $Q_R$ is the quantum yield of rhodamine, $I_x$ and $I_R$ are the fluorescence intensity integral of the test sample and rhodamine, respectively, $OD_R$ and $OD_x$ are the maximum absorbance of rhodamine and test sample, $\eta_x$ and $\eta_R$ are the refractive index of the solvent in which test sample and rhodamine are dissolved. The values, $Q_R$=0.94, $I_R$=1.88*$10^8$, $OD_R$=1.134, $\eta_R$=1.36 (Rhodamine was dissolved in ethanol) for Rhodamine were used to calculate the $\Phi$.

### *4.2.9. Interaction studies of Cat-AuNCs with $H_2O_2$*

100 µL of $H_2O_2$ solutions in MQ water was mixed with 100 µL of Cat-AuNCs solutions and incubated for 10 mins at 25 ºC before fluorescence measurements were performed. The volume of the solution was made up to 1 mL by adding 800 µL MQ to the reaction solution.

Fluorescence lifetime was measured using the time correlated single-photon counting (TCSPC) method on an Edinburgh Instrument Life-Spec II instrument (UK). A $\lambda_{375nm}$ laser diode was used as the excitation source. The fluorescence decays of Cat-AuNCs with and without 100 mM $H_2O_2$ were analyzed by reconvolution method using the FAST software provided by Edinburgh Instruments. The goodness of fit was determined by the reduced chi-square ($\chi^2$) values and weighted residuals, which were between the ranges of ± 4.

The morphology change after the interaction was observed using Field Emission Transmission Electron Microscope (FETEM) (JOEL, Model: 2100F) operated at an accelerating voltage of 200 kV. For the analysis, the samples were prepared by evaporating a drop of 200 times dilute solution of the Cat-AuNCs reacted with 100 mM $H_2O_2$ on a carbon coated copper TEM grid.

#### *4.2.10. Fluorometric detection of $H_2O_2$*

Aliquots (0.5 mL) containing Cat-AuNCs (protein concentration 7.6 mg $mL^{-1}$) as the fluorescence probe and 0.5 mL of different concentration of $H_2O_2$ were mixed and incubated at room temperature (25 ℃) for 10 minutes and then the fluorescence intensities were monitored by exciting at $\lambda_{370nm}$. The fluorescence response towards different $H_2O_2$ concentration was independently tested. The response curve was generated by plotting $I_{460}/I_{670}$ vs. $H_2O_2$ concentration, where $I_{460}$ and $I_{670}$ are fluorescence intensity at $\lambda_{460nm}$ and $\lambda_{670nm,}$ respectively in absence (control) and presence of $H_2O_2$.

#### *4.2.11. Colorimetric detection of $H_2O_2$*

Aliquots (0.7 mL) of Cat-AuNCs and 0.3 mL of different concentration of $H_2O_2$ were mixed and incubated for 30 minutes at 60 ℃ and the absorbance were monitored from $\lambda_{400nm}$-$\lambda_{700nm}$ using spectrophotometer (Cary 400 Scan UV-Visible Spectrophotometer) at 25 ℃. The absorbance at $\lambda_{520nm}$ towards different $H_2O_2$ concentration was independently recorded and the response curve was generated by plotting absorbance at $\lambda_{520nm}$ vs $H_2O_2$ concentration.

#### *4.2.12. Synthesis and purification of SF stabilized gold nanoclusters (SF-AuNCs)*

For the synthesis, all the glassware was washed with aqua regia and the solvent for all samples was MQ. Silk fibroin (SF) from *Bomryx mori* was extracted following a reported method (Rockwood et al., 2011). 2mL of SF solution (5 % w/v) in MQ was transferred into a glass tube. Next, 400 µl of 1M NaOH was added to SF solution to bring the pH of the solution above 11. This SF+NaOH solution was also used as control for the characterization study. After 2 minutes of incubation, 2mL of $HAuCl_4$ solution (2.5 mM) was added to the SF+NaOH solution and stirred for 5 min. The final reaction solution was incubated at 60 ℃ for 3 hours. The SF-AuNCs solution thus prepared was then purified by dialysis method using a dialysis tube with molecular weight cut-off of 1 kDa for 24 h with the water changed every 8 hours. The final solution was stored at 4°C and was stable for 2 months. The prepared SF-AuNCs were characterised by UV-visible absorption spectroscopy, fluorescence spectroscopy and Transmission Electron Microscopy (TEM). Further, the secondary structures of SF in the SF-Au NCs were analyzed by CD spectrometry as described in earlier sections.

#### *4.2.13. Statistical analysis of data*

The statistical analysis of the data was performed in OriginPro 9.0. A minimum of triplicate analyses was performed for all the samples. The mean with the standard deviation is represented as error bars in the data. The LoD was calculated using the formula 3σ/m, where σ is the standard deviation of the blank signals and m represents the slope of the calibration curve.

## 3. Results and Discussion

### *4.3.1. Synthesis and Characterization of Cat-AuNCs*

The AuNCs were synthesized inside catalase protein following a simple two-step process involving treatment of catalase (16 mg $mL^{-1}$ or 67 µM) with different concentrations of $HAuCl_4$ ($Au^{3+}$) solutions first, followed by alkali treatment as mentioned in section 2.2. Fluorescence spectra were then recorded for the synthesised AuNCs after exciting the samples in a wavelength range of 300 to 450 nm. All the AuNCs samples showed an excitation peak around $\lambda_{370nm}$ (Fig 4.1 dashed). The fluorescent color of the AuNCs (under UV-illuminator) was gradually transformed from red into blue with the increasing $Au^{3+}$ concentrations from 1 mM to 5 mM (Fig 4.1 inset). The AuNCs formed with 1 mM $Au^{3+}$ solution exhibited red fluorescence, while with 4 mM and above $Au^{3+}$ solution exclusively produced blue fluorescence. The emissions were spread over the wavelength region of 400 - 700 nm. Two clear peaks, corresponding to the wavelengths of ~460 nm and ~670 nm, were emerged within the emission range (Fig 4.1). Further, a marginal blue-shift of the spectra was observed with the increasing concentration of $Au^{3+}$. The peak intensities in these two wavelengths, however, reciprocally varied to the concentration of the $Au^{3+}$ solutions. At 1 mM $Au^{3+}$ (with Au:protein ratio of 15) the peak intensity ratio ($\lambda_{670nm}$ : $\lambda_{460nm}$) of 3.5 was detected; whereas, at 5 mM $Au^{3+}$ (with Au:protein ratio of 75) the intensity ratio was 0.25.

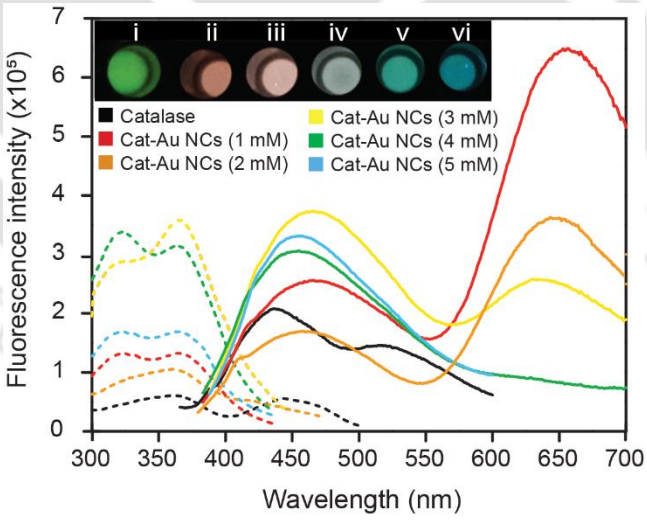


**Figure 4.1**: Excitation (dashed lines) and emission (solid lines) spectra of Cat-AuNCs prepared by using different $Au^{3+}$ concentrations. Inset: Sample pictures under UV light; i-Catalase, and Cat-AuNCs prepared by using $Au^{3+}$ concentrations (mM) of: ii-1 (RF Cat-AuNCs), iii-2, iv-3, v-4, vi-5 (BF Cat-AuNCs).

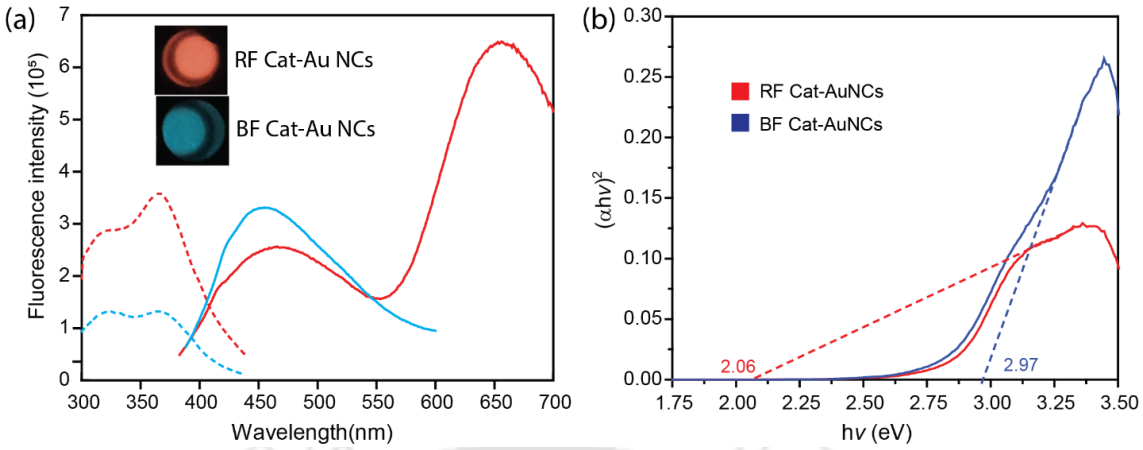


**Figure 4.2**: (a) Characteristics of RF Cat-AuNCs and BF Cat-AuNCs. (b) Band gap calculation using absorbance study.

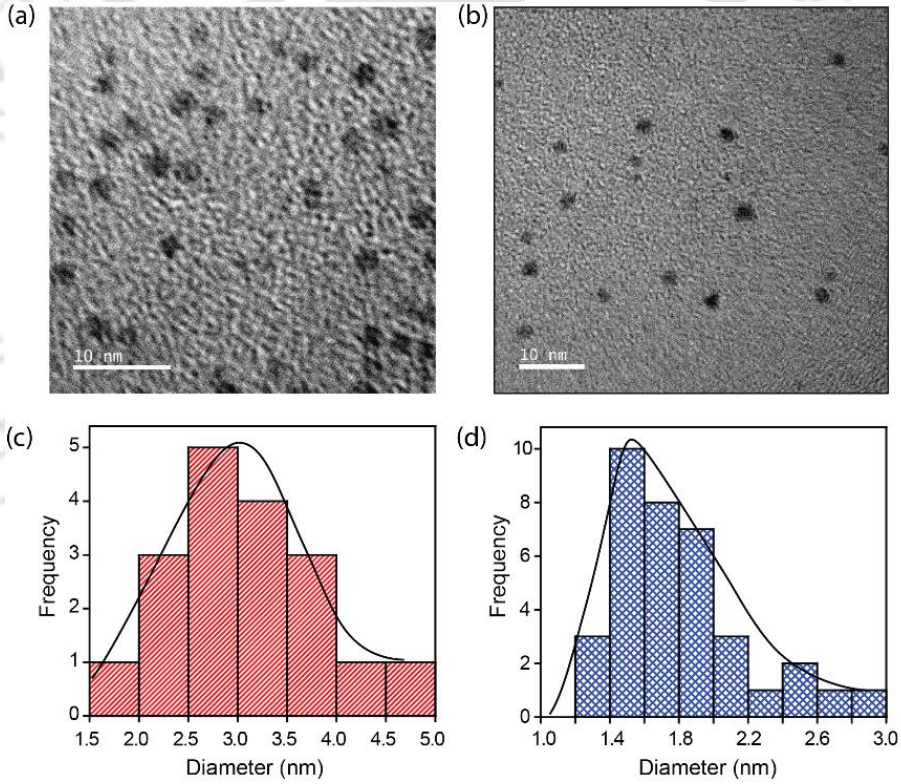


**Figure 4.3:** FETEM images of the AuNCs: (c) RF Cat-AuNCs and (d) BF Cat-AuNCs. Histogram figures displayed size distributions of (e) RF Cat-AuCNs and (f) BF Cat-AuNCs.

Based on the above finding, we synthesized separately the two types of Cat-AuNCs, classifying them as RF Cat-AuNCs (dominant $\lambda_{em}$ :670nm) and BF Cat-AuNCs ($\lambda_{em}$ :460nm) with Au:protein molar ratio of 15 and 75, respectively and analyzed their spectral pattern (Fig 4.2a). The band gaps

discerned for the NCs were 2.06 eV (3.5%) for RF Cat-AuNCs and 2.97 eV (1%) for BF Cat-AuNCs (Fig 4.2b) with the corresponding Quantum yield (QY) shown in the parentheses.

The morphology of the two clusters was analyzed by using FETEM (Fig 4.3a,b). The average sizes of the RF Cat-AuNCs and BF Cat-AuNCs discerned from the histogram analysis using ImageJ software were 3 nm and 1.5 nm, respectively (Fig 4.3c,d). Thus, the size of the blue emission cluster was nearly half of the red emission one.

The spherical jellium model has been widely used for emission energy and the energy level spacing in nanoclusters (Thungon et al., 2020). According to this model, the size of the nanoclusters is related to the emission energy by $E_f/N^{1/3}$. Where $E_f$ is the Fermi energy of the bulk metal and N is the number of atoms in a cluster. Therefore, as the number of atoms (and hence size) increases, the emission energy decreases and redshift occurs (Kawasaki et al., 2011; Zheng et al., 2004). The results comply well with the model, the smaller BF Cat-AuNCs emitted at shorter wavelengths ($\lambda_{em}$ 460nm), while the larger one (RF Cat-AuNCs) emitted at longer wavelengths (dominant at $\lambda_{em}$ 670nm). The size characteristics of the NCs that emitted at ~$\lambda_{455nm}$ and ~$\lambda_{670nm}$ were previously reported as $Au_8$NCs and $Au_{25}$NCs, respectively (Kawasaki et al., 2011; Xie et al., 2009). The emission wavelength of the RF Cat-AuNCs is closer to the previously reported Cat-AuNCs (Meng et al., 2018) and other red emission NCs such as BSA-$Au_{25}$NCs (Wang et al., 2011;Xie et al., 2009), HSA-$Au_{25}$NCs (Santhosh et al., 2014; Santhosh et al., 2016), and lysozyme-$Au_{25}$NCs (Wei et al., 2010; Xie et al., 2010). Whereas, the emission characteristics of BF Cat-AuNCs is closer to that of blue pepsin-$Au_8$NCs (Kawasaki et al., 2011), dendrimer-$Au_8$AuNCs (Zheng et al., 2004; Zheng et al., 2003), polymer-AuNCs (Huang et al., 2012) as well as BSA-$Au_8$NCs (Le Guével et al., 2011). Correlating the above facts, we assume the number of Au atoms present in BF Cat-AuNCs and RF Cat-AuNCs were 8 and 25, respectively.

The blue emission Cat-AuNCs with however, dual emission characteristics ($\lambda_{490nm}$ and $\lambda_{650nm}$), has been previously reported where the cause of the blue emission ascribed to the protein's amino acid residues (Meng et al., 2018). Similarly, the blue emission ($\lambda_{450nm}$) characteristics of HRP-AuNCs has also been ascribed to the amino acids of the protein (Wen et al., 2011). However, few other reports have attributed to the size or conformation of the proteins to form the small size blue emissions NC. Blue emitting ($\lambda_{em}$ 455nm, $\lambda_{ex}$ 380nm) lysozyme stabilized AuNCs were formed because of the compact protein conformation at low pH of 3 that act as smaller templates to produce the smaller NCs ($Au_8$NCs) (Chen and Tseng, 2012). Whereas, upon elevating the pH, the proteins become denatured, resulting in larger space within the structures that stabilizes larger NC ($Au_{25}$NCs) (Chen and Tseng, 2012). In another study, pepsin was used to stabilize AuNCs. By varying the pH

conditions as shown in the brackets, blue (pH 9), green (pH 1) and red (pH 12) emitting AuNCs were prepared (Kawasaki et al., 2011). Here, the emissions for the red $Au_{25}$NCs at $\lambda_{670nm}$, green $Au_{13}$NCs at $\lambda_{510nm}$, and blue $Au_5$NCs and $Au_8$NCs at $\lambda_{480nm}$ were documented. The authors postulated that the red fluorescent $Au_{25}$NCs were stabilized by the weak-bonding random-coiled structures of the protein formed at elevated pH conditions, producing larger space within the protein matrix for accommodating more gold atoms to form $Au_{25}$NCs (Kawasaki et al., 2011). At lower pH, the stabilization of $Au_8$NCs was due to autolysis of pepsin creating small internal spaces for stabilizing smaller clusters. Similarly, a blue-fluorescent BSA-$Au_8$NCs ($\lambda_{em}$ 450nm) was prepared by controlling the pH condition during the synthesis(Le Guével et al., 2011), where BSA-$Au_{25}$NCs at pH 11 and BSA-$Au_8$NCs at pH 8 were prepared. Most of the previous reports indicate that the blue fluorescent NCs in the stabilizing protein are due to the smaller NC sizes, mainly the $Au_8$, rather than the autofluorescence properties of the proteins.

We confirmed the presence of the smaller NCs by two methods. One with analysis of the intrinsic blue fluorescence characteristics by the tryptophan (trp) emission spectra by exciting the Cat-AuNCs at $\lambda_{295nm}$, because at this wavelength the interference from tyrosine (tyr) fluorescence is nullified (Yang et al., 2015). Moreover, the trp fluorescence is highly sensitive to the local environment, and hence, changes in its emission spectra, which may be quenching of intensity or shifting of spectra (Ghisaidoobe and Chung, 2014; Möller and Denicola, 2002), indicate the changes in protein conformations. Catalase contains 8 trp residues (Goodsell, 2004) and we observed an emission peak at $\lambda_{330nm}$ when excited at $\lambda_{295nm}$ (Fig 4.4a). When catalase was treated with NaOH, a shift of the emission peak to $\lambda_{345\ nm}$ occurred, which is due to the change in the secondary structure of the protein caused by its denaturation at high pH condition as seen from the CD spectra (Table 4.1). In case of RF Cat-AuNCs, the emission peak position remained same with the alkali treated catalase (Fig 4.4a). Interestingly, in case of BF Cat-AuNCs, apart from the peak at $\lambda_{345\ nm}$ due to trp emission, a new intense peak at $\lambda_{410nm}$ was also emerged. A minor broadening of shoulder at ~ $\lambda_{410nm}$ occurred for RF Cat-AuNCs can also been ascribed to the formation of meagre amount of BF-Cat-AuNCs with it, that is also seen from the less intense peak at ~$\lambda_{460nm}$ were generated when RF Cat-AuNCs was excited $\lambda_{370nm}$ (Fig 4.2a) This confirms that the blue clusters are responsible for this new peak at $\lambda_{410nm}$ when excited at trp wavelength. Another simple fluorescence spectral study was performed as reported earlier (Le Guével et al., 2011), where the emission at $\lambda_{370nm}$ of the controls with the clusters were compared. We found that the controls did not show a typical fluorescence of BF Cat-AuNCs with a peak at $\lambda_{460nm}$ (Fig 4.3b) Hence, we confirm that the emission peak at at $\lambda_{460nm}$ is due to the smaller blue clusters and not the auto-luminescence of the amino acids.

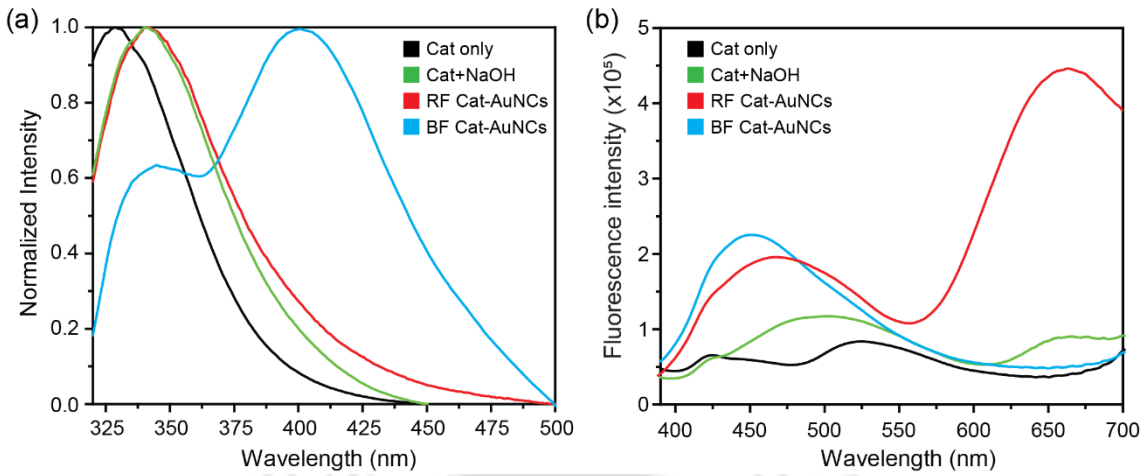


**Figure 4.4:** Emission of spectra of catalase under different conditions when excited at (a) $\lambda_{295nm}$ and (b) $\lambda_{370nm}$.

### *4.3.2. Impact of protein secondary structure on the formation of AuNCs*

Catalase primarily consists of two structural features, the α-helix and *β*-sheets which are bound together by a long wrapping loop (Collins and Dawson, 2013). When the enzyme was treated with NaOH, the *α*-helix structures reduced from 21.3% to 7.8%, while the *β*-sheets increased from 15.2% to 29.5% (Table 4.1). During the synthesis, catalase was first treated with two different concentrations of $Au^{3+}$ solution, 1 mM, and 5 mM, followed by treatment with NaOH and incubation at 60 ℃. Catalase treated with 1 mM $Au^{3+}$ solution contained 14.3% *α*-helix structures and 23.8% *β*-sheets while the solution treated with 5 mM $Au^{3+}$ solution contained 11.2% *α*-helix structures and 26.4% *β*-sheets (Table 4.1). The *β*-sheets structure was more in latter solution because of its pH was lower than the former. The impact of pH on the secondary structures is known, and even a slight lowering of pH could lead to more *β*-sheet structures in proteins (Chance, 1952; O'Brien et al., 2012). As NaOH was added and the clusters were formed, the pH of both the AuNCs solution attained a similar value but the percentage of *β*-sheet contents of the protein was increased slightly in BF Cat-AuNCs than RF Cat-AuNCs (Table 4.1).

Previous reports suggested that the smaller NCs ($Au_8$) are formed within small internal spaces of the protein but there has been no mention of *β*-sheets structures. To understand the role of *β*-sheet structures in protein on the formation of BF clusters, we synthesized AuNCs using silk fibroin (SF) proteins, which is well-known for its *β*-sheet dominant structures, the percentage of which varies with extractions and treatments (Kaushik et al., 2020). Following the synthesis procedure as discussed above, where the SF solution was treated sequentially with NaOH and $Au^{3+}$ (2.5 mM) solution, the synthesized SF-AuNCs exhibited white bluish fluorescence under UV light and had an

emission peak at $\lambda_{405nm}$ (excitation at $\lambda_{340nm}$) (Fig 4.5a), which is correspond to $Au_5$NCs (Kawasaki et al., 2011). The formation of smaller NCs in SF with an average size of 1.2 nm was confirmed by FETEM (Fig 4.5b). Notably, when $Au^{3+}$ (2.5 mM) was added to SF+NaOH solution, the *β*-sheet content increased more than that of the native SF. Under low pH conditions, SF solutions develop higher amount of *β*-sheet structures and turn into gel (Das and Dhar, 2014). Our findings corroborated to the report that decreasing pH of the reaction solution (by adding $Au^{3+}$), the *β*-sheet structures of the SF increased (Table 4.1). Thus, smaller $Au_8$NCs were stabilized within the β-sheet structures of catalase at comparatively lower pH generated by increasing the $Au^{3+}$ concentration from 1 mM to 5 mM in the reaction medium. At 1 mM $Au^{3+}$ concentration more (comparing to BF AuNCs) helix, turn and random coils are generated in catalase protein in RF-AuNCs (Table 4.1). There are several basic studies on the formation of AuNCs in different protein matrices such as Lysozyme (VI) (Chen and Tseng, 2012), BSA (Le Guével et al., 2011), and pepsin (Kawasaki et al., 2011). A critical finding by Kawasaki et al. indicated that the random coiled pepsin structures stabilizes $Au_{25}$NCs (Kawasaki et al., 2011), supporting our findings on the stabilization of $Au_{25}$NCs in the catalase proteins. Regarding the transformation from RF to BF AuNCs observed in the present studies, the pH led structural transition of the catalase protein in the initial reaction solution as elaborated above, has been attributed as the most plausible reason.

**Table 4.1**: The secondary structural transitions of catalase occurred under different treatment conditions.

| **Samples/ Structures** | **Catalase (native)** | **Catalase+ NaOH** | **Catalase+ 1mM $Au^{3+}$** | **RF Cat-AuNCs** | **Catalase+ 5mM $Au^{3+}$** | **BF Cat-AuNCs** |
|---|---|---|---|---|---|---|
| ***α*-Helix** | 21.3 | 7.8 | 14.3 | 5.4 | 11.2 | 6 |
| ***β*-Sheets** | 15.2 | 29.5 | 23.8 | 29.1 | 26.4 | 30.1 |
| **Turns** | 19.4 | 19.1 | 19.2 | 21.6 | 19.6 | 20.2 |
| **Randoms** | 44.1 | 43.5 | 42.8 | 43.8 | 42.8 | 43.1 |
| **pH** | 7 | 12.8 | 3.7 | 12.03 | 2.3 | 12.2 |

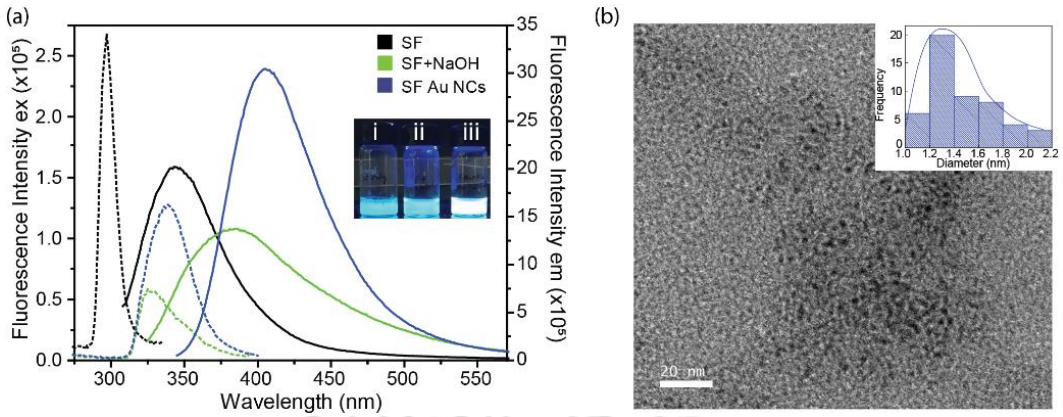


**Figure 4.5:** (a) Excitation and emission spectra of SF, SF+NaOH and SF-AuNCs (inset: (i) SF, (ii) SF+NaOH, (iii) SF-AuNCs under UV illumination); (b) TEM image of SF-AuNCs (inset: histogram of the cluster sizes).

### *4.3.3. Enzyme activity study of Cat-AuNCs*

The alkaline (>pH 11) treatment involved during the AuNCs preparation process released the prosthetic heme group from the catalase protein as evident from the lack of typical heme absorbance at $\lambda_{400nm}$ (Gouterman, 1961) in the spectra (Fig 4.6a). The treatment affected the structural integrity of the protein as evident from the drastic change in its secondary structural components (Table 4.1). No residual catalase activity was detected in the NaOH treated catalase proteins and the two Cat-AuNCs as no change in $H_2O_2$ absorbance at $\lambda_{240nm}$ was detected in these cases (Fig 4.6b). Worth mentioning, the heme group is the active site of the catalase enzyme where the catalytic oxidation of $H_2O_2$ takes place (Goodsell, 2004). Hence, we infer that the loss of structural integrity of the catalase protein at high pH condition led to the release of heme and thus deactivating the enzyme. Therefore, we can safely conclude that any change of optical response for $H_2O_2$ due to its interaction with Cat-AuNCs was not a catalase enzyme-based process.

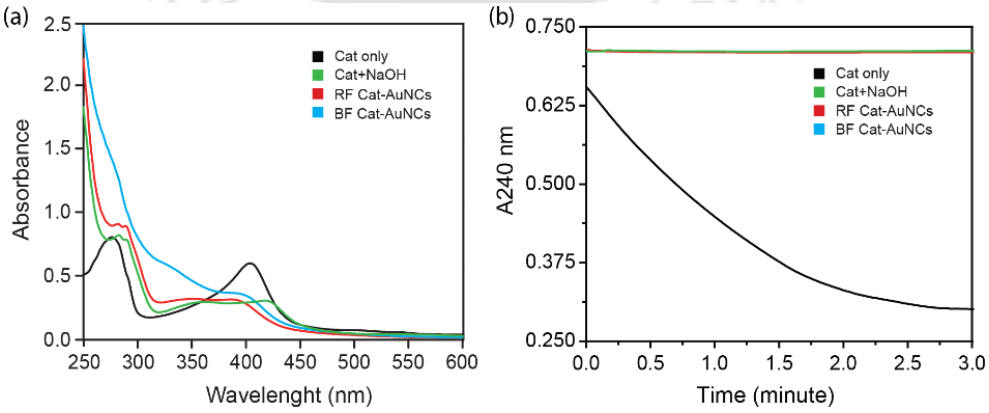

**Figure 4.6**: (a) Spectral characteristics of the native and different treated catalase proteins to probe the presence of heme group. (b) Catalase activity of the native and different treated catalase proteins.

### *4.3.4. Interaction study between Cat-AuNCs and $H_2O_2$*

The Cat-AuNCs were incubated with different concentrations of $H_2O_2$, and the fluorescence intensity of the reaction solutions was recorded after 10 mins of incubation. RF Cat-AuNCs showed a decrease in fluorescence intensity at $\lambda_{670nm}$ while the intensity at ~ $\lambda_{460nm}$ increased marginally with the increasing concentration of $H_2O_2$ and stabilized after 1M $H_2O_2$ (Fig 4.7a,b). In case of BF Cat-AuNCs, the intensity at $\lambda_{460nm}$ increased marginally with the concentration of $H_2O_2$ and precariously stabilized after 150 mM of $H_2O_2$ (Fig 4.7c,d). Again at $\lambda_{670nm}$, these BF Cat-AuNCs exhibited an unsteady decrease in intensity of a lower magnitude with the increasing concentration of $H_2O_2$ (Fig 4.7d). The increase $\lambda_{460nm}$ peak intensity in both RF and BF Cat-AuNCs, could be because of the changes in the protein structure (Table 4.2), which led to an increase in its intrinsic fluorescence slightly.

Interestingly, when the BF Cat-AuNCs were allowed to react with $H_2O_2$ and then stored for 5 hours in MQ at 25 ℃, red color was developed, the intensity of which was increased with the increasing $H_2O_2$ concentration (Fig 4.8b inset). The absorbance study revealed a localised surface plasmon resonance (LSPR) band at $\lambda_{520nm}$, indicating the formation of gold nanoparticles (AuNPs). No similar phenomenon was observed in the case of RF Cat-AuNCs (Fig 4.8a).

The excited lifetimes ($\tau$) of RF Cat-AuNCs in the absence and presence of 100 mM $H_2O_2$ were found to be 3.93 ns and 2.68 ns, respectively (Fig 4.8c). The results show that the interaction of the RF AuNCs with $H_2O_2$ is a dynamic process and occurred with the excited state of the NCs leading to the quenching phenomena (Lakowicz, 2000).

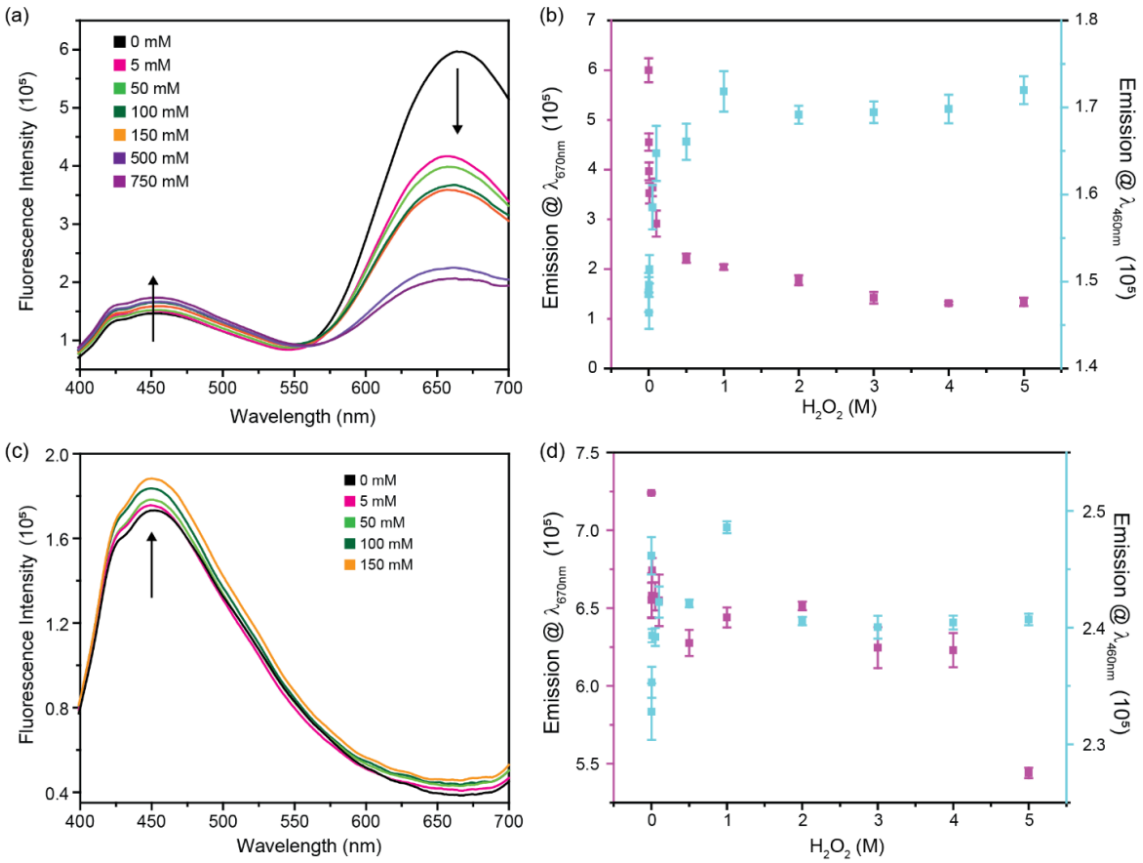


**Figure 4.7**: Fluorescence intensity profile of (a) RF Cat-AuNCs and (c) BF Cat-AuNCs with different concentrations of $H_2O_2$. Corresponding emission intensity of $\lambda_{670nm}$ (pink) and $\lambda_{460nm}$ (blue) with the concentration of $H_2O_2$ for (b) RF Cat-AuNCs and (d) BF Cat-AuNCs.

In the case of BF Cat-AuNCs, there was no formation of RF-Cat-AuNCs during the interaction process of BF Cat-AuNCs with $H_2O_2$, as the emission at $\lambda_{670nm}$ did not increase, rather it was decreased (Fig 4.7b). The excited lifetimes ($\tau$) of BF Cat-AuNCs in the absence and presence of 100 mM $H_2O_2$ were found to be 3.96 ns and 3.98 ns, respectively (Fig 4.8d). Thus, the lifetime of BF AuNCs did not change in presence of even high $H_2O_2$ concentration, indicating that $H_2O_2$ is not interacting with the excited state of the BF Cat-AuNCs and hence no dynamic process is involved in the interaction with these NCs.

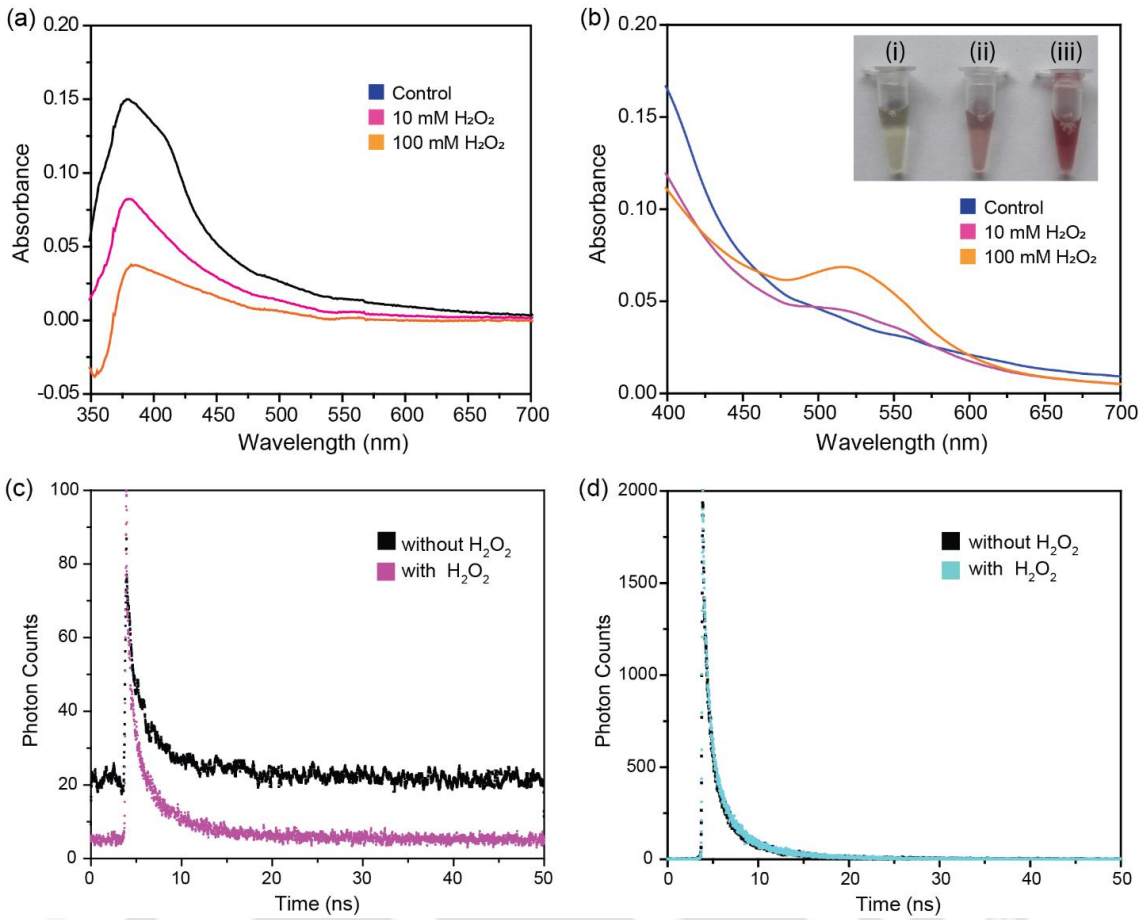


**Figure 4.8**: (a) Absorbance spectra of (a) RF Cat-AuNCs and (b) BF Cat-AuNCs (inset: Photograph on color developed with nil (i), 10 mM (ii), and 100 mM (iii) $H_2O_2$) after incubation at 25 °C for 5 hours with different concentrations of $H_2O_2$. Fluorescence decay of the (c) RF Cat-AuNCs (emission at $\lambda_{670nm}$) without (black) and with (pink) 100 mM $H_2O_2$ and (d) BF Cat-AuNCs (emission $\lambda_{460nm}$) without (black) and with (light blue) 100 mM $H_2O_2$ as a function of time. The excitation in both cases was at $\lambda_{375nm}$.

DLS-based zeta potential measurements were performed to further understand the mechanism of the interactions. The zeta potential data revealed a negative charge of −23.8 ± 9.1 mV and -35.1 ± 11.8 mV for the RF Cat-AuNCs and BF Cat-AuNCs. When the AuNCs were treated with 100 mM $H_2O_2$, the zeta potential of RF Cat-AuNCs reduced to -21.4 ± 9.2 mV and that of BF Cat-AuNCs also reduced to -20.4 ± 12.7 mV. This suggested there could be electrostatic mode of interaction between of $H_2O_2$ with the AuNCs, which is stronger for BF Cat-AuNCs (Δ zeta potential=14.7 mV) than RF Cat-AuNCs (Δ zeta potential=2.4 mV). These strong interactions of $H_2O_2$ with BF Cat-AuNCs might contribute to the aggregational transformation of these smaller AuNCs to NPs.

Finally, the morphological change in the Cat-AuNCs after interaction with 100 mM $H_2O_2$ was monitored using TEM. The RF Cat-AuNCs in absence of $H_2O_2$ were evenly distributed; however,

after the interaction, the NCs were agglomerated to form clumps (Fig 4.9 a,b). There were some larger clusters formed, but they did not lead to the formation of nanoparticles as is evident from the TEM image and absorbance data (Fig 4.8a). The BF Cat-AuNCs, instead, were grown to bigger dimensions to the level of nanoparticles with an average size of 10 nm after interacting with $H_2O_2$ (Fig 4.9 c,d). The result confirmed that in presence of $H_2O_2$ the protein $\beta$-sheet structure is significantly disrupted leading to the transformation of BF Cat-AuNCs into nanoparticles through reorganization of the NCs originally present in the smaller spaces under the $\beta$-sheets. The probable mechanism of interaction between RF Cat-AuNCs and BF Cat-AuNCs has been depicted in Scheme 4.1.

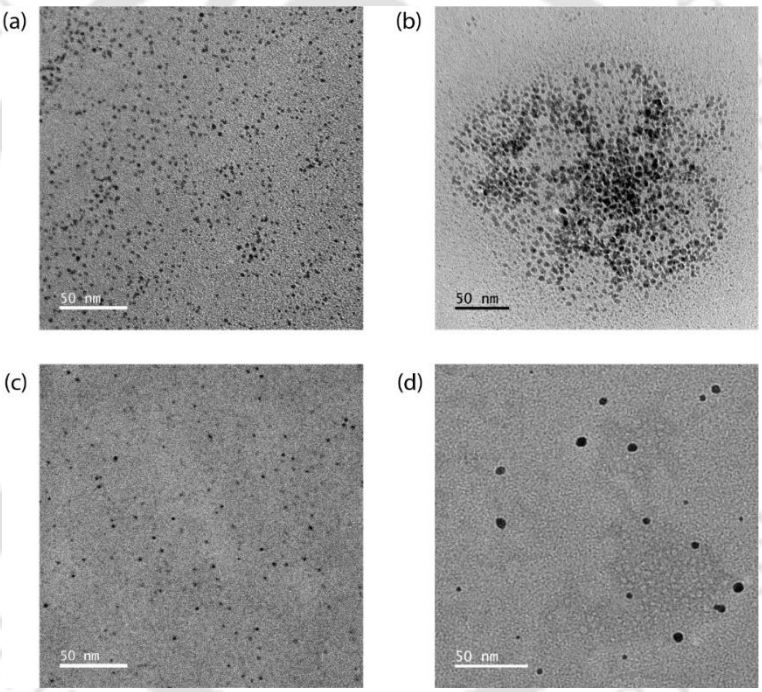


**Figure 4.9**: TEM images of RF Cat-AuNCs (a) without and (b) with 100 mM $H_2O_2$; and BF Cat-AuNCs (c) without and (d) with 100 mM $H_2O_2$.

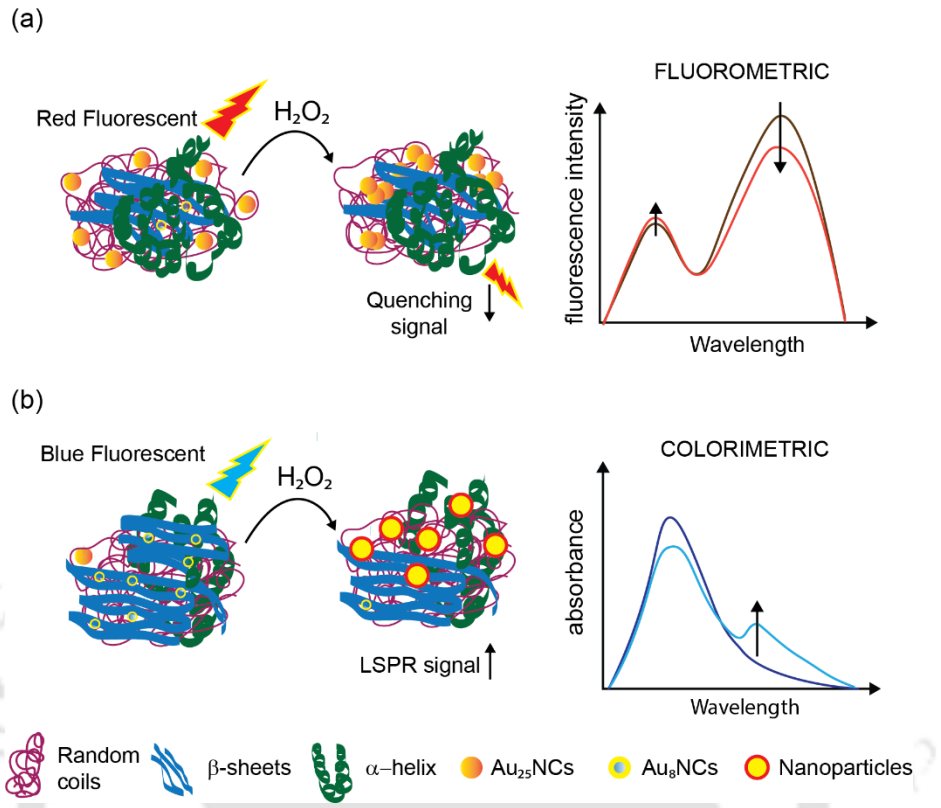


**Scheme 4.1:** Interaction mechanism of $H_2O_2$ with (a) RF Cat-AuNCs and (b) BF Cat-AuNCs.

### *4.3.5. Cat-AuNC as an optical probe for detection of $H_2O_2$*

4.3.5.1 Fluorescence-based detection of $H_2O_2$

RF Cat-AuNCs were selected as the fluorescent probe for the detection of $H_2O_2$ because of its dual fluorescence signals, intensity decreased at $\lambda_{670nm}$ and increased at $\lambda_{460nm}$ with the increasing concentration of $H_2O_2$ leading to the development of a ratiometric intensity-based detection system. Ratiometric fluorescence intensity signals have an advantage over relative fluorescence intensity signals because the former method could nullify the photobleaching and the changes due to environmental effects (Wang et al., 2012a). Different concentrations of $H_2O_2$ were incubated with AuNCs at 25 ℃ for 10 minutes and the fluorescence intensity at $\lambda_{460nm}$ ($I_{460nm}$) and intensity at $\lambda_{670nm}$ ($I_{670nm}$) were monitored. The quenching of the red fluorescence with the emergence of a blueish fluorescence could be observed even with naked eyes when the samples were placed under UV light (Fig 4.10a inset). A dynamic response plot of $I_{460nm}/I_{670nm}$ against the concentration of $H_2O_2$ was prepared (Fig 4.10a). A linear calibration plot ($y = 0.0061x + 0.26$) with lower $H_2O_2$ concentration range from the response plot was constructed (Fig 4.10b). The LoD of 0.6 mM and a linear range of 1-50 mM ($R^2 = 0.99$) for $H_2O_2$ were discerned.

The fluorescence quenching phenomena of the catalase and HRP stabilized AuNCs were previously explored for detection of $H_2O_2$, where the quenching events were reported as the catalytic activity of the respective enzymes being used as stabilizing matrices for the NCs (Meng et al., 2018; Wen et al., 2011). In this report, since the catalytic function of the enzyme has been nullified during the process of preparing the NCs, hence the cause of quenching the fluorescence has been solely credited to the NCs-based photophysical phenomenon.

4.3.5.2 Colorimetry-based detection of $H_2O_2$

The SPR phenomenon developed as a result of the interaction between BF Cat-AuNCs and $H_2O_2$ was exploited to detect $H_2O_2$ colorimetrically using the NCs as an optical probe. The SPR band intensity at $\lambda_{520nm}$ increased with the increasing concentration of $H_2O_2$ (Fig 4.10c). A calibration plot was constructed using the lower concentration range of $H_2O_2$ which gives a linear response (Fig 4.10d). An LoD of 1 mM, and a linear detection range of 20-200 mM ($R^2$=0.99) were discerned for $H_2O_2$. Interestingly, the reaction could be accelerated to develop the red color in a short period (30 minutes) by increasing the incubating temperature to 60 ℃ for the reaction. Moreover, the color change could be easily observed even with the naked eyes (Fig 4.10c inset) which have, thus potential to develop an optical biosensor for $H_2O_2$ with yes/no format. This elevated temperature did not have any influence on transforming the NCs to NPs without $H_2O_2$ even after incubating the solution for 12 hours at the temperature. Further, the optical properties of the BF Cat-AuNCs did not change following this heat treatment, indicating its high photostability up to this temperature and thus its suitability for developing point-of-care sensors

The photostability of both the AuNCs over storage time was analyzed. RF Cat-AuNCs could retain 80 % of the initial fluorescence intensity even after 2 months, whereas BF Cat-AuNCs retained 90 % its initial fluorescence after 2 months when both were stored at 4 ℃. The AuNCs stored in 25 ℃ however, lost almost 50 % of their optical properties after 1 month.

The methods presented here offer an unprecedented wide linear detection range with albeit low sensitivity compared to the other methods. Other stark advantages of the present techniques are the dual detection scope by using the Cat-AuNCs as fluorometric and colorimetric probes and label-free colorimetric detection using BF Cat-AuNCs probe as no conventional chromogenic agents such as TMB and ABTS are required for the assay. Further, the SPR phenomenon-based colorimetric method has further scope to develop as a simple $H_2O_2$ biosensor with a yes/no format as the color response could be easily identified through the naked eye.

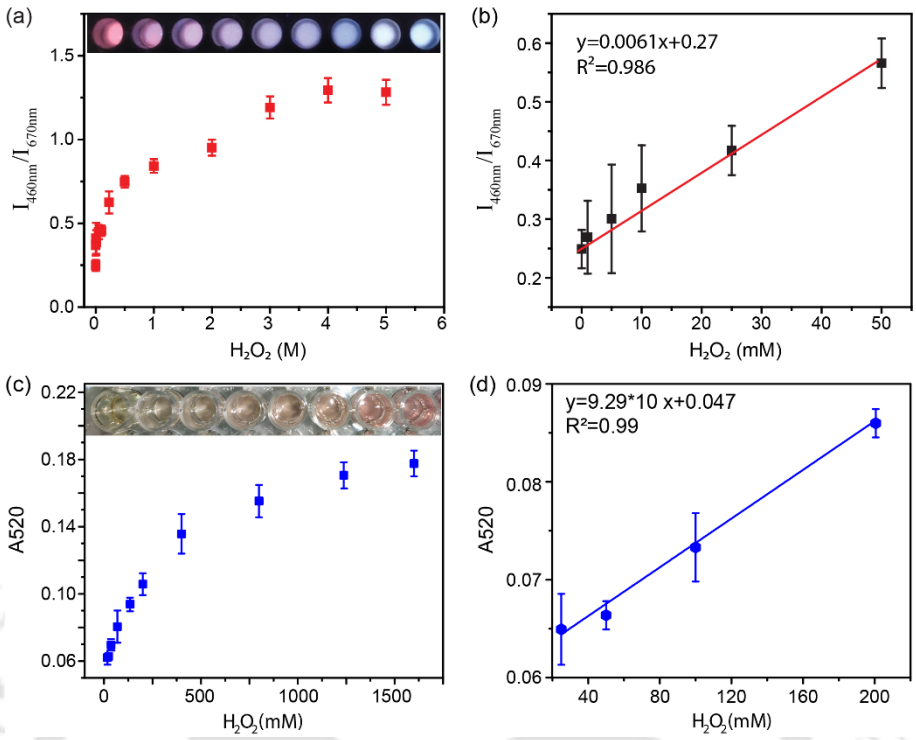


**Figure 4.10**: (a) Response curve for $H_2O_2$ using RF Cat-AuNCs as a fluorescence probe (Image: RF Cat-AuNCs treated with increasing $H_2O_2$ concentration under UV light). (b) Calibration plot for $H_2O_2$ sensing using RF Cat-AuNCs as fluorescence probe. (c) Response curve for $H_2O_2$ using BF Cat-AuNCs as a colorimetric probe (Image: BF Cat-AuNCs treated with increasing $H_2O_2$ concentration under visible light). (d) Calibration plot for $H_2O_2$ sensing using BF Cat-AuNCs as colorimetric probe.

### 4.4. Conclusion

The present work demonstrated the successful transmuting of catalase to non-enzymatic $H_2O_2$ sensing function by expelling the heme prosthetic group from the catalase protein and inducting AuNCs in the protein matrix through a method of simple two-step chemical procedure. The $H_2O_2$ sensing functions were acquired due to the formation of two different AuNCs in the catalase protein matrix, denoted as RF Cat-AuNCs (red fluorescent) and BF Cat-AuNCs (blue fluorescent), of distinct sizes and photophysical properties. Interestingly, the formation of the NCs was dependent on the concentration of the precursor $Au^{3+}$ solutions, at a lower concentration RF Cat-AuNCs of bigger sizes (3 nm) and at a high concentration BF Cat-AuNCs of smaller sizes (1.5 nm) were formed. This study also unveiled the possible role of the secondary structure of the catalase protein on the synthesis of these two AuNCs in the protein matrices, where the increase in $\beta$-sheet structures of the protein due to the initial pH of the synthesis process is likely to facilitate the synthesis of BF Cat-AuNCs. Another novel finding that emerged from this investigation is that BF Cat-AuNC quantum dots are

transformed into plasmonic nanoparticles (NPs) upon their interaction with hydrogen peroxide. This phenomenon could be translated to designing an analytical method for sensitive colorimetric detection of the peroxide without using any external colorimetric labels (such as TMB and ABTS). Additionally, a dynamic quenching-based interaction of RF Cat-AuNCs with $H_2O_2$ was translated to develop an analytical method for determining the peroxide. Both these fluorometric and colorimetric approaches offered a wide linear concentration range for the detection of $H_2O_2$. These Cat-AuNCs probes may be highly promising for determining hydrogen peroxide in various samples following the developed fluorometric and colorimetric approaches.

# CHAPTER V

## CONCLUSIONS AND FUTURE DIRECTIONS OF RESEARCH

# Chapter V
# Conclusions and future directions of research

The main goal of the present work was to explore new strategies for developing rapid, sensitive, functionally stable, and portable hydrogen peroxide ($H_2O_2$) sensors. The focus was on the optical transduction principles considering some traits that support the development of simple, cost-effective and portable sensing devices. To achieve this goal, three independent proofs-of-concept were successively explored. (i) A carboxy-functionalized water-soluble pH-sensitive organic dye, **c-P4VB** was investigated first for the fluorometric detection of $H_2O_2$ using chromatographic paper as the support material. The concept was then protracted to detect alcohol by coupling alcohol oxidase (AOx) to the paper platform. (ii) Next, we explored silk-fibroin (SF) film as a platform for immobilization of the peroxidase enzymes along with the chromogen (ABTS) for colorimetric detection of $H_2O_2$. This concept was also linked to detecting alcohol by coupling AOx to the detection platform, and lastly, (iii) Catalase protein stabilized AuNCs were explored as fluorometric as well as colorimetric probes for the detection of $H_2O_2$. The key findings of these studies are briefly described below.

Firstly, a novel carboxy-functionalized organic fluorophore, sodium 6-(4-methoxy-2,5-bis((E)-2-(pyridin-4-yl)vinyl)phenoxy)hexanoate or **c-P4VB** was synthesized and explored for developing a simple $H_2O_2$ sensor. The chemical nature of the dye renders it water soluble, pH-sensitive, and sticky to the cellulose fibres in the chromatographic paper. The dye responded to $H_2O_2$, which is a weak acid, through strong fluorescence spectral shifts. A better selectivity of the dye towards $H_2O_2$ could be achieved and the reason has been ascribed to its substrate ($H_2O_2$) induced aggregation behaviour. The dye was then immobilized onto chromatographic paper to develop a sensitive and photo-stable **c-P4VB** paper-based $H_2O_2$ sensor. The application of the as-prepared peroxide sensing **c-P4VB**-paper was further extended to develop an alcohol biosensor using AOx that catalyses the formation of $H_2O_2$ in presence of the substrate alcohol. The biosensor was fabricated as a novel µPAD and successfully tested commercially available samples to validate its function.

Secondly, a colorimetric $H_2O_2$ biosensor was developed by using SF films as an immobilization support system for peroxidase enzymes (HRP) and reagents (ABTS). The concept was then translated to detect alcohol by coupling the enzyme AOx to the sensor platform with HRP. These films were

made non-dissolvable for the enzymes and dissolvable for the ABTS. Interestingly, the SF film not only performed as an immobilization matrix but also took part in the reaction in transducing the chromogen color into an intense purple one instead of the usual green color. The formation of dicationic ABTS radicals in the reaction has been made responsible for this atypical purple color on the sensing platform. The enzymes and reagent immobilized SF films were then assembled with chromatographic paper strips and successfully developed a hybrid µPAD methanol biosensor. This bi-enzyme SF film could retain unprecedented high activity (90%) of the AOx until 40 days of storage at 4 ℃. The next positive trait that could be introduced in the developed µPAD device is the void of the coffee ring effect in the detection zone enacted by incorporating wave-designed microfluidic channels in the spacer paper surface. The waved micro-channels facilitated the uniform distribution of the dye particles and samples across the paper spacer zone that in turn enabled uniform contact of these reactants with the enzyme particles for homogeneous color distribution over the detection film. The coffee ring-free detection film abetted error-free capture of pixel signal for quantitative detection of methanol. This finding is expected to spur further advances in the developed sensor to couple smart phone as a peripheral system for its onsite applications.

In the final proof of concept, catalase protein stabilized AuNCs were synthesised through a mild heat-driven synthesis process and explored for their non-enzymatic $H_2O_2$ sensing function. We successfully transmuted catalase to non-enzymatic $H_2O_2$ sensing function by releasing the heme prosthetic group from the protein and stabilizing the AuNCs in the Apo protein matrix. Two different AuNCs were formed in the protein matrix, denoted as RF Cat-AuNCs (red fluorescent) and BF Cat-AuNCs (blue fluorescent). They were of distinct sizes and photophysical properties, which depend on the concentration of the precursor $Au^{3+}$ solutions added during the synthesis procedure which impacts the initial pH of the solution. At the lower concentration of $Au^{3+}$ (pH 3.7), RF Cat-AuNCs of bigger sizes (3 nm) and at high concentrations $Au^{3+}$ (pH 2.3) BF Cat-AuNCs of smaller sizes (1.5 nm) were formed. Our study also unveiled the possible role of the secondary structure of the catalase protein on the synthesis of these two AuNCs in the protein matrices due to the initial pH, where the $\beta$-sheet structures of the protein are likely to facilitate the synthesis of BF Cat-AuNCs. The role of the $\beta$-sheet structures was further endorsed by the findings of synthesized SF-AuNCs that exclusively produced blue fluorescent with smaller cluster size (1.2 nm). Another novel finding that emerged from this study is the transformation of BF Cat-AuNC quantum dots into plasmonic nanoparticles (NPs) upon their interaction with $H_2O_2$. This phenomenon is advantageous to design an analytical method for sensitive colorimetric detection of the peroxide without using any external colorimetric labels (such as TMB and ABTS), thus making this sensor with lesser reagents. Additionally, a dynamic quenching-based interaction of RF Cat-AuNCs with $H_2O_2$ was translated to develop an

analytical method for determining the peroxide. Both these fluorometric and colorimetric approaches offered a wide linear concentration range for detection of $H_2O_2$. The performance factors of the sensors developed in this work are presented in table 5.1.

**Table 5.1:** Critical performance factors of the $H_2O_2$ detection methods developed through this thesis work.

| **Detection method** | | **Detection platform** | **LoD (mM)** | **Dynamic Range (mM)** | **Reaction time** |
|---|---|---|---|---|---|
| **Organic dye** | Fluorometric (emission shift) | **c-P4VB** paper sensor | 16.7 | 16.7 – 2900 | 10 secs |
| **Enzyme** | Colorimetric (pixel intensity) | HRP-SF film | 0.6 | 0.6-300 | 1 min |
| **AuNCs** | Fluorometric (Quenching) | RF Cat-AuNCs | 0.6 | 0.6-3000 | 10 mins |
| | Colorimetric (pixel intensity) | BF Cat-AuNCs | 1 | 1-1600 | 30 mins (60 ℃) |

As seen from the table, the LoD for $H_2O_2$ is the best for HRP-SF-based colorimetric sensor followed by the fluorescence-based RF Cat-AuNCs sensor. The dynamic range was the widest for the fluorescence-based RF Cat-Au NCs method. In terms of reaction time, **c-P4VB** paper-based fluorescence sensor is the fastest one. Even though all the performance parameters for each of these methods are not as good as many of the methods reported in the literature, some critical findings achieved through this work shed new light on this direction, some of which are mentioned above. In the organic dye-based method the selective response signal in the form of fluorescence colour shift is interesting and can be explored further to develop a low-cost simple peroxide sensor that is otherwise difficult to achieve with a single wavelength band as a signal. For the peroxidase-based system, the stability of the AOx enzyme attained a new height confirming the high potential of SF-film as a robust biocompatible immobilization substrate for developing biosensors for real-world applications. Further, this work demonstrates the effectiveness of dissolvable SF-film for immobilization of ABTS prompting its potential to develop a reagent-free system for constructing the µPAD. Lastly, transmuting catalase to non-enzymatic $H_2O_2$ sensing catalysts by incorporating AuNCs in the protein matrix opened a new avenue for exploiting this strategy for developing sensors. Our finding on $H_2O_2$ induced transformation of the AuNCs to AuNPs gives an extra edge to the detection principle for designing a multifaceted approach for peroxide detection using Catalase

protein stabilized AuNCs as an optical probe. The major advantages of exploiting the AuNPs-based colorimetric detection comprises reagent-free detection as no separate chromogen is required to perform the test and scope for easy detection of the peroxide through visual observation of the plasmonic color.

The works embodied in this thesis require further investigation to improve the scope of the described strategies to develop biosensors for practical applications. Following are some major challenges that may be addressed in future research to fulfil the goals set in the direction.

(i) The signal interference in **c-P4VB**-based optical sensor needs to be reduced. A suitable chemical modification of the chromogen and its better immobilization strategies on the paper substrates may be explored to avert unwanted interferences.

(ii) The application of the peroxidase-based sensors may be extended to other analytes of clinical importance such as glucose and cholesterol using a similar set-up by including the appropriate oxidase enzymes to create a multiple detections platform for the μPAD biosensor. Similarly, the application of the catalase stabilized AuNCs need to be further explored for sensing other analytes such as alcohol or glucose.

(iii) The Catalase protein stabilized AuNCs-based concept needs to be translated to sensor platforms by adopting suitable immobilization strategies of these clusters onto different matrices for developing a standalone biosensor for on-site applications.

(iv) The proposed sensors should be coupled with a suitable app in Smartphone devices for their point of care and onsite applications.

# BIBLIOGRAPHY

# Bibliography

**Ainley, A.D., Challenger, F.,** 1930. Studies of the boron – carbon linkage . Part I . The oxidation and nitration of phenylboric acid. J. Chem. Soc. 2171–2180.

**Åkerström, B., Maghzal, G.J., Winterbourn, C., Kettle, A.J.,** 2007. The lipocalin α1 -microglobulin has radical scavenging activity. J. Biol. Chem. 282, 31493–31503. https://doi.org/10.1074/jbc.M702624200

**Ali, M., Tahir, M.N., Siwy, Z., Neumann, R., Tremel, W., Ensinger, W.,** 2011. Hydrogen peroxide sensing with horseradish peroxidase-modified polymer single conical nanochannels. Anal. Chem. 83, 1673–1680. https://doi.org/10.1021/ac102795a

**Alpeeva, I.S., Sakharov, I.Y.,** 2005. Soybean peroxidase-catalyzed oxidation of luminol by hydrogen peroxide. J. Agric. Food Chem. 53, 5784–5788. https://doi.org/10.1021/jf0506075

**Alzahrani, E.,** 2017. Colorimetric Detection Based on Localised Surface Plasmon Resonance Optical Characteristics for the Detection of Hydrogen Peroxide Using Acacia Gum–Stabilised Silver Nanoparticles. Anal. Chem. Insights 12, 20–22. https://doi.org/10.1177/1177390116684686

**Amorim, A.M., Gasques, M.D.G., Andreaus, J., Scharf, M.,** 2002. The application of catalase for the elimination of hydrogen peroxide residues after bleaching of cotton fabrics. An. Acad. Bras. Cienc. 74, 433–436. https://doi.org/10.1590/S0001-37652002000300006

**André, R., Natálio, F., Tremel, W.,** 2013. Chapter 6 - Nanoparticles as Enzyme Mimics, in: New and Future Developments in Catalysis, Editor: Steven L. Suib, Elsevier. pp. 149–173.

**Kumar A., S., Lo, P.-H., Chen, S.-M.,** 2009. Electrochemical Analysis of $H_2O_2$ and Nitrite Using Copper Nanoparticles/Poly(o-phenylenediamine) Film Modified Glassy Carbon Electrode. J. Electrochem. Soc. 156, E118. https://doi.org/10.1149/1.3129604

**Azevedo, A.M., Prazeres, D.M.F., Cabral, J.M.S., Fonseca, P.,** 2005. Ethanol biosensors based on alcohol oxidase. Biosens. Bioelectron. 21, 235–247. https://doi.org/10.1016/j.bios.2004.09.030

**Bai, Z., Li, G., Liang, J., Su, J., Zhang, Y., Chen, H., Huang, Y., Sui, W., Zhao, Y.,** 2016. Non-enzymatic electrochemical biosensor based on Pt NPs/RGO-CS-Fc nano-hybrids for the detection of

hydrogen peroxide in living cells. Biosens. Bioelectron. 82, 185–194. https://doi.org/10.1016/j.bios.2016.04.004

**Bihar, E., Deng, Y., Miyake, T., Saadaoui, M., Malliaras, G.G.,** 2016. A Disposable paper breathalyzer with an alcohol sensing organic electrochemical transistor. Sci. Rep. 27582, 2–7.

**Biswas, A., Banerjee, S., Gart, E. V., Nagaraja, A.T., McShane, M.J.,** 2017. Gold Nanocluster Containing Polymeric Microcapsules for Intracellular Ratiometric Fluorescence Biosensing. ACS Omega 2, 2499–2506. https://doi.org/10.1021/acsomega.7b00199

**Blum, L.J.,** 1993. Chemiluminescent flow injection analysis of glucose in drinks with a bienzyme fiberoptic biosensor. Enzyme Microb. Technol. 15, 407–411. https://doi.org/10.1016/0141-0229(93)90127-N

**Bocanegra-Rodríguez, S., Jornet-Martínez, N., Molins-Legua, C., Campíns-Falcó, P.,** 2020. New Reusable Solid Biosensor with Covalent Immobilization of the Horseradish Peroxidase Enzyme: In Situ Liberation Studies of Hydrogen Peroxide by Portable Chemiluminescent Determination. ACS Omega 5, 2419–2427. https://doi.org/10.1021/acsomega.9b03958

**Bungthong C, Wrigley C, Sonteera T, Siriamornpun S., 2021** Amino Acid Profile and Biological Properties of Silk Cocoon as Affected by Water and Enzyme Extraction. Molecules. 7;26(11):3455. doi: 10.3390/molecules26113455. PMID: 34200149; PMCID: PMC8201060

**Burmistrova, N.A., Meier, R.J., Schreml, S., Duerkop, A.,** 2014. Reusable optical sensing microplate for hydrogen peroxide using a fluorescent photoinduced electron transfer probe (HP Green). Sensors Actuators, B Chem. 193, 799–805. https://doi.org/10.1016/j.snb.2013.12.025

**Cai, K., Lv, Z., Chen, K., Huang, L., Wang, J., Shao, F., Wang, Y., Han, H.,** 2013. Aqueous synthesis of porous platinum nanotubes at room temperature and their intrinsic peroxidase-like activity. Chem. Commun. 49, 6024–6026. https://doi.org/10.1039/c3cc41880d

**Campomanes, P., Rothlisberger, U., Alfonso-Prieto, M., Rovira, C.,** 2015. The Molecular Mechanism of the Catalase-like Activity in Horseradish Peroxidase. J. Am. Chem. Soc. 137, 11170–11178. https://doi.org/10.1021/jacs.5b06796

**Cao, R., Pan, Z., Tang, H., Wu, J., Tian, J., Nilghaz, A., Li, M.,** 2020. Understanding the coffee-ring effect of red blood cells for engineering paper-based blood analysis devices. Chem. Eng. J. 391, 123522. https://doi.org/10.1016/j.cej.2019.123522

**Chakma, B., Jain, P., Singh, N.K., Goswami, P.,** 2016. Development of an Indicator Displacement Based Detection of Malaria Targeting HRP-II as Biomarker for Application in Point-of-Care Settings. Anal. Chem. 88, 10316–10321. https://doi.org/10.1021/acs.analchem.6b03315

**Chakraborty, I., Pradeep, T.,** 2017. Atomically Precise Clusters of Noble Metals: Emerging Link between Atoms and Nanoparticles. Chem. Rev. 117, 8208–8271. https://doi.org/10.1021/acs.chemrev.6b00769

**Chakraborty, S., Hill, A.L., Shirsekar, G., Afzal, A.J., Wang, G.L., Mackey, D., Bonello, P.,** 2016. Quantification of hydrogen peroxide in plant tissues using Amplex Red. Methods 109, 105–113. https://doi.org/10.1016/j.ymeth.2016.07.016

**Khazraji, A. C., Robert, S.,** 2013. Interaction effects between cellulose and water in nanocrystalline and amorphous regions: A novel approach using molecular modeling. J. Nanomater. 2013. https://doi.org/10.1155/2013/409676

**Chance, B.,** 1952. The effect of pH upon the equilibria of catalase compounds. J. Biol. Chem. 194, 483–496. https://doi.org/10.1016/s0021-9258(18)55800-2

**Chang, J., Li, H., Hou, T., Duan, W., Li, F.,** 2018. Paper-based fluorescent sensor via aggregation induced emission fluorogen for facile and sensitive visual detection of hydrogen peroxide and glucose. Biosens. Bioelectron. 104, 152–157. https://doi.org/10.1016/j.bios.2018.01.007

**Chang, Y., Zhang, Z., Hao, J., Yang, W., Tang, J.,** 2016. BSA-stabilized Au clusters as peroxidase mimetic for colorimetric detection of Ag+. Sensors Actuators B Chem. 232, 692–697. https://doi.org/10.1016/j.snb.2016.04.039

**Chaudhari, K., Xavier, P.L., Pradeep, T.,** 2011. Understanding the evolution of luminescent gold quantum clusters in protein templates. ACS Nano 5, 8816–8827. https://doi.org/10.1021/nn202901a

**Chen, J., Shu, Y., Li, H., Xu, Q., Hu, X.,** 2018. Nickel metal-organic framework 2D nanosheets with enhanced peroxidase nanozyme activity for colorimetric detection of $H_2O_2$. Talanta 189, 254–261. https://doi.org/10.1016/j.talanta.2018.06.075

**Chen, S., Yuan, R., Chai, Y., Hu, F.,** 2013. Electrochemical sensing of hydrogen peroxide using metal nanoparticles: A review. Microchim. Acta 180, 15–32. https://doi.org/10.1007/s00604-012-0904-4

**Chen, T.-H., Tseng, W.-L.,** 2012. (Lysozyme Type VI)-Stabilized Au8 Clusters: Synthesis Mechanism and Application for Sensing of Glutathione in a Single Drop of Blood. Small 8, 1912–1919.

**Chen, W., Cai, S., Ren, Q.Q., Wen, W., Zhao, Y. Di,** 2012. Recent advances in electrochemical sensing for hydrogen peroxide: A review. Analyst 137, 49–58. https://doi.org/10.1039/c1an15738h

**Chen, X., Tian, X., Shin, I., Yoon, J.,** 2011. Fluorescent and luminescent probes for detection of reactive oxygen and nitrogen species. Chem. Soc. Rev. 40, 4783–4804. https://doi.org/10.1039/c1cs15037e

**Chen, Xiaomei, Wu, G., Cai, Z., Oyama, M., Chen, Xi,** 2014. Advances in enzyme-free electrochemical sensors for hydrogen peroxide, glucose, and uric acid. Microchim. Acta 181, 689–705. https://doi.org/10.1007/s00604-013-1098-0

**Chen, Y.S., Chen, Z.W., Yuan, Y.W., Chen, K.C., Liu, C.P.,** 2020. Fluorescence Quenchers Manipulate the Peroxidase-like Activity of Gold-Based Nanomaterials. ACS Omega 5, 24487–24494. https://doi.org/10.1021/acsomega.0c02956

**Chevrier, D.M., Chatt, A., Zhang, P.,** 2012. Properties and applications of protein- stabilized fluorescent gold nanoclusters : short review. J. Nanophotonics 6. https://doi.org/10.1117/1.JNP.6

**Chinnadayyala, S.R., Kakoti, A., Santhosh, M., Goswami, P.,** 2014. A novel amperometric alcohol biosensor developed in a 3rd generation bioelectrode platform using peroxidase coupled ferrocene activated alcohol oxidase as biorecognition system. Biosens. Bioelectron. 55, 120–126. https://doi.org/10.1016/j.bios.2013.12.005

**Chinnadayyala, S.R., Santhosh, M., Singh, N.K., Goswami, P.,** 2015. Alcohol oxidase protein mediated in-situ synthesized and stabilized gold nanoparticles for developing amperometric alcohol biosensor. Biosens. Bioelectron. 69, 151–161. https://doi.org/10.1016/j.bios.2015.02.015

**Chung, H., Cho, H., Kong, K.,** 2009. Immobilization of Hansenula polymorpha Alcohol Oxidase for Alcohol Biosensor Applications. Bull. Korean Chem. Soc. 30, 57–60.

**Cicek, N., Ekiz, F., Arslan, Y., Gundogdu, C., Ergun, Y., Toppare, L.,** 2014. A novel conducting polymer based platform for ethanol sensing. Sensors Actuators B. Chem. 193, 306–314. https://doi.org/10.1016/j.snb.2013.12.007

**Cinti, S., Basso, M., Moscone, D., Arduini, F.,** 2017. A paper-based nanomodified electrochemical biosensor for ethanol detection in beers. Anal. Chim. Acta 960, 123–130. https://doi.org/10.1016/j.aca.2017.01.010

**Claiborne, A., Fridovich, I.,** 1979. Chemical and Enzymatic Intermediates in the Peroxidation of o-Dianisidine by Horseradish Peroxidase. 2. Evidence for a Substrate Radical-Enzyme Complex and Its Reaction with Nucleophiles. Biochemistry 18, 2329–2335. https://doi.org/10.1021/bi00578a030

**Collins, D.P., Dawson, J.H.,** 2013. Recent History of Heme-Containing Proteins: Advances in Structure, Functions, and Reaction Intermediate Determination, in: Comprehensive Inorganic Chemistry II (Second Edition): From Elements to Applications. pp. 65–102. https://doi.org/10.1016/B978-0-08-097774-4.00306-5

**Comina, G., Suska, A., Filippini, D.,** 2014. PDMS lab-on-a-chip fabrication using 3D printed templates. Lab Chip 14, 424–430. https://doi.org/10.1039/c3lc50956g

**Cren, É.C., Cardozo Filho, L., Silva, E.A., Meirelles, A.J.A.,** 2009. Breakthrough curves for oleic acid removal from ethanolic solutions using a strong anion exchange resin. Sep. Purif. Technol. 69, 1–6. https://doi.org/10.1016/j.seppur.2009.06.027

**Crespi, A., Gu, Y., Ngamsom, B., Hoekstra, H.J.W.M., Dongre, C., Pollnau, M., Ramponi, R., Van Den Vlekkert, H.H., Watts, P., Cerullo, G., Osellame, R.,** 2010. Three-dimensional Mach-Zehnder interferometer in a microfluidic chip for spatially-resolved label-free detection. Lab Chip 10, 1167–1173. https://doi.org/10.1039/b920062b

**Cui, R., Han, Z., Zhu, J.J.,** 2011. Helical carbon nanotubes: Intrinsic peroxidase catalytic activity and its application for biocatalysis and biosensing. Chem. - A Eur. J. 17, 9377–9384. https://doi.org/10.1002/chem.201100478

**Cui, S., Zhao, J., Zhang, H., Chen, W.,** 2016. High-density culture of Lactobacillus plantarum coupled with a lactic acid removal system with anion-exchange resins. Biochem. Eng. J. 115, 80–84. https://doi.org/10.1016/j.bej.2016.08.005

**Das, M., Goswami, P.,** 2013. Direct electrochemistry of alcohol oxidase using multiwalled carbon nanotube as electroactive matrix for biosensor application. Bioelectrochemistry 89, 19–25. https://doi.org/10.1016/j.bioelechem.2012.08.007

**Das, P., Bachu, V., Barbora, L., Dutta, A., Sarma, M.K., Goswami, P.,** 2022. Passive fuel delivery and efficient anoxic condition in anode improve performance of methanol biofuel cell, Applied Energy, 305, 117824, ISSN 0306-2619, https://doi.org/10.1016/j.apenergy.2021.117824.

**Das, S., Dhar, B.B.**, 2014. Green Synthesis of Noble Metal Nanoparticles Using Cysteine Modified Silk Fibroin : Catalysis and Anti-bacterial Activity. RSC Adv. 4, 46285–46292. https://doi.org/10.1039/C4RA06179A

**Das, S., Gogoi, S., Singh, N.K., Goswami, P.,** 2021a. Analytical application of H 2 O 2 -induced chiroptical graphitic carbon dots . Nano Express 2, 040003. https://doi.org/10.1088/2632-959x/ac3389

**Das, S., Goswami, P.,** 2020. Nanozymes as Potential Catalysts for Sensing and Analytical Application, *in:* Advance Materials and Techniques for Biosensors and Bioanalytical Applications, Editor:Pranab Goswami, CRC Press Tailor& Francis. ISBN 9781003083856, https://doi.org/10.1201/9781003083856

**Das, S., Ngashangva, L., Goswami, P.,** 2021b. Carbon dots: An emerging smart material for analytical applications, Micromachines. https://doi.org/10.3390/mi12010084

**Das, S., Ngashangva, L., Mog, H., Gogoi, S., Goswami, P.,** 2021c. An insight into the mechanism of peroxidase-like activity of carbon dots. Opt. Mater. (Amst). 115, 111017. https://doi.org/10.1016/j.optmat.2021.111017

**Datta, S., Christena, L.R., Rajaram, Y.R.S.,** 2013. Enzyme immobilization: an overview on techniques and support materials. 3 Biotech 3, 1–9. https://doi.org/10.1007/s13205-012-0071-7

**De Marcos, S., Callizo, E., Mateos, E., Galbán, J.,** 2014. An optical sensor for pesticide determination based on the autoindicating optical properties of peroxidase. Talanta 122, 251–256. https://doi.org/10.1016/j.talanta.2014.01.011

**Deegan, R.D., Bakajin, O., Dupont, T.F., Huber, G., Nagel, S.R., Witten, T.A.,** 1997. Capillary flow as the cause of ring stains from dried liquid drops. Nature 389, 827–829.

**Demura, M., Asakura, T.,** 1991. Porous membrane of Bombyx mori silk fibroin: structure characterization, physical properties and application to glucose oxidase immobilization. J. Memb. Sci. 59, 39–52. https://doi.org/10.1016/S0376-7388(00)81220-X

**Deng, H.H., Hong, G.L., Lin, F.L., Liu, A.L., Xia, X.H., Chen, W.,** 2016. Colorimetric detection of urea, urease, and urease inhibitor based on the peroxidase-like activity of gold nanoparticles. Anal. Chim. Acta 915, 74–80. https://doi.org/10.1016/j.aca.2016.02.008

**Deng, M., Xu, S., Chen, F.,** 2014. Enhanced chemiluminescence of the luminol- hydrogen peroxide system by BSA-stabilized Au nanoclusters as a peroxidase mimic and its application. Anal. Methods 16, 3117–3123. https://doi.org/10.1039/c3ay42135j

**Dey, R.S., Raj, C.R.,** 2010. Development of an amperometric cholesterol biosensor based on graphene-Pt nanoparticle hybrid material. J. Phys. Chem. C 114, 21427–21433. https://doi.org/10.1021/jp105895a

**Ding, L., Chen, S., Zhang, W., Zhang, Y., Wang, X.D.,** 2018. Fully Reversible Optical Sensor for Hydrogen Peroxide with Fast Response. Anal. Chem. 90, 7544–7551. https://doi.org/10.1021/acs.analchem.8b01159

**Drachuk, I., Gupta, M.K., Tsukruk, V. V.,** 2013. Biomimetic coatings to control cellular function through cell surface engineering. Adv. Funct. Mater. 23, 4437–4453. https://doi.org/10.1002/adfm.201300038

**Dröge, W., Schipper, H.M.,** 2007. Oxidative stress and aberrant signaling in aging and cognitive decline. Aging Cell 6, 361–370. https://doi.org/10.1111/j.1474-9726.2007.00294.x

**Duan, Y., Liu, Y., Han, H., Zhang, X., Zhang, M., Liao, Y., Han, T.,** 2021. A donor- p -acceptor aggregation-induced emission compound serving as a portable fluorescent sensor for detection and differentiation of methanol and ethanol in the gas phase. Spectrochim. Acta Part A Mol. Biomol. Spectrosc. 252, 119515. https://doi.org/10.1016/j.saa.2021.119515

**Dungchai, W., Chailapakul, O., Henry, C.S.,** 2011. A low-cost, simple, and rapid fabrication method for paper-based microfluidics using wax screen-printing. Analyst 136, 77–82. https://doi.org/10.1039/c0an00406e

**Gao, L., Yan, X.,** 2016. Nanozymes: an emerging field bridging nanotechnology and biology. Sci. China Life Sci. 59, 400–402. https://doi.org/10.1007/s11427-016-5044-3

**Gao, L., Zhuang, J., Nie, L., Zhang, J., Zhang, Y., Gu, N., Wang, T., Feng, J., Yang, D., Perrett, S., Yan, X.,** 2007. Intrinsic peroxidase-like activity of ferromagnetic nanoparticles. Nat. Nanotechnol. 2, 577–583. https://doi.org/10.1038/nnano.2007.260

**Gao, Z., Xu, M., Hou, L., Chen, G., Tang, D.,** 2013. Irregular-shaped platinum nanoparticles as peroxidase mimics for highly efficient colorimetric immunoassay. Anal. Chim. Acta 776, 79–86. https://doi.org/10.1016/j.aca.2013.03.034

**Geng, Z., Zhang, X., Fan, Z., Lv, X., Su, Y., Chen, H.,** 2017. Recent progress in optical biosensors based on smartphone platforms. Sensors (Switzerland) 17, 1–19. https://doi.org/10.3390/s17112449

**Ghisaidoobe, A.B.T., Chung, S.J.,** 2014. Intrinsic Tryptophan Fluorescence in the Detection and Analysis of Proteins : A Focus on Förster Resonance Energy Transfer Techniques. Int. J. Mol. Sci. 15, 22518–22538. https://doi.org/10.3390/ijms151222518

**Ghosh, A., Mitchell, D.A., Chanda, A., Ryabov, A.D., Popescu, D.L., Upham, E.C., Collins, G.J., Collins, T.J.,** 2008. Catalase-peroxidase activity of iron(III)-TAML activators of hydrogen peroxide. J. Am. Chem. Soc. 130, 15116–15126. https://doi.org/10.1021/ja8043689

**Ghosh, R., Gopalakrishnan, S., Savitha, R., Renganathan, T., Pushpavanam, S.,** 2019. Fabrication of laser printed microfluidic paper-based analytical devices (LP-µPADs) for point-of-care applications. Sci. Rep. 9, 1–11. https://doi.org/10.1038/s41598-019-44455-1

**Giorgio, M., Trinei, M., Migliaccio, E., Pelicci, P.G.,** 2007. Hydrogen peroxide: A metabolic by-product or a common mediator of ageing signals? Nat. Rev. Mol. Cell Biol. 8, 722–728. https://doi.org/10.1038/nrm2240

**Goodsell, D.S.,** 2004. Catalase. RCSB Protein Data Bank. https://doi.org/10.2210/rcsb_pdb/mom_2004_9

**Goswami, P.,** 2020. Advance Materials and Techniques for Biosensors and Bioanalytical Applications, Editor:Pranab Goswami, CRC Press Tailor& Francis. ISBN 9781003083856, https://doi.org/10.1201/9781003083856

**Goswami, P., Chinnadayyala, S.S.R., Chakraborty, M., Kumar, A.K., Kakoti, A.,** 2013. An overview on alcohol oxidases and their potential applications. Appl. Microbiol. Biotechnol. 97, 4259–4275. https://doi.org/10.1007/s00253-013-4842-9

**Gotor, R., Bell, J., Rurack, K.,** 2019. Tailored fluorescent solvatochromic test strips for quantitative on-site detection of gasoline fuel adulteration. J. Mater. Chem. C 7, 2250–2256. https://doi.org/10.1039/c8tc04818e

**Gouterman, M.,** 1961. Spectra of Porphyrins. J. Mol. Spectrosc. 6, 138–163. https://doi.org/10.1016/0370-2693(87)90819-7

**Gramss, G.,** 2017. Reappraising a controversy: Formation and role of the azodication (ABTS 2+ ) in the laccase-ABTS catalyzed breakdown of lignin. Fermentation 3. https://doi.org/10.3390/fermentation3020027

**Guo, Y., Amunyela, H.T.N.N., Cheng, Y., Xie, Y., Yu, H., Yao, W., Li, H.W., Qian, H.,** 2020. Natural protein-templated fluorescent gold nanoclusters: Syntheses and applications. Food Chem. 335. https://doi.org/10.1016/j.foodchem.2020.127657

**Guo, Y., Deng, L., Li, J., Guo, S., Wang, E., Dong, S.,** 2011a. Hemin - Graphene Hybrid Nanosheets with Intrinsic Peroxidase-like Activity. ACS Nano 5, 1282–1290.

**Guo, Y., Li, J., Dong, S.,** 2011b. Hemin functionalized graphene nanosheets-based dual biosensor platforms for hydrogen peroxide and glucose. Sensors Actuators, B Chem. 160, 295–300. https://doi.org/10.1016/j.snb.2011.07.050

**Hayat, A., Haider, W., Raza, Y., Marty, J.L.,** 2015. Colorimetric cholesterol sensor based on peroxidase like activity of zinc oxide nanoparticles incorporated carbon nanotubes. Talanta 143, 157–161. https://doi.org/10.1016/j.talanta.2015.05.051

**He, P., Liu, H., Li, Z., Liu, Y., Xu, X., Li, J.,** 2004. Electrochemical deposition of silver in room-temperature ionic liquids and its surface-enhanced Raman scattering effect. Langmuir 20, 10260–10267. https://doi.org/10.1021/la0484801

**He, W., Zhou, Y.T., Wamer, W.G., Hu, X., Wu, X., Zheng, Z., Boudreau, M.D., Yin, J.J.,** 2013. Intrinsic catalytic activity of Au nanoparticles with respect to hydrogen peroxide decomposition and superoxide scavenging. Biomaterials 34, 765–773. https://doi.org/10.1016/j.biomaterials.2012.10.010

**Hitomi, Y., Takeyasu, T., Funabiki, T., Kodera, M.,** 2011. Detection of enzymatically generated hydrogen peroxide by metal-based fluorescent probe. Anal. Chem. 83, 9213–9216. https://doi.org/10.1021/ac202534g

**Hitomi, Y., Takeyasu, T., Kodera, M.,** 2014. Development of Green-Emitting Iron Complex-Based Fluorescent Probes for Intracellular Hydrogen Peroxide Imaging. Bull. Chem. Soc. Jpn. 87, 819–824.

**Hitomi, Y., Takeyasu, T., Kodera, M.,** 2013. Iron complex-based fluorescent probes for intracellular hydrogen peroxide detection. Chem. Commun. 49, 9929–9931. https://doi.org/10.1039/c3cc44471f

**Hnaien, M., Lagarde, F., Jaffrezic-Renault, N.,** 2010. A rapid and sensitive alcohol oxidase/catalase conductometric biosensor for alcohol determination. Talanta 81, 222–227. https://doi.org/10.1016/j.talanta.2009.11.061

**Hofmann, S., Wong Po Foo, C.T., Rossetti, F., Textor, M., Vunjak-Novakovic, G., Kaplan, D.L., Merkle, H.P., Meinel, L.,** 2006. Silk fibroin as an organic polymer for controlled drug delivery. J. Control. Release 111, 219–227. https://doi.org/10.1016/j.jconrel.2005.12.009

**Hu, L., Yuan, Y., Zhang, L., Zhao, J., Majeed, S., Xu, G.,** 2013. Copper nanoclusters as peroxidase mimetics and their applications to $H_2O_2$ and glucose detection. Anal. Chim. Acta 762, 83–86. https://doi.org/10.1016/j.aca.2012.11.056

**Huang, X., Li, B., Li, L., Zhang, H., Majeed, I., Hussain, I., Tan, B.,** 2012. Facile Preparation of Highly Blue Fluorescent Metal Nanoclusters in Organic Media. J. Phys. Chem. C 116, 448–455.

**Ibarlucea, B., Fernández-Sánchez, C., Demming, S., Büttgenbach, S., Llobera, A.,** 2011. Selective functionalisation of PDMS-based photonic lab on a chip for biosensing. Analyst 136, 3496–3502. https://doi.org/10.1039/c0an00941e

**III, J.D.A., Finke, R.G.,** 1999. A review of modern transition-metal nanoclusters : their synthesis, characterization, and applications in catalysis. J. Mol. Catal. A Chem. 145, 1–44.

**Jamil, S., Nasir, M., Ali, Y., Nadeem, S., Rashid, S., Javed, M.Y., Hayat, A.,** 2021. Cr2O3-TiO2-Modified Filter Paper-Based Portable Nanosensors for Optical and Colorimetric Detection of Hydrogen Peroxide. ACS Omega. https://doi.org/10.1021/acsomega.1c03119

**Jiang, C., Zhu, J., Li, Z., Luo, J., Wang, J., Sun, Y.,** 2017. Chitosan-gold nanoparticles as peroxidase mimic and their application in glucose detection in serum. RSC Adv. 7, 44463–44469. https://doi.org/10.1039/c7ra08967h

**Jiang, H., Chen, Z., Cao, H., Huang, Y.**, 2012. Peroxidase-like activity of chitosan stabilized silver nanoparticles for visual and colorimetric detection of glucose. Analyst 137, 5560–5564. https://doi.org/10.1039/c2an35911a

**Jiang, X., Sun, C., Guo, Y., Nie, G., Xu, L.,** 2014. Peroxidase-like activity of apoferritin paired gold clusters for glucose detection. Biosens. Bioelectron. 64, 165–170. https://doi.org/10.1016/j.bios.2014.08.078

**Jin, L., Meng, Z., Zhang, Y., Cai, S., Zhang, Z., Li, C., Shang, L., Shen, Y.,** 2017. Ultrasmall Pt Nanoclusters as Robust Peroxidase Mimics for Colorimetric Detection of Glucose in Human Serum. ACS Appl. Mater. Interfaces 9, 10027–10033. https://doi.org/10.1021/acsami.7b01616

**Jin, L., Shang, L., Guo, S., Fang, Y., Wen, D., Wang, L., Yin, J., Dong, S.,** 2011. Biomolecule-stabilized Au nanoclusters as a fluorescence probe for sensitive detection of glucose. Biosens. Bioelectron. 26, 1965–1969. https://doi.org/10.1016/j.bios.2010.08.019

**Jung, Y., Kim, J., Awofeso, O., Kim, H., Regnier, F., Bae, E.,** 2015. Smartphone-based colorimetric analysis for detection of saliva alcohol concentration. Appl. Opt. 54, 9183. https://doi.org/10.1364/AO.54.009183

**Jv, Y., Li, B., Cao, R.,** 2010. Positively-charged gold nanoparticles as peroxidase mimic and their application in hydrogen peroxide and glucose detection. Chem. Commun. 46, 8017–8019. https://doi.org/10.1039/c0cc02698k

**Kadnikova, E.N., Kostić, N.M.,** 2002. Oxidation of ABTS by hydrogen peroxide catalyzed by horseradish peroxidase encapsulated into sol-gel glass. Effects of glass matrix on reactivity. J. Mol. Catal. B Enzym. 18, 39–48. https://doi.org/10.1016/S1381-1177(02)00057-7

**Kakoti, A., Siddiqui, M.F., Goswami, P.,** 2015. A low cost design and fabrication method for developing a leak proof paper based microfluidic device with customized test zone. Biomicrofluidics 9, 1–5. https://doi.org/10.1063/1.4918641

**Kaneko, T., Yoshimoto, Y., Hori, T., Takagi, S., Ooyama, J., Terao, T., Kinefuchi, I.,** 2020. Relation between oxygen gas diffusivity and porous characteristics under capillary condensation of water in cathode catalyst layers of polymer electrolyte membrane fuel cells. Int. J. Heat Mass Transf. 150, 119277. https://doi.org/10.1016/j.ijheatmasstransfer.2019.119277

**Karim, M.N., Anderson, S.R., Singh, S., Ramanathan, R., Bansal, V.,** 2018. Nanostructured silver fabric as a free-standing NanoZyme for colorimetric detection of glucose in urine. Biosens. Bioelectron. 110, 8–15. https://doi.org/10.1016/j.bios.2018.03.025

**Karyakin, A.A., Karyakina, E.E., Gorton, L.,** 2000. Amperometric biosensor for glutamate using Prussian Blue-based "artificial peroxidase" as a transducer for hydrogen peroxide. Anal. Chem. 72, 1720–1723. https://doi.org/10.1021/ac990801o

**Kaushik, S., Thungon, P.D., Goswami, P.,** 2020. Silk Fibroin: An Emerging Biocompatible Material for Application of Enzymes and Whole Cells in Bioelectronics and Bioanalytical Sciences. ACS Biomater. Sci. Eng. 6, 4337–4355. https://doi.org/10.1021/acsbiomaterials.9b01971

**Kawasaki, H., Hamaguchi, K., Osaka, I., Arakawa, R.,** 2011. Ph-dependent synthesis of pepsin-mediated gold nanoclusters with blue green and red fluorescent emission. Adv. Funct. Mater. 21, 3508–3515. https://doi.org/10.1002/adfm.201100886

**Khoo, H.K., Ong, H.C.,** 2014. Generalization of hue in the RGB cube space. Int. Conf. Signal Process. Proceedings, ICSP 2015-January, 631–636. https://doi.org/10.1109/ICOSP.2014.7015080

**Koh, L.D., Cheng, Y., Teng, C.P., Khin, Y.W., Loh, X.J., Tee, S.Y., Low, M., Ye, E., Yu, H.D., Zhang, Y.W., Han, M.Y.,** 2015. Structures, mechanical properties and applications of silk fibroin materials. Prog. Polym. Sci. 46, 86–110. https://doi.org/10.1016/j.progpolymsci.2015.02.001

**Kozhevnikov, V.N., Mandl, C., Miltschitzky, S., Duerkop, A., Wolfbeis, O.S., Koenig, B.,** 2005. Strong emission increase of a dicarboxyterpyridene europium (III) complex in the presence of citrate and hydrogen peroxide. Inorganica Chim. Acta 358, 2445–2448. https://doi.org/10.1016/j.ica.2005.01.015

**Krug, A., Suleiman, A.A., Guilbault, G.G., Kellner, R.,** 1992. Colorimetric determination of free and total cholesterol by flow injection analysis with a fiber optic detector. Enzyme Microb. Technol. 14, 313–316. https://doi.org/10.1016/0141-0229(92)90157-J

**Kuah, E., Toh, S., Yee, J., Ma, Q., Gao, Z.,** 2016. Enzyme Mimics : Advances and Applications . Chemistry (Easton). 22, 8404–8430. https://doi.org/10.1002/chem.201504394

**Kuivila, H.G.,** 1955. Electrophilic Displacement Reactions. VI. Catalysis by Strong Acids in the Reaction between Hydrogen Peroxide and Benzeneboronic Acid. J. Am. Chem. Soc. 77, 4014–4016. https://doi.org/10.1021/ja01620a017

**Kumar, A.K., Goswami, P.,** 2008. Purification and properties of a novel broad substrate specific alcohol oxidase from Aspergillus terreus MTCC 6324. Biochim. Biophys. Acta - Proteins Proteomics 1784, 1552–1559. https://doi.org/10.1016/j.bbapap.2008.06.009

**Lakowicz, J.R.,** 2000. Principles of Fluorescence Spectroscopy, Second ed., Springer. https://doi.org/10.1006/abio.2000.4850

**Laloi, C., Apel, K., Danon, A.,** 2004. Reactive oxygen signalling: The latest news. Curr. Opin. Plant Biol. 7, 323–328. https://doi.org/10.1016/j.pbi.2004.03.005

**Lane, S., Vagin, S., Wang, H., Heinz, W.R., Morrish, W., Zhao, Y., Rieger, B., Meldrum, A.,** 2018. Wide-gamut lasing from a single organic chromophore. Light Sci. Appl. 7, 1–9. https://doi.org/10.1038/s41377-018-0102-1

**Laser, H.,** 1955. Peroxidatic activity of catalase. Biochem. J. 61, 122–127. https://doi.org/10.1016/0005-2744(70)90052-5

**Lawrence, B. D., Cronin-golomb, M., Georgakoudi, I., Kaplan, D.L., Omenetto, F.G.,** 2008a. Bioactive Silk Protein Biomaterial Systems for Optical Devices. Biomacromolecules 9, 1214–1220.

**Lawrence, B. D., Omenetto, F., Chui, K., Kaplan, D.L.,** 2008b. Processing methods to control silk fibroin film biomaterial features. J. Mater. Sci. 43, 6967–6985. https://doi.org/10.1007/s10853-008-2961-y

**Lawrence, B.D., Wharram, S., Kluge, J.A., Leisk, G.G., Omenetto, F.G., Rosenblatt, M.I., Kaplan, D.L.,** 2010. Effect of hydration on silk film material properties. Macromol. Biosci. 10, 393–403. https://doi.org/10.1002/mabi.200900294

**Le Guével, X., Hötzer, B., Jung, G., Hollemeyer, K., Trouillet, V., Schneider, M.,** 2011. Formation of fluorescent metal (Au, Ag) nanoclusters capped in bovine serum albumin followed by fluorescence and spectroscopy. J. Phys. Chem. C 115, 10955–10963. https://doi.org/10.1021/jp111820b

**Lebiga, E., Fernandez, R.E., Beskok, A.,** 2015. Confined chemiluminescence detection of nanomolar levels of $H_2O_2$ in a paper-plastic disposable microfluidic device using a smartphone. Analyst 140, 5006–5011. https://doi.org/10.1039/c5an00720h

**Lebiga, E., Krenek, K.M., Fernandez, R.E., Lippert, A., Beskok, A.,** 2014. Chemiluminescence Sensor System for H202 Detection 2568–2569.

**Lee, D., Kim, S.H., Byun, Y.T.,** 2018. Paper-based hydrogen peroxide sensors using porphyrin with central ions of Ti. Twelfth Int. Conf. Sens. Technol. 2018–2021.

**Li, B., Zhang, Z., Jin, Y.,** 2001. Chemiluminescence flow biosensor for hydrogen peroxide with immobilized reagents. Sensors Actuators, B Chem. 72, 115–119. https://doi.org/10.1016/S0925-4005(00)00623-7

**Li, H., Guo, Y., Xiao, L., Chen, B.,** 2014. A fluorometric biosensor based on $H_2O_2$-sensitive nanoclusters for the detection of acetylcholine. Biosens. Bioelectron. 59, 289–292. https://doi.org/10.1016/j.bios.2014.03.054

**Li, J., Qiu, J.D., Xu, J.J., Chen, H.Y., Xia, X.H.,** 2007. The synergistic effect of prussian-blue-grafted carbon nanotube/ poly(4-vinylpyridine) composites for amperometric sensing. Adv. Funct. Mater. 17, 1574–1580. https://doi.org/10.1002/adfm.200600033

**Li, X., Akbarabadi, M., Karpyn, Z.T., Piri, M., Bazilevskaya, E.,** 2015. Experimental investigation of carbon dioxide trapping due to capillary retention in saline aquifers. Geofluids 15, 563–576. https://doi.org/10.1111/gfl.12127

**Li, Y., Yang, Q., Li, M., Song, Y.,** 2016. Rate-dependent interface capture beyond the coffee-ring effect. Sci. Rep. 6, 1–8. https://doi.org/10.1038/srep24628

**Li, Y.M., Chen, X.T., Li, J., Liu, H.H.,** 2004. Direct voltammetry and catalysis of hemoenzymes in methyl cellulose film. Electrochim. Acta 49, 3195–3200. https://doi.org/10.1016/j.electacta.2004.02.033

**Liana, D.D., Raguse, B., Justin Gooding, J., Chow, E.,** 2012. Recent advances in paper-based sensors. Sensors (Switzerland) 12, 11505–11526. https://doi.org/10.3390/s120911505

**Lin, L., Song, X., Chen, Y., Rong, M., Zhao, T., Wang, Y., Jiang, Y., Chen, X.,** 2015. Intrinsic peroxidase-like catalytic activity of nitrogen-doped graphene quantum dots and their application in the colorimetric detection of $H_2O_2$ and glucose. Anal. Chim. Acta 869, 89–95. https://doi.org/10.1016/j.aca.2015.02.024

**Lin, T., Zhong, L., Wang, J., Guo, L., Wu, H., Guo, Q., Fu, F.F., Chen, G.,** 2014. Graphite-like carbon nitrides as peroxidase mimetics and their applications to glucose detection. Biosens. Bioelectron. 59, 89–93. https://doi.org/10.1016/j.bios.2014.03.023

**Lin, V.S., Dickinson, B.C., Chang, C.J.,** 2013. Boronate-based fluorescent probes: Imaging hydrogen peroxide in living systems. Methods Enzymol. 526, 19–43. https://doi.org/10.1016/B978-0-12-405883-5.00002-8

**Lin, W.Z., Yeung, C.Y., Liang, C.K., Huang, Y.H., Liu, C.C., Hou, S.Y.,** 2018. A colorimetric sensor for the detection of hydrogen peroxide using DNA-modified gold nanoparticles. J. Taiwan Inst. Chem. Eng. 89, 49–55. https://doi.org/10.1016/j.jtice.2018.05.005

**Ling, Y., Zhang, N., Qu, F., Wen, T., Gao, Z.F., Li, N.B., Luo, H.Q.,** 2014. Fluorescent detection of hydrogen peroxide and glucose with polyethyleneimine-templated Cu nanoclusters. Spectrochim. Acta - Part A Mol. Biomol. Spectrosc. 118, 315–320. https://doi.org/10.1016/j.saa.2013.08.097

**Lippert, A.R., Van De Bittner, G.C., Chang, C.J.,** 2011. Boronate oxidation as a bioorthogonal reaction approach for studying the chemistry of hydrogen peroxide in living systems. Acc. Chem. Res. 44, 793–804. https://doi.org/10.1021/ar200126t

**Liu, B., Sun, Z., Huang, P.J.J., Liu, J.,** 2015a. Hydrogen peroxide displacing DNA from nanoceria: Mechanism and detection of glucose in serum. J. Am. Chem. Soc. 137, 1290–1295. https://doi.org/10.1021/ja511444e

**Liu, C.P., Wu, T.H., Lin, Y.L., Liu, C.Y., Wang, S., Lin, S.Y.,** 2016. Tailoring Enzyme-Like Activities of Gold Nanoclusters by Polymeric Tertiary Amines for Protecting Neurons Against Oxidative Stress. Small 12, 4127–4135. https://doi.org/10.1002/smll.201503919

**Liu, H., Zhou, P., Wu, X., Sun, J., Chen, S.,** 2015b. Radical scavenging by acetone: A new perspective to understand laccase/ABTS inactivation and to recover redox mediator. Molecules 20, 19907–19913. https://doi.org/10.3390/molecules201119672

**Liu, M.M., Lian, X., Liu, H., Guo, Z.Z., Huang, H.H., Lei, Y., Peng, H.P., Chen, W., Lin, X.H., Liu, A.L., Xia, X.H.,** 2019a. A colorimetric assay for sensitive detection of hydrogen peroxide and glucose in microfluidic paper-based analytical devices integrated with starch-iodide-gelatin system. Talanta 200, 511–517. https://doi.org/10.1016/j.talanta.2019.03.089

**Liu, S.G., Mo, S., Han, L., Li, N., Fan, Y.Z., Li, N.B., Luo, H.Q.,** 2019b. Oxidation etching induced dual-signal response of carbon dots/silver nanoparticles system for ratiometric optical sensing of $H_2O_2$ and $H_2O_2$ -related bioanalysis. Anal. Chim. Acta 1055, 81–89. https://doi.org/10.1016/j.aca.2018.12.015

**Liu, X., Huang, D., Lai, C., Qin, L., Zeng, G., Xu, P., Li, B., Yi, H., Zhang, M.,** 2019c. Peroxidase-Like Activity of Smart Nanomaterials and Their Advanced Application in Colorimetric Glucose Biosensors. Small 15, 1–27. https://doi.org/10.1002/smll.201900133

**Lo, L.-C., Chu, C.,** 2003. Development of highly selective and sensitive probes for hydrogen peroxide. Chem. Commun. 21, 2728–2729.

**Long, Y., Wang, X., Shen, D., Zheng, H.,** 2016. Detection of glucose based on the peroxidase-like activity of reduced state carbon dots. Talanta 159, 122–126. https://doi.org/10.1016/j.talanta.2016.06.012

**Long, Y.J., Li, Y.F., Liu, Y., Zheng, J.J., Tang, J., Huang, C.Z.,** 2011. Visual observation of the mercury-stimulated peroxidase mimetic activity of gold nanoparticles. Chem. Commun. 47, 11939–11941. https://doi.org/10.1039/c1cc14294a

**Lopez-Gallego, F., Betancor, L., Hidalgo, A., Dellamora-Ortiz, G., Mateo, C., Fernández-Lafuente, R., Guisán, J.M.,** 2007. Stabilization of different alcohol oxidases via immobilization and post immobilization techniques. Enzyme Microb. Technol. 40, 278–284. https://doi.org/10.1016/j.enzmictec.2006.04.021

**López-Marzo, A.M., Merkoçi, A.,** 2016. Paper-based sensors and assays: A success of the engineering design and the convergence of knowledge areas. Lab Chip 16, 3150–3176. https://doi.org/10.1039/c6lc00737f

**Lu, D., Liu, L., Li, F., Shuang, S., Li, Y., Choi, M.M.F., Dong, C.,** 2014. Lysozyme-stabilized gold nanoclusters as a novel fluorescence probe for cyanide recognition. Spectrochim. Acta - Part A Mol. Biomol. Spectrosc. 121, 77–80. https://doi.org/10.1016/j.saa.2013.10.009

**Lu, Q., Wang, X., Hu, X., Cebe, P., Omenetto, F., Kaplan, D.L.,** 2010. Stabilization and release of enzymes from silk films. Macromol. Biosci. 10, 359–368. https://doi.org/10.1002/mabi.200900388

**Lu, S, Wang, X., Lu, Q., Hu, X., Uppal, N., Omenetto, F.G., Kaplan, D.L.,** 2009b. Stabilization of Enzymes in Silk Films. Biomacromolecules 10, 1032–1042. https://doi.org/10.1021/bm800956n

**Lu, Shen-zhou, Wang, X., Uppal, N., Kaplan, D.L., Li, M.,** 2009a. Stabilization of horseradish peroxidase in silk materials. Front. Mater. Sci. China 3, 367–373. https://doi.org/10.1007/s11706-009-0058-4

**Maeda, H., Fukuyasu, Y., Yoshida, S., Fukuda, M., Saeki, K., Matsuno, H., Yamauchi, Y., Yoshida, K., Hirata, K., Miyamoto, K.,** 2004. Fluorescent Probes for Hydrogen Peroxide Based on a Non-Oxidative Mechanism. Angew. Chemie 116, 2443–2445. https://doi.org/10.1002/ange.200452381

**Mahadeva, S.K., Walus, K., Stoeber, B.,** 2015. Paper as a platform for sensing applications and other devices: A review. ACS Appl. Mater. Interfaces 7, 8345–8362. https://doi.org/10.1021/acsami.5b00373

**Makamba, H., Kim, J.H., Lim, K., Park, N., Hahn, J.H.,** 2003. Surface modification of poly(dimethylsiloxane) microchannels. Electrophoresis 24, 3607–3619. https://doi.org/10.1002/elps.200305627

**Makuła, P., Pacia, M., Macyk, W.,** 2018. How To Correctly Determine the Band Gap Energy of Modified Semiconductor Photocatalysts Based on UV-Vis Spectra. J. Phys. Chem. Lett. 9, 6814–6817. https://doi.org/10.1021/acs.jpclett.8b02892

**Manea, F., Houillon, F.B., Pasquato, L., Scrimin, P.,** 2004. Nanozymes: Gold-nanoparticle-based transphosphorylation catalysts. Angew. Chemie - Int. Ed. 43, 6165–6169. https://doi.org/10.1002/anie.200460649

**Mangos, T.J., Haas, M.J.,** 1996. Enzymatic Determination of Methanol with Alcohol Oxidase, Peroxidase, and the Chromogen 2,2′-Azinobis(3-ethylbenzthiazoline-6-sulfonic acid) and Its Application to the Determination of the Methyl Ester Content of Pectins. J. Agric. Food Chem. 44, 2977–2981. https://doi.org/10.1021/jf960274z

**Marelli, B., Brenckle, M.A., Kaplan, D.L., Omenetto, F.G.,** 2016. Silk Fibroin as Edible Coating for Perishable Food Preservation. Sci. Rep. 6, 1–11. https://doi.org/10.1038/srep25263

**Martinez, A.W., Phillips, S.T., Whitesides, G.M.,** 2008. Three-dimensional microfluidic devices fabricated in layered paper and tape. Proc. Natl. Acad. Sci. U. S. A. 105, 19606–19611. https://doi.org/10.1073/pnas.0810903105

**Martinez, A.W., Phillips, S.T., Whitesides, G.M., Carrilho, E.,** 2010. Diagnostics for the developing world: Microfluidic paper-based analytical devices. Anal. Chem. 82, 3–10. https://doi.org/10.1021/ac9013989

**Mateo, C., Palomo, J.M., Fernandez-Lorente, G., Guisan, J.M., Fernandez-Lafuente, R.,** 2007. Improvement of enzyme activity, stability and selectivity via immobilization techniques. Enzyme Microb. Technol. 40, 1451–1463. https://doi.org/10.1016/j.enzmictec.2007.01.018

**Matilainen, K., Hämäläinen, T., Savolainen, A., Sipiläinen-Malm, T., Peltonen, J., Erho, T., Smolander, M.,** 2012. Performance and penetration of laccase and ABTS inks on various printing substrates. Colloids Surfaces B Biointerfaces 90, 119–128. https://doi.org/10.1016/j.colsurfb.2011.10.015

**Mazzei, F., Botrè, F., Favero, G.,** 2007. Peroxidase based biosensors for the selective determination of D,L-lactic acid and L-malic acid in wines. Microchem. J. 87, 81–86. https://doi.org/10.1016/j.microc.2007.05.009

**Meier, J., Ho, E.M., Stapleton, J.A., Iverson, N.M.,** 2019. Hydrogen Peroxide Sensors for Biomedical Applications. Chemosensors 7. https://doi.org/10.3390/chemosensors7040064

**Meng, F., Yin, H., Li, Y., Zheng, S., Gan, F., Ye, G.,** 2018. One-step synthesis of enzyme-stabilized gold nanoclusters for fluorescent ratiometric detection of hydrogen peroxide, glucose and uric acid. Microchem. J. 141, 431–437. https://doi.org/10.1016/j.microc.2018.06.006

**Miller, E.W., Albers, A.E., Pralle, A., Isacoff, E.Y., Chang, C.J.,** 2005. Boronate-based fluorescent probes for imaging cellular hydrogen peroxide. J. Am. Chem. Soc. 127, 16652–16659. https://doi.org/10.1021/ja054474f

**Miyairi, S., Sugiura, M., Fukul, S.,** 1978. Immobilization of B-Glucosidase in Fibroin Membrane. Agric. Biol. Chem. 42, 1661–1667. https://doi.org/10.1080/00021369.1978.10863228

**Molaabasi, F., Hosseinkhani, S., Moosavi-Movahedi, A.A., Shamsipur, M.,** 2015. Hydrogen peroxide sensitive hemoglobin-capped gold nanoclusters as a fluorescence enhancing sensor for the label-free detection of glucose. RSC Adv. 5, 33123–33135. https://doi.org/10.1039/c5ra00335k

**Möller, M., Denicola, A.,** 2002. Protein Tryptophan Accessibility Studied by Fluorescence Quenching. Biochem. Mol. Biol. Educ. 30, 175–178.

**Mu, J., Wang, Y., Zhao, M., Zhang, L.,** 2012. Intrinsic peroxidase-like activity and catalase-like activity of $Co_3O_4$ nanoparticles. Chem. Commun. 48, 2540–2542. https://doi.org/10.1039/c2cc17013b

**Mutyala, S., Mathiyarasu, J.,** 2016. A reagentless non-enzymatic hydrogen peroxide sensor presented using electrochemically reduced graphene oxide modified glassy carbon electrode. Mater. Sci. Eng. C 69, 398–406. https://doi.org/10.1016/j.msec.2016.06.069

**Narayanaswamy, N., Narra, S., Nair, R.R., Saini, D.K., Kondaiah, P., Govindaraju, T.,** 2016. Stimuli-responsive colorimetric and NIR fluorescence combination probe for selective reporting of cellular hydrogen peroxide. Chem. Sci. 7, 2832–2841. https://doi.org/10.1039/c5sc03488d

**Navas Díaz, A., Ramos Peinado, M.C., Torijas Minguez, M.C.,** 1998. Sol-gel horseradish peroxidase biosensor for hydrogen peroxide detection by chemiluminescence. Anal. Chim. Acta 363, 221–227. https://doi.org/10.1016/S0003-2670(98)00080-4

**Nelson, D.L., Cox, M.M.,** 2009. Enzyme. Lehninger. Princ. Biochem. 191–232.

**Ni, P., Dai, H., Wang, Y., Sun, Y., Shi, Y., Hu, J., Li, Z.,** 2014. Visual detection of melamine based on the peroxidase-like activity enhancement of bare gold nanoparticles. Biosens. Bioelectron. 60, 286–291. https://doi.org/10.1016/j.bios.2014.04.029

**Nie, J., Liang, Y., Zhang, Y., Le, S., Li, D., Zhang, S.,** 2013. One-step patterning of hollow microstructures in paper by laser cutting to create microfluidic analytical devices. Analyst 138, 671–676. https://doi.org/10.1039/c2an36219h

**Nishat, S., Jafry, A.T., Martinez, A.W., Awan, F.R.,** 2021. Paper-based microfluidics: Simplified fabrication and assay methods. Sensors Actuators, B Chem. 336, 129681. https://doi.org/10.1016/j.snb.2021.129681

**O'Brien, E.P., Brooks, B.R., Thirumalai, D.,** 2012. Effects of pH on proteins: Predictions for ensemble and single-molecule pulling experiments. J. Am. Chem. Soc. 134, 979–987. https://doi.org/10.1021/ja206557y

**Okawa, Y., Yokoyama, N., Sakai, Y., Shiba, F.,** 2015. Direct electron transfer biosensor for hydrogen peroxide carrying nanocomplex composed of horseradish peroxidase and Au-nanoparticle - Characterization and application to bienzyme systems. Anal. Chem. Res. 5, 1–8. https://doi.org/10.1016/j.ancr.2015.05.001

**Peeling, R.W., Holmes, K.K., Mabey, D., Ronald, A.,** 2006. Rapid tests for sexually transmitted infections (STIs): The way forward. Sex. Transm. Infect. 82, 1–6. https://doi.org/10.1136/sti.2006.024265

**Peng, C., Duan, X., Xie, Z., Liu, C.,** 2014. Shape-controlled generation of gold nanoparticles assisted by dual-molecules: The development of hydrogen peroxide and oxidase-based biosensors. J. Nanomater. 2014. https://doi.org/10.1155/2014/576082

**Periasamy, A.P., Ho, Y.H., Chen, S.M.,** 2011. Multiwalled carbon nanotubes dispersed in carminic acid for the development of catalase based biosensor for selective amperometric determination of H 2O 2 and iodate. Biosens. Bioelectron. 29, 151–158. https://doi.org/10.1016/j.bios.2011.08.010

**Ping, J., Wang, Y., Fan, K., Wu, J., Ying, Y.,** 2011. Direct electrochemical reduction of graphene oxide on ionic liquid doped screen-printed electrode and its electrochemical biosensing application. Biosens. Bioelectron. 28, 204–209. https://doi.org/10.1016/j.bios.2011.07.018

**Presnova, G. V., Rybcova, M.Y., Egorov, A.M.,** 2008. Electrochemical biosensors based on horseradish peroxidase. Russ. J. Gen. Chem. 78, 2482–2488. https://doi.org/10.1134/S1070363208120293

**Preucil, F.,** 1953. Color hue and ink transfer. Their relation to perfect reproduction. Proc. Int. Conf Tech. Assoc. Graph. Arts 102–110.

**Priyanga, N., Raja, A.S., Pannipara, M., Al-Sehemi, A.G., Phang, S.M., Xia, Y., Tsai, S.Y., Annaraj, J., Sambathkumar, S., kumar, G.G.,** 2021. Hierarchical MnS@$MoS_2$ architectures on tea bag filter paper for flexible, sensitive, and selective non-enzymatic hydrogen peroxide sensors. J. Alloys Compd. 855. https://doi.org/10.1016/j.jallcom.2020.157103

**Qian, J., Liu, Y., Liu, H., Yut, T., Deng, J.,** 1997. Immobilization of horseradish peroxidase with a regenerated silk fibroin membrane and its application to a tetrathiafulvalene-mediating H202 sensor. Biosens. Bioelectron. 12, 1213–1218.

**Rafatmah, E., Hemmateenejad, B.,** 2019. Colorimetric and visual determination of hydrogen peroxide and glucose by applying paper-based closed bipolar electrochemistry. Microchim. Acta 186. https://doi.org/10.1007/s00604-019-3793-y

**Ragavan, K. V., Ahmed, S.R., Weng, X., Neethirajan, S.,** 2018. Chitosan as a peroxidase mimic: Paper based sensor for the detection of hydrogen peroxide. Sensors Actuators, B Chem. 272, 8–13. https://doi.org/10.1016/j.snb.2018.05.142

**Rapoport, R., Hanukoglu, I., Sklan, D.,** 1994. A Fluorometric Assay for Hydrogen Peroxide, Suitable for NAD(P)H-Dependent Superoxide Generating Redox Systems. Anal. Biochem. 218, 309–313. https://doi.org/10.1006/abio.1994.1183

**Reddy, S.M., Jones, J.P., Lewis, T.J., Vadgama, P.M.,** 1998. Development of an oxidase-based glucose sensor using thickness-shear-mode quartz crystals. Anal. Chim. Acta 363, 203–213. https://doi.org/10.1016/S0003-2670(98)00131-7

**Rezende, F., Brandes, R.P., Schröder, K.,** 2018. Detection of hydrogen peroxide with fluorescent dyes. Antioxidants Redox Signal. 29, 585–602. https://doi.org/10.1089/ars.2017.7401

**Rhee, S.G.,** 2006. $H_2O_2$, a necessary evil for cell signaling. Science (80-. ). 312, 1882–1883. https://doi.org/10.1126/science.1130481

**Rocchitta, G., Spanu, A., Babudieri, S., Latte, G., Madeddu, G., Galleri, G., Nuvoli, S., Bagella, P., Demartis, M.I., Fiore, V., Manetti, R., Serra, P.A.,** 2016. Enzyme biosensors for biomedical

applications: Strategies for safeguarding analytical performances in biological fluids. Sensors (Switzerland) 16. https://doi.org/10.3390/s16060780

**Rockwood, D.D.N., Preda, R.R.C., Yücel, T., Wang, X., Lovett, M.L., Kaplan, D.L.,** 2011. Materials fabrication from Bombyx mori silk fibroin. Nat. Protoc. 6, 1–43. https://doi.org/10.1038/nprot.2011.379.Materials

**Sánchez-Calvo, A., Costa-García, A., Blanco-López, M.C.,** 2020. Paper-based electrodes modified with cobalt phthalocyanine colloid for the determination of hydrogen peroxide and glucose. Analyst 145, 2716–2724. https://doi.org/10.1039/c9an02413a

**Santhosh, M., Chinnadayyala, S.R., Kakoti, A., Goswami, P.,** 2014. Selective and sensitive detection of free bilirubin in blood serum using human serum albumin stabilized gold nanoclusters as fluorometric and colorimetric probe. Biosens. Bioelectron. 59, 370–6. https://doi.org/10.1016/j.bios.2014.04.003

**Santhosh, M., Chinnadayyala, S.R., Singh, N.K., Goswami, P.,** 2016. Human serum albumin-stabilized gold nanoclusters act as an electron transfer bridge supporting specific electrocatalysis of bilirubin useful for biosensing applications. Bioelectrochemistry 111, 7–14. https://doi.org/10.1016/j.bioelechem.2016.04.003

**Sanz, V., de Marcos, S., Galbán, J.,** 2007. A reagentless optical biosensor based on the intrinsic absorption properties of peroxidase. Biosens. Bioelectron. 22, 956–964. https://doi.org/10.1016/j.bios.2006.04.008

**Saxena, U., Goswami, P.,** 2012. Electrical and optical properties of gold nanoparticles: Applications in gold nanoparticles-cholesterol oxidase integrated systems for cholesterol sensing. J. Nanoparticle Res. 14. https://doi.org/10.1007/s11051-012-0813-9

**Saxena, U., Goswami, P.,** 2010. Silk Mat as Bio-matrix for the Immobilization of Cholesterol Oxidase. Appl. Biochem. Biotechnol. 162, 1122–1131. https://doi.org/10.1007/s12010-010-8923-2

**Schäferling, M., Grögel, D.B.M., Schreml, S.,** 2011. Luminescent probes for detection and imaging of hydrogen peroxide. Microchim. Acta 174, 1–18. https://doi.org/10.1007/s00604-011-0606-3

**Schmid, G.,** 1990. Clusters and colloids: bridges between molecular and condensed material. Endeavour 14, 172–178.

**Scott, S.L., Chen, W.J., Bakac, A., Espenson, J.H.,** 1993. Spectroscopic parameters, electrode potentials, acid ionization constants, and electron exchange rates of the 2,2′-azinobis(3-

ethylbenzothiazoline-6-sulfonate) radicals and ions. J. Phys. Chem. 97, 6710–6714. https://doi.org/10.1021/j100127a022

**Sechi, D., Greer, B., Johnson, J., Hashemi, N.,** 2013. Three-dimensional paper-based microfluidic device for assays of protein and glucose in urine. Anal. Chem. 85, 10733–10737. https://doi.org/10.1021/ac4014868

**Seed, B.,** 1982. Diazotizable arybmine cellulose papers for the coupling and hybridization of nucleic acids. Nucleic Acids Res. 10, 5753–5763.

**Sempels, W., De Dier, R., Mizuno, H., Hofkens, J., Vermant, J.,** 2013. Auto-production of biosurfactants reverses the coffee ring effect in a bacterial system. Nat. Commun. 4, 1–8. https://doi.org/10.1038/ncomms2746

**Semwal, V., Gupta, B.D.,** 2021. Highly selective SPR based fiber optic sensor for the detection of hydrogen peroxide. Sensors Actuators, B Chem. 329, 129062. https://doi.org/10.1016/j.snb.2020.129062

**Shah, J., Purohit, R., Singh, R., Karakoti, A.S., Singh, S.,** 2015. ATP-enhanced peroxidase-like activity of gold nanoparticles. J. Colloid Interface Sci. 456, 100–107. https://doi.org/10.1016/j.jcis.2015.06.015

**Shamkhalichenar, H., Choi, J.-W.,** 2020. Review—Non-Enzymatic Hydrogen Peroxide Electrochemical Sensors Based on Reduced Graphene Oxide. J. Electrochem. Soc. 167, 037531. https://doi.org/10.1149/1945-7111/ab644a

**Shamkhalichenar, H., Choi, J.-W.,** 2017. An Inkjet-Printed Non-Enzymatic Hydrogen Peroxide Sensor on Paper. J. Electrochem. Soc. 164, B3101–B3106. https://doi.org/10.1149/2.0161705jes

**Shang, L., Dong, S., Nienhaus, G.U.,** 2011. Ultra-small fluorescent metal nanoclusters : Synthesis and biological applications. Nano Today 6, 401–418. https://doi.org/10.1016/j.nantod.2011.06.004

**Sharma, L., Gouraj, S., Raut, P., Tagad, C.,** 2020. Development of a surface-modified paper-based colorimetric sensor using synthesized Ag NPs-alginate composite. Environ. Technol. (United Kingdom) 0, 1–10. https://doi.org/10.1080/09593330.2020.1732471

**Shi, W., Wang, Q., Long, Y., Cheng, Z., Chen, S., Zheng, H., Huang, Y.,** 2011. Carbon nanodots as peroxidase mimetics and their applications to glucose detection. Chem. Commun. 47, 6695–6697. https://doi.org/10.1039/c1cc11943e

**Shiang, Y.-C., Huang, C.-C., Chang, H.-T.,** 2009. Gold nanodot-based luminescent sensor for the detection of hydrogen peroxide and glucose. Chem. Commun. 3437–3439.

**Singh, S., Jain, D.V.S., Singla, M.L.,** 2015. In-situ electrochemical synthesis of prussian blue composite with gold nanoparticles and its application in hydrogen peroxide biosensor. Adv. Mater. Lett. 6, 760–767. https://doi.org/10.5185/amlett.2015.5796

**Solanki, P.R., Kaushik, A., Ansari, A.A., Sumana, G., Malhotra, B.D.,** 2011. Horse radish peroxidase immobilized polyaniline for hydrogen peroxide sensor. Polym. Adv. Technol. 22, 903–908. https://doi.org/10.1002/pat.1594

**Solís-Oba, M., Ugalde-Saldívar, V.M., González, I., Viniegra-González, G.,** 2005. An electrochemical-spectrophotometrical study of the oxidized forms of the mediator 2,2′-azino-bis-(3-ethylbenzothiazoline-6-sulfonic acid) produced by immobilized laccase. J. Electroanal. Chem. 579, 59–66. https://doi.org/10.1016/j.jelechem.2005.01.025

**Song, J., Guo, J., Liu, Y., Tan, Q., Zhang, S., Yu, Y.,** 2019. A Comparative Study on Properties of Cellulose/Antarctic Krill Protein Composite Fiber by Centrifugal Spinning and Wet Spinning. Fibers Polym. 20, 1547–1554. https://doi.org/10.1007/s12221-019-8725-2

**Song, Y., Wang, X., Zhao, C., Qu, K., Ren, J., Qu, X.,** 2010. Label-free colorimetric detection of single nucleotide polymorphism by using single-walled carbon nanotube intrinsic peroxidase-like activity. Chem. - A Eur. J. 16, 3617–3621. https://doi.org/10.1002/chem.200902643

**Soylemez, S., Kanik, F.E., Uzun, S.D., Hacioglu, S.O., Toppare, L.,** 2014. Development of an efficient immobilization matrix based on a conducting polymer and functionalized multiwall carbon nanotubes: synthesis and its application to ethanol biosensors. J. Mater. Chem. B 2, 511–521. https://doi.org/10.1039/c3tb21356k

**Strong, E.B., Schultz, S.A., Martinez, A.W., Martinez, N.W.,** 2019. Fabrication of Miniaturized Paper-Based Microfluidic Devices (MicroPADs). Sci. Rep. 9, 1–9. https://doi.org/10.1038/s41598-018-37029-0

**Sun, H., Sakka, Y.,** 2014. Luminescent metal nanoclusters : controlled synthesis and functional applications. Sci. Technol. Adv. Mater. 15, 1–13. https://doi.org/10.1088/1468-6996/15/1/014205

**Sun, J., Zhao, J., Wang, L., Li, H., Yang, F., Yang, X.,** 2018. Inner Filter Effect-Based Sensor for Horseradish Peroxidase and Its Application to Fluorescence Immunoassay. ACS Sensors 3, 183–190. https://doi.org/10.1021/acssensors.7b00830

**Taga, K., Weger, S., Göbel, R., Keller, R.,** 1993. Colorimetric activity assays of enzyme-modified MIR fibers. Sensors Actuators B. Chem. 11, 553–559. https://doi.org/10.1016/0925-4005(93)85303-R

**Tao, Y., Li, M., Ren, J., Qu, X.,** 2015. Metal nanoclusters : novel probes for diagnostic and therapeutic applications. Chem. Soc. Rev. https://doi.org/10.1039/c5cs00607d

**Thepchuay, Y., Sonsa-ard, T., Ratanawimarnwong, N., Auparakkitanon, S., Sitanurak, J., Nacapricha, D.,** 2020. Paper-based colorimetric biosensor of blood alcohol with in-situ headspace separation of ethanol from whole blood. Anal. Chim. Acta 1103, 115–121. https://doi.org/10.1016/j.aca.2019.12.043

**Thungon, P.D., Kakoti, A., Ngashangva, L., Goswami, P.,** 2017. Advances in developing rapid, reliable and portable detection systems for alcohol. Biosens. Bioelectron. 97, 83–99. https://doi.org/10.1016/j.bios.2017.05.041

**Thungon, P.D., Kundu, T., Goswami, P.,** 2020. Metal nanoclusters as transducing elements for biosensing applications, *in:* Advance Materials and Techniques for Biosensors and Bioanalytical Applications, Editor:Pranab Goswami, CRC Press Tailor& Francis. ISBN 9781003083856, https://doi.org/10.1201/9781003083856

**Thungon, P.D., Wang, H., Vagin, S.I., Dyck, C.V., Goswami, P., Rieger, B., Meldrum, A.,** 2022. A fluorescent alcohol biosensor using a simple μPAD based detection scheme, Front. Sens, 3, https://www.frontiersin.org/article/10.3389/fsens.2022.840130.

**Tian, J., Liu, Q., Asiri, A.M., Qusti, A.H., Al-Youbi, A.O., Sun, X.,** 2013. Ultrathin graphitic carbon nitride nanosheets: A novel peroxidase mimetic, Fe doping-mediated catalytic performance enhancement and application to rapid, highly sensitive optical detection of glucose. Nanoscale 5, 11604–11609. https://doi.org/10.1039/c3nr03693f

**Tortorich, R.P., Shamkhalichenar, H., Choi, J.W.,** 2018. Inkjet-printed and paper-based electrochemical sensors. Appl. Sci. 8. https://doi.org/10.3390/app8020288

**Trofimchuk, E., Hu, Y., Nilghaz, A., Hua, M.Z., Sun, S., Lu, X.,** 2020. Development of paper-based microfluidic device for the determination of nitrite in meat. Food Chem. 316. https://doi.org/10.1016/j.foodchem.2020.126396

**Varma, S., Mattiasson, B.,** 2005. Amperometric biosensor for the detection of hydrogen peroxide using catalase modified electrodes in polyacrylamide. J. Biotechnol. 119, 172–180. https://doi.org/10.1016/j.jbiotec.2005.01.020

**Vatsyayan, P., Bordoloi, S., Goswami, P.,** 2010. Large catalase based bioelectrode for biosensor application. Biophys. Chem. 153, 36–42. https://doi.org/10.1016/j.bpc.2010.10.002

**Veal, E.A., Day, A.M., Morgan, B.A.,** 2007. Hydrogen Peroxide Sensing and Signaling. Mol. Cell 26, 1–14. https://doi.org/10.1016/j.molcel.2007.03.016

**Vepari, C., Kaplan, D.L.,** 2007. Silk as a biomaterial. Prog. Polym. Sci. 32, 991–1007. https://doi.org/10.1016/j.progpolymsci.2007.05.013

**Vijayakumar, A.R., Csöregi, E., Heller, A., Gorton, L.,** 1996. Alcohol biosensors based on coupled oxidase-peroxidase systems. Anal. Chim. Acta 327, 223–234. https://doi.org/10.1016/0003-2670(96)00093-1

**Wang, B., Liu, F., Wu, Y., Chen, Y., Weng, B., Li, C.M.,** 2018a. Synthesis of catalytically active multielement-doped carbon dots and application for colorimetric detection of glucose. Sensors Actuators, B Chem. 255, 2601–2607. https://doi.org/10.1016/j.snb.2017.09.067

**Wang, G.L., Jin, L.Y., Dong, Y.M., Wu, X.M., Li, Z.J.,** 2015a. Intrinsic enzyme mimicking activity of gold nanoclusters upon visible light triggering and its application for colorimetric trypsin detection. Biosens. Bioelectron. 64, 523–529. https://doi.org/10.1016/j.bios.2014.09.071

**Wang, H., Vagin, S.I., Lane, S., Lin, W., Shyta, V., Heinz, W.R., Van Dyck, C., Bergren, A.J., Gardner, K., Rieger, B., Meldrum, A.,** 2019. Metal-Organic Framework with Color-Switching and Strongly Polarized Emission. Chem. Mater. 31, 5816–5823. https://doi.org/10.1021/acs.chemmater.9b01897

**Wang, H., Vagin, S.I., Rieger, B., Meldrum, A.,** 2020a. An Ultrasensitive Fluorescent Paper-Based CO2 Sensor. ACS Appl. Mater. Interfaces 12, 20507–20513. https://doi.org/10.1021/acsami.0c03405

**Wang, M., Mei, Q., Zhang, K., Zhang, Z.,** 2012. Protein-gold nanoclusters for identification of amino acids by metal ions modulated ratiometric fluorescence. Analyst 137, 1618–1623. https://doi.org/10.1039/c2an16302k

**Wang, N., Li, B., Qiao, F., Sun, J., Fan, H., Ai, S.,** 2015b. Humic acid-assisted synthesis of stable copper nanoparticles as a peroxidase mimetic and their application in glucose detection. J. Mater. Chem. B 3, 7718–7723. https://doi.org/10.1039/c5tb00684h

**Wang, N., Miller, C.J., Wang, P., Waite, T.D.,** 2017. Quantitative determination of trace hydrogen peroxide in the presence of sulfide using the Amplex Red/horseradish peroxidase assay. Anal. Chim. Acta 963, 61–67. https://doi.org/10.1016/j.aca.2017.02.033

**Wang, S., Chen, W., Liu, A.L., Hong, L., Deng, H.H., Lin, X.H.,** 2012b. Comparison of the peroxidase-like activity of unmodified, amino-modified, and citrate-capped gold nanoparticles. ChemPhysChem 13, 1199–1204. https://doi.org/10.1002/cphc.201100906

**Wang, X., Wang, H., Niu, Y., Wang, Y., Feng, L.,** 2020b. A facile AIE fluorescent probe for broad range of pH detection. Spectrochim. Acta - Part A Mol. Biomol. Spectrosc. 226, 117650. https://doi.org/10.1016/j.saa.2019.117650

**Wang, X., Wu, Q., Shan, Z., Huang, Q.,** 2011. BSA-stabilized Au clusters as peroxidase mimetics for use in xanthine detection. Biosens. Bioelectron. 26, 3614–3619. https://doi.org/10.1016/j.bios.2011.02.014

**Wang, Y., Wang, X., Xie, Y., Zhang, K.,** 2018b. Functional nanomaterials through esterification of cellulose: a review of chemistry and application. Cellulose 25, 3703–3731. https://doi.org/10.1007/s10570-018-1830-3

**Wei, H., Wang, E.,** 2013. Nanomaterials with enzyme-like characteristics (nanozymes): next-generation artificial enzymes. Chem. Soc. Rev. 42, 6060–93. https://doi.org/10.1039/c3cs35486e

**Wei, H., Wang, E.,** 2008. Fe3O4 magnetic nanoparticles as peroxidase mimetics and their applications in $H_2O_2$ and glucose detection. Anal. Chem. 80, 2250–2254. https://doi.org/10.1021/ac702203f

**Wei, H., Wang, Z., Yang, L., Tian, S., Hou, C., Lu, Y.,** 2010. Lysozyme-stabilized gold fluorescent cluster: Synthesis and application as $Hg^{2+}$ sensor. Analyst 135, 1406. https://doi.org/10.1039/c0an00046a

**Wen, F., Dong, Y., Feng, L., Wang, S., Zhang, S., Zhang, X.,** 2011. Horseradish Peroxidase Functionalized Fluorescent Gold Nanoclusters for Hydrogen Peroxide Sensing Characterization. Anal. Chem. 83, 1193–1196.

**Whitaker, S.,** 1986. Flow in porous media I: A theoretical derivation of Darcy's law. Transp. Porous Media 1, 3–25. https://doi.org/10.1007/BF01036523

**Wilcoxon, J.P., Abrams, B.L.,** 2006. Synthesis, structure and properties of metal nanoclusters. Chem. Soc. Rev. 35, 1162–1194. https://doi.org/10.1039/b517312b

**Williams, M.B., Reese, H.D.,** 1950. Colorimetric Determination of Ethyl Alcohol. Anal. Chem. 22, 1556–1561.

**Wolfbeis, O.S., Axel, D., Wu, M.,** 2002. A Europium-Ion-Based Luminescent Sensing Probe for Hydrogen Peroxide. Angew. Chemie - Int. Ed. Commun. 1, 4495–4498.

**Won, Y.H., Huh, K., Stanciu, L.A.,** 2011. Au nanospheres and nanorods for enzyme-free electrochemical biosensor applications. Biosens. Bioelectron. 26, 4514–4519. https://doi.org/10.1016/j.bios.2011.05.012

**Wu, D., Deng, X., Huang, X., Wang, K., Liu, Q.,** 2013. Low-cost preparation of photoluminescent carbon nanodots and application as peroxidase mimetics in colorimetric detection of $H_2O_2$ and glucose. J. Nanosci. Nanotechnol. 13, 6611–6616. https://doi.org/10.1166/jnn.2013.7556

**Wu, M., Lin, Z., Schäferling, M., Dürkop, A., Wolfbeis, O.S.,** 2005. Fluorescence imaging of the activity of glucose oxidase using a hydrogen-peroxide-sensitive europium probe. Anal. Biochem. 340, 66–73. https://doi.org/10.1016/j.ab.2005.01.050

**Wu, M., Lin, Z., Wolfbeis, O.S.,** 2003. Determination of the activity of catalase using a europium(III)-tetracycline-derived fluorescent substrate. Anal. Biochem. 320, 129–135. https://doi.org/10.1016/S0003-2697(03)00356-7

**Wu, Y., Shen, Q., Hu, S.,** 2006. Direct electrochemistry and electrocatalysis of heme-proteins in regenerated silk fibroin film. Anal. Chim. Acta 558, 179–186. https://doi.org/10.1016/j.aca.2005.11.031

**Xiao, H., Li, P., Hu, X., Shi, X., Zhang, W., Tang, B.,** 2016. Simultaneous fluorescence imaging of hydrogen peroxide in mitochondria and endoplasmic reticulum during apoptosis. Chem. Sci. 7, 6153–6159. https://doi.org/10.1039/c6sc01793b

**Xie, J., Zheng, Y., Ying, J.Y.,** 2010. Highly selective and ultrasensitive detection ofHg2+ based on fluorescence quenching of Au nanoclusters by $Hg^{2+}$–$Au^{+}$ interactions. Chem. Commun. 46, 961–963. https://doi.org/10.1039/B920748A

**Xie, J., Zheng, Y., Ying, J.Y.,** 2009. Protein-directed synthesis of highly fluorescent gold nanoclusters. J. Am. Chem. Soc. 131, 888–9. https://doi.org/10.1021/ja806804u

**Xu, H.V., Zhao, Y., Tan, Y.N.,** 2019. Nanodot-Directed Formation of Plasmonic-Fluorescent Nanohybrids toward Dual Optical Detection of Glucose and Cholesterol via Hydrogen Peroxide Sensing. ACS Appl. Mater. Interfaces 11, 27233–27242. https://doi.org/10.1021/acsami.9b08708

**Xu, M., Bunes, B.R., Zang, L.,** 2011a. Paper-based vapor detection of hydrogen peroxide: Colorimetric sensing with tunable interface. ACS Appl. Mater. Interfaces 3, 642–647. https://doi.org/10.1021/am1012535

**Xu, S., Zhang, X., Wan, T., Zhang, C.,** 2011b. A third-generation hydrogen peroxide biosensor based on horseradish peroxidase cross-linked to multi-wall carbon nanotubes. Microchim. Acta 172, 199–205. https://doi.org/10.1007/s00604-010-0479-x

**Xu, Y., Sherwood, J., Qin, Y., Crowley, D.,** 2014. The role of protein characteristics in the formation and fluorescence of Au nanoclusters. Nanoscale 6, 1515–1524. https://doi.org/10.1039/c3nr06040c

**Yamada, K., Henares, T.G., Suzuki, K., Citterio, D.,** 2015. Paper-based inkjet-printed microfluidic analytical devices. Angew. Chemie - Int. Ed. 54, 5294–5310. https://doi.org/10.1002/anie.201411508

**Yang, H., Xiao, X., Zhao, X., Wu, Y.,** 2015. Intrinsic Fluorescence Spectra of Tryptophan, Tyrosine and Phenyloalanine, in: 5th International Conference on Advanced Design and Manufacturing Engineering (ICADME 2015). pp. 224–233. https://doi.org/10.2991/icadme-15.2015.46

**You, X., Pak, J.J.,** 2014. Graphene-based field effect transistor enzymatic glucose biosensor using silk protein for enzyme immobilization and device substrate. Sensors Actuators, B Chem. 202, 1357–1365. https://doi.org/10.1016/j.snb.2014.04.079

**Yu, F., Huang, Y., Cole, A.J., Yang, V.C.,** 2009. The artificial peroxidase activity of magnetic iron oxide nanoparticles and its application to glucose detection. Biomaterials 30, 4716–4722. https://doi.org/10.1016/j.biomaterials.2009.05.005

**Yunker, P.J., Still, T., Lohr, M.A., Yodh, A.G.,** 2011. Suppression of the coffee-ring effect by shape-dependent capillary interactions. Nature 476, 308–311. https://doi.org/10.1038/nature10344

**Yunus, S., Attout, A., Vanlancker, G., Bertrand, P., Ruth, N., Galleni, M.,** 2011. A method to probe electrochemically active material state in portable sensor applications. Sensors Actuators, B Chem. 156, 35–42. https://doi.org/10.1016/j.snb.2011.03.070

**Żamojć, K., Zdrowowicz, M., Jacewicz, D., Wyrzykowski, D., Chmurzyński, L.,** 2016. Fluorescent Probes Used for Detection of Hydrogen Peroxide under Biological Conditions. Crit. Rev. Anal. Chem. 46, 171–200. https://doi.org/10.1080/10408347.2015.1014085

**Zdarta, J., Meyer, A.S., Jesionowski, T., Pinelo, M.,** 2018. A general overview of support materials for enzyme immobilization: Characteristics, properties, practical utility. Catalysts 8. https://doi.org/10.3390/catal8020092

**Zeng, D., Luo, W., Li, J., Liu, H., Ma, H., Huang, Q., Fan, C.,** 2012. Gold nanoparticles-based nanoconjugates for enhanced enzyme cascade and glucose sensing. Analyst 137, 4435–4439. https://doi.org/10.1039/c2an35900f

**Zeng, H.H., Qiu, W. Bin, Zhang, L., Liang, R.P., Qiu, J.D.,** 2016. Lanthanide Coordination Polymer Nanoparticles as an Excellent Artificial Peroxidase for Hydrogen Peroxide Detection. Anal. Chem. 88, 6342–6348. https://doi.org/10.1021/acs.analchem.6b00630

**Zhai, J., Zhai, Y., Wen, D., Dong, S.,** 2009. Prussian blue/multiwalled carbon nanotube hybrids: Synthesis, assembly and electrochemical behavior. Electroanalysis 21, 2207–2212. https://doi.org/10.1002/elan.200904680

**Zhang, L., Wang, E.,** 2014. Metal nanoclusters: New fluorescent probes for sensors and bioimaging. Nano Today 9, 132–157. https://doi.org/10.1016/j.nantod.2014.02.010

**Zhang, T., Fan, H., Liu, G., Jiang, J., Zhou, J., Jin, Q.,** 2008. Different effects of Fe2+ and Fe3+ on conjugated polymer PPESO3: A novel platform for sensitive assays of hydrogen peroxide and glucose. Chem. Commun. 5414–5416. https://doi.org/10.1039/b808586b

**Zhang, Y., Sun, Y., Liu, Z., Xu, F., Cui, K., Shi, Y., Wen, Z., Li, Z.,** 2011. Au nanocages for highly sensitive and selective detection of H 2O2. J. Electroanal. Chem. 656, 23–28. https://doi.org/10.1016/j.jelechem.2011.01.037

**Zhang, Y., Tsitkov, S., Hess, H.,** 2016. Proximity does not contribute to activity enhancement in the glucose oxidase-horseradish peroxidase cascade. Nat. Commun. 7, 1–9. https://doi.org/10.1038/ncomms13982

**Zhang, Y., Zhang, C., Xu, C., Wang, X., Liu, C., Waterhouse, G.I.N., Wang, Y., Yin, H.,** 2019. Ultrasmall Au nanoclusters for biomedical and biosensing applications : A mini-review. Talanta 200, 432–442. https://doi.org/10.1016/j.talanta.2019.03.068

**Zhao, Q., Chen, S., Huang, H., Zhang, L., Wang, L., Liu, F., Chen, J., Zeng, Y., Chu, P.K.,** 2014. Colorimetric and ultra-sensitive fluorescence resonance energy transfer determination of $H_2O_2$ and glucose by multi-functional Au nanoclusters. Analyst 139, 1498–1503. https://doi.org/10.1039/c3an01906c

**Zhao, Z., Jiang, H.,** 2010. Enzyme-based Electrochemical Biosensors, in: Biosensors Edited by Pier Andrea Serra. ISBN 978-953-7619-99-2, InTech, pp. 1–21. https://doi.org/10.5772/7200

**Zheng, A.X., Cong, Z.X., Wang, J.R., Li, J., Yang, H.H., Chen, G.N.,** 2013. Highly-efficient peroxidase-like catalytic activity of graphene dots for biosensing. Biosens. Bioelectron. 49, 519–524. https://doi.org/10.1016/j.bios.2013.05.038

**Zheng, J., Nicovich, P.R., Dickson, R.M.,** 2007. Highly Fluorescent Noble-Metal Quantum Dots. Annu. Rev. Phys. Chem. 58, 409–431. https://doi.org/10.1146/annurev.physchem.58.032806.104546

**Zheng, J., Petty, J.T., Dickson, R.M.,** 2003. High Quantum Yield Blue Emission from Water-Soluble Au 8 Nanodots. J. Am. Chem. Soc. 125, 7780–7781.

**Zheng, J., Zhang, C., Dickson, R.M.,** 2004. Highly fluorescent, water-soluble, size-tunable gold quantum dots. Phys. Rev. Lett. 93, 5–8. https://doi.org/10.1103/PhysRevLett.93.077402

**Zheng, M., Li, P., Yang, C., Zhu, H., Chen, Y., Tang, Y., Zhou, Y., Lu, T.,** 2012. Ferric ion immobilized on three-dimensional nanoporous gold films modified with self-assembled monolayers for electrochemical detection of hydrogen peroxide. Analyst 137, 1182–1189. https://doi.org/10.1039/c2an15957k

**Zheng, Y., Lai, L., Liu, W., Jiang, H., Wang, X.,** 2017. Recent advances in biomedical applications of fluorescent gold nanoclusters. Adv. Colloid Interface Sci. 242, 1–16. https://doi.org/10.1016/j.cis.2017.02.005

**Zheng, Z.Q., Yao, J.D., Wang, B., Yang, G.W.,** 2015. Light-controlling , flexible and transparent ethanol gas sensor based on ZnO nanoparticles for wearable devices. Nat. Publ. Gr. 1–8. https://doi.org/10.1038/srep11070

**Zhou, M., Diwu, Z., Panchuk-Voloshina, N., Haugland, R.P.,** 1997. A stable nonfluorescent derivative of resorufin for the fluorometric determination of trace hydrogen peroxide: Applications in detecting the activity of phagocyte NADPH oxidase and other oxidases. Anal. Biochem. 253, 162–168. https://doi.org/10.1006/abio.1997.2391

**Zhou, M., Zhai, Y., Dong, S.,** 2009. Electrochemical sensing and biosensing platform based on chemically reduced graphene oxide. Anal. Chem. 81, 5603–5613. https://doi.org/10.1021/ac900136z

**Zhou, Z., Shi, Z., Cai, X., Zhang, S., Corder, S.G., Li, X., Zhang, Y., Zhang, G., Chen, L., Liu, M., Kaplan, D.L., Omenetto, F.G., Mao, Y., Tao, Z., Tao, T.H.,** 2017. The Use of Functionalized Silk Fibroin Films as a Platform for Optical Diffraction-Based Sensing Applications. Adv. Mater. 29, 1605471. https://doi.org/10.1002/adma.201605471

# LIST OF PUBLICATIONS AND AWARDS

## Patents filed

1. Pranab Goswami, Mallesh Santhosh, Priyanki Das, **Phurpa D Thungon**.
   Title of the invention: Silk sericin enhances the conductivity and stability of graphite paste ink. Patent No. 348844 / Application No. 201631022633 / Patentee: Prof. Pranab Goswami (**Granted and published**).

2. Pranab Goswami, Naveen Kumar Singh, **Phurpa Dema Thungon**, Vinay Bachu.
   Title of the invention: A modified syringe for detection of various enzymes for various instrument free detection. (Application No. 201831030902)

## Publications in Refereed journals

1. **Phurpa Dema Thungon**, Pooja Rani Kuri, Vinay Bachu and Pranab Goswami, Silk-fibroin film as enzyme stabilizing material and optical signal transducer for developing μPAD methanol biosensor, ***Biosensors and Bioelectronics-X*** (2022), Volume 11,100147, https://doi.org/10.1016/j.biosx.2022.100147.

2. **Phurpa Dema Thungon**, Hui Wang, Sergei I. Vagin, Colin Van Dyck, Pranab Goswami, B. Rieger, Alkiviathes Meldrum, A fluorescent alcohol biosensor using a simple μPAD based detection scheme, ***Frontiers in Sensors*** (2022), Volume 3, 10.3389/fsens.2022.840130.

3. Sharbani Kaushik, **Phurpa Dema Thungon (Equal 1st author contribution),** and Pranab Goswami, Silk Fibroin: An Emerging Biocompatible Material for Application of Enzymes and Whole Cells in Bioelectronics and Bioanalytical Sciences, ***ACS Biomaterials Science & Engineering*** **(**2020), 6 (8), 4337-4355, https://doi.org/10.1021/acsbiomaterials.9b01971

4. Naveen Kumar Singh, **Phurpa Dema Thungon**, Pedro Estrela, Pranab Goswami, Development of an aptamer-based field effect transistor biosensor for quantitative detection of Plasmodium falciparum glutamate dehydrogenase in serum samples, ***Biosensors and Bioelectronics***, (2019),123, 30-35, https://doi.org/10.1016/j.bios.2018.09.085.

5. **Phurpa Dema Thungon**, Ankana Kakoti (Equal 1st author contribution), Lightson Ngashangva (Equal 1st author contribution), Pranab Goswami, Advances in developing rapid, reliable and

portable detection systems for alcohol. ***Biosensors and Bioelectronics*** (2017), 15 (97) 83-99. doi: 10.1016/j.bios.2017.05.041

**6.** Sharbani Kaushik, Mrinal Kumar Sarma, **Phurpa Dema Thungon**, Mallesh Santhosh, Pranab Goswami, Thin films of silk-fibroin and its blend with chitosan strongly promote biofilm growth of Synechococcus sp. BDU 140432, ***Journal of Colloid and Interface Science*** (2016), 479, 251-259. doi: 10.1016/j.jcis.2016.06.065.

## Book Chapter:

1. **Phurpa Dema Thungon**, Torsha Kundu and Pranab Goswami, Metal Nanoclusters as Signal transducing element in: Advance Materials and Techniques for Biosensors and Bioanalytical Applications, Editor:Pranab Goswami, ***CRC Press Tailor& Francis***, 2021. ISBN 9781003083856, https://doi.org/10.1201/9781003083856.

## Award:

1. Selected under SERB-University of Alberta Overseas Visiting Doctoral Fellowship to work as visiting PhD scholar in University of Alberta (1st May 2019- 31st July 2020)

## Conference/workshop Proceedings:

1. Pooja Rani Kuri, **Phurpa Dema Thungon**, Pranab Goswami, Two Dimensional µPAD for alcohol detection, Research Conclave (2019), IIT Guwahati.

2. **Phurpa Dema Thungon**, Torsha Kundu, Pranab Goswami, Studies on the two types of fluorescent gold nanoclusters stabilized by catalase, Frontiers in Chemical Sciences (FICS - 2018).

3. **Phurpa Dema Thungon**, Torsha Kundu, Naveen Kumar Singh, Pranab Goswami, Study of enzyme stability in silk films to develop biosensors, International Conference on Advancement in Science and Technology (ICAST-2018).

4. **Phurpa Dema Thungon**, Torsha Kundu, Naveen Kumar Singh, Pranab Goswami, Silk Stabilized fluorescent AuNCs: Synthesis and application for sensing, International Conference on Advanced Nanomaterials and Nanotechnology (ICANN-2017) December 19-23, (2017).

5. Naveen Kumar Singh, **Phurpa Dema Thungon**, Vinay B, Pranab Goswami, Development of Plasmodium falciparum glutamate dehydrogenase based sensor for Malaria. International conference on advance in biological system and material science in nano world (ABSMSNW-2017) February 19-23, (2017).

6. **Phurpa Dema Thungon**, Naveen Kumar Singh, Pranab Goswami, Study of Peroxidase mimicking agents/ Nanoenzymes for development of alcohol biosensors, IUMRS-International Conference of Young Researchers on Advanced Materials (IUMRS-ICYRAM 2016) December 11-15, (2016).

# Front Page of the Papers and Book chapter published

11 (2022) 100147

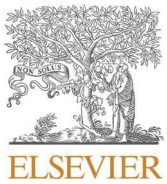

Contents lists available at ScienceDirect

Biosensors and Bioelectronics: X

journal homepage: www.journals.elsevier.com/biosensors-and-bioelectronics-x

# Silk-fibroin film as enzyme stabilizing material and optical signal transducer for developing alcohol oxidase-based μPAD methanol biosensor

Phurpa Dema Thungon, Pooja Rani Kuri, Vinay Bachu, Pranab Goswami *

*Department of Biosciences and Bioengineering, Indian Institute of Technology Guwahati, Assam, 781039, India*

ARTICLE INFO

*Keywords:*
Silk fibroin
Alcohol oxidase
ABTS
Peroxidase
Enzyme stability
Methanol biosensors
Coffee ring effect
μPAD

ABSTRACT

The commercial success of paper-based microfluidic biosensor devices with enzyme as recognition elements may be achieved greatly by improving the enzyme stability, averting the coffee-ring effect on the detection zone, and making it a stand-alone system. We have addressed these issues here by introducing silk-fibroin (SF) film for immobilizing enzymes and chromogenic reagent (ABTS), and wave-design microfluidic channels in the chromatographic paper for developing a hybrid microfluidic paper-based analytical device (μPAD), for methanol detection through peroxidase reaction. The activity of alcohol oxidase (AOx), used as a biorecognition element, could be wholly retained in a non-dissolvable SF film (pore size <3.5 μm) until 40 days of storage at room temperature (RT) by reducing oxygen permeability to the film. Similarly, ABTS in a dissolvable SF film was protected from air-oxidation even up to two months of storage at RT. The detection approach exploited purple color as a high contrast response signal generated from ABTS di-cation formed from the reaction of SF protein with the ABTS radicals generated from the substrate-dependent peroxidase reaction. The wave-designed microfluidic channels could significantly reduce the coffee ring effect in the detection film. The bi-enzyme SF films prepared by co-immobilizing AOx with peroxidase (HRP) offered high sensitivity to the device with a detection limit (LoD) of 1 ± 0.05 mM and a dynamic range of 1 mM–2 M for methanol. The stand-alone hybrid μPAD biosensor for methanol has a high potential for commercial applications.

## 1. Introduction

Alcohol sensors for methanol have high importance in the field of fuel, fermentation, pharmaceuticals, and forensic analysis. Currently available devices for sensing alcohol are based on the chemical, electrochemical, and infrared (IR) principles that are mostly, expensive, less selective and technically complex systems (Thungon et al., 2017). Efforts are on to introduce alcohol biosensors to make these devices more selective. The biorecognition elements used to develop alcohol biosensors are few, among which alcohol oxidase (AOx) and alcohol dehydrogenase are prominent (Goswami et al., 2013). The major advantage of AOx over its dehydrogenase counterpart lies in its ability to function independently since its co-factor (Flavin adenine dinucleotide) is avidly bound to the redox center; this obviates the need of supplementing the cofactor to the reaction medium during the operation. However, applications of AOx in the commercial paradigm are yet to be witnessed because of its limited stability (Thungon et al., 2017). A critical finding emerged recently indicating that the AOx activity rapidly declined upon its constant interaction with molecular oxygen, an electron acceptor for the enzyme-catalyzed reaction (Das et al., 2022). Hence, to improve the enzyme's stability, a suitable biocompatible immobilization material needs to be explored that should additionally be able to screen the atmospheric oxygen from the enzyme under the storage conditions.

The important features required for the immobilization support material are its availability, low cost, biocompatibility, and chemical and thermal stability (Zdarta et al., 2018). The emerging biomaterials, silk fibroin (SF), and paper are expected to fulfill these requirements. SF, a fibrous protein found in the cocoons of *Bombyx mori* (*B. mori*), is a versatile biomaterial due to its good thermal stability and biocompatibility (Drachuk et al., 2013; Kaushik et al., 2020). Moreover, it could be transformed into different types of scaffolds, such as fiber, film, or hydrogels (Vepari and Kaplan, 2007). There are few reports on the immobilization of less complex enzymes such as horseradish peroxidase (HRP) (Lu et al., 2009b, 2010), glucose oxidase (GOx) (Lu et al., 2009a; You and Pak, 2014), and cholesterol oxidase (Saxena and Goswami, 2010) in silk fibroins. However, investigations on the immobilization of AOx and other complex multimeric enzymes in silk-fibroins have not

* Corresponding author.
*E-mail address:* pgoswami@iitg.ac.in (P. Goswami).

https://doi.org/10.1016/j.biosx.2022.100147
Received 29 December 2021; Received in revised form 1 April 2022; Accepted 12 April 2022
Available online 3 May 2022

frontiers | Frontiers in Sensors

ORIGINAL RESEARCH
published: 04 May 2022
doi: 10.3389/fsens.2022.840130

# A Fluorescent Alcohol Biosensor Using a Simple microPAD Based Detection Scheme

*Phurpa Dema Thungon*[1,2], *Hui Wang*[1], *Sergei I. Vagin*[3], *Colin Van Dyck*[4], *Pranab Goswami*[2], *B. Rieger*[3] *and Alkiviathes Meldrum*[1]*

[1]Department of Physics, University of Alberta, Edmonton, AB, Canada, [2]Department of Biosciences and Bioengineering, Indian Institute of Technology Guwahati, Guwahati, India, [3]Wacker Chair of Macromolecular Chemistry, Technical University of Munich, Munich, Germany, [4]Department of Physics, University of Mons, Mons, Belgium

A paper-based microfluidic detection device for the detection of ethanol is demonstrated in this work. The method is based on a fluorophore consisting of short-chain conjugated molecular unit susceptible to the protonation of its terminal pyridine groups, along with a carboxyl-functionalized sidechain that acts as a binder and renders it water-soluble. The resulting fluorescent paper device yields large fluorescence changes when exposed to reactions that yield $H_2O_2$ in aqueous solutions. Using an enzyme-catalyzed rection that produces $H_2O_2$ from ethanol, we developed a two-zone, cut-out paper device containing a reaction zone in which the ethanol-containing analyte is placed, and an adjacent sensor zone where we observe a fluorescence color shift proportional to the ethanol concentration. The limit of detection of the fluidic ethanol biosensor was 0.05 v/v% and the dynamic range was 0.05–2 v/v%. This method was employed to detect the alcohol concentration of consumer vodkas using only a paper sensor and a smartphone camera.

**Keywords: paper, fluorescence, hydrogen peroxide, ethanol, sensor, alcohol**

OPEN ACCESS

***Edited by:***
*Chatchawal Wongchoosuk, Kasetsart University, Thailand*

***Reviewed by:***
*Daniel S. Correa, Brazilian Agricultural Research Corporation (EMBRAPA), Brazil*
*Chalongrat Daengngam, Prince of Songkla University, Thailand*

***Correspondence:**
*Alkiviathes Meldrum*
*ameldrum@ualberta.ca*

***Specialty section:***
*This article was submitted to Chemical Sensors, a section of the journal Frontiers in Sensors*

***Received:*** *20 December 2021*
***Accepted:*** *18 March 2022*
***Published:*** *04 May 2022*

***Citation:***
*Thungon PD, Wang H, Vagin SI, Dyck CV, Goswami P, Rieger B and Meldrum A (2022) A Fluorescent Alcohol Biosensor Using a Simple microPAD Based Detection Scheme. Front. Sens. 3:840130. doi: 10.3389/fsens.2022.840130*

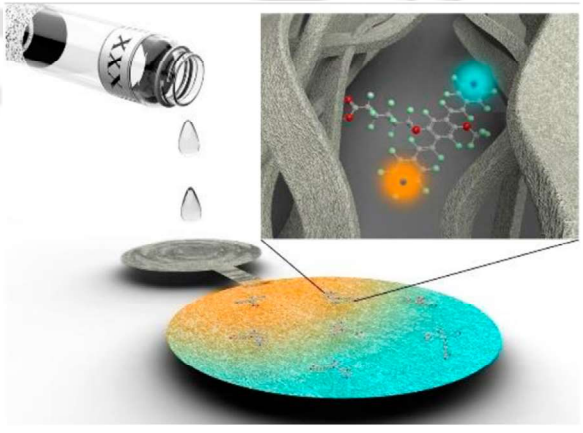

**GRAPHICAL ABSTRACT |**

ACS Biomaterials SCIENCE & ENGINEERING

pubs.acs.org/journal/abseba

Review

# Silk Fibroin: An Emerging Biocompatible Material for Application of Enzymes and Whole Cells in Bioelectronics and Bioanalytical Sciences

Sharbani Kaushik,[§] Phurpa Dema Thungon,[§] and Pranab Goswami*

Cite This: *ACS Biomater. Sci. Eng.* 2020, 6, 4337−4355

Read Online

ACCESS | Metrics & More | Article Recommendations

**ABSTRACT:** Enzymes and whole cells serve as the active biological entities in a myriad of applications including bioprocesses, bioanalytics, and bioelectronics. Conserving the natural activity of these functional biological entities during their prolonged use is one of the major goals for validating their practical applications. Silk fibroin (SF) has emerged as a biocompatible material to interface with enzymes as well as whole cells. These biomaterials can be tailored both physically and chemically to create excellent scaffolds of different forms such as fibers, films, and powder for immobilization and stabilization of enzymes. The secondary structures of the SF-protein can be attuned to generate hydrophobic/hydrophilic pockets suitable to create the biocompatible microenvironments. The fibrous nature of the SF protein with a dominant hydrophobic property may also serve as an excellent support for promoting cellular adhesion and growth. This review compiles and discusses the recent literature on the application of SF as a biocompatible material at the interface of enzymes and cells in various fields, including the emerging area of bioelectronics and bioanalytical sciences.

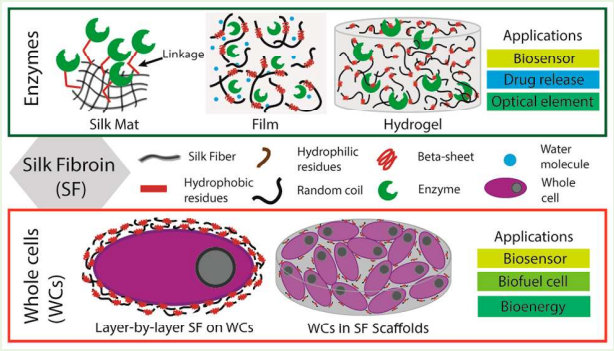


**KEYWORDS:** *silk fibroin, enzymes, whole cells, biocompatible, bioelectronics, biosensors, biofuel cell*

## 1. INTRODUCTION

The biobased electronics and analytical devices, such as biosensors and biofuel cells, have gained tremendous research interest over the past decade owing to their great application potential in the field of healthcare, biomedical sciences, environmental studies, and sports.[1,2] One of the critical issues that decides the commercial success of such biobased devices is their stability, which considers both the shelf- and operational life of the construct. The active biological entities (e.g., enzyme, cells, antibody) being used to emulate the desired functionality to the device is mainly responsible for the stability issues. A strategy that is widely adopted to prolong the functional (catalytic, interactive, metabolic, etc.) activity and vitality of the biological entities is their immobilization into a suitable biocompatible material or platform. Such support systems should also be resilient mechanically and chemically as well as offer easy diffusion of the substrates or targets to facilitate the intended biocatalytic or metabolic function of the entities.[3] The other objective of the immobilization is to improve the cost economy of the product or device as this action enables one to recycle the biological entities. For some applications of the microbial cells such as in biofuel cells and biocatalytic processes, the platform that supports dense microbial- or biofilm growth is also desired additionally. Exploring novel biocompatible platforms that support fast microbial- or biofilm growth has been an active area of research in recent times, particularly in the field of bioenergy and bioprocesses.[4,5]

Several natural as well as synthetic polymers, bioinks, and polyelectrolyte solutions have been assessed for their "enzyme/cell-bearing" abilities as scaffolds, capsules, or films with their set of advantages and setbacks.[6,7] Of late, bio-based materials have received enormous importance in the field owing to their natural placid and biocompatible properties for housing labile protein-based enzymes and even bacterial cells.[7−9] The silk fibroin (SF), a biomaterial of emerging applications in different fields, is yet to be adequately explored as a support material for enzymes and microorganisms for application in the field of bioelectronics and bioanalytical sciences.

**Received:** December 26, 2019
**Accepted:** June 16, 2020
**Published:** June 17, 2020

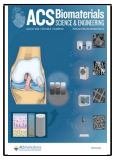







https://dx.doi.org/10.1021/acsbiomaterials.9b01971
*ACS Biomater. Sci. Eng.* 2020, 6, 4337−4355

Biosensors and Bioelectronics 97 (2017) 83–99

Contents lists available at ScienceDirect

Biosensors and Bioelectronics

journal homepage: www.elsevier.com/locate/bios

# Advances in developing rapid, reliable and portable detection systems for alcohol

Phurpa Dema Thungon[1], Ankana Kakoti[1], Lightson Ngashangva[1], Pranab Goswami*

*Department of Biosciences and Bioengineering, Indian Institute of Technology Guwahati, Guwahati, Assam 781039, India*

ARTICLE INFO

*Keywords:*
Alcohol detection
Sensors
Biosensors
Enzymatic
Microbial
Lab-on-chip

ABSTRACT

Development of portable, reliable, sensitive, simple, and inexpensive detection system for alcohol has been an instinctive demand not only in traditional brewing, pharmaceutical, food and clinical industries but also in rapidly growing alcohol based fuel industries. Highly sensitive, selective, and reliable alcohol detections are currently amenable typically through the sophisticated instrument based analyses confined mostly to the state-of-art analytical laboratory facilities. With the growing demand of rapid and reliable alcohol detection systems, an all-round attempt has been made over the past decade encompassing various disciplines from basic and engineering sciences. Of late, the research for developing small-scale portable alcohol detection system has been accelerated with the advent of emerging miniaturization techniques, advanced materials and sensing platforms such as lab-on-chip, lab-on-CD, lab-on-paper etc. With these new inter-disciplinary approaches along with the support from the parallel knowledge growth on rapid detection systems being pursued for various targets, the progress on translating the proof-of–concepts to commercially viable and environment friendly portable alcohol detection systems is gaining pace. Here, we summarize the progress made over the years on the alcohol detection systems, with a focus on recent advancement towards developing portable, simple and efficient alcohol sensors.

## 1. Introduction

Rapid, sensitive, selective and quantitative detection of alcohols have great importance in law enforcement and forensic sectors, and clinical-, chemical-, pharmaceutical- and fermentation- industries (Azevedo et al., 2005; Patel et al., 2001). Conventionally, chromatography and its coupling with various spectrometric techniques have been used for reliable and sensitive detection of alcohols. These classical methods are however, complex, expensive, time consuming and difficult to use in onsite measurements. Most of the current and future requirements, including in rapidly growing alcohol based fuel industries, however, demand portable, low cost, and selective alcohol detection system. There has been a paradigm shift of research interest from the lab to field based alcohol detection systems over the last decade. Different alcohol sensors have been developed by adopting physical, chemical and biological tenets through independent as well as interdisciplinary approaches. A parallel effort to develop Lab-on-Chip based miniaturized platforms for detection of alcohol has been also taking stride by integrating knowledge from various fields and techniques, such as, microelectromechanical system (MEMS) and micro fluidics. The progress made on the subject during the last decade is enormous which justifies forwarding a comprehensive review on it for ready reference of the interested readers. Here, we made an effort to summarize various methods and techniques evolved so far for the detection of alcohols with a major focus on ethanol sensors. The detection approaches have been delineated into different categories encompassing the conventional sophisticated instrument based systems, physical, chemical and biological sensors and emerging miniaturized platforms being developed by integrating concepts and techniques from multiple disciplines. Finally, a critical assessment on the developed systems and future prospects on the field have been highlighted.

## 2. Conventional Instrument based analysis of alcohols

The use of alcoholic beverages is associated with the genesis of civilization and on record, beer brewing has been practiced since the 6th millennium BC (Arnold, 1911). Different primitive alcohol detection methods were evolved among which, the densitometry based alcoholmeter is relatively better known (Gay-Lussac, 1824). Over the

* Corresponding author.
*E-mail address:* pgoswami@iitg.ernet.in (P. Goswami).
[1] Equal 1st author contributions.

http://dx.doi.org/10.1016/j.bios.2017.05.041
Received 6 March 2017; Received in revised form 16 May 2017; Accepted 22 May 2017
Available online 25 May 2017
0956-5663/

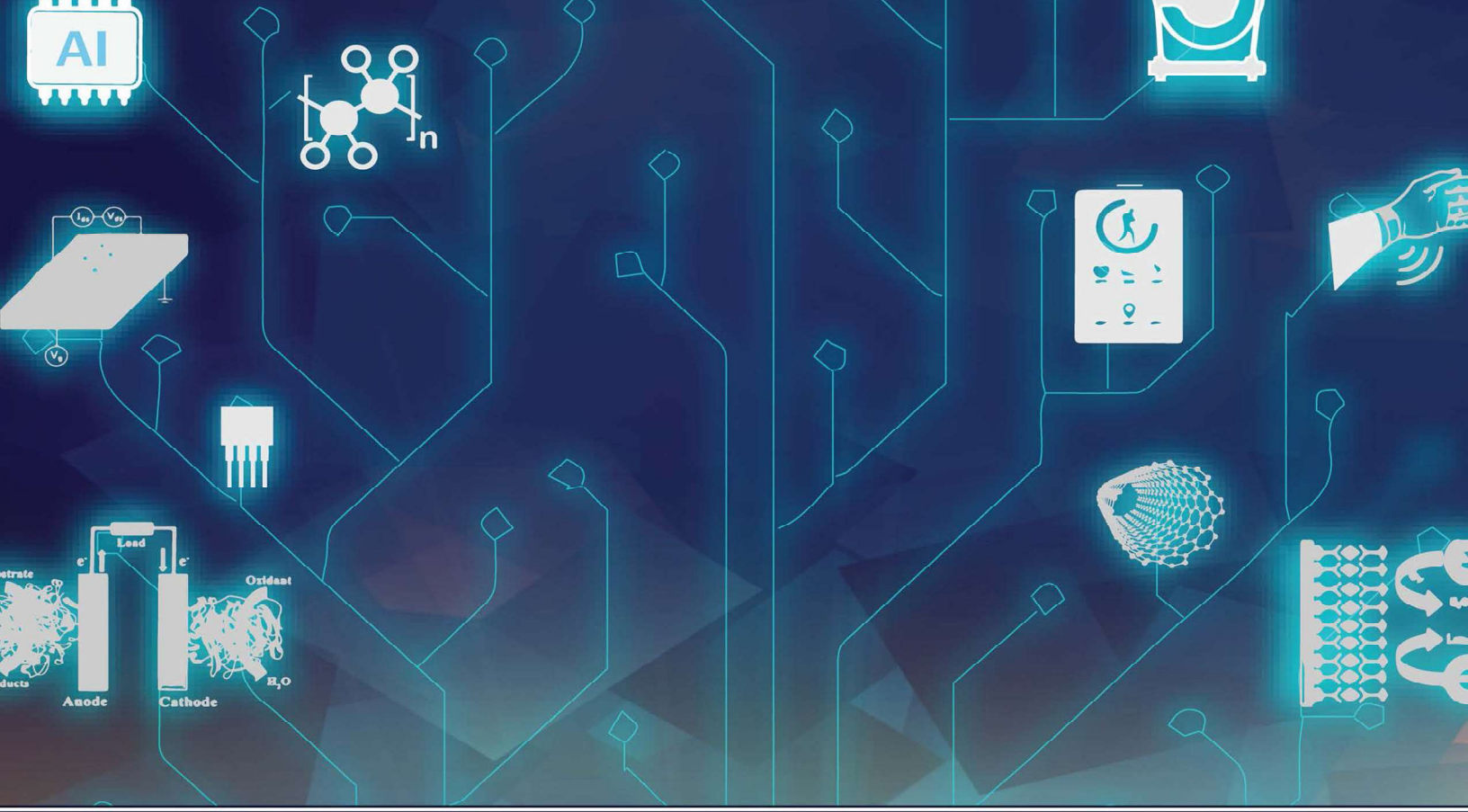


# ADVANCED MATERIALS AND TECHNIQUES FOR BIOSENSORS AND BIOANALYTICAL APPLICATIONS

EDITED BY

PRANAB GOSWAMI

CRC Press
Taylor & Francis Group

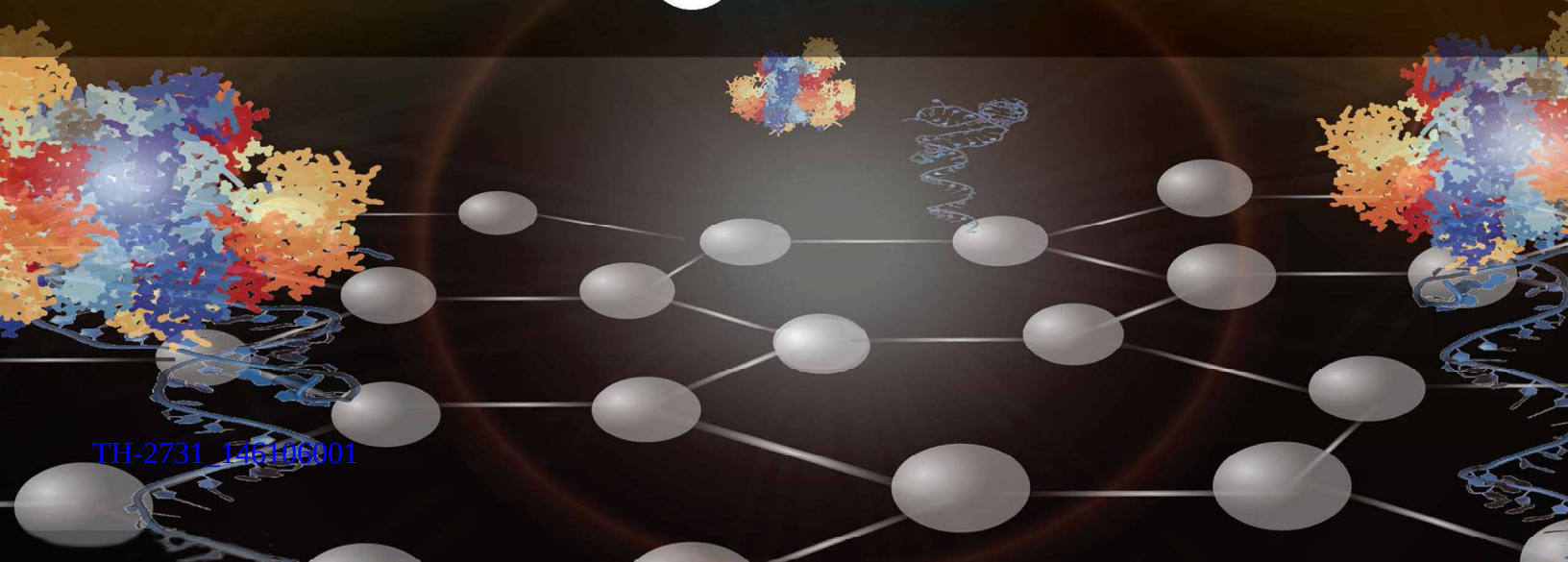

# 6 Metal Nanoclusters as Signal Transducing Element

*Phurpa Dema Thungon and Pranab Goswami*
Indian Institute of Technology Guwahati, Assam, India

*Torsha Kundu*
International Management Institute, Kolkata, India

## CONTENTS

# COPYRIGHT PERMISSIONS

## The Molecular Mechanism of the Catalase-like Activity in Horseradish Peroxidase

**Author:** Pablo Campomanes, Ursula Rothlisberger, Mercedes Alfonso-Prieto, et al

**Publication:** Journal of the American Chemical Society

**Publisher:** American Chemical Society

**Date:** Sep 1, 2015



### PERMISSION/LICENSE IS GRANTED FOR YOUR ORDER AT NO CHARGE

This type of permission/license, instead of the standard Terms and Conditions, is sent to you because no fee is being charged for your order. Please note the following:

- Permission is granted for your request in both print and electronic formats, and translations.
- If figures and/or tables were requested, they may be adapted or used in part.
- Please print this page for your records and send a copy of it to your publisher/graduate school.
- Appropriate credit for the requested material should be given as follows: "Reprinted (adapted) with permission from {COMPLETE REFERENCE CITATION}. Copyright {YEAR} American Chemical Society." Insert appropriate information in place of the capitalized words.
- One-time permission is granted only for the use specified in your RightsLink request. No additional uses are granted (such as derivative works or other editions). For any uses, please submit a new request.

If credit is given to another source for the material you requested from RightsLink, permission must be obtained from that source.

BACK CLOSE WINDOW



TH-2731_146106001

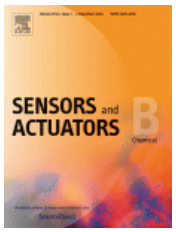

## Highly selective SPR based fiber optic sensor for the detection of hydrogen peroxide

**Author:** Vivek Semwal,Banshi D. Gupta

**Publication:** Sensors and Actuators B: Chemical

**Publisher:** Elsevier

**Date:** 15 February 2021



## Order Completed

Thank you for your order.

This Agreement between Indian Institute of Technology Guwahati -- Phurpa Thungon ("You") and Elsevier ("Elsevier") consists of your license details and the terms and conditions provided by Elsevier and Copyright Clearance Center.

Your confirmation email will contain your order number for future reference.

| | |
|---|---|
| License Number | 5261751402579 |
| License date | Mar 04, 2022 |

Printable Details

### Licensed Content

| | |
|---|---|
| Licensed Content Publisher | Elsevier |
| Licensed Content Publication | Sensors and Actuators B: Chemical |
| Licensed Content Title | Highly selective SPR based fiber optic sensor for the detection of hydrogen peroxide |
| Licensed Content Author | Vivek Semwal,Banshi D. Gupta |
| Licensed Content Date | Feb 15, 2021 |
| Licensed Content Volume | 329 |
| Licensed Content Issue | n/a |
| Licensed Content Pages | 1 |

### Order Details

| | |
|---|---|
| Type of Use | reuse in a thesis/dissertation |
| Portion | figures/tables/illustrations |
| Number of figures/tables/illustrations | 1 |
| Format | both print and electronic |
| Are you the author of this Elsevier article? | No |
| Will you be translating? | No |

### About Your Work

| | |
|---|---|
| Title | Exploring optical sensors for Hydrogen Peroxide on silk and paper platforms using chemical dye, peroxidase and gold nanoclusters as signal generating systems |
| Institution name | Indian Institute of Technology Guwahati |
| Expected presentation date | May 2022 |

### Additional Data

| | |
|---|---|
| Portions | Figure 6 |

## Requestor Location

| | |
|---|---|
| Requestor Location | Indian Institute of Technology Guwahati<br>A 227, Subansiri Hostel<br>IIT Guwahati<br><br>Guwahati, Assam 781039<br>India<br>Attn: Indian Institute of Technology Guwahati |

## Tax Details

| | |
|---|---|
| Publisher Tax ID | GB 494 6272 12 |

## Price

| | |
|---|---|
| Total | 0.00 USD |

Total: 0.00 USD

CLOSE WINDOW ORDER MORE



TH-2731_146106001

## Inner Filter Effect-Based Sensor for Horseradish Peroxidase and Its Application to Fluorescence Immunoassay

**Author:** Jian Sun, Jiahui Zhao, Lei Wang, et al
**Publication:** ACS Sensors
**Publisher:** American Chemical Society
**Date:** Jan 1, 2018



### PERMISSION/LICENSE IS GRANTED FOR YOUR ORDER AT NO CHARGE

This type of permission/license, instead of the standard Terms and Conditions, is sent to you because no fee is being charged for your order. Please note the following:

- Permission is granted for your request in both print and electronic formats, and translations.
- If figures and/or tables were requested, they may be adapted or used in part.
- Please print this page for your records and send a copy of it to your publisher/graduate school.
- Appropriate credit for the requested material should be given as follows: "Reprinted (adapted) with permission from {COMPLETE REFERENCE CITATION}. Copyright {YEAR} American Chemical Society." Insert appropriate information in place of the capitalized words.
- One-time permission is granted only for the use specified in your RightsLink request. No additional uses are granted (such as derivative works or other editions). For any uses, please submit a new request.

If credit is given to another source for the material you requested from RightsLink, permission must be obtained from that source.

BACK CLOSE WINDOW

## Nickel metal-organic framework 2D nanosheets with enhanced peroxidase nanozyme activity for colorimetric detection of H2O2

**Author:** Jingyuan Chen,Yun Shu,Huilei Li,Qin Xu,Xiaoya Hu

**Publication:** Talanta

**Publisher:** Elsevier

**Date:** 1 November 2018



### Order Completed

Thank you for your order.

This Agreement between Indian Institute of Technology Guwahati -- Phurpa Thungon ("You") and Elsevier ("Elsevier") consists of your license details and the terms and conditions provided by Elsevier and Copyright Clearance Center.

Your confirmation email will contain your order number for future reference.

| | |
|---|---|
| License Number | 5261760492996 |
| License date | Mar 04, 2022 |

Printable Details

## Licensed Content

| | |
|---|---|
| Licensed Content Publisher | Elsevier |
| Licensed Content Publication | Talanta |
| Licensed Content Title | Nickel metal-organic framework 2D nanosheets with enhanced peroxidase nanozyme activity for colorimetric detection of H2O2 |
| Licensed Content Author | Jingyuan Chen,Yun Shu,Huilei Li,Qin Xu,Xiaoya Hu |
| Licensed Content Date | Nov 1, 2018 |
| Licensed Content Volume | 189 |
| Licensed Content Issue | n/a |
| Licensed Content Pages | 8 |

## Order Details

| | |
|---|---|
| Type of Use | reuse in a thesis/dissertation |
| Portion | figures/tables/illustrations |
| Number of figures/tables/illustrations | 1 |
| Format | both print and electronic |
| Are you the author of this Elsevier article? | No |
| Will you be translating? | No |

## About Your Work

| | |
|---|---|
| Title | Exploring optical sensors for Hydrogen Peroxide on silk and paper platforms using chemical dye, peroxidase and gold nanoclusters as signal generating systems |
| Institution name | Indian Institute of Technology Guwahati |
| Expected presentation date | May 2022 |

## Additional Data

| | |
|---|---|
| Portions | Scheme 1 |

## Requestor Location

| | |
|---|---|
| Requestor Location | Indian Institute of Technology Guwahati<br>A 227, Subansiri Hostel<br>IIT Guwahati<br><br>Guwahati, Assam 781039<br>India<br>Attn: Indian Institute of Technology Guwahati |

## Tax Details

| | |
|---|---|
| Publisher Tax ID | GB 494 6272 12 |

## Price

| | |
|---|---|
| Total | 0.00 USD |

Total: 0.00 USD

CLOSE WINDOW ORDER MORE



TH-2731_146106001

## Horseradish Peroxidase Functionalized Fluorescent Gold Nanoclusters for Hydrogen Peroxide Sensing

**Author:** Fang Wen, Yanhua Dong, Lu Feng, et al
**Publication:** Analytical Chemistry
**Publisher:** American Chemical Society
**Date:** Feb 1, 2011



### PERMISSION/LICENSE IS GRANTED FOR YOUR ORDER AT NO CHARGE

This type of permission/license, instead of the standard Terms and Conditions, is sent to you because no fee is being charged for your order. Please note the following:

- Permission is granted for your request in both print and electronic formats, and translations.
- If figures and/or tables were requested, they may be adapted or used in part.
- Please print this page for your records and send a copy of it to your publisher/graduate school.
- Appropriate credit for the requested material should be given as follows: "Reprinted (adapted) with permission from {COMPLETE REFERENCE CITATION}. Copyright {YEAR} American Chemical Society." Insert appropriate information in place of the capitalized words.
- One-time permission is granted only for the use specified in your RightsLink request. No additional uses are granted (such as derivative works or other editions). For any uses, please submit a new request.

If credit is given to another source for the material you requested from RightsLink, permission must be obtained from that source.

BACK CLOSE WINDOW



TH-2731_146106001

# American Physical Society
# Reuse and Permissions License

04-Mar-2022

This license agreement between the American Physical Society ("APS") and Phurpa Thungon ("You") consists of your license details and the terms and conditions provided by the American Physical Society and SciPris.

## Licensed Content Information

| | |
|---|---|
| **License Number:** | **RNP/22/MAR/051062** |
| **License date:** | 04-Mar-2022 |
| **DOI:** | 10.1103/PhysRevLett.93.077402 |
| **Title:** | Highly Fluorescent, Water-Soluble, Size-Tunable Gold Quantum Dots |
| **Author:** | Jie Zheng, Caiwei Zhang, and Robert M. Dickson |
| **Publication:** | Physical Review Letters |
| **Publisher:** | American Physical Society |
| **Cost:** | USD $ 0.00 |

## Request Details

**Does your reuse require significant modifications**: No

| | |
|---|---|
| **Specify intended distribution locations:** | India |
| **Reuse Category:** | Reuse in a thesis/dissertation |
| **Requestor Type:** | Student |
| **Items for Reuse:** | Figures/Tables |
| **Number of Figure/Tables:** | 1 |
| **Figure/Tables Details:** | Figure 1 |
| **Format for Reuse:** | Print and Electronic |
| **Total number of print copies:** | Up to 1000 |

## Information about New Publication:

| | |
|---|---|
| **University/Publisher:** | Indian Institute of Technology Guwahati |
| **Title of dissertation/thesis:** | Exploring optical sensors for Hydrogen Peroxide on silk and paper platforms using chemical dye, peroxidase and gold nanoclusters as signal generating systems |
| **Author(s):** | Phurpa Dema Thungon |
| **Expected completion date:** | May. 2022 |

## License Requestor Information

| | |
|---|---|
| **Name:** | Phurpa Thungon |
| **Affiliation:** | Individual |
| **Email Id:** | phurpa@iitg.ac.in |
| **Country:** | India |

# American Physical Society
# Reuse and Permissions License

**TERMS AND CONDITIONS**

The American Physical Society (APS) is pleased to grant the Requestor of this license a non-exclusive, non-transferable permission, limited to Print and Electronic format, provided all criteria outlined below are followed.

1. You must also obtain permission from at least one of the lead authors for each separate work, if you haven't done so already. The author's name and affiliation can be found on the first page of the published Article.
2. For electronic format permissions, Requestor agrees to provide a hyperlink from the reprinted APS material using the source material's DOI on the web page where the work appears. The hyperlink should use the standard DOI resolution URL, http://dx.doi.org/{DOI}. The hyperlink may be embedded in the copyright credit line.
3. For print format permissions, Requestor agrees to print the required copyright credit line on the first page where the material appears: "Reprinted (abstract/excerpt/figure) with permission from [(FULL REFERENCE CITATION) as follows: Author's Names, APS Journal Title, Volume Number, Page Number and Year of Publication.] Copyright (YEAR) by the American Physical Society."
4. Permission granted in this license is for a one-time use and does not include permission for any future editions, updates, databases, formats or other matters. Permission must be sought for any additional use.
5. Use of the material does not and must not imply any endorsement by APS.
6. APS does not imply, purport or intend to grant permission to reuse materials to which it does not hold copyright. It is the requestor's sole responsibility to ensure the licensed material is original to APS and does not contain the copyright of another entity, and that the copyright notice of the figure, photograph, cover or table does not indicate it was reprinted by APS with permission from another source.
7. The permission granted herein is personal to the Requestor for the use specified and is not transferable or assignable without express written permission of APS. This license may not be amended except in writing by APS.
8. You may not alter, edit or modify the material in any manner.
9. You may translate the materials only when translation rights have been granted.
10. APS is not responsible for any errors or omissions due to translation.
11. You may not use the material for promotional, sales, advertising or marketing purposes.
12. The foregoing license shall not take effect unless and until APS or its agent, Aptara, receives payment in full in accordance with Aptara Billing and Payment Terms and Conditions, which are incorporated herein by reference.
13. Should the terms of this license be violated at any time, APS or Aptara may revoke the license with no refund to you and seek relief to the fullest extent of the laws of the USA. Official written notice will be made using the contact information provided with the permission request. Failure to receive such notice will not nullify revocation of the permission.
14. APS reserves all rights not specifically granted herein.
15. This document, including the Aptara Billing and Payment Terms and Conditions, shall be the entire agreement between the parties relating to the subject matter hereof.

## Detection of Enzymatically Generated Hydrogen Peroxide by Metal-Based Fluorescent Probe

**Author:** Yutaka Hitomi, Toshiyuki Takeyasu, Takuzo Funabiki, et al
**Publication:** Analytical Chemistry
**Publisher:** American Chemical Society
**Date:** Dec 1, 2011



### PERMISSION/LICENSE IS GRANTED FOR YOUR ORDER AT NO CHARGE

This type of permission/license, instead of the standard Terms and Conditions, is sent to you because no fee is being charged for your order. Please note the following:

- Permission is granted for your request in both print and electronic formats, and translations.
- If figures and/or tables were requested, they may be adapted or used in part.
- Please print this page for your records and send a copy of it to your publisher/graduate school.
- Appropriate credit for the requested material should be given as follows: "Reprinted (adapted) with permission from {COMPLETE REFERENCE CITATION}. Copyright {YEAR} American Chemical Society." Insert appropriate information in place of the capitalized words.
- One-time permission is granted only for the use specified in your RightsLink request. No additional uses are granted (such as derivative works or other editions). For any uses, please submit a new request.

If credit is given to another source for the material you requested from RightsLink, permission must be obtained from that source.

BACK CLOSE WINDOW



TH-2731_146106001

CCC | Marketplace™

This is a License Agreement between Phurpa Thungon ("User") and Copyright Clearance Center, Inc. ("CCC") on behalf of the Rightsholder identified in the order details below. The license consists of the order details, the CCC Terms and Conditions below, and any Rightsholder Terms and Conditions which are included below.

All payments must be made in full to CCC in accordance with the CCC Terms and Conditions below.

| | | | |
|---|---|---|---|
| **Order Date** | 04-Mar-2022 | **Type of Use** | Republish in a thesis/dissertation |
| **Order License ID** | 1195770-1 | | |
| **ISSN** | 1473-0189 | **Publisher** | ROYAL SOCIETY OF CHEMISTRY |
| | | **Portion** | Chart/graph/table/figure |

## LICENSED CONTENT

| | | | |
|---|---|---|---|
| **Publication Title** | Lab on a chip | **Publication Type** | e-Journal |
| **Article Title** | PDMS lab-on-a-chip fabrication using 3D printed templates. | **Start Page** | 424 |
| | | **End Page** | 430 |
| **Author/Editor** | Royal Society of Chemistry (Great Britain) | **Issue** | 2 |
| | | **Volume** | 14 |
| **Date** | 01/01/2001 | **URL** | http://www.rsc.org/loc |
| **Language** | English | | |
| **Country** | United Kingdom of Great Britain and Northern Ireland | | |
| **Rightsholder** | Royal Society of Chemistry | | |

## REQUEST DETAILS

| | | | |
|---|---|---|---|
| **Portion Type** | Chart/graph/table/figure | **Distribution** | Worldwide |
| **Number of charts / graphs / tables / figures requested** | 1 | **Translation** | Original language of publication |
| | | **Copies for the disabled?** | No |
| **Format (select all that apply)** | Print, Electronic | **Minor editing privileges?** | No |
| **Who will republish the content?** | Academic institution | **Incidental promotional use?** | No |
| **Duration of Use** | Current edition and up to 5 years | **Currency** | USD |
| **Lifetime Unit Quantity** | Up to 499 | | |
| **Rights Requested** | Main product | | |

## NEW WORK DETAILS

TH-2731_146106001

| | | | |
|---|---|---|---|
| **Title** | Exploring optical sensors for Hydrogen Peroxide on silk and paper platforms using chemical dye, peroxidase and gold nanoclusters as signal generating systems | **Institution name** | Indian Institute of Technology Guwahati |
| | | **Expected presentation date** | 2022-05-25 |
| **Instructor name** | Phurpa Dema Thungon | | |

## ADDITIONAL DETAILS

| | | | |
|---|---|---|---|
| **Order reference number** | N/A | **The requesting person / organization to appear on the license** | Phurpa Thungon |

## REUSE CONTENT DETAILS

| | | | |
|---|---|---|---|
| **Title, description or numeric reference of the portion(s)** | Figure 2 | **Title of the article/chapter the portion is from** | PDMS lab-on-a-chip fabrication using 3D printed templates. |
| **Editor of portion(s)** | Comina, Germán; Suska, Anke; Filippini, Daniel | **Author of portion(s)** | Comina, Germán; Suska, Anke; Filippini, Daniel |
| **Volume of serial or monograph** | 14 | **Issue, if republishing an article from a serial** | 2 |
| **Page or page range of portion** | 424-430 | **Publication date of portion** | 2014-01-21 |

# CCC Terms and Conditions

1. Description of Service; Defined Terms. This Republication License enables the User to obtain licenses for republication of one or more copyrighted works as described in detail on the relevant Order Confirmation (the "Work(s)"). Copyright Clearance Center, Inc. ("CCC") grants licenses through the Service on behalf of the rightsholder identified on the Order Confirmation (the "Rightsholder"). "Republication", as used herein, generally means the inclusion of a Work, in whole or in part, in a new work or works, also as described on the Order Confirmation. "User", as used herein, means the person or entity making such republication.

2. The terms set forth in the relevant Order Confirmation, and any terms set by the Rightsholder with respect to a particular Work, govern the terms of use of Works in connection with the Service. By using the Service, the person transacting for a republication license on behalf of the User represents and warrants that he/she/it (a) has been duly authorized by the User to accept, and hereby does accept, all such terms and conditions on behalf of User, and (b) shall inform User of all such terms and conditions. In the event such person is a "freelancer" or other third party independent of User and CCC, such party shall be deemed jointly a "User" for purposes of these terms and conditions. In any event, User shall be deemed to have accepted and agreed to all such terms and conditions if User republishes the Work in any fashion.

3. Scope of License; Limitations and Obligations.

   3.1. All Works and all rights therein, including copyright rights, remain the sole and exclusive property of the Rightsholder. The license created by the exchange of an Order Confirmation (and/or any invoice) and payment by User of the full amount set forth on that document includes only those rights expressly set forth in the Order Confirmation and in these terms and conditions, and conveys no other rights in the Work(s) to User. All rights not expressly granted are hereby reserved.

   3.2. General Payment Terms: You may pay by credit credit or through an account with us payable at the end of

# Colorimetric and visual determination of hydrogen peroxide and glucose by applying paper-based closed bipolar electrochemistry

**Author:** Elmira Rafatmah et al
**Publication:** Microchimica Acta
**Publisher:** Springer Nature
**Date:** Oct 4, 2019



## Order Completed

Thank you for your order.

This Agreement between Indian Institute of Technology Guwahati -- Phurpa Thungon ("You") and Springer Nature ("Springer Nature") consists of your license details and the terms and conditions provided by Springer Nature and Copyright Clearance Center.

Your confirmation email will contain your order number for future reference.

| | |
|---|---|
| License Number | 5261770709219 |
| License date | Mar 04, 2022 |

Printable Details

### Licensed Content

| | |
|---|---|
| Licensed Content Publisher | Springer Nature |
| Licensed Content Publication | Microchimica Acta |
| Licensed Content Title | Colorimetric and visual determination of hydrogen peroxide and glucose by applying paper-based closed bipolar electrochemistry |
| Licensed Content Author | Elmira Rafatmah et al |
| Licensed Content Date | Oct 4, 2019 |

### Order Details

| | |
|---|---|
| Type of Use | Thesis/Dissertation |
| Requestor type | academic/university or research institute |
| Format | print and electronic |
| Portion | figures/tables/illustrations |
| Number of figures/tables/illustrations | 1 |
| Will you be translating? | no |
| Circulation/distribution | 1 - 29 |
| Author of this Springer Nature content | no |

### About Your Work

| | |
|---|---|
| Title | Exploring optical sensors for Hydrogen Peroxide on silk and paper platforms using chemical dye, peroxidase and gold nanoclusters as signal generating systems |
| Institution name | Indian Institute of Technology Guwahati |
| Expected presentation date | May 2022 |

### Additional Data

| | |
|---|---|
| Portions | Figure 2 |

TH-2731_146106001

## Requestor Location

| | |
|---|---|
| Requestor Location | Indian Institute of Technology Guwahati<br>A 227, Subansiri Hostel<br>IIT Guwahati<br><br>Guwahati, Assam 781039<br>India<br>Attn: Indian Institute of Technology Guwahati |

## Tax Details

## $ Price

| | |
|---|---|
| Total | 0.00 USD |

Total: 0.00 USD

CLOSE WINDOW ORDER MORE



TH-2731_146106001